MEMS devices for neuronal recording: Mimicking the Physical Properties of Patch-Clamp Pipettes

Keith Baldwin

A thesis submitted for the degree of Doctor of Philosophy.
The University of Edinburgh.
October 2006

Abstract

The patch-clamp technique pioneered by Sakmann and Neher has provided much insight into neuronal function. However, it is desirable to record from many neurons simultaneously, to examine network behaviour.

The patch-clamp technique is limited by mechanical considerations (vibration and space) to recording only from small numbers of cells simultaneously. Planar-patch-clamp is a proposed solution to these mechanical issues. By integrating many patch-pipette structures on a planar substrate, the vibration and space problems are resolved, potentially allowing patch clamp to be performed on many neurons in a network.

This work focuses on creating MEMS devices to mimic the function of patch pipettes. It is hypothesised that the closer the devices approximate the physical structure of patch pipettes, the more successful they will be in achieving seals and recording from cells.

To test this hypothesis, devices were fabricated with a range of physical properties. The parameters varied were aperture diameter, aperture profile, aperture depth, surface roughness and surface chemistry. Devices with apertures of 1.5m and 2.5m were fabricated, with either a flat profile or a protruding nozzle. The surface material was thermal silicon dioxide, which was optionally doped with boron to change the surface chemistry. Devices were also manufactured with 2m diameters. These had a rougher, PECVD silicon dioxide surface, which produced a more rounded aperture profile.

Using glass patch-pipettes as a control experiment, attempts were made to form seals using these devices and N2A cells. The results obtained showed that aperture depth has a significant effect on seal formation (the deeper the aperture, the higher the seal resistance). Although it was anticipated (on the basis of the control experiments) that aperture diameter would also play a role, this was not witnessed: attempts are made to explain this discrepancy. A significant difference was also found between the PECVD oxide devices and thermal oxide devices (thermal oxide producing higher seal resistances). This is thought to be due to surface roughness, but may also be caused by variations in aperture diameter or aperture depth. It is thus concluded that matching surface roughness and aperture depth to those of glass pipettes is of most importance in the manufacture of planar patch-clamp devices. Although surface chemistry and aperture profile apparently do not affect seal formation, further investigation is required to determine this for certain.

Declaration of originality

I hereby declare that the research recorded in this thesis and the thesis itself was composed and originated entirely by myself in the School of Engineering and Electronics at The University of Edinburgh.

Exceptions:

The contact angle data and roughness data presented in chapter 4 were recorded by Brad Dworak, and these data were originally presented in his PhD thesis [1]. The introduction chapter also borrows from this thesis.

Some of the patch clamp data were gathered by Dr. John Curtis in the School of Biomedical Sciences, University of Edinburgh.

Some of the bubble number data used to derive the relationship between bubble number and tip diameter (chapter 5) were gathered by Simeon Bamford in the School of Biomedical Sciences, University of Edinburgh.

Keith Baldwin

Acknowledgements

I would like to thank my supervisors: Prof. Alan Murray, for his unending support and guidance throughout the project, Dr. Nikki Macleod for her advice and input to the project and Prof. Anthony Walton for providing a home for me at the Scottish Microelectronics Centre, and for his wife's excellent cake.

This project could not have gone ahead without the enthusiasm and expertise provided by Dr. John Curtis, whose many ideas helped shape the work described here. I have Dr. Brad Dworak to thank for kicking off this project, and collaborating with me for much of it. I would like to thank Simeon Bamford for his contributions to the project somewhere around the middle. I also thank Evangelos Delivopoulos, the latest addition to the team, for dragging himself out of bed on those cold winter afternoons.

Many people at the Scottish Microelectronics Centre provided me with invaluable assistance, but I would particularly like to thank: Dr. Tom Stevenson, for his tireless efforts printing the tiny holes for which I spent so long searching, Alan Gundlach, for his insight on all aspects of device manufacture, Dr. Bill Parkes, for endless discussions about deep silicon etching, Dr. Andy Bunting, for his help running the oxidation furnace, Gerry McDade who spent time and effort drilling out countless lumps of perspex in pursuit of the perfect base unit, and Alec Ruthven, for letting me destroy the saw.

Thanks also to Prof. Chris Wilikinson from the department of Electronics and Electrical Engineering at Glasgow University for providing the photolithography mask used to print the apertures.

I would also like to thank(?) Dr. Stefan Enderling and Dr. Natalie Plank for convincing me to use LaTeXand their help with the many problems this caused.

Finally, I would like to thank Adrianna Teriakidis for her amazing fish pie, and I would thank Finlay Stewart to put more clothes on.

Contents

List of figures

List of tables

Glossary and Acronyms

Glossary

Aperture The narrowest part of a planar patch clamp device, with which the cell makes contact.

Aperture Depth The length of the sealing surface inside the aperture.

Aperture Profile The profile observed by viewing an aperture in elevation, after sectioning.

Bleb That part of the cell membrane drawn into the aperture during seal formation.

Chamber The wider bottom section of a planar patch clamp device, filled with intracellular solution.

Nozzle A feature which protrudes above the substrate surface in a planar patch clamp device.

PECVD Devices The devices whose fabrication was originally presented by Dworak [1].

Shank The narrow, tapered section of a pipette, analogous to the Aperture.

Stem The wide, un-melted section of a pipette, analogous to the Chamber.

Surface Roughness The roughness of the sealing surface, in most cases inside the aperture.

Thermal Oxide Devices The devices whose manufacture is presented here.

Well The space underneath the silicon device, containing intracellular solution.

Acronyms

AFM	Atomic Force Microscope
CHO	Chinese Hamster Ovary
EAD	Estimated Aperture Depth
ECM	Extracellular Matrix
EPSP	Excitatory Post Synaptic Potential
FIB	Focussed Ion Beam
HEK	Human Embryo Kidney
HF	Hydrogen Fluoride (Hydrofluoric Acid)
HMDS	HexaMethylDiSilazane
ICP	Inductively Coupled Plasma
IPSP	Inhibitory Post Synaptic Potential
LPCVD	Low Pressure Chemical Vapour Deposition
MEA	Micro-electrode Array
MEMS	Micro-Electro-Mechanical-Systems
MT	(Device) Membrane Thickness
PDMS	PolyDiMethylSiloxane
PECVD	Plasma Enhanced Chemical Vapour Deposition
RIE	Reactive Ion Etching
SEM	Scanning Electron Microscope
SOI	Silicon on Insulator
XPS	X-ray Photo-electron Spectroscopy

Chapter 1
Introduction

1.1 Aims

The ultimate challenge in the biological sciences is to understand the function of the brain - the biological processes by which we perceive, think and feel. The brain itself is composed of millions of interconnected neurons and glial cells. The task at hand for those at the forefront of neural science is to explain how millions of neurons interact to produce the phenomena associated with the brain.

Much is known about the function of isolated neurons, due largely to the pioneering work of Hodgkin, Huxley and Katz [7–10] on the ionic conduction of membranes. Network behaviour (the interactions between neurons) has also been studied. Many studies of neuronal activity and network behaviour use conductive electrodes to detect electrical signals extracellularly. Typically this is carried out in living organisms or slices taken directly from the brain. Advances in cell culturing and MEA fabrication have however facilitated the use of in-vitro cultures as a tool for the study of living neuronal networks [11–13]. Many attempts to investigate in-vitro network activity involve using multiple planar surface electrodes to form resistive or capacitive connections to the neurons for extracellular measurements [14].

MEA devices made with up to 60 electrodes or more yield a significant bandwidth of data on network behaviour (e.g. circadian rhythms and differentiating firing patterns in dissociated cell cultures of hippocampal neurons) [15, 16]. Also, under certain conditions long-term neurological studies can be conducted for periods of up to several months [17]. However, the extracellular nature of these recordings makes it difficult to map and isolate single synaptic events to individual cells and synapses. Typically, only spiking events are detected and counted. Other evidence suggests that this approach has limitations regarding cell/substrate adhesion and the proximity between the cell and electrode [18]. Furthermore, it has been suggested that neurons do not form ion channels well along the contact surface, decreasing the quality of electrode recordings [19].

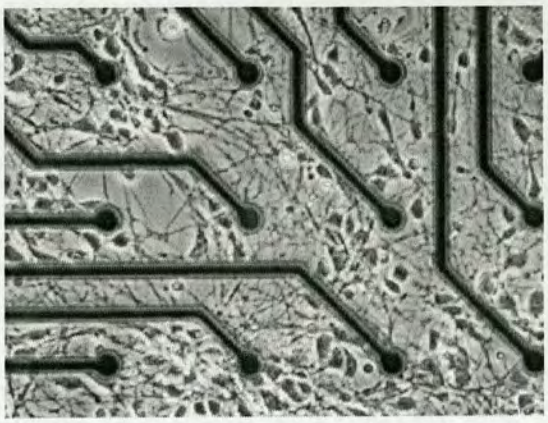

Figure 1.1: *An example of a random, in-vitro culture grown on a micro-electrode array. Taken from Potter, 2005 [2].*

Intracellular recording techniques have two main advantages over these extracellular recordings; the certainty with which one can associate recorded activity with a particular neuron, and the ability to study not only spiking activity but the behaviour of sub-threshold events that integrate and determine the spiking activity of the network under study. Indeed the importance of sub-threshold activity to the output of a network is becoming increasingly clear. The measured biophysical properties of a neuron in isolation or in a low activity de-afferented in-vitro preparation (brain slice) may not represent that found in vivo. Here there is a constant barrage of post synaptic EPSPs and IPSPs (excitatory and inhibitory post synaptic potentials - see figure 1.3) resulting in a network activity dependent fluctuation of membrane resistance and membrane potential [20]. With this in mind attempts have been made to assess the biophysical properties of neurons more accurately by injecting them with computer simulated network activity modelled noise [21]. A multi-electrode intracellular study of a neuronal network would therefore provide an insight into the interaction between spike output and sub-threshold activity and also how components of the network interact to produce any given level of sub-threshold activity.

The technique of intracellular recording was introduced to neuroscience in the 1950s with the development of the sharp microelectrode by Sir John Eccles [22]. This involves penetrating a cell membrane with a sharp micropipette (tip $< 1\mu m$). Pipettes with tips of this diameter are formed by melting and extruding glass capillaries until they break. By varying the temperature, pulling force and speed, it is possible to control the tip diameter at which the capillary breaks [23]. Such pipettes are normally filled with saline solution, allowing a silver electrode inside the pipette to directly record the potential inside the cell.

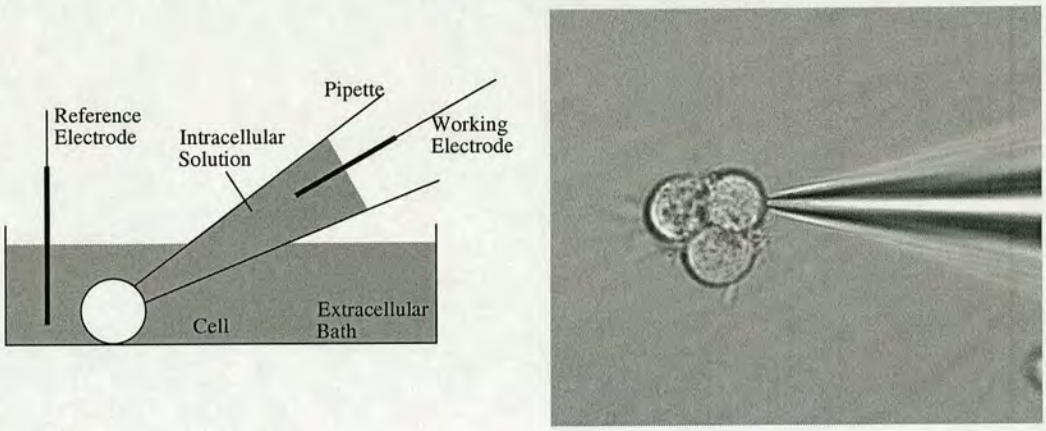

Figure 1.2: *A typical patch clamp experiment. Left: The working electrode is positioned inside the glass pipette and the reference electrode in the bath outside the cell. Both electrodes are normally silver chloride coated silver, to improve baseline stability. Right: plan view of an actual patch-clamp experiment on N2A cells.*

A more refined approach called patch-clamp was developed by Sakmann and Neher in the 1970s [24]. This involves sealing a micropipette (tip $\sim 1 \mu m$) onto the cell membrane, to make low noise measurements of the membrane 'patch' bounded by the pipette tip. The quality of the seal (measured in terms of its resistance) determines the resolution of recordings which can be made. With a seal resistance greater than one gigaohm, the opening and closing of single ion channels in the membrane can be observed. Intracellular patch clamp (commonly referred to as 'whole-cell' patch-clamp) did not appear until the 1980s [25]. This is an extension of the extracellular (cell-attached) patch-clamp in which suction is applied to the membrane in order to rupture it, providing a conductive pathway to the interior of the cell. The recorded potential is that of the entire membrane, hence the name whole-cell. The giga-ohm seal between cell and glass electrode and the lower pipette resistance improve the signal to noise ratio relative to sharp recordings. The giga-ohm seal also reduces artefacts associated with membrane damage around the penetration site of sharp electrode recordings [26]. The patch method of intracellular recording is thus favourable especially when small sub-threshold events are of particular interest.

Extending the use of intracellular techniques to networks of neurons has inherent limitations. Generally, examining the neuronal activity of multiple patch clamped neurons is not an easy task. Manoeuvring patch-pipettes is difficult because the positioning devices are bulky and are sensitive to vibration from the surrounding environment. To date, up to three neurons have been recorded from simultaneously using conventional sharp or patch micropipette recordings

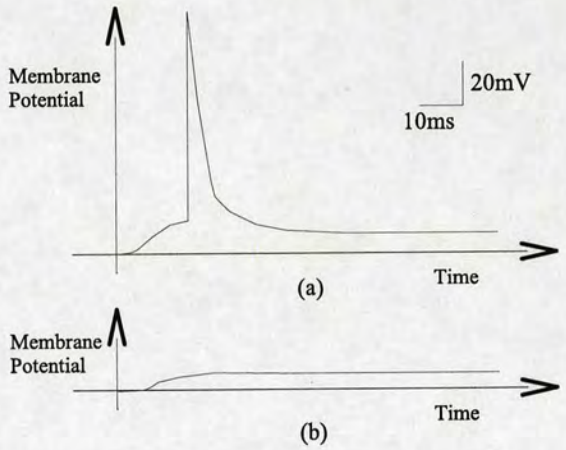

Figure 1.3: *(a) An example of an action potential (b) An example of an excitatory post-synaptic potential (taken from the same cell). From Sakmann and Neher, 1995 [3].*

to study synaptic transmission [27]. The development of a multi-electrode planar patch device - a hybrid of microelectrode arrays and patch-clamp - would therefore have significant impact on the study of neuronal interaction, signal integration and the formation of coherent behaviour in neuronal networks.

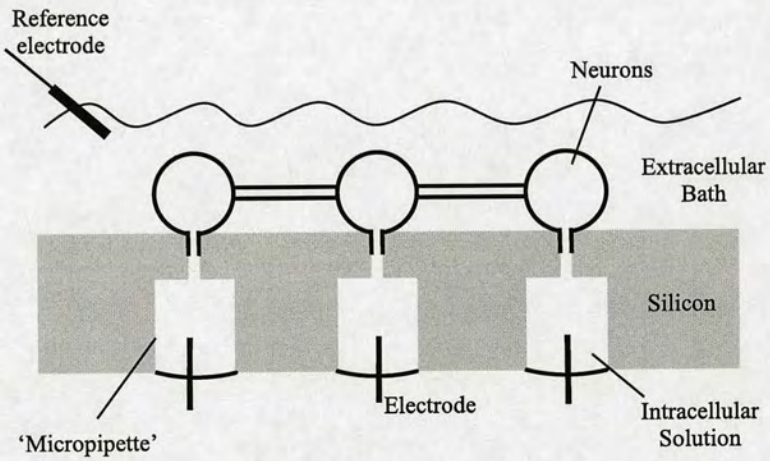

Figure 1.4: *The proposed planar patch clamp setup*

In order to create a multi-channel patch-clamp system, it is necessary to produce functional patch apertures on a planar substrate. It is desirable that these apertures produce seals on neurons with as high a resistance as possible. The higher the seal resistance with which cells can seal onto these apertures, the higher the quality of recordings which will be obtained. A high seal resistance will also reduce the rate at which the health of the cells deteriorates after

membrane rupture.

Dworak [1] concluded that the mechanism of patch-clamp seal formation is not well understood. Therefore, there is little to indicate how to design patch-clamp apertures for high seal resistance. The geometry, surface properties and profile might all have an effect on seal formation. However, since glass pipettes are the benchmark standard for patch-clamp seal formation, it is hypothesised that:

Matching the physical properties mentioned above to those of glass pipettes will optimise seal formation in planar patch-clamp devices.

In order to test this hypothesis, single aperture planar patch-clamp devices were constructed with a range of physical properties. This study builds on the work of Dworak [1], who previously constructed planar patch-clamp devices (referred to from here on as PECVD devices). In addition to these devices, another set of apertures was constructed with a range of physical properties:

Aperture Diameter Aperture diameter is thought to be a crucial variable in seal formations as pipette bore is known to affect seal resistance with glass pipettes. Apertures of three different diameters were created.

Aperture Profile Aperture profile (i.e. the shape of the tip) is thought to play some role, as fire-polishing, a technique known to round pipette tips, is reported to increase seal stability. Device apertures with two different radii of curvature were created. Also, nozzles which protrude from the planar surface were created, to more closely approximate the tip of a pipette.

Surface Material The surface material used by Dworak on his devices (PECVD silicon dioxide) was measured to be fairly rough, while glass is very smooth. For contrast, smooth thermal silicon dioxide was chosen for the new devices. This surface was optionally boron doped with the aim of making the surface chemistry more like that of glass.

Taper Glass pipettes taper inside the tip, as a result of the way in which they are pulled. Attempts were made to produce a similar taper in the apertures of the new devices, in contrast with the PECVD devices, which had vertical apertures.

Aperture Depth Aperture depth was not varied intentionally, though process variations resulted in apertures with a range of depths.

The next chapter of this thesis will deal with the current state of knowledge on patch-clamp seal formation, and the current progress in the field of planar patch clamp.

Chapter 3 discusses the different techniques used in constructing patch clamp devices on silicon, including a discussion of the shape of the aperture, and the different surfaces used.

Chapter 4 describes the measurement of the physical and electrical properties of the device.

Chapter 5 discusses the control experiments performed to verify the health of the N2A cells used to test the devices, and to test their sealing properties and whole cell characteristics.

Chapter 6 details the experiments undertaken to test the seal formation of the devices with N2A cells.

Chapter 7 discusses the results obtained with the devices and glass and explains these results within the context of the literature examined in chapter 2.

Finally, chapter 8 summarises the thesis and draws conclusions about the effect of different parameters on seal formation and suggests further work in this area.

Chapter 2
Background

This chapter discusses the current theories on seal formation, and the attempts which have been made to record from cells using planar patch-clamp devices.

2.1 Current Theories of Seal Formation

Given the stable nature of gigaohm seals (they persist when suction is removed) and their high impedance to electrical current, it is generally assumed that there is a strong interaction between the cell membrane and glass. The nature of this interaction is poorly understood. Hamill et al. [25] attempt to relate seal resistance to membrane/glass proximity by macroscopic resistance calculations, with the aim of identifying an interaction mechanism. However, Corey and Stevens [28] dispute the validity of such calculations, which result in a separation $\sim$1Å. Instead they suggest that Van der Waals forces, hydrogen bonding and (divalent) salt bridges must all be present, but the relative importance of each is unknown. Support for the presence of salt bridges (an ion with a 2+ charge bridging negative sites on the membrane and the glass) is given by the improved seal formation resulting from increasing Ca^{2+} concentration in the intracellular solution [29].

Opsahl and Webb [30] performed experiments on phospholipid vesicles, which suggest that direct lipid-glass adhesion does occur, whereupon the lipid becomes immobilised on the glass surface. Sokabe, Sachs and Jing [31] reject this theory, based on estimates of tension in the cell membrane. They conclude that the lipid membrane must be free to move over the surface of the glass, as expansion of the cell membrane alone could not support the bleb length increases they witnessed post-sealing. Also, in some cases they noted that the cell membrane expanded into the pipette, without the seal region moving. It is hypothesised that membrane proteins denature onto the glass surface and act as anchor points between the membrane and the glass, around which the lipid membrane can flow freely. Sachs and Qin [32] also suggest a mechanism for conduction through the seal, namely nanoscopic aqueous paths snaking through the glass-membrane interface.

Although the underlying mechanism remains unclear, it is certain that cell membranes do seal onto glass. It has also been shown that quartz can be used to form gigaohm seals on living cells [33]. It should be noted that the electrical properties of quartz are superior to those of borosilicate glass, and the primary reason that glass is more widely used is because of its lower melting point, making it easier to manufacture pipettes. Seal formation is not just limited to hydrophilic surfaces. Coleman et al. [34] have obtained seals with pipettes dipped in Hexamethyldisilazane (HMDS) which makes the surface hydrophobic.

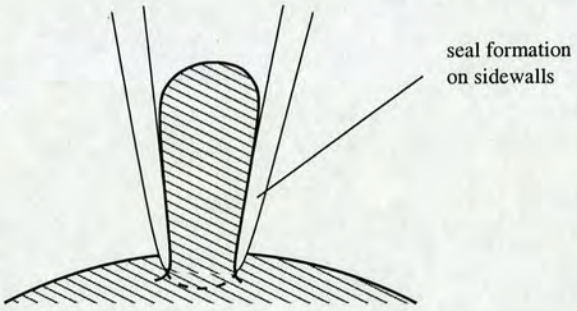

Figure 2.1: *An illustration of seal formation with a glass pipette, illustrating the likely location of seal formation*

Different theories have also been presented on the location of seal formation. Sakmann and Neher [3] suggest that seals can form around the tip of the pipette, but can also extend into the pipette itself. The widespread use of fire-polishing, a technique to round the tip of pipettes, lends some credibility to the importance of the tip area. The fact the tip having a larger radius of curvature (in profile) seems to improve seal stability [28] indicates that the tip must play some role in seal formation. Sokabe and Sachs [35] however, argue that observations of gradual (rather than spontaneous) seal formation imply the seal itself must be distributed over a large area. This is supported by observations that pipettes containing excised patches are not affected by physically contacting the tip.

In addition, the relative surface areas inside the pipette and on the tip, point to the interior of the pipette being the most significant contributor to seal formation. Corey and Stevens [28] and Opsahl and Webb [30] report 'bleb' lengths up to $10\mu m$[1]. Ruknudin, Song and Sachs [36] who have performed a more detailed study using electron microscopy, report bleb lengths between $5\mu m$ and $100\mu m$, with $10 - 20\mu m$ a common value. They also report a dependence of bleb lengths on cell type (different cell types producing blebs of different lengths) and suction method (gentle prolonged suction producing smaller blebs than sharp sucks applied by mouth).

[1] A bleb is the portion of the cell drawn into the pipette upon sealing.

However, Sokabe and Sachs [35] suggest that there is no dependence of seal resistance on bleb length.

The final parameter described in the literature which affects seal formation is the bore of the pipette used to form seals. It is widely known that the larger the pipette bore, the harder it is to obtain giga-ohm seals [37]. However, bores which are too small hinder the rupturing of the membrane to obtain the whole cell configuration. Diameters of $1 - 2\mu m$ are generally thought to be optimal, but this depends on the cell type used.

2.2 Current Progress in Planar Patch Clamp

The majority of work in the field of planar patch clamp is focussed on developing single cell devices for high throughput ion channel measurements, to facilitate drug screening. Some of this work has been performed in industry, and in many cases the precise technical details are proprietary information, and not published in the literature. Notable industrial players include Sophion Biosciences (Denmark), Nanion (Germany), Cytocentrics (Germany) and Molecular Devices (USA) who have recently acquired Aviva Biosciences, Axon Instruments and Essen Instruments, along with their intellectual property in this field. However, there is much valuable work which has been performed by academic groups. Established researchers in this field include Klemic and Sigworth at Yale, Fertig and Behrends at Ludwig-Maximilians in Munich (from which Nanion emerged), and two groups in Lausanne (Schmidt et al. and Lehnert et al.). There are also two groups at UCLA (Pantoja et al. and Matthews and Judy), and groups in Berkley (Lee et al.), Georgia (Han et al.), Lehigh University (Pandey et al.) and a group from the Commissariat a l'Energie Atomique in Grenoble (Sordel et al.).

2.2.1 Nitride Membrane Devices

The first attempts at forming seals on a planar device were made by Fertig et al. [38]. These first attempts made use of a micron sized aperture in a 120nm thick nitride membrane (see figure 2.2). Such devices were also tested by Schmidt et al. [39], Pandey et al. [40] and Klemic et al. [41]. Although some success was had in recording properties from artificial lipid bilayers (Schmidt) and membrane patches (Fertig) sealed on to the top of the nitride membrane, these devices failed to yield giga-ohm seals on living cells. Pandey [42] reports seals of only $20M\Omega$ on CHO cells with 1-$2\mu m$ apertures in a 100nm thick membrane. The failure to obtain seals is

attributed to the lack of area inside the aperture onto which a bleb could seal.

2.2.2 Silicon/Oxide Membrane Devices

Subsequent attempts to create planar patch clamp devices in silicon focussed on devices with a thicker, silicon membrane, generally coated with silicon dioxide to mimic glass.

Such devices have been brought to market by Sophion Biosciences. The precise details of the manufacturing process are unclear. It appears that their devices consist of a 0.5-1.2μm aperture in a 10μm silicon membrane and that the surface layer of the devices is silicon dioxide [43]. The devices also appear to have a large radius of curvature in profile [44]. Recent data [45] gives the success rate for both gigaohm seal formation and whole cell recording as 80%. The success rate for successful completion of experiments lasting 25 minutes was about 50%. Experiments were performed with Chinese hamster ovary (CHO).

Cyctocentrics are another company which have produced silicon based devices. Their devices consist of a protruding nozzle made of silicon dioxide to mimic the pipette tip [46]. This nozzle is surrounded by a larger aperture, used to provide suction to manoeuvre cells towards the nozzle. The entire structure is fabricated in silicon dioxide (at least some of which is deposited by PECVD), on a silicon substrate. They suggest [47] that for successful gigaohm seals, an aperture less than 2μm in diameter and greater than 10μm in depth, which seems to correspond to images of their devices. Experimental data has been published for both N2A [47] and CHO [46] cell lines. The N2A cells produced gigaohm seals with a 68% success rate, and an average seal resistance of 1.2$G\Omega$. 77% went whole cell. The CHO cells formed gigaohm seals with 92% success rate and produced stable whole cell recordings 75% of the time; the median seal resistance was 2.6$G\Omega$.

Lehnert, Laine and Gijs were the first academic group to present results from thick membrane devices. Like Cyctocentrics, these devices also feature a protruding nozzle [48]. This is fabricated by growing thermal silicon dioxide on the inside of a deep etched silicon aperture and etching back the silicon to reveal the nozzle. The nozzles themselves are greater than or equal to 2.5μm in (inner) diameter and 10-30μm deep. The nozzle wall is 500nm thick. The average seal resistance formed on CHO cells with the 2.5μm device is 180$M\Omega$. The maximum seal obtained is 240$M\Omega$. These seal values decrease for larger diameters devices. The poor seals obtained are probably attributable to the excessive diameter of the apertures. The sidewall

roughness produced by the deep silicon etching (visible in images of the devices) could also detrimentally affect seal formation. Modification of the these devices [49] by applying a thin layer of Polydimethylsiloxane (PDMS) improves their sealing properties. The PDMS, after curing, has to be activated in an oxygen plasma to render the surface hydrophilic [50]. The result is an increase in average seal resistance to $300M\Omega$. However, this could be as much to do with the PDMS narrowing the aperture of the nozzle, as the surface properties themselves. The PDMS could also serve to reduce the sidewall roughness.

Pantoja et al. [51] have produced devices with PECVD silicon dioxide coated apertures ranging from $0.7\mu m$ and $2\mu m$ in diameter and $10-40\mu m$ in depth. The aperture is formed by deep silicon etching and oxide deposition (0.5-1μm thick). These devices have been tested with many different cell types. Giga-ohm seals have been achieved with CHO and RINm5F cells. However, the average resistances obtained for each cell type with apertures of different diameters are all in the range 50-100$M\Omega$. Results obtained with RAW264.7 cells, indicate a dependence of seal resistance on diameter, with the smaller apertures performing better. However, this trend does not hold for the apertures with diameters below $1\mu m$, a fact which is attributed to the different manufacturing processes to which these apertures were subjected. It is also suggested that apertures greater than $2\mu m$ are unsuitable for sealing. No analysis is given on the effect of the device aperture depth. The reason for inconsistent seal formation of these devices could be the roughness of the silicon dioxide deposited by PECVD, or sidewall roughness produced by deep etching.

However, Sordel et al. believe that PECVD silicon dioxide has a positive effect on seal resistance. This conclusion is based upon devices fabricated by creating a $2.5\mu m$ aperture in a $2.1\mu m$ thick membrane in a thermal silicon dioxide layer [52]. These devices, tested with Human Embryo Kidney (HEK) yielded an average seal resistance of $30M\Omega$ and no seals above $100M\Omega$. These devices were subsequently coated with a $1.5\mu m$ layer of PECVD silicon dioxide, which reduced the aperture diameter to $1.7\mu m$ [53]. The resulting average seal resistance was $155M\Omega$, with a maximum of $7G\Omega$. However, only 6 seals out of 157 were greater than $1G\Omega$ and 37 greater than $100M\Omega$. The improved sealing results could easily be attributed to the reduction of the hole diameter cause by the PECVD oxide, rather than the surface itself. However, it is claimed that reduction in diameter is not the only cause of the resistance increase, as devices printed at a diameter $1.7\mu m$ without PECVD oxide did not perform as well as those with PECVD (Although this data is not presented). It is suggested that the roughness of

PECVD oxide may help seal formation. However, it seems more likely that increase in aperture depth (3.6 vs. 2.1μm) explains the improved performance, as these aperture depths are some way below the expected bleb lengths for most cells.

Matthews and Judy initially produced devices with a 30μm thick silicon membrane and a Bosch etched aperture [54]. This was subsequently coated in thermal oxide or LPCVD oxide. The thickness of this oxide was varied to produce aperture diameters between 500nm and 2.5μm. However, no sealing results were presented for these devices, and this design was modified [55]. The new design consisted of a 20μm membrane with apertures of the same diameters. However, the new manufacturing process involved growing thermal oxide on a Bosch etched aperture as before, but this time the oxide was stripped, to remove the sidewall roughness, and amorphous silicon (a-Si) was deposited to round the apertures. Thermal oxide was then re-grown on the a-Si layer. This process has the advantage of deep etching without the sidewall roughness, and the low roughness of thermal oxide without the faceting produced by growing it on crystalline silicon. This process also produces apertures with a rounded profile. However, it can be seen from images presented of these devices that there is still some evidence of sidewall roughness after the a-Si deposition, so this may not have been completely removed. Also, the roughness of a-Si is somewhat greater [56] than that of glass or a crystalline silicon wafer (but less than that of PECVD oxide), and the resulting thermal oxide grown may reflect this. Gigaohm seals have been achieved with these devices using CHO cells, though they cannot be obtained reliably. No success rate or mean seal resistance is given, nor the aperture diameter with which these were obtained.

The final group to have constructed silicon based planar patch devices is Lee et al [57]. They report thermal oxide nozzles very similar to the nozzles produced by Lehnert. The membranes of these devices are 75μm thick, with aperture diameters of 1, 3 and 10μm. The nozzle wall is 1.5μm thick, and the entire device is coated with 350nm of silicon nitride. No attempts to form seals with these devices were reported.

2.3 Glass Devices

After failing to obtain gigaohm seals with nitride membrane devices, Fertig et al. developed a process for making planar patch clamp devices from a glass substrate. The manufacturing process [58] involves locally thinning a glass membrane to create an 80μm deep membrane.

A particle accelerator is then used to penetrate this membrane with a high energy gold ion. This ion leaves a conical damage track which is susceptible to etching. Immersing this in Hydrofluoric acid (HF) dissolves the damage track, leaving a conical aperture with a taper similar to that of pipette. By varying the etch time, the aperture diameter can be controlled. Sub-micron apertures have been reported, but specific dimensions are not given. Such devices were used to record from channels in lipid bilayers. Subsequent attempts were made with devices having a thinner $20\mu m$ membrane. Tests were performed on CHO and NIE115 (mouse neuroblastoma) cells. Seal resistances of 1-10$G\Omega$ were obtained routinely [59], though success rates were not given. Whole cell recordings were reported to be obtained 30% of the time [60]. This technology was spun out to form the company Nanion Technologies. Recent publications by Nanion indicate gigaohm seal success rates of up to 70% [61].

Aviva Biosciences is another company to have produced commercially available devices using glass substrates. They were acquired by Axon Instruments, who in turn were acquired by Molecular Devices. Molecular devices now produce the PatchXpress, an automated patch clamp system using the SealChip originally designed by Aviva. Little is known about the SealChip, other than it is made of glass covered with a proprietary coating which improves seal formation. Whole cell recordings are reported with a 75% success rate [62].

2.4 Other Materials

When Klemic and Sigworth abandoned nitride membranes, they turned instead to PDMS as a substrate for planar patch devices. First attempts involved moulding the PDMS, against either a glass micropipette or a micro-machined polyurethane master [63]. Apertures were produced with 2-20μm diameter and constant taper. The PDMS devices needed to be treated in an oxygen plasma to make them hydrophilic before patching could succeed. A 13% giga-ohm seal formation rate was observed with Xenopus Oocytes. In order obtain better control of the device aperture dimension a new technique was developed, where a hole was blown into a thin layer of PDMS prior to curing [64]. Using a metal mask to confine a nitrogen stream to the desired aperture size, the diameter could be accurately controlled. The thin layer of PDMS (20-100μm once cured) was then peeled from the metal mask, and mounted in a larger frame. It was then treated with an oxygen plasma as before, yielding giga-ohm seal success rates of 25%, 10% and 7% with Oocytes, RBL and CHO respectively. About 50% of gigaohm seals produced whole cell recordings, but in many cases suction caused the cell membrane to rupture before a

gigaohm seal was obtained. Further investigation [65] revealed that long (2 days), high temperature (180°) curing periods and long (4 hours) plasma exposure promoted seal formation. This modification of the process increased the giga-ohm seal rate to 24% for RBL cells.

Lee et al. have also used PDMS as a patch clamp surface material. However, rather than adopting the conventional planar patch approach, they have produced horizontal apertures [66]. Cylindrical hollows moulded in PDMS are bonded onto flat glass substrates, creating patch apertures with two different surface materials. No plasma treatment was used, and an average seal resistance of $120M\Omega$ was obtained, with a maximum of $200M\Omega$. When the lateral aperture was raised up to $20\mu m$ above the glass substrate, so that it was entirely bounded by PDMS, seal resistances of around $350M\Omega$ were obtained 75% of the time [67].

IonWorks HT is another planar patch clamp system offered by Molecular Devices. It was originally developed by Essen Instruments [68][69], who were subsequently acquired by Molecular Devices. The idea behind IonWorks HT is not the formation of giga-ohm seals, but rather the formation of megaohm seals, and the use of the perforated patch technique [70]. This involves perfusing an antibiotic, such as amphotericin, into the intracellular side of the device, to make the membrane patch permeable to ions and hence electric current. In this way the intracellular potential can be measured, without rupturing the membrane. This has advantages over whole cell recordings in terms of cell health [71], but the primary reason for which it is used in the IonWorks HT is throughput. Antibiotic perfusion is more reliable than the mechanical processes of sealing and going whole cell, thus higher yield of intracellular recordings is expected. Given the lower seal resistance, the quality of the recordings will be diminished, but this is acceptable if the measured signal is sufficiently large. Intracellular recording rates as high as 80% have been reported. Useful seals are formed 94% of the time, although useful is defined as being greater than $50M\Omega$. Average seal resistances of $120M\Omega$ have been achieved, with values as high as $300M\Omega$ [72]. Precise details of the physical device properties are not given other than that the device is made from a polymer membrane, in which a hole is etched by laser.

Stett et al. at Reutinglen (who went on to form Cytocentrics) have also made attempts to form seals with polymer membranes [73]. They use a membrane $6.5\mu m$ thick coated with 100nm of silicon nitride. The apertures are 2 or $4\mu m$ wide and are produced by a focussed ion beam (FIB). Devices were tested with CHO, and Purkinje heart cells from sheep. Median seal resistance values of $25M\Omega$ with Purkinje cells, and $22.8M\Omega$ with CHO were obtained for $2\mu m$ devices. $4\mu m$ devices performed significantly worse ($1.3M\Omega$). However, gigaohm

seals were observed for the $2\mu m$ devices, though extremely rarely (4 out of 75 attempts) and a single whole cell recording was achieved. It was noted that cells which did form gigaohm seals were significantly more difficult to remove from the apertures than those which only reached mega-ohm levels, and the resistance of megaohm seals was dependent on suction being applied, where as gigaohm seals were stable in the absence of suction. These devices have a relatively wide and shallow aperture, which could explain the inconsistent results obtained. However, it is suggested that some of the sealing is expected to occur on the top surface of the membrane. The FIB etching of the aperture should leave a fairly smooth surface inside the aperture, but the roughness of the nitride layer is unknown.

Finally, Han et al. have produced polyimide membranes for electro-physiological recordings, but their approach is somewhat different. They have produced $3\mu m$ apertures in a $6\mu m$ thick membrane. Gold electrodes are embedded in the polyimide membrane at opposite sides of each aperture. Chromaffin cells are sucked into the aperture, allowing conventional patch clamp recordings to be performed, and also recordings between the electrodes in the membrane. Seal resistances up to $1.2G\Omega$ have been obtained, but it is not clear which electrodes were used to measure this impedance [74].

2.5 Previous work in Edinburgh

Initial attempts at patching on silicon based devices were made by Brad Dworak [1] using a simple device structure based around a silicon nitride membrane, similar to those used by Fertig [38], Schmidt [39] and Klemic [41]. The structure of these devices is shown in figure 2.2. No seals or recordings were achieved with these devices, and this approach was abandoned after other groups failed to achieve meaningful seals with similar devices.

Motivated by the observation that seal formation may occur along the sidewalls of the pipette and not just around the tip [3][30], it was concluded that the 0.5μm silicon nitride membrane in the previous devices would not have provided sufficient surface area for seal formation. The next generation of devices were designed and constructed with a thicker 10-15μm silicon membrane. In addition, the radius of curvature of the aperture was increased to mimic fire-polished pipettes. These devices also featured a vertically etched back cavity to allow closer spacing of planar patch devices.

The process flow is shown in figure 2.3. The front hole was deep etched in an inductively

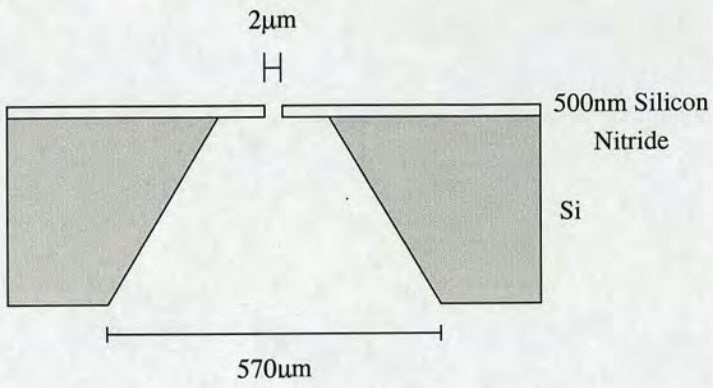

Figure 2.2: *The structure of the first silicon patch clamp devices*

coupled plasma (ICP) Bosch etcher using a thermal oxide mask. This etch continued until it reached the embedded oxide stop layer. Subsequently, the back side chamber was deep etched, using a combination of thermal oxide and photoresist as a mask (to allow for the necessary etch depth to be reached without the mask breaking down). This left the buried oxide layer, which was removed with 48% Hydrofluoric acid and a surfactant. Thermal oxide was grown as an insulator. To achieve the desired radius of curvature, silicon dioxide was deposited by Plasma Enhanced Chemical Vapour Deposition (PECVD) [75]. Different surface finishes were then obtained by annealing or boron doping the PECVD oxide. The details of this process can be found in appendix A.

These devices were tested with neurons obtained by primary dissection of pond snails (lymnea stagnalis) and acute dissociation by trituration. However, patching on cells from a primary dissection is hindered by extracellular matrix (ECM) proteins [28]. In order to ameliorate these problems, the cells were treated with trypsin, but this may have compromised the integrity of the cell membranes. Cell damage during the trituration process was also a cause for some concern. These cells never sealed reliably onto glass pipettes, and the devices produced only transient seal resistances of around 50MΩ, with a single seal reaching $600M\Omega$.

2.6 Summary

In summary, the precise nature of gigaohm seal formation is not known. However, gigaohm seals have been formed on planar devices with a wide range of surface properties and geometries. The important details of the various attempts at planar patch clamp are summarised in

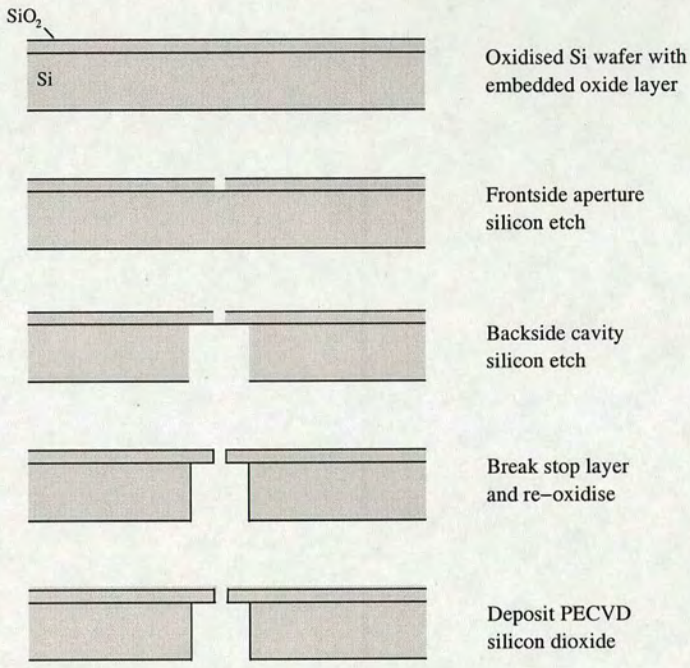

Figure 2.3: *Process outline for the PECVD oxide devices. Grey represents silicon, and black represents silicon oxide.*

table 2.1. However, the real difficulty seems to be in forming gigaohm seals consistently. The only groups which claim reliable gigaohm seal formation are commercial, and the details of the devices used are not disclosed. Nonetheless, the glass micropipette still forms seals more reliably than many of these devices [60], and the details of their manufacture are well known. Mimicking the properties of glass pipettes is thus an obvious choice in developing a planar patch clamp device.

Group	Principal Investigator	Device Type	Surface material	Aperture diameter	Aperture depth	Average seal resistance	Gigaohm seal success rate	Whole Cell success rate	Cell type
Ludwig-Maximilians	Fertig	Nitride Membrane	Si3N4		120nm				Lipid bilayer
Yale	Klemic	Nitride Membrane	Si3N4						
Lausanne	Schmidt	Nitride Membrane	Si3N4	0.6-7μm	100-150nm				Lipid bilayer
Lehigh	Pandey	Nitride Membrane	Si3N4	1-2μm	100nm	20M			CHO
UCLA	Pantoja	Silicon Membrane	PECVD SiO2	0.7-2μm	10-40μm	50-100M	7.94%		CHO, RIN, HIT, RAW
UCLA	Judy	Silicon Membrane	Thermal SiO2 on a-Si	0.5-11μm	20μm		Some		CHO
Lausanne	Lehnert	Silicon Membrane Nozzle	Thermal SiO2	2.5μm	10-30μm	180M	0		CHO
			PDMS + O2 plasma	<2.5μm	10-30μm	300M	Some		CHO
CEA, Grenoble	Sordel	Silicon Dioxide Membrane	Thermal SiO2	2.5μm	2.1μm	30M	0		HEK
			PECVD SiO2	1.7μm	3.6μm	155M	3.82%		HEK
Berkley	Lee	Silicon Membrane Nozzle	Si3N4	1, 3, 10μm	75μm				
Yale	Klemic	PDMS	PDMS + O2 plasma	2-20μm	Constant taper		13%		Xenopus Oocyte
				2μm	20-100μm		25%, 10%, 7%	50%	Oocytes, CHO, RBL
							24%		RBL
Berkley	Lee	PDMS	PDMS	2μm	>100μm	120M	0		HeLa
				2μm	>100μm				HeLa
Reutinglen	Stett	Polyimide membrane	Si3N4	2, 4μm	6.5μm	25M	5.33%		CHO, PUC
Georgia Tech	Han	Polyimide membrane	Polyimide	3μm	6μm		Some		Chromaffin

Group	Principal Investigator	Device Type	Surface material	Aperture diameter	Aperture depth	Average seal resistance	Gigaohm seal success rate	Whole Cell success rate	Cell type
Sophion Biosciences	Taboryski	Silicon Membrane	SiO2	0.5-1.2μm	10μm		80%	80%	CHO
Cytocentrics	Stett	Silicon Membrane Nozzle	SiO2	<2μm	>10μm	1.2G	68%	77%	N2A
						2.6G	92%	82%	CHO
Nanion	Fertig	Glass ion track etch	Glass	~1μm	80μm				Lipid bilayer
					20μm		Routinely	30%	CHO, NIE
					20μm		70%		CHO, HEK, RBL
Molecular devices (PatchXpress)	Xu	Glass chip	Proprietary surface coating					75%	
Molecular devices (IonWorksHT)	Kiss	Polymer membrane	Polymer	~1μm		50-300M		80%	CHO

Table 2.1. Summary of planar patch clamp literature at time of writing. Previous page, academic groups. This page, commercial groups. See text for a detailed discussion.

Chapter 3
Device Manufacture

3.1 Introduction

This chapter describes the approaches taken in manufacturing the thermal oxide planar patch clamp devices. Firstly, preparatory work required for the construction of the devices is discussed. Then the manufacturing process itself is outlined followed by the methods used to clean the devices. The final section describes the characteristics of the devices produced.

3.2 Preparatory Work for Planar Patch-Clamp Device Fabrication

The construction of planar patch-clamp devices with the desired properties (as described in chapter 1) presented three main problems: creating circular thermal oxide coated apertures, using a Bosch process to create a negative taper, and the construction of protruding nozzles.

3.2.1 Circular Features in Thermal Silicon Dioxide

Thermal oxidation is a high temperature process for creating a layer of silicon dioxide on a bare silicon wafer. The substrate to be oxidised is placed in a furnace at a temperature around $1000°C$ and exposed to oxygen (dry oxidation) or steam (wet oxidation). As the substrate is oxidised, a layer of silicon dioxide is formed. As this layer increases, the reactive species (O_2 or H_2O) has to diffuse through a thicker layer of oxide before it reaches and reacts with the silicon underneath. Hence, as the thickness of the oxide increases, the oxidation rate decreases. The result is that the oxidation time required varies as $\sqrt{thickness}$.

The process of oxidation consumes the silicon substrate. Because the volume of silicon consumed is 45% of the volume of oxide it produces, the oxide layer will be 45% below the original silicon surface, and 55% above the surface. For a more detailed treatment see Deal and Grove [4] or Sze [76].

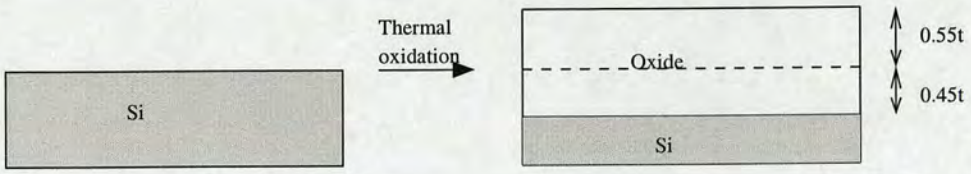

Figure 3.1: *Relative ratios of oxide growth and silicon consumption during thermal oxidation*

A serious drawback of growing thermal oxide on circular features is that, during thermal oxidation, different silicon crystal planes oxidise at different rates. On a circular feature, where a continuum of crystal planes is exposed to the oxidative species, the shape of the feature changes during oxidation. In the case of the <100> silicon wafers used here, the <110> plane oxidises faster than the <100> plane, resulting in a square feature, as shown in figure 3.2.

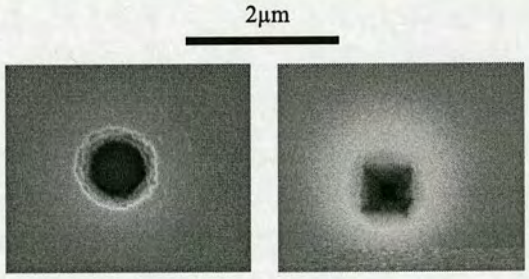

Figure 3.2: *A circular aperture in silicon. Left: before oxidation. Right: post-oxidation.*

However, the oxidation consumes a thickness of silicon equal to 45% of the thickness of the oxide layer. Since certain planes oxidise faster, the silicon on these planes will be consumed at a greater rate. If an initial oxide layer was grown to thickness d, then stripped in hydrofluoric acid, a diamond like shape should be left in the silicon (see figure 3.4). Thus, those planes which oxidise the fastest will be furthest from the centre of the feature, and it should be possible to re-oxidise into a circle. In fact, if the thickness of oxide protruding from the surface is equal to the amount of silicon consumed, then each plane should oxidise to the point from which it started, yielding a round feature. The thickness of the second oxide layer, s should be given by:

$$s \times 0.55 = d \times 0.45. \tag{3.1}$$

Although this approach worked well for larger holes, for features smaller than $2\mu m$ the end result was unacceptably square (for a final oxide thickness of $1\mu m$). Hence, attempts were made to derive a better model (see appendix C). Verification of this model failed due to poor

repeatability of the process, but at no point during any of the tests was an acceptably circular hole less than $2\mu m$ produced. Also note that in none of the experiments described above did any of the aperture shapes resemble a diamond.

Instead, it was decided to use the model of equation 3.1, and reduce the final oxide thickness, s to $0.5\mu m$. In addition, it was noted that the oxidation rates for the <100> and <110> planes showed a greater difference at lower temperatures. This fact is illustrated by a plot of the grove model for oxidation, shown in figure 3.3. It can be seen that, for a given oxide thickness grown on the <100> plane, the <110> plane will exhibit more of a difference if both are grown at 950°C than if they are grown at 1100°C. Thus, it was decided to grow the first oxide layer at 950°C to create a larger difference in the positions of the crystal planes in silicon, and to grow the final oxide layer at 1100°C.

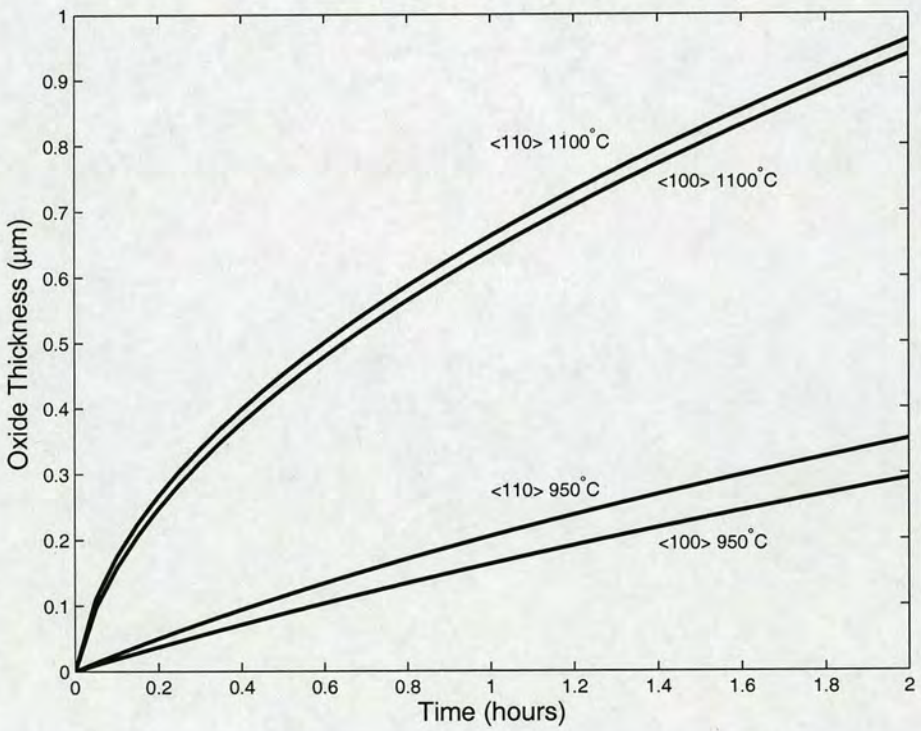

Figure 3.3: *The oxidation curves of <100> and <110> planes at 1100°C and 950°C, as predicted by Groves' model [4]. Curve parameters taken from [5].*

The effect of reducing the oxide thickness, and growing the layers at different temperatures is shown in figure 3.5. It can be seen that the etch used to create the aperture produced a slight squaring of the hole (b), and thus the shape left in the silicon by the oxidation (d) was not that of a diamond. However, it is apparent that the hole left in the silicon is less square than the

original shape before oxidation (b). The final result (e) was deemed to be acceptably round, and thus this process was used for the product wafers. However, due to process variations on the product wafer run (most likely during the Bosch etch) some of the larger holes did display diamond-like characteristics (see figure 3.6).

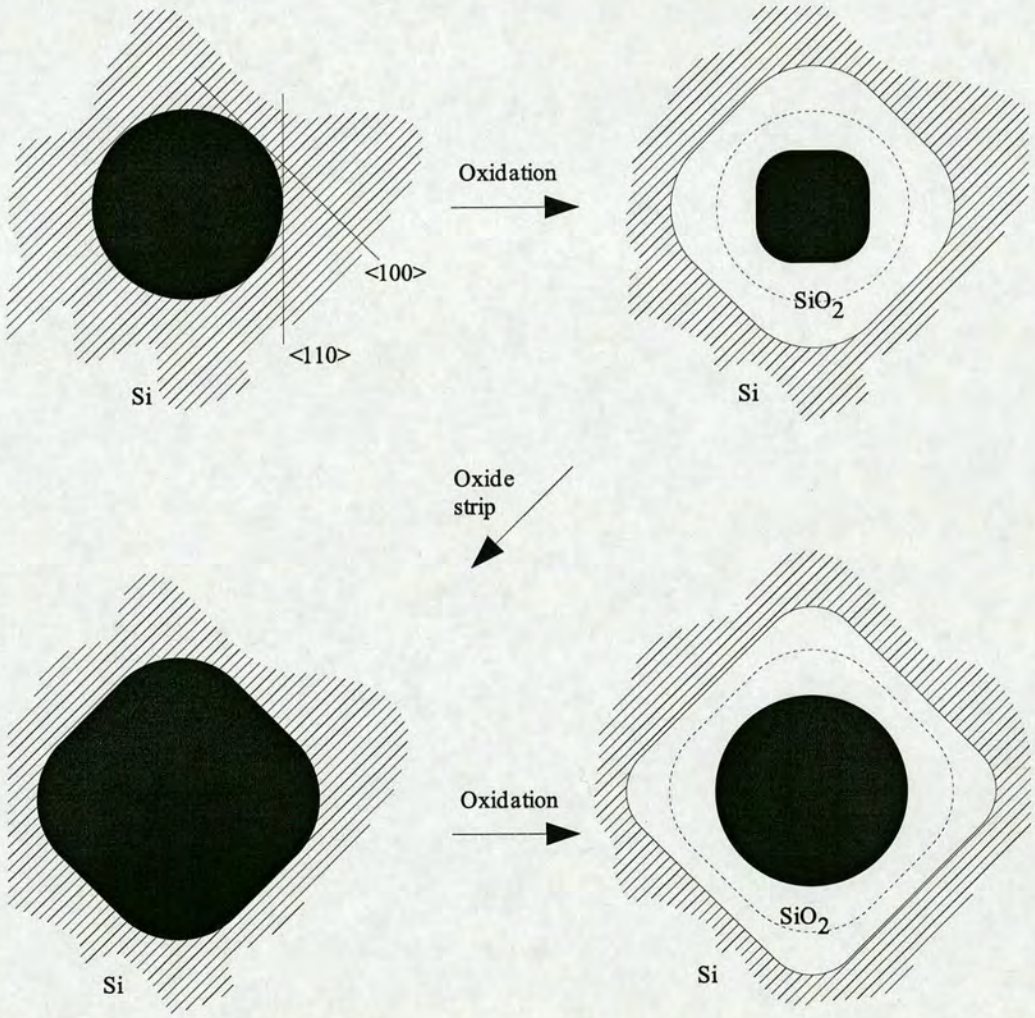

Figure 3.4: *The hypothesised oxidation model for a circular aperture.*

3.2.2 Taper

Deep silicon etch processes [77][78] are normally configured to produce vertical sidewalls, to minimise critical dimension change during etching. Some experimentation was needed to create such a process which produced a pipette like taper.

Attempts were made to modify the Bosch process used in the fabrication of the PECVD oxide

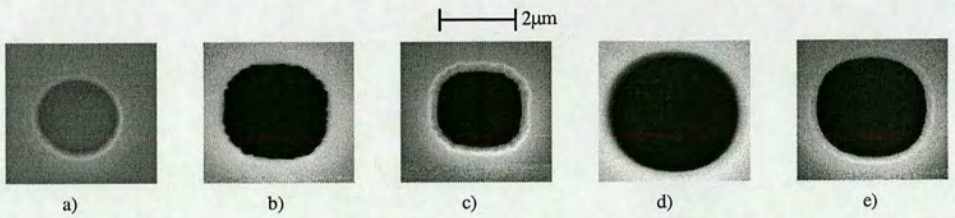

Figure 3.5: *The final oxidation process used. a) The shape of the silicon dioxide hard mask. b) The shape of the hole after silicon etch and oxide strip. c) After the first oxidation. d) After a subsequent oxide strip. e) after the second oxidation*

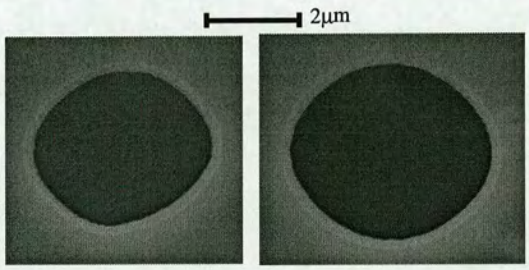

Figure 3.6: *Examples of the slight diamond shape shown by some of the larger product devices*

devices, the details of which are given in appendix A. The following etch parameters were altered:

- increased O2 flow
- increased SF6 flow
- increased platen power
- shortened cycle time
- increased etch/passivation ratio

Test samples were created, consisting of exposed lines ($2\mu m$ in width) in photoresist on bare silicon. Different test samples were exposed to etches in which a single parameter had been modified. The results of these trials can be seen in image 3.8. Some anomalous results from the same experiment are shown in figure 3.9. These features, whilst etched with an identical process to that used in figure 3.8 a). show a significant taper and irregular etch depth. However, these results, though desirable, were caused by an unknown error, presumed to be related to the photo-lithography, and were not reproducible, even within a single silicon sample.

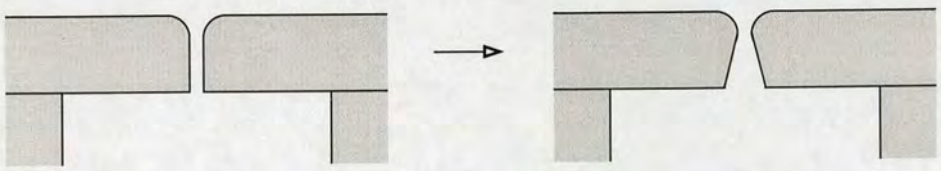

Figure 3.7: *Attempts were made to match the taper of the devices to that of a glass pipette*

Ignoring the anomalous results, it was noted that most of the processes tested undercut the etch mask, but none of them produced a taper. Hence, it was decided to increase the parameters throughout the course of the etch. This created a process which started with a vertical Bosch etch on the first cycle, with increasing undercut on each successive cycle. The result of these tests can be seen in figure 3.10. The most negative repeatable taper produced in any of these tests is that shown in figure 3.10 f). This process was thus used in the fabrication of the product devices.

A non-Bosch process was also considered for the frontside etch, shown in figure 3.11. However, attempts to make this process produce a taper failed, so this technique was abandoned in favour of the tapered Bosch process.

3.2.3 Nozzles

The method used to create protruding nozzles follows a process developed by Lehnert et al. [48]. A planar device was used as the starting point. The front side was anisotropically reactive ion etched to remove the oxide layer on the top, but not the sidewalls. The silicon was etched isotropically in an SF_6 plasma. The silicon to oxide selectivity of SF_6 is approximately 100 to 1, so this etch had a negligible effect on the oxide, leaving it protruding above the surface. The structure was then re-oxidised. This process is illustrated in figure 3.12 and a typical nozzle can be seen in figure 3.13.

3.3 Fabrication of Planar Patch Clamp Devices

The process used in the fabrication of the devices is outlined in figure 3.14. A detailed specification is given in appendix A. Different types of device were produced by altering 3 process parameters:

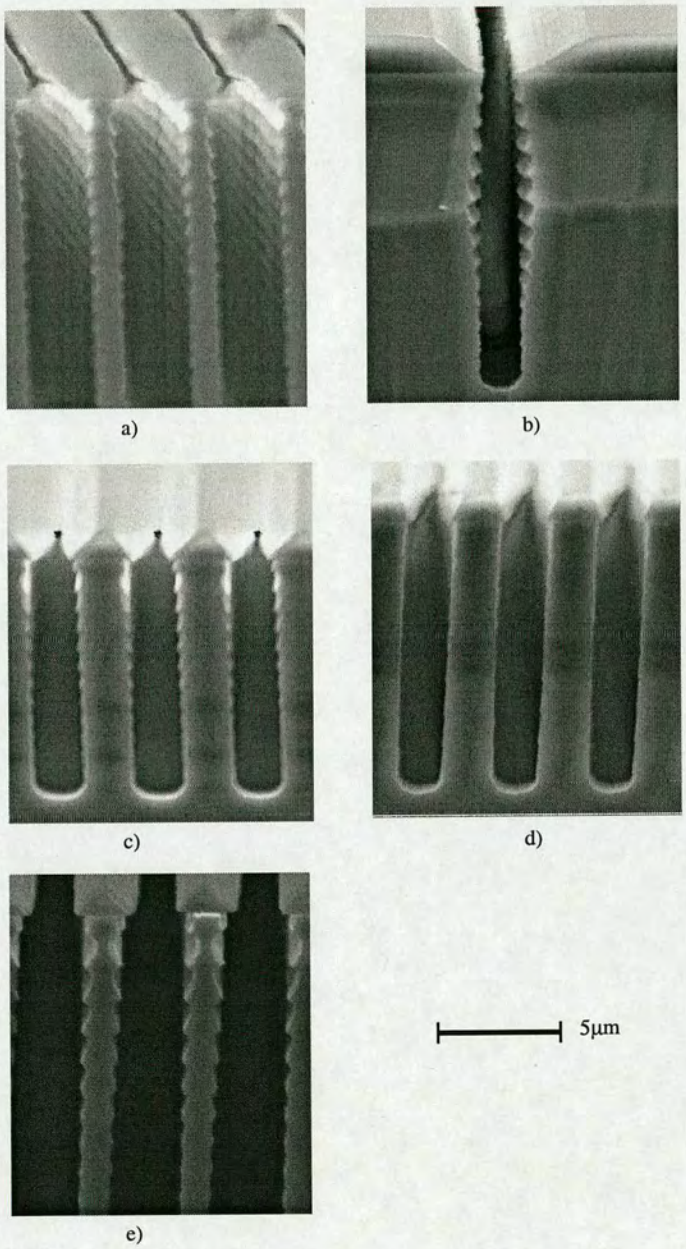

Figure 3.8: *The result of experiments to alter the taper of the Bosch process by varying single parameters. a) O_2 flow increased to 26sccm (+100%). b) SF_6 flow increased to 195sccm (+50%). c) Platen power increased to 15W (+25%). d) Cycle time reduced to 10s (-50%). e) Increased etch/passivation ratio to 18/8 (+50%)*

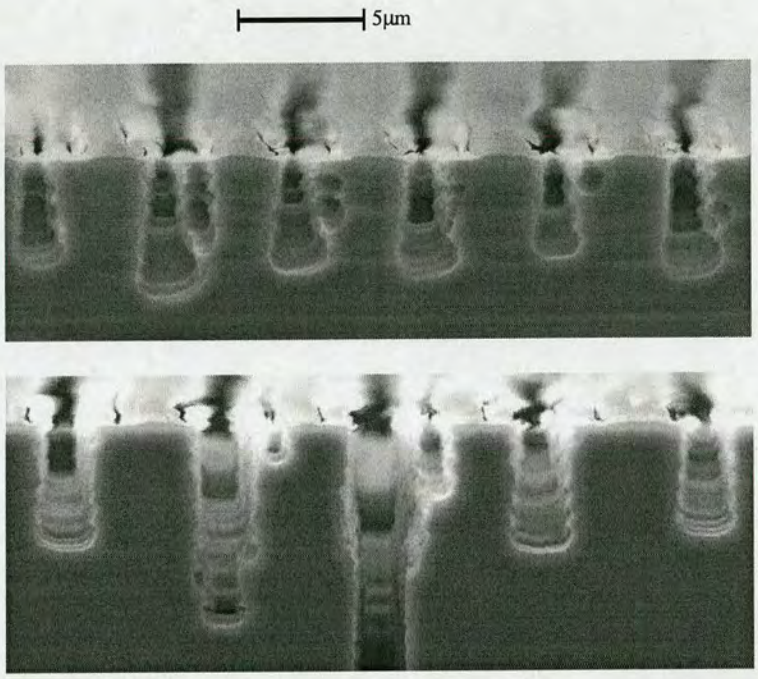

Figure 3.9: *Anomalous results from Bosch etch tests. These samples were etched with O_2 flow increased to 26sccm (identical to the process used in figure 3.8 a).*

- Aperture Diameter (1μm, 1.5μm, 2μm, 3μm and 4μm)
- Surface Chemistry (boron-doped or plain thermal oxide)
- Aperture Topography (flat or protruding nozzle)

This produced a total of 20 varieties of device (4 types for each aperture diameter). A single SOI wafer was used for devices of each aperture diameter; each of these was divided into quarters after the oxidation and each quarter processed as appropriate.

After processing, several devices on each wafer were imaged using a scanning electron microscope (SEM), and the aperture diameters were measured. The hole sizes measured (1.5μm, 3.2μm, 3.7μm, 4μm and 4.5μm) were all larger than the target values expected. This is attributed to unanticipated process variations. Two of the wafers (3.2μm and 3.7μm) were oxidised further to create more practical aperture diameters (2.5μm and 3μm). These devices could not be oxidised further without the apertures becoming unacceptably square. The final hole sizes created are summarised in table 3.1.

Table 3.1 also gives the yield for the different device groups. The devices were printed in an 11$\times$11 grid with 3 missing from each corner. This produced a maximum of 109 devices per

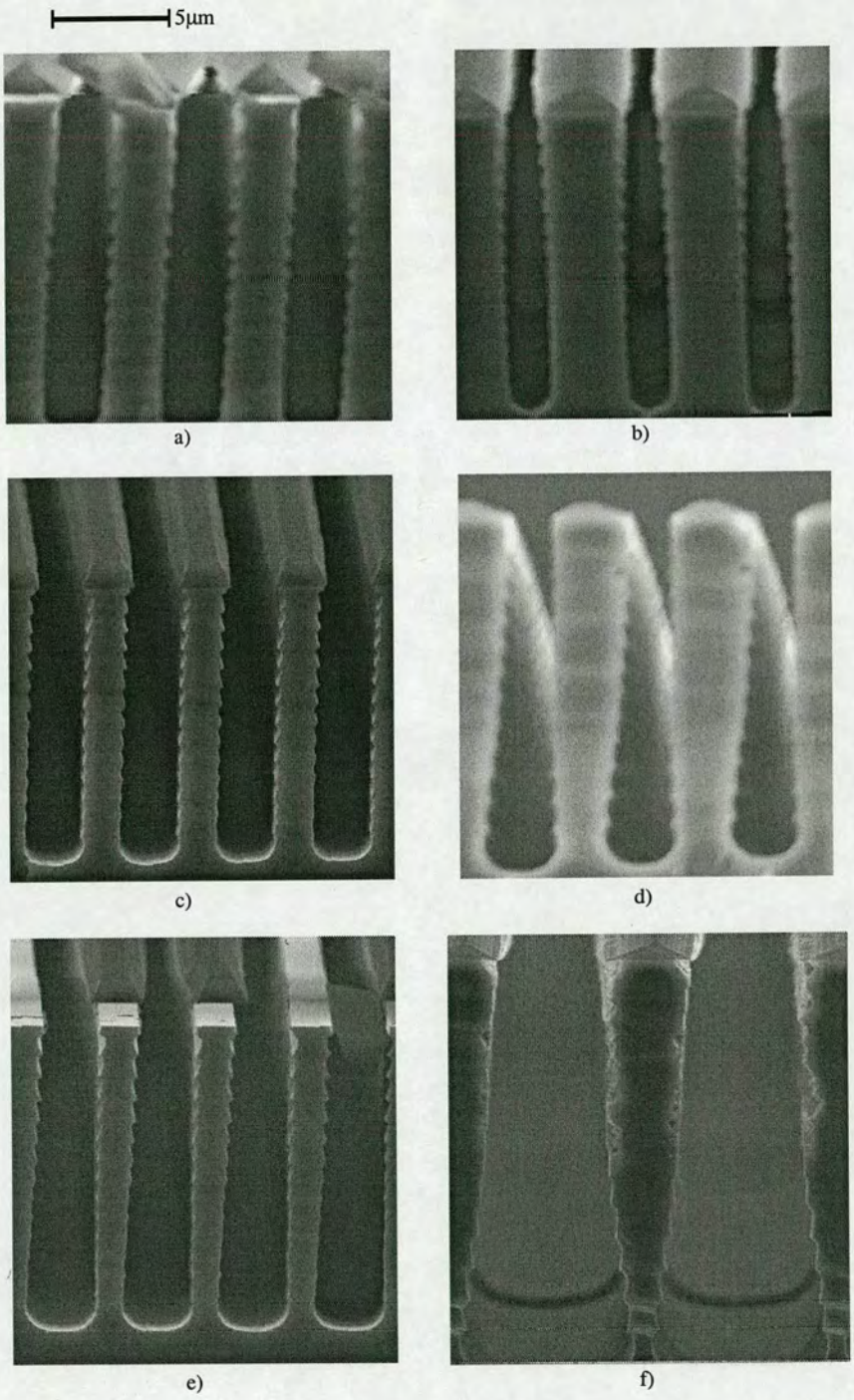

Figure 3.10: *The result of experiments to alter the taper of the Bosch process by ramping parameters. a) SF_6 flow ramped at 26sccm/min (130sccm→260sccm). b) O_2 flow ramped at 8sccm/min (13sccm→52sccm). c) C_4F_8 flow ramped at -17sccm/min (85sccm→0sccm). d) Etch cycle duration ramped at 0.8s/cycle (12s→24s). e) Platen power ramped at 2.2W/minute (12W→24W). f) Etch cycle duration ramped at 0.8s/cycle, SF_6 flow ramped at 26sccm/min, O_2 flow ramped at 1.2sccm/min and platen power ramped at 2.2W/min.*

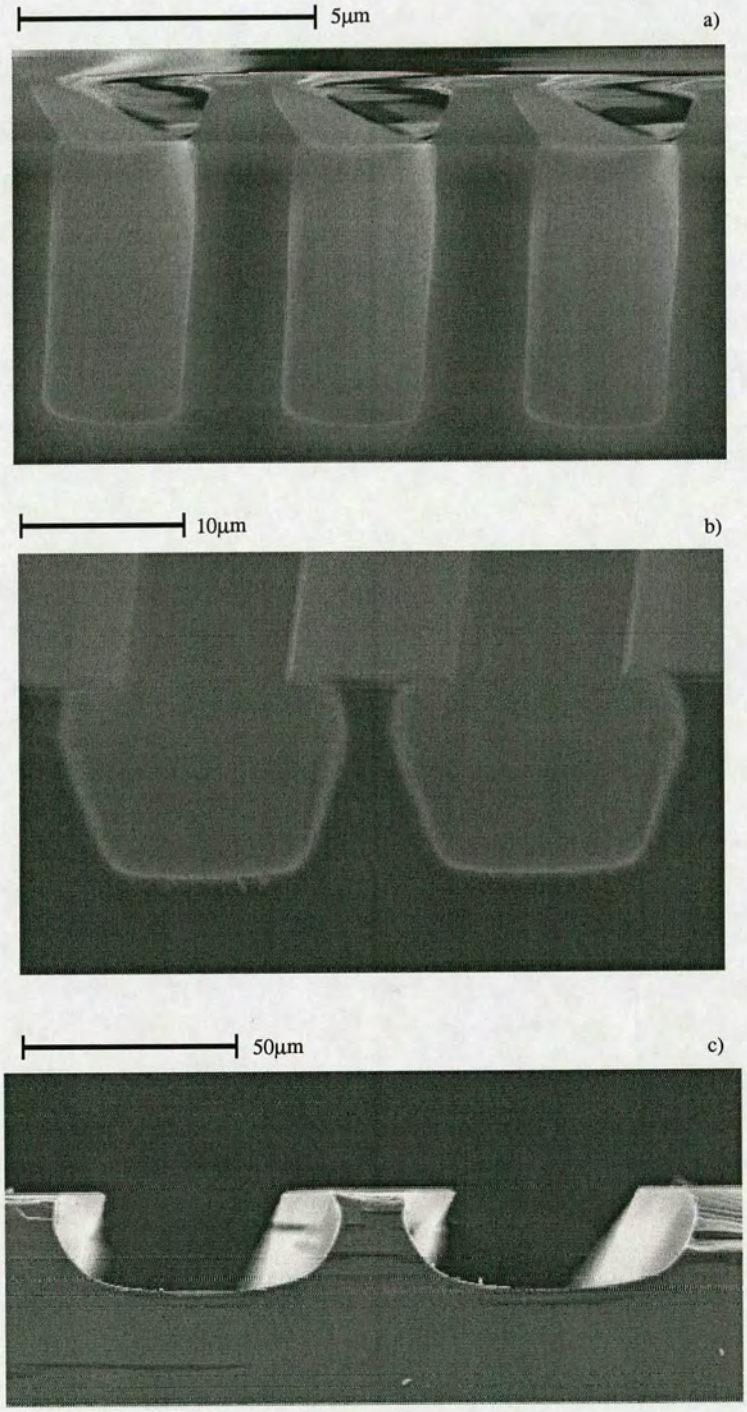

Figure 3.11: *Attempts to achieve a negative taper with a non-Bosch process. a) Vertical non-Bosch process, 90sccm C_4F_8 50sccm SF_6. b) The effect of ramping the SF_6 flow to 100sccm. c) The effect of ramping the C_4F_8 flow to zero.*

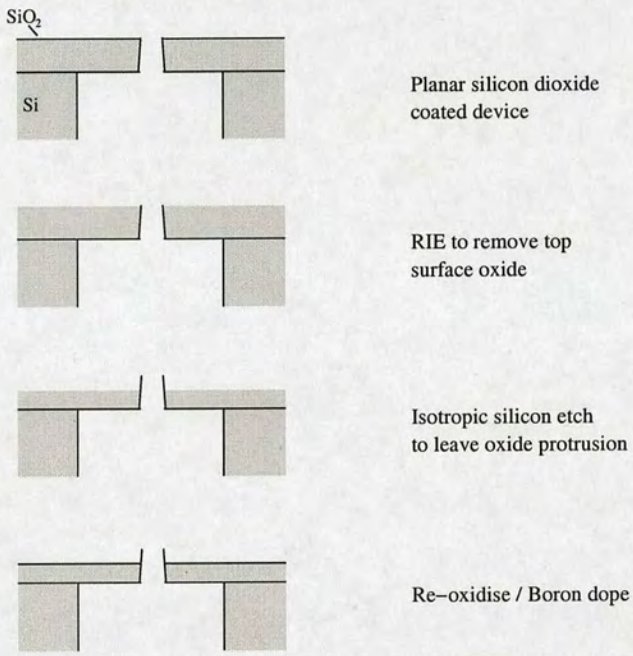

Figure 3.12: *The process for creating protruding nozzles in silicon dioxide. Grey represents silicon, and black represents silicon dioxide.*

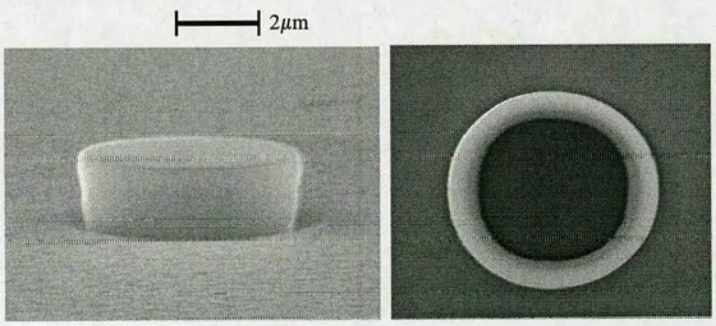

Figure 3.13: *A typical example of a nozzle produced using the process of figure 3.12*

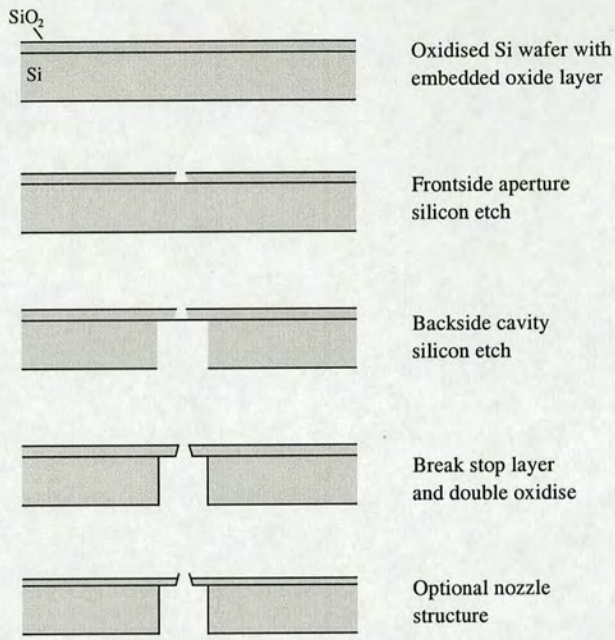

Figure 3.14: *The process used for creating silicon patch clamp devices. Grey represents silicon, black represents silicon dioxide.*

Wafer	Nominal diameter	Actual diameter	Nozzles		Flat holes	
			Boron	Un-doped	Boron	Un-doped
A	1μm	1.5μm	3	5	8	9
B	1.5μm	2.5μm	22	27	27	33
C	2μm	3μm	22	27	27	33
D	3μm	4μm	22	27	27	33
E	4μm	4.5μm	22	27	27	33

Table 3.1: *Wafer organisation*

wafer, which was met in all cases except wafer A, which produced only 25 intact devices. The low yield obtained from wafer A is due to the size of apertures printed. Since the aperture size was approaching the critical dimension limit of the stepper (whose wavelength is 436nm) many of the features did not develop properly. Only the apertures printed towards the edge of the wafer (which were larger because of a focussing error in the stepper) survived the development process.

3.4 Device Cleaning

Given the small number of $1.5\mu m$ devices produced, it was desirable to be able to re-use the devices. This necessitated being able to clean biological debris from the surface. Acid piranha solution (also known as RCA2 or Caro's acid) was found to be suitable for removing organic debris. The details of this process are found in appendix A.

Tests were performed on thermal oxide and boron doped thermal oxide surfaces, to examine the effects that this solution had on the surface. 11 samples of each surface were cleaned in acid piranha solution and rinsed 3 times in de-ionised water. 11 control samples of each surface were rinsed 3 times in de-ionised water. All the surfaces were then imaged using a Digital Instruments Atomic Force Microscope (AFM), and roughness values were extracted.

The roughness values are given in table 3.2.

Surface	R_a	R_{max}
Thermal oxide control	0.14	7.60
Thermal oxide piranha treated	0.20	22.88
Boron-doped thermal oxide control	0.12	15.21
Boron-doped thermal oxide piranha treated	0.13	11.48

Table 3.2: *Roughness measurements for surfaces treated with Acid Piranha solution. For all groups, n = 11.*

T-tests performed on these data show that difference in R_a between cleaned and un-cleaned for the boron doped samples is insignificant (P = 0.481), but that the difference for the thermal oxide sample is significant (P = 0.003). However, upon examination of the AFM traces (figures 3.15-3.18) for the thermal oxide surfaces, it appears that the change in the value of R_a is caused not by a general roughening of the surfaces, but by the appearance of particulates. The absence of such particulates on the boron-doped surfaces suggests either that some reaction does occur between the thermal oxide and the acid solution, to either erode the surface, or leave it more attractive to particulates.

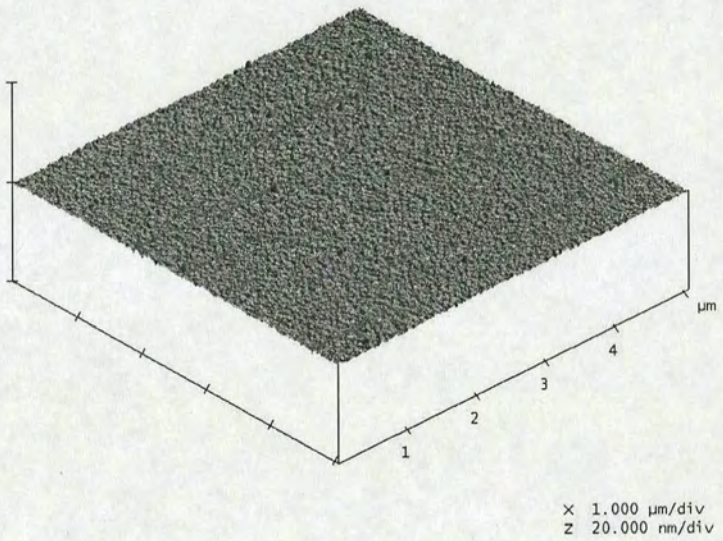

Figure 3.15: *A typical AFM plot for an un-treated thermal oxide surface.*

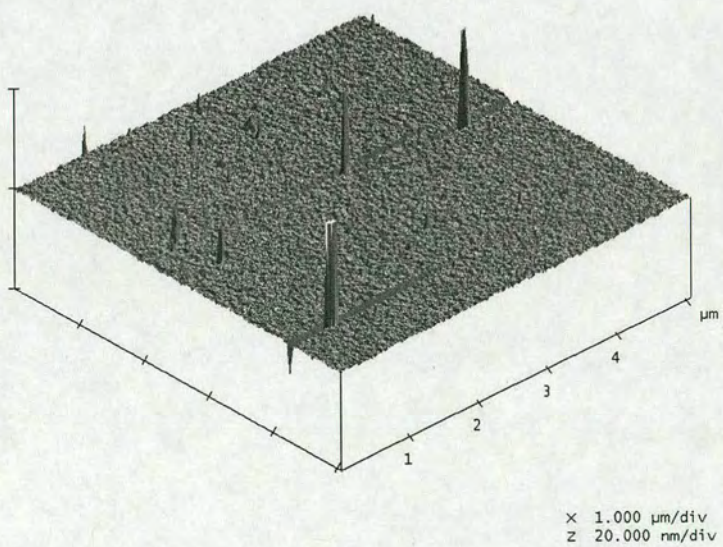

Figure 3.16: *A typical AFM plot for an piranha-cleaned thermal oxide surface.*

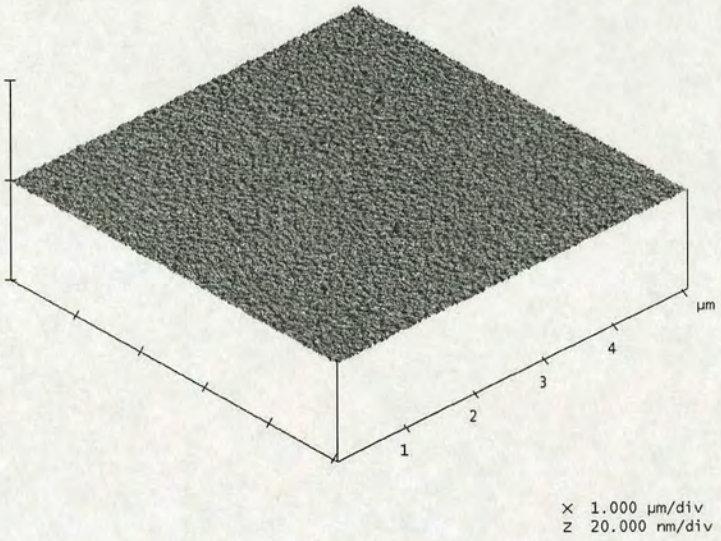

Figure 3.17: *A typical AFM plot for an un-treated boron-doped thermal oxide surface.*

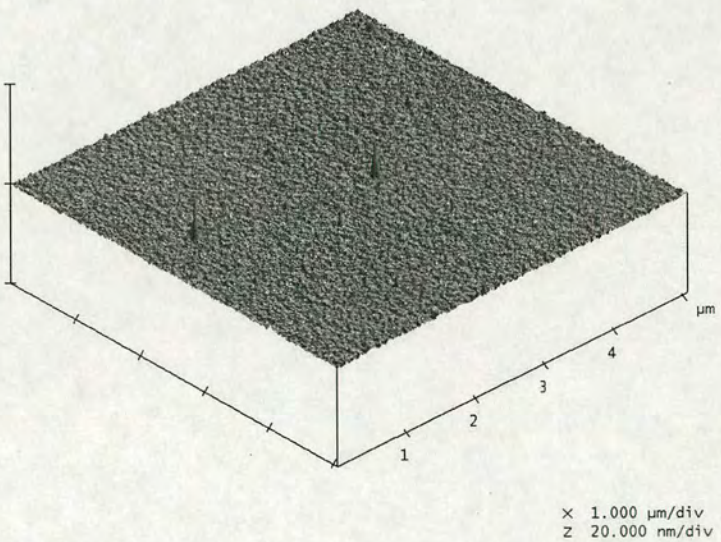

Figure 3.18: *A typical AFM plot for an piranha-cleaned boron-doped thermal oxide surface.*

Chapter 4
Device Characterisation

The characterisation of the planar patch clamp devices took two forms, physical and electrical. The physical characterisation of the device was performed by examining the devices under a Scanning Electron Microscope (SEM) and an Atomic Force Microscope (AFM). The electrical characterisation involved measuring the resistance and capacitance between the front and back sides of the device. This section discusses only the $1.5\mu m$ and $2.5\mu m$ devices described in the previous chapter, as larger devices were not tested with cells. The PECVD devices [1] are discussed as these were also tested with N2A cells (chapter 6). As a benchmark comparison, the properties of typical glass pipettes are given first.

4.1 Glass Pipette Characterisation

To allow a direct comparison of physical properties, several glass pipettes were also examined. All glass pipettes were pulled from thick walled borosilicate glass capillaries (Clark/Warner Instruments) using a Sutter Instruments Model P-87 electrode puller (see appendix B for pulling program details). Several pipettes were imaged in an SEM (figure 4.1). It can be seen from these images, that the surface of the tip appears quite rough and the radius of curvature is very sharp. Also note the presence of the reed in the tip. The diameter of this reed was measured to be roughly 250nm.

The side views also allow a rough estimation of the taper inside the pipette tip. The outer wall slopes at 3.9°. Assuming that the ratio of inner to outer diameters (as defined by the glass capillary from which the pipette is pulled) remains constant, the inside taper can be calculated as follows:

$$tan(\theta_{inner}) = R_d tan(\theta_{outer})$$

Where R_d is the ratio of diameters (equal to 0.57 in this case). Hence the inner taper is estimated as:

$$\theta_{inner} = tan^{-1}(0.57 \times tan(3.9°)) = 2.24°$$

The roughness of the glass pipettes is difficult to measure with an AFM, particularly inside the tip. However, the roughness of glass cover-slips (also formed from melted glass) was measured by Dworak [1] to be 0.13nm (R_a). The contact angle of borosilicate glass is 24.31°.

The material composition of the patch glass is given in table 4.1 [79]. The boron content by mass is 4.05%.

SiO_2	B_2O_3	Na_2O	Al_2O_3
80.9%	12.9%	4.4%	1.8%

Table 4.1: *Material composition for borosilicate patch glass.*

The electrical properties of 8 typical glass electrodes were also measured, in the same fashion as for the devices (this procedure is detailed in section 4.3). These are summarised in table 4.2.

	Mean Resistance	Mean Time Constant	Mean Capacitance
Glass (Bubble number 8, 1.5μm)	6.11$M\Omega$	43.88μs	7.19pF

Table 4.2: *Electrical parameters for typical patch pipettes.*

4.2 Physical Device Characterisation

4.2.1 Hole Diameter

The diameter of all frontside apertures were measured using a scanning electron microscope. These dimensions are summarised in table 4.3.

Nominal	Mean Diameter (μm)	Std Dev.
1.5μm	1.48	0.40
2.5μm	2.53	0.23
PECVD (2μm)	1.99	0.131

Table 4.3: *Aperture diameters for thermal and PECVD oxide devices.*

The diameter of the aperture was either 1.5μm, 2.5μm or 2μm(PECVD). However, in none

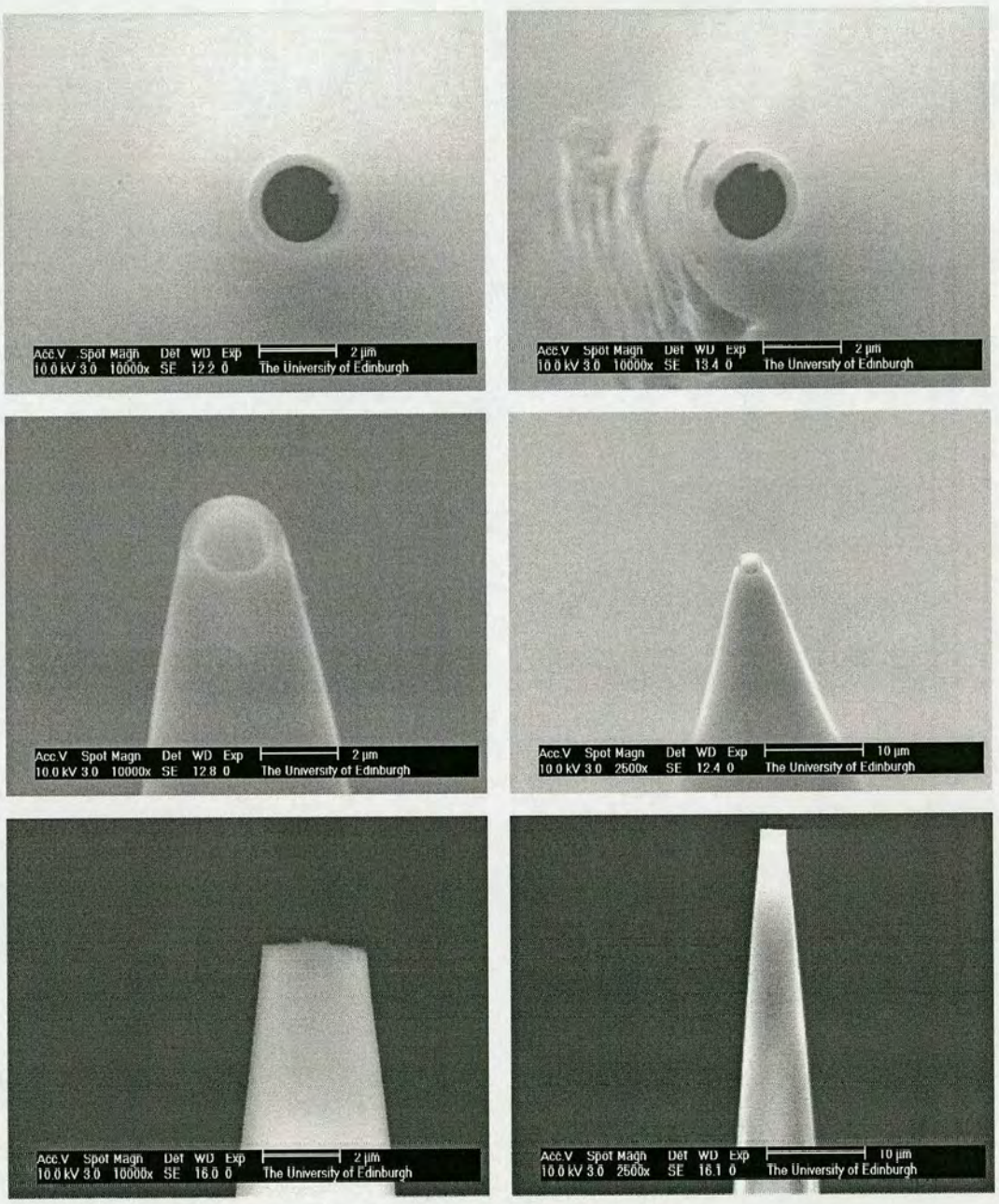

Figure 4.1: *Various images of patch pipettes as used in the seal formation experiments on N2A cells. The end-on views of the tip (top) and the tilted views show the presence of the reed on the inside of the pipette (the area where seal formation is thought to occur). The side view of the pipettes suggest that the surface of the tip is quite rough.*

of these cases was the intended diameter achieved. The intended hole size for the PECVD devices was in fact $1.5\mu m$. For the thermal oxide devices a number of different hole sizes were printed, with intended diameters of $1\mu m$, $1.5\mu m$, $2\mu m$, $3\mu m$ and $4\mu m$. However, all the hole sizes shifted upwards from the target values, leaving only the PECVD devices, and the smaller thermal oxide devices with a practical hole size for mammalian neuronal cells. (The proposed hole sizes of $3\mu m$ and $4\mu m$, would also have been too large for mammalian cells, but these were originally intended for use with larger snail neurons.) The cause of this hole size change is thought probably to lie in the photo-lithography step in which the apertures were printed. This could have occurred because the focus and exposure settings used to print the holes on the Optimetrix stepper were chosen on the basis of a focus-exposure matrix, printed in the centre of a wafer. However, due to a focussing error intrinisic to the stepper[1], a hole printed at the centre of a wafer is in better focus than one at the edge. Hence, the holes at the edges will be slightly larger. As the majority of features on a wafer will lie towards the edge, the majority of holes will be larger than the hole size chosen from a test piece printed at the centre.

This centre-edge variability also determined the yield of the $1.5\mu m$ devices. As $1\mu m$ is approaching the minimum resolution with which the stepper (wavelength = 436nm) could print, many of the holes did not print at all (rather, the exposure dose delivered was so small that the photoresist failed to clear during development). Thus, it was only the larger holes at the edge which survived the develop process.

However, the aperture diameters produced here are ideal for the tests carried out on N2A cells (see chapter 6) as $1.5\mu m$ is the diameter of glass pipette which produced the greatest seal resistance with N2A cells (see chapter 5).

4.2.2 Radius of Curvature

The aperture profile of 4 flat devices and 4 nozzles were measured with an Atomic Force Microscope. Typical traces are shown in figures 4.2 - 4.3. A PECVD profile is also shown for comparison. SEM images of the apertures are shown in figures 4.5 - 4.7.

It can be seen from figure 4.1 and figures 4.2 - 4.7 that the radii of curvature of all devices exceed that of glass. The PECVD has the greatest radius of curvature and hence the thermal

[1]The Optimetrix stepper uses capcitance measurements to determine the height of the wafer, and hence the focal plane in which to print. Edge effects introduce an error into these measurements and hence into the focus in which the apertures are printed.

oxide devices more closely approximate the glass pipettes used in these experiments. However fire-polishing - a technique involving superficial melting of the end of glass pipette - is used to round the tip and is reported to increase seal resistance [28]. Thus the larger radii of the PECVD devices are of some interest.

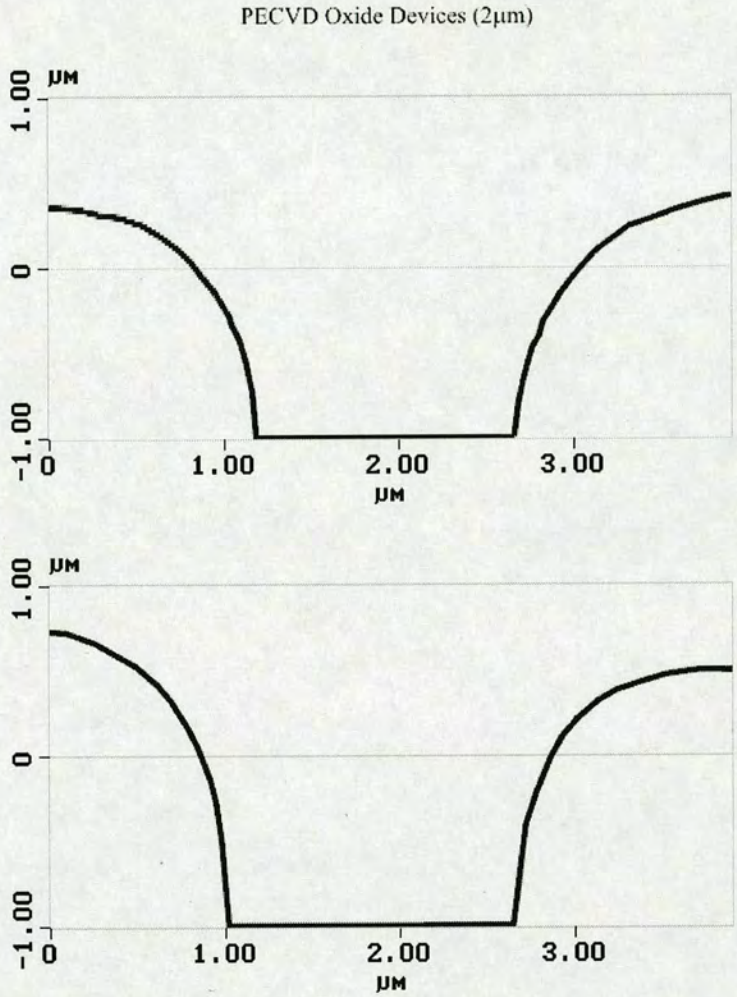

Figure 4.2: *Typical AFM profile traces for PECVD devices.*

4.2.3 Roughness of the Sealing Surface

The roughness of the sealing surface (the area inside the aperture) is not easily measured. It is probably not well represented by the roughness of the top surface of the device as this may have been roughened during processing. This is particularly true of the nozzles, whose top surface is roughened by the bulk silicon etch which produced the protruding features. In any

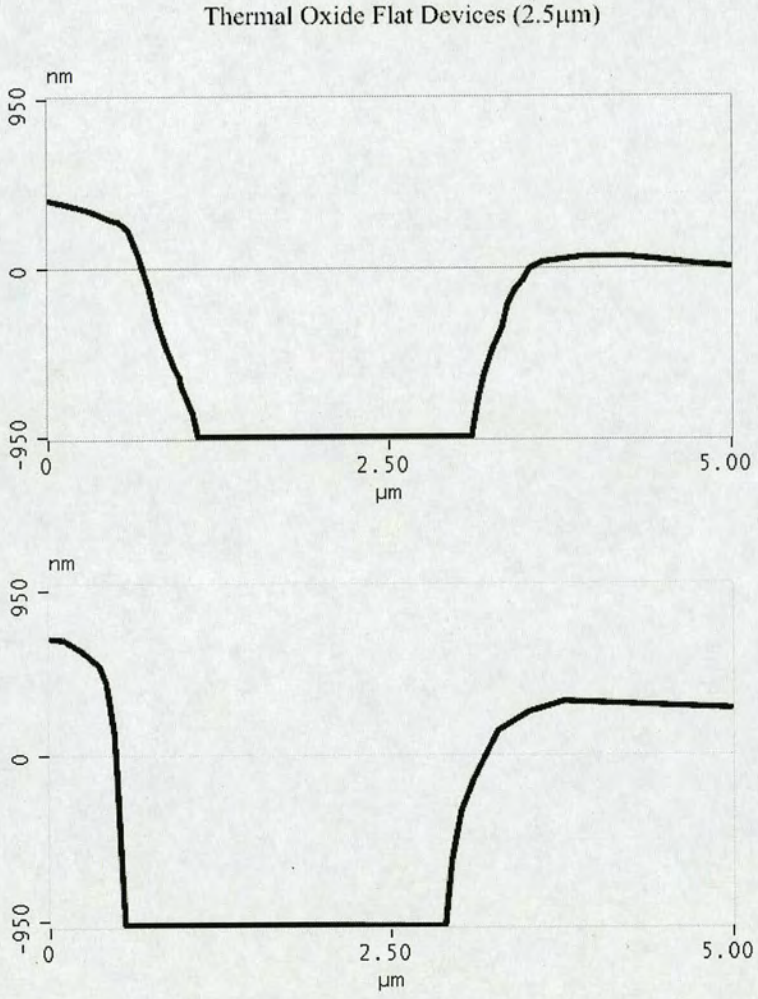

Figure 4.3: *Typical AFM traces for thermal oxide flat devices (2.5μm).*

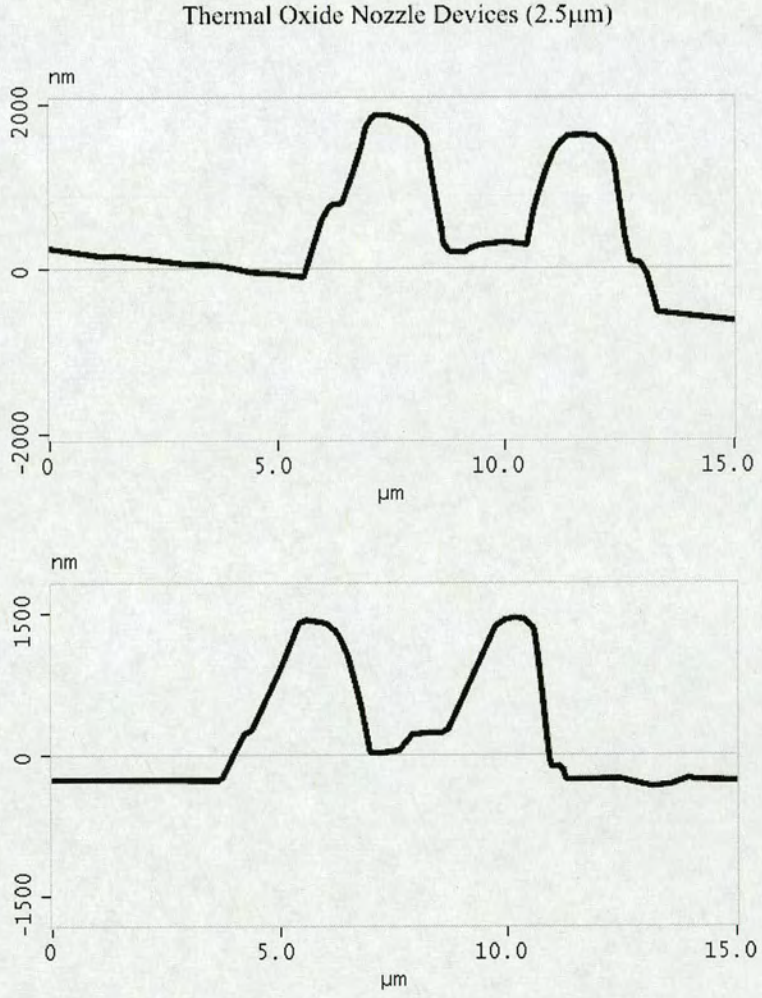

Figure 4.4: *Typical AFM traces for thermal oxide nozzle devices (2.5μm).*

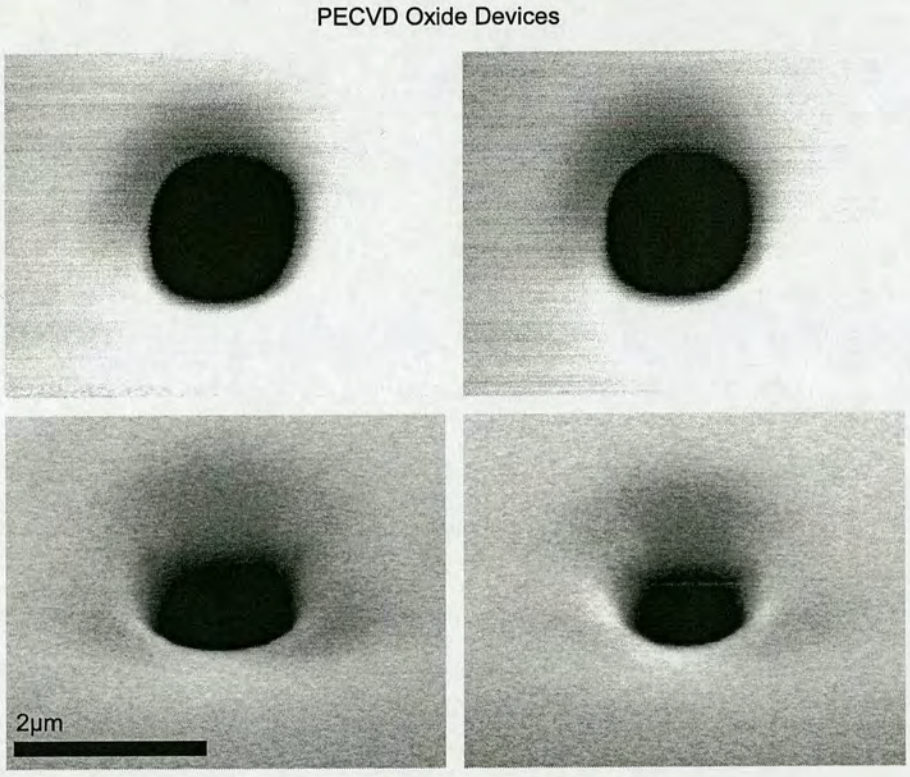

Figure 4.5: *Flat and tilted SEM scans for typical PECVD oxide devices.*

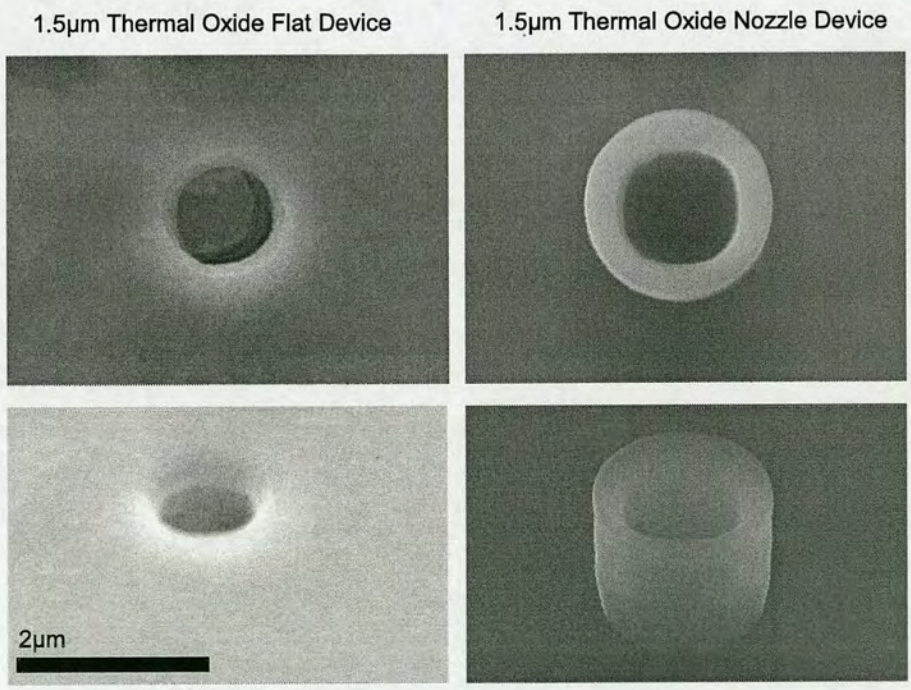

Figure 4.6: *Flat and tilted SEM scans for typical* $1.5\mu m$ *thermal oxide devices. Left: flat, Right: nozzle.*

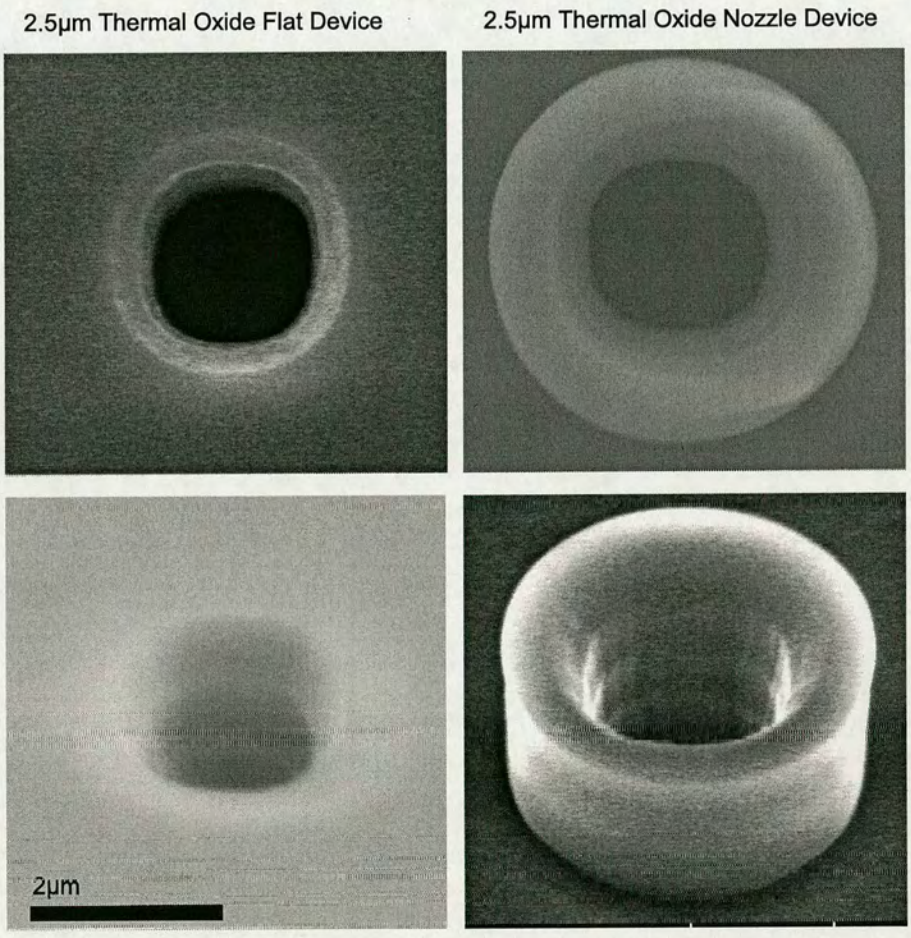

Figure 4.7: *Flat and tilted SEM scans for typical* $2.5\mu m$ *thermal oxide devices. Left: flat, Right: nozzle.*

case, the roughness of the top surface does not account for any sidewall ripple produced by Bosch etching. Irrespective of these large scale perturbations, an indication of the small scale roughness (on the order of nanometers) of the sealing surface can be obtained by depositing or growing the surface material on unprocessed bulk silicon. Measurements for the various surface materials involved, taken with an AFM, are given in table 4.4. Typical scans for PECVD oxide and thermal oxide are shown in figures 4.8 and 4.9.

Surface	Mean Roughness (R_a)	Contact Angle(°)	Boron Content
Thermal Oxide	0.17	36.39	-
Thermal Oxide + Boron	0.18	21.04	1.33%
PECVD	1.13	9	-
PECVD + Boron	0.33	20.75	1.73%

Table 4.4: *Surface roughness, contact angle and boron content for silicon dioxide surfaces. Surface roughness was measured by AFM. Contact angle was measured with 3μl droplets of 26% NaCl solution. Boron Content (by mass) was measured by XPS.*

In terms of small scale roughness, the interior of a patch pipette aperture is likely to be incredibly smooth, as it is formed from melted glass. The mean roughness of borosilicate glass cover-slips was measured as 0.13nm [1]. Thermal silicon dioxide approaches this value. The PECVD silicon dioxide is significantly rougher, although boron-doping does improve the situation.

4.2.4 Surface Chemistry

The contact angles of untreated and boron doped silicon dioxide surfaces were measured by Dworak [1]. These results are also shown in table 4.4. The contact angles of the boron doped oxides are very similar to that of glass (24.31°), but plain thermal oxide is more hydrophobic. This is believed to be due to the greater order in the chemical structure of thermal oxide which promotes the formation of siloxane bridges, rather than 'dangling' silanol groups [80]. It is supposed that boron doping disrupts the lattice structure, creating more sites for silanol groups to form. The hydrophilicity of untreated PECVD oxide is attributed to its porous nature.

In addition to these measurements, the boron content of the different surfaces was measured using X-ray photoelectron spectroscopy (XPS). The boron content is given by mass in table 4.4. The measured values are somewhat less than the boron content of patch glass (4.05%). This could possibly be increased by doping the surface more heavily with boron (lengthening the

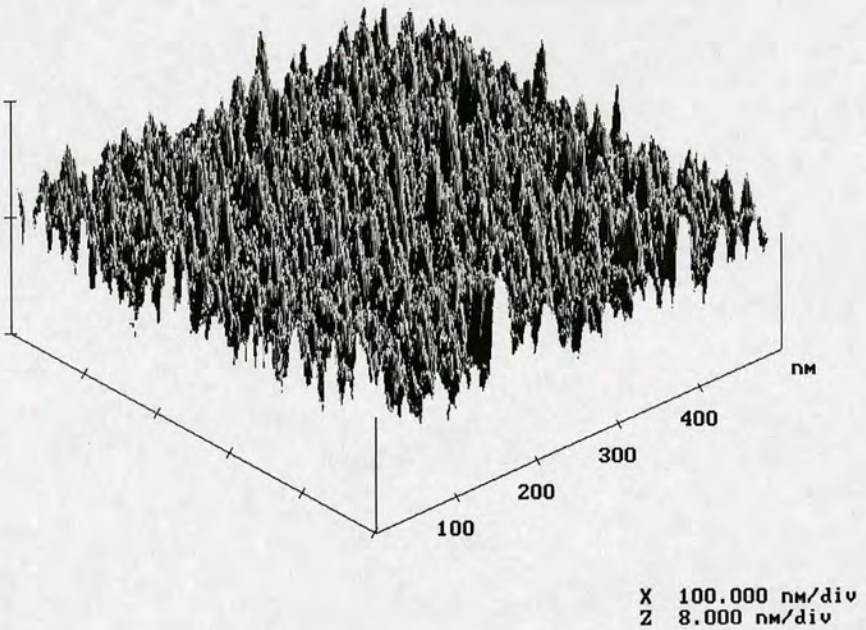

Figure 4.8: *A typical AFM scan of PECVD oxide deposited on un-processed silicon.*

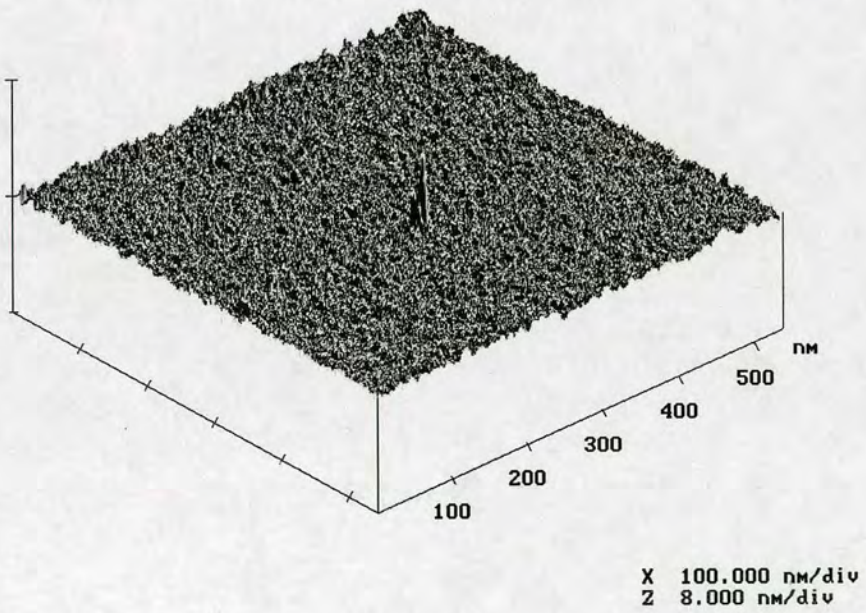

Figure 4.9: *A typical AFM scan of thermal oxide grown on un-processed silicon.*

deposition time). However, XPS is not suited to detection of boron, due its low atomic mass, so the figure for the devices may be an underestimate.

4.2.5 Aperture Depth

The depth of the sealable area inside the hole was determined by the thickness of the device layer of the SOI wafers used. The nominal thickness of the device layer was $15\mu m \pm 1\mu m$. However, the actual range of device layer thickness was between $8\mu m$ and $27\mu m$ and the maximum variation within one wafer was $10\mu m$.

All thermal oxide devices which produced seals were sectioned (by scoring with a diamond scribe and snapping) and the thickness of the device membrane (the SOI device layer) was measured for each device (see table 4.5). The membrane thickness of the device varies considerably between device types, caused by variations within the batch of SOI wafers. However, there is also some variation within device types (particularly the $2.5\mu m$ devices) due to non-uniformities in the device layer of the individual wafers (in the case of the $2.5\mu m$ wafer, there was a substantial wedge angle).

Group	Mean Membrane Thickness	Std Dev.	Mean EAD	Std Dev.	Mean Taper	Std Dev.
1.5μm	6.99μm	0.63	5.7μm	0.94	0.38°	0.87
2.5μm	12.32μm	2.19	9.9μm	2.53	2.22°	1.58

Table 4.5: *Device layer thickness, estimated aperture depth and taper for measured thermal oxide devices.*

There was some undercut caused by the front side etch hitting the buried oxide layer, which reduced the effective depth of these apertures (see figure 4.12). This undercut is caused by the variation in the device layer thickness, which caused the deep etch to hit the stop layer sooner than expected. A possible method of eliminating this undercut is to etch the back hole first, and remove the stop layer before performing the Bosch etch on the frontside. This would prevent the frontside etch from hitting the stop layer.

In an attempt to measure this undercut, the lateral diameter of the undercut (viewed from the backside) and the diameter of the aperture from the backside were also measured. Figure 4.10 illustrates these dimensions. These dimensions were only measured after testing with cells, so many devices were obscured by biological debris, which prevented measurement of these

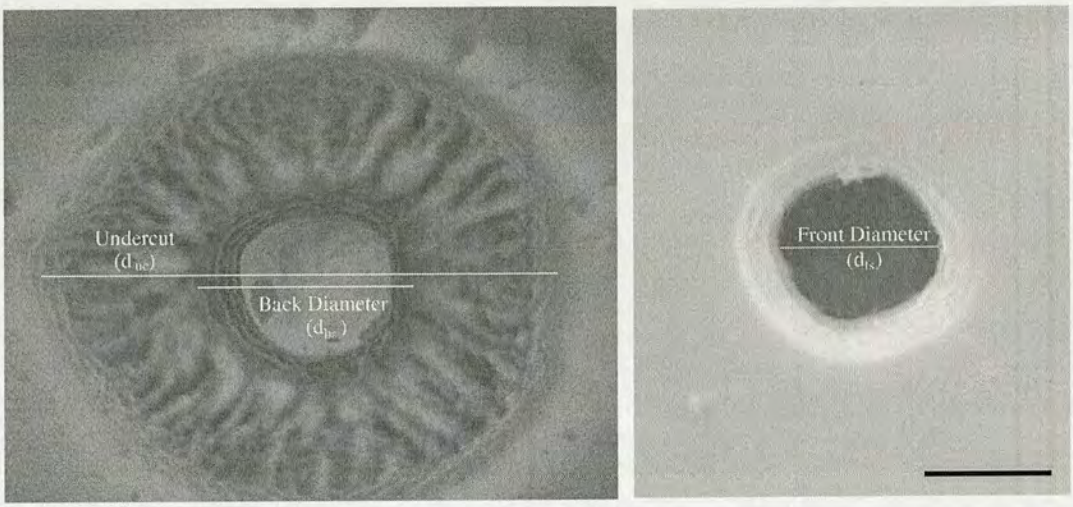

Figure 4.10: *The various diameters measured for each device. Left: the back of the device membrane. Right: the front of the device membrane. A flat* $2.5\mu m$ *boron-doped device is seen in this example. Note that it is possible to see the ripples on the sidewall from the back side. The scale bar is* $2\mu m$

values. For the cases in which they were measurable, the horizontal diameter of the undercut was used to estimate the vertical erosion of the device membrane. It was assumed that the undercut in the vertical direction would be equal to the lateral etch (which seems reasonable from figure 4.12). The radius of the undercut, minus the radius of the aperture was subtracted from the membrane thickness to produce a value for the estimated aperture depth (EAD). Thus,

$$EAD = t_{mem} - \frac{(d_{uc} - d_{bs})}{2} \tag{4.1}$$

These values are given in table 4.5.

Membrane thicknesses for the PECVD devices were not measured explicitly. However, evidence provided by depth measurements of alignment marks taken while the wafer was intact and FIB cross-sections, led Dworak [1] to conclude the membrane thickness was $8 \pm 3\mu m$.

Despite the fact that the device layer thicknesses did not comply with their stated tolerance, their variation provided a mechanism by which the effect of seal length on seal resistance could be examined. The depth of a glass pipette aperture is of the order of 10mm - so large as to be effectively infinite on the scale of membrane patches - but the bleb length measurements

presented in chapter 5 suggest that at most the first $40\mu m$ affect seal formation. The fact that the device apertures are shallower than this value allows an investigation of how the area available for seal formation affects seal resistance.

4.2.6 Taper

Using the membrane thickness measurements and the front and rear hole sizes (figure 4.10), it is also possible to calculate the taper angle achieved by the altered Bosch etch process,

$$Taper = tan^{-1}(\frac{d_{bs} - d_{fs}}{2.EAD}) \tag{4.2}$$

The calculated values are summarised in table 4.5. A taper of zero represents a vertical sidewall.

It can been seen from table 4.5 that there is in fact little taper in the $1.5\mu m$ devices, but the $2.5\mu m$ devices show a mean taper comparable with that estimated for glass (2.24°). That larger features develop a larger taper is a readily explainable phenomenon, in that higher aspect ratio (narrower) features allow a smaller ion flux to reach the sidewalls, and thus inhibit lateral etching to a greater degree [81].

The Bosch etch performed on the PECVD devices was optimised for vertical etching, so there is no reason to believe there was any taper on these holes. Figure 4.12 supports this conclusion.

4.2.7 Nozzle height

The extent of the nozzle protrusion was measured on the SEM in the same manner as the membrane thickness. As some of the nozzles were apparently damaged during the seal testing process, this data is incomplete. However, the nozzle height was consistently $2\mu m$ across all devices measured. The nozzle height is also included in the membrane thickness values for nozzle devices. For those devices in which the nozzle had been damaged, the height was assumed to be $2\mu m$.

The motivation for creating protruding nozzles was the hypothesis that a nozzle pressing into the cell membrane (in the same way as a glass pipette does) might provide better mechanical isolation for the membrane patch, allowing suction to have a greater effect on the membrane. For this purpose, a nozzle $2\mu m$ in height is sufficient. A larger protrusion pressing into a cell

body $\sim 10\mu m$ in diameter would cause significant deformation of the cell. Control of this nozzle height is in any case a trivial matter, simply being a case of etching back the surrounding silicon to a greater or lesser extent. However, the thickness of the device membrane is a limiting factor here. To create a longer nozzle, the membrane must be thinned. If the membrane becomes too thin, then the mechanical stability of the devices is compromised. Hence the height of the nozzle was limited to $2\mu m$.

4.2.8 Backside Chamber Undercut

For several devices, the undercut on the underside of the SOI layer was also measured (see figure 4.11). The average undercut was $21\mu m$.

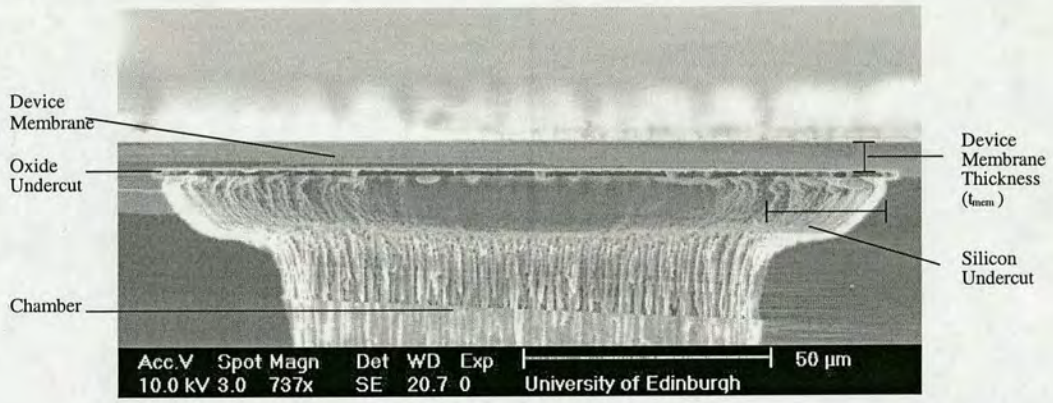

Figure 4.11: *A typical device section showing the membrane, chamber, and the undercut caused by the back-side etch*

4.2.9 Focussed Ion Beam Microscopy

Three devices were also sectioned and imaged with a Focus Ion Beam (FIB) microscope. The resulting images can be seen in figure 4.12 along with an image of a PECVD device. Two of the thermal oxide devices were sectioned after use with cells, and biological debris is clearly visible in the apertures. However, these images allow us to verify the undercut and taper estimations made above, and the aperture curvature.

The FIB images also give some idea of the large scale ($\sim 1\mu m$) roughness of the devices. Figure 4.12 d) shows that some sidewall ripple remains on the thermal oxide devices after oxidation; this ripple is a remnant of the scalloping caused by the Bosch etch used to form the apertures. Although attempts were made to ameliorate this roughness by performing two

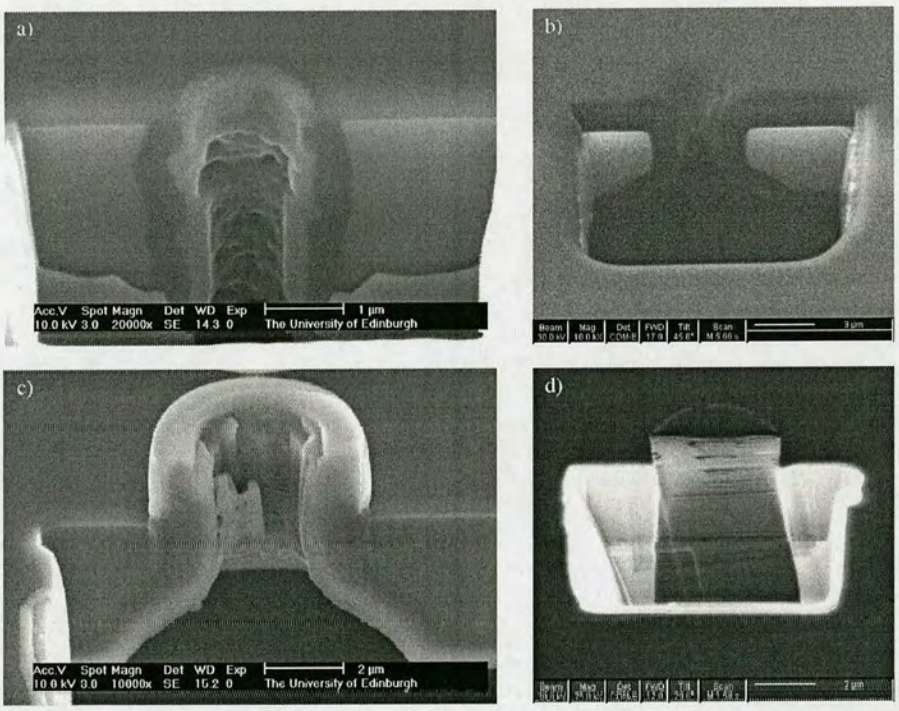

Figure 4.12: *Images of devices cross-sectioned with a focussed ion beam (FIB) microscope. a) SEM image of a* $1.5\mu m$ *flat device, note the biological debris, which prevents examination of the patching surface. However, note that there is little taper. Image taken at an angle of* $30°$*. b) FIB image of a PECVD device, note the rounded aperture and the thick oxide layer [1]. c) SEM image of* $2.5\mu m$ *nozzle device. Biological debris is also present here, and there is little taper. d) FIB image of an unused* $2.5\mu m$ *device. Note the surface roughness caused by Bosch process scalloping, visible near the top of the aperture. There is some evidence of taper here, but this is likely exaggerated by the section intersecting the aperture near its edge.*

oxidations of the surface, this was not quite achieved in the thermal oxide devices. The PECVD devices seem to have a better large scale roughness, as no ripple is visible. Although they were etched in the same way, they have a thicker thermal oxide layer, and PECVD oxide, which helps to smooth larger features. In both these cases, the large scale perturbations in the sealing surface are smaller than the reed inside the glass pipettes, which causes a deformation around 250nm in diameter.

Matthews and Judy [55] have eliminated the problem of sidewall scalloping by using thermal oxidation to consume the silicon to the point where it is smooth, and then removing the oxide. This is similar in purpose to the first oxidation performed on the thermal oxide devices. In this case, silicon consumed by the first oxidation has to be replaced by oxide in the second oxidation, in order to maintain the aperture diameter. Squaring caused by the second oxidation limits the extent to which the first oxidation can proceed. Matthews and Judy have overcome this problem by depositing a layer of amorphous silicon (a-Si) between the two oxidations. This decreases the diameter without squaring and creates a non-crystalline surface which will oxidise isotropically during the second oxidation. The trade-off here is the amorphous silicon will cause the final layer of thermal oxide to be slightly rougher than glass, though smoother than PECVD oxide [56].

Another alternative is to use a non-bosch (single step) deep etch which does not produce scalloping. This would produce vertical sidewalls and could be used for apertures up to $15\mu m$ deep. Alternatively, a Bosch etch could be used, and the sidewalls smoothed by hydrogen annealing [82]. This technique is the best method for producing smooth sidewalls, as it would melt the surface of the silicon, in a manner analogous to the fire-polishing of glass pipettes. This would round the profile of the hole and increase the sidewall taper, and also disrupt the lattice structure of the silicon, allowing isotropic thermal oxide growth. To date, no examples of this technique being used in planar patch-clamp have been published.

4.3 Electrical Characterisation

The electrical characteristics of the devices were tested immediately prior to the seal formation attempts discussed in chapter 6. During testing of the electrical properties, the devices were mounted on a perspex frame and fixed into the test rig described in chapter 6. The intracellular chamber and the well in the perspex frame were filled with N2A patch solution and the

connection to the top of the device made with N2A extracellular solution (see appendix B for compositions). The characteristics were recorded with an Axon Instruments Axo-clamp 2B patch-clamp amplifier connected to a desktop PC through an Axon Instruments Digidata 1320 Analogue to Digital Converter. 10nA current pulses 100ms in duration were passed through the device, and the voltage response measured. The resistance of each device was calculated directly from the height of the voltage and current traces. The time constant was calculated by fitting an exponential curve to the relaxation response to the current pulse. The capacitance was calculated by dividing the time constant by the resistance. The results are given in table 4.6.

Device Group	Mean Resistance	Std Dev	Mean Time Constant	Std Dev	Mean Capacitance	Std Dev
$1.5\mu m$	$2.51M\Omega$	1.61	$486\mu s$	453.6	$193pF$	80.4
$2.5\mu m$	$1.34M\Omega$	0.79	$208\mu s$	60.0	$155pF$	101.1
PECVD ($2\mu m$)	$1.37M\Omega$	0.26	$73\mu s$	17	$56pF$	18.8

Table 4.6: *Mean electrical parameters for planar patch-clamp devices (by aperture diameter).*

These values are explained by the electrical model for the devices (figure 4.13).

.

The component values in the model can be calculated from the material parameters. The resistivity of patch solution was measured as $0.540M\Omega.\mu m$.

$$
\begin{aligned}
R_S &= \frac{\rho.L}{A} = \frac{0.540M\Omega.\mu m.300\mu m}{(80\mu m)^2} = 25k\Omega \\
R_{A1.5} &= \frac{0.540M\Omega.\mu m.7\mu m}{\pi(0.75\mu m)^2} = 2.14M\Omega \\
R_{A2.5} &= \frac{0.540M\Omega.\mu m.12\mu m}{\pi(1.25\mu m)^2} = 1.32M\Omega \\
R_{APECVD} &= \frac{0.540M\Omega.\mu m.8\mu m}{\pi(1\mu m)^2} = 1.37M\Omega
\end{aligned} \tag{4.3}
$$

Since the shank and aperture are in series, the shank resistance R_S can be neglected from the model, and the resistance of the device can be represented by R_A alone. This agrees well with the experimental values given in table 4.6. The resistance value for $1.5\mu m$ devices is smaller than for $2.5\mu m$ as expected. However, the value for the $2\mu m$ PECVD devices is almost the same as for the $2.5\mu m$ devices. This is due to the difference in aperture depths between these

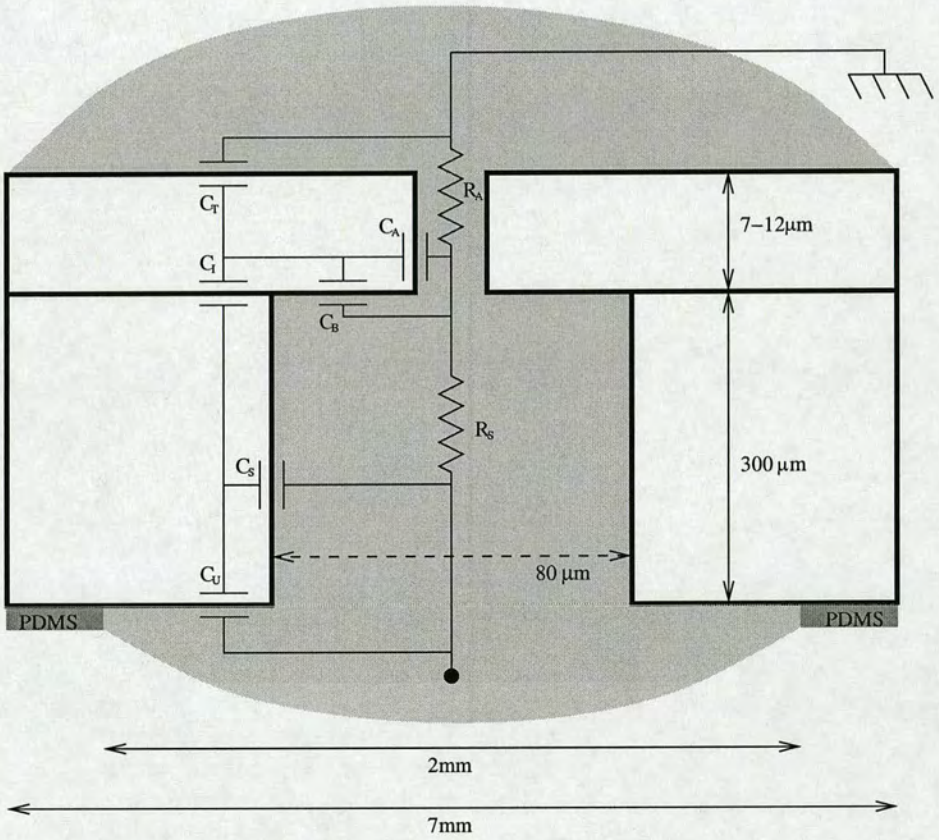

Figure 4.13: *The passive electrical model for a patch device. Adapted from Dworak [1]*

devices; the PECVD devices are shallower, which reduces their resistance.

Similarly, values for the capacitance can be calculated ($C = \epsilon_0 \epsilon_r A/d$), taking ϵ_r for SiO_2 to be 3.9 [83]. The thickness of the oxide is $0.52\mu m$ for the $1.5\mu m$ devices, $1.3\mu m$ for the $2.5\mu m$ devices, and $2\mu m$ for the PECVD devices. The calculated values are given in table 4.7.

	$1.5\mu m$ (pF)	$2.5\mu m$ (pF)	PECVD (pF)
C_A	0.0063	0.0025	0.0017
C_B	0.43	0.17	0.22
C_I	1300	1300	1700
C_S	6.37	2.55	5.5
C_T	3250	1300	850
C_U	208	83.4	27
$C_S + C_U$	214	85.0	32.5

Table 4.7: *Theoretical capacitance values for different elements of the device electrical model (figure 4.13)*

In order to calculate the overall capacitance of the devices, we neglect C_A and C_B because they are so small. Then we note that the parallel combination of C_S and C_U is in series with C_T and C_I. Since C_S and C_U are much smaller, they will dominate the series combination and hence the overall capacitance of the device.

Hence, the capacitance of the device is approximately equal to C_S + C_U. The value for the $1.5\mu m$ devices is the largest, as these have the thinnest oxide layer. The oxide on the $2.5\mu m$ devices was thickened slightly to reduce the aperture diameter, so their capacitance is slightly better. The PECVD devices have the thickest oxide and the smallest capacitance. With the exception of the $2.5\mu m$ devices these theoretical values agree with the experimental values given in table 4.6. However, the standard deviations for the experimental values are large. This variation arises from the fact that C_U is determined by the underside area covered by PDMS. Since this was applied by hand there is a large variation in area and hence in the device capacitance.

A familiar rule of thumb is that the membrane time constant of a cell should be ten times that of the pipette [84]. Typical membrane time constants of mammalian hippocampal pyramidal cells [85] range from 20 to 40 ms and those for the N2A cells measured here fall within this range. These values are much greater than the minimum value of 4ms (10×0.4ms; see table 4.6) obtained for the planar devices. However, because the capacitance makes a much bigger contribution to time constant than in a glass pipette, this rule of thumb breaks down.

This is demonstrated by the whole cell recordings taken with devices (chapter 6) in which it is impossible to measure the cell capacitance because it is dominated by that of the device.

However, if one considers the intended application of these patch devices (that is, in an array with $\sim 100\mu m$ spacing) it is apparent that some sort of micro-fluidic platform will be required to confine the solution for each hole. In this case, C_U will be eliminated, and C_S (a maximum of 6.37pF) will be the sole contributor to device capacitance, which would be superior to that of a pipette.

Devices fabricated by other groups show a range of electrical properties. The resistance is dependent on the diameter and depth of the aperture as described above, thus the resistances obtained vary from 0.5-40$M\Omega$, depending on the aperture geometry used. A wide range of capacitance values were also observed. The glass devices produced by Nanion [59] have the best capacitance reported ($< 1pF$). Like pipettes these glass devices are composed entirely of insulator, and thus it is only the device membrane ($20\mu m$) that is responsible for the capacitance. Lee et al. [66] also match this figure with their lateral patch clamp devices made from PDMS, by having membrane greater than $100\mu m$ thick. The drawback of this is that their resistance is somewhat high for a $2\mu m$ aperture ($10 - 14M\Omega$).

The other groups which have made silicon devices report a range of capacitances similar to those described here. Matthews and Judy [54] have reported capacitances of 300pF as fabricated, and 10pF when the backside of the device is bonded to a $1mm^2$ PDMS gasket. Pantoja et al. [51] have stamped PDMS onto the back of their devices to achieve a capacitance of 15pF. Lehnert et al [48] measured a capacitance of 150pF without confinement of the intracellular solution, and Lee et al. [57] report the capacitance of their devices as 50nF, though no reason is given for this large value.

Chapter 5
Conventional Patch-Clamp Control Experiments

5.1 Introduction

This chapter details the procedures involved in, and results obtained from, the control experiments performed to verify the health of the N2A cell line used in device testing. Because of the variation of seal performance with the cell type, these experiments also served to characterise the expected sealing behaviour and typical whole cell behaviour of the N2A cells. The chapter also outlines the procedures involved in cell line maintenance and harvesting, the full details of which are given in appendix B. A secondary set of experiments is described at the end of the chapter, in which the bleb length of the seals is measured (that distance to which the cell membrane extends during sealing).

5.2 Choice of Cell Type

Initial attempts were made using these devices to patch acutely dissociated neurons from pond snails (lymnea stagnalis). However, the variable health of the cells and quality of seal formation using glass impeded the gathering of meaningful data on seal formation with devices [1]. To improve the situation, the cell lines AtT20 (derived from a mouse pituitary gland tumour) and N2A (rat neuroblastoma) were tested. Both were derived from brain tumours, and thus shared some common properties with neuronal cells. The advantage of AtT20 was that the cells exhibited spiking behaviour, and thus provided a clear indication when whole cell had been achieved. However, the N2A cell line (although non-spiking) provided better seals more reliably, and since seal formation was the main factor of interest, this cell-line was used primarily. In addition, the N2A cells divided more rapidly, facilitating a high turnover of experiments.

5.3 Cell Culture and Harvest

The N2A cells were grown in 25ml culture flasks in culture medium containing Penicillin-Streptomycin (composition given in appendix B). A passage was performed every 2-3 days. Details of the passage procedure can be found in appendix B. When cells were needed for experiments, they were grown in anti-biotic free medium for at least 2 days before harvesting.

Harvesting consisted of removing the medium and detaching the cells from the culture flask using trypsin. The cells plus trypsin were then diluted with D-MEM and centrifuged to compact the cells. The D-MEM could then be removed, and the cells re-suspended in extracellular solution. Full details of the harvesting procedure and all solutions involved are given in appendix B.

Between experiments, the cell suspension was kept in the 15 ml centrifuge tube on a shaker table, to help reduce clumping.

5.4 Cell Viability Testing with Conventional Patch-Clamp

Prior to and subsequent to, using cells for device testing, the health of the cells was verified by attempting to form giga-ohm seals with glass pipettes. $100\mu l$ of cell suspension was pipetted into a 35mm petri dish, and the dish filled with extracellular solution. After several minutes (to allow the cells to settle) patching attempts were made. An image of a typical patching experiment is shown in figure 1.2.

Glass pipettes were pulled from borosilicate glass capillaries (Warner Instruments) using a Sutter Instruments Model P-87 electrode puller (see appendix B for pulling program details). Electrodes of around $1.5\mu m$ were pulled as this was the size which sealed most successfully. To ensure consistency in size, the bubble number [6] was measured (rather than the electrode bore, which was more time-consuming) for each electrode pulled. The bubble number is found by using a syringe to apply positive pressure to a pipette tip submerged in alcohol. The bubble number is traditionally defined as the mark (on a 10ml syringe) to which the plunger needs to be depressed before bubbles emerge from the pipette tip. Hence the larger the pipette tip, the larger the bubble number. A bubble number of 6-6.5 in alcohol was found to seal most successfully; this corresponded to a tip diameter of around $1.5\mu m$.

The pipettes were filled with $0.2\mu m$ filtered patch solution (see appendix B for composition) and mounted in an Axon Instruments HS-2 headstage with a standard half-cell. Positive pres-

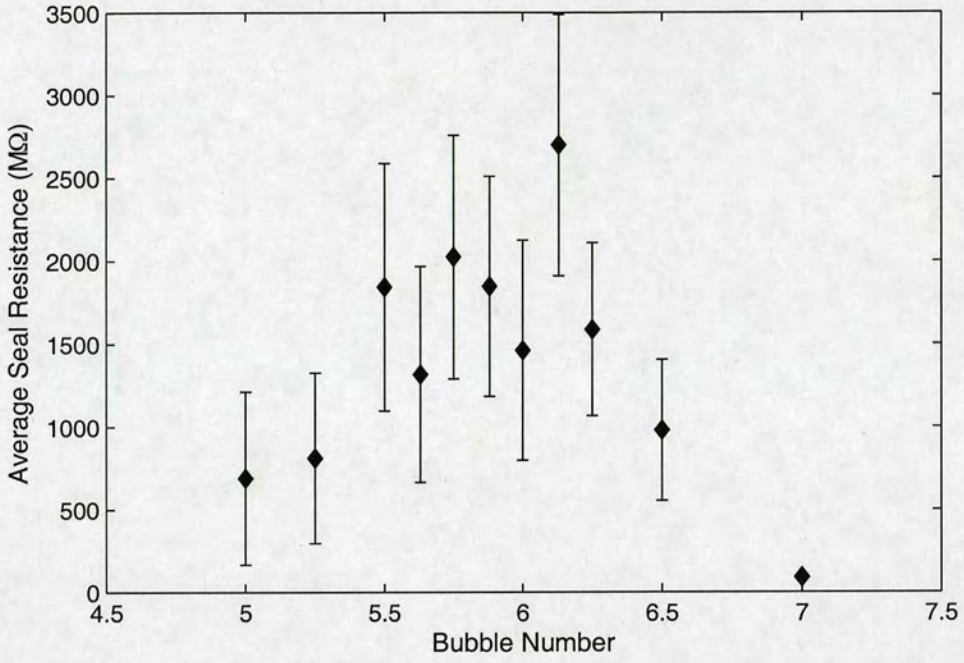

Figure 5.1: *Average seal resistance obtained vs. bubble number for glass pipettes used in patch experiments on N2A cells.*

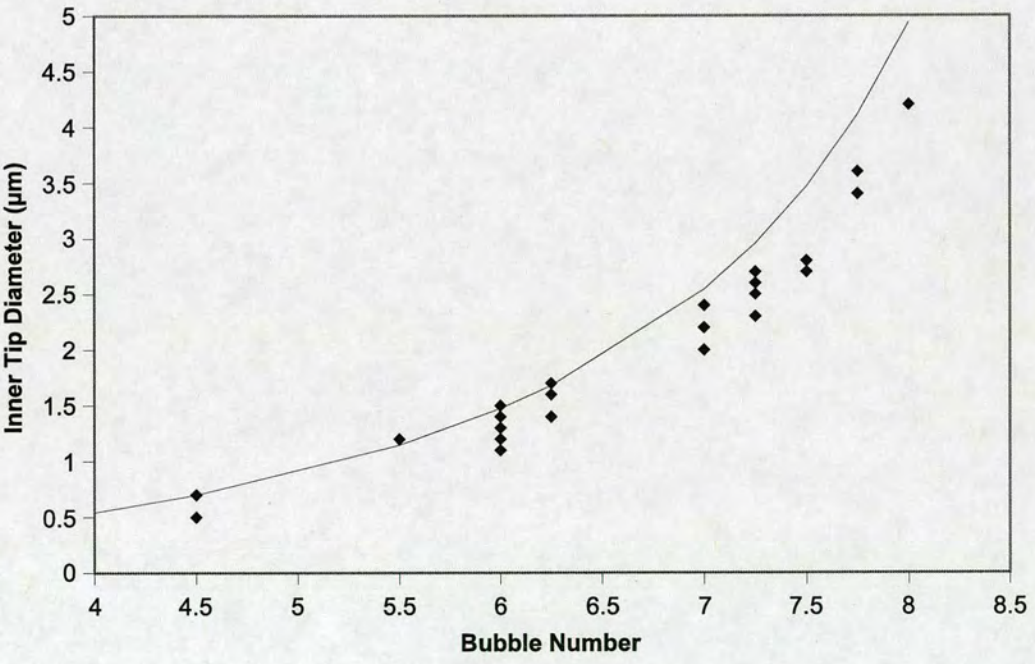

Figure 5.2: *Inside tip diameter vs. bubble number for glass pipettes used in seal formation experiments. The solid line is the best theoretical fit as described by Mittman [6].*

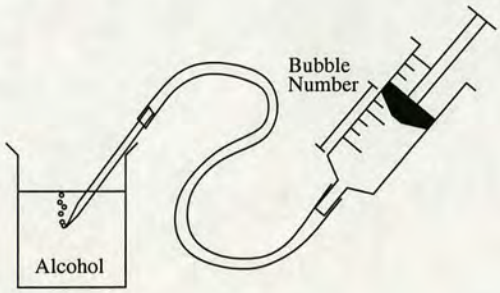

Figure 5.3: *The bubble number technique used to gauge tip diameter*

sure was applied (by mouth) to the inside of the electrodes to repel extracellular debris from the tip. The tip was submerged in solution and the resistance measured. The electrode potential was recorded with an Axon Instruments Axoclamp-2B intracellular amplifier. The signal was digitised and fed into a desktop PC using an Axon Instruments Digidata 1320 A/D Converter. The recording system was controlled from the PC using Axon Instruments' pClamp 9.0 software. Current pulses 250ms in duration (500ms period) were passed into the electrode. The size of the pulses was 1nA initially. Using a remotely controlled micro-manipulator the pipette tip was moved up to a cell membrane. The positive pressure was then released. In most cases negative pressure was then applied (again by mouth) to instigate seal formation. In some cases the positive pressure repelled the cell, and the tip had to be repositioned before suction. In rare cases, the release of positive pressure alone was enough to instigate seal formation, and no suction was required. As the seal resistance (judged by the voltage deflection caused by the current pulses) started to increase rapidly the suction was released. When the seal resistance reached $100M\Omega$ the current pulse was reduced from 1nA to 0.1nA. When the resistance had stabilised (normally around $2G\Omega$) suction was applied to rupture the membrane to achieve the whole cell configuration. As the cells did not spike, the shape of the cell I-V characteristic was used to determine whether the whole cell configuration had been achieved. Generally, the measured resistance decreased (though this was not always significant) and the time constant increased as the membrane was ruptured. A reduction in 50Hz noise, and other features, such as overshoot or sag also indicated the successful rupturing of the membrane. Two examples of typical traces recorded at the point of membrane rupture are shown in figure 5.5. If membrane rupture was successful, a current-voltage characteristic for the cell membrane was recorded on the computer.

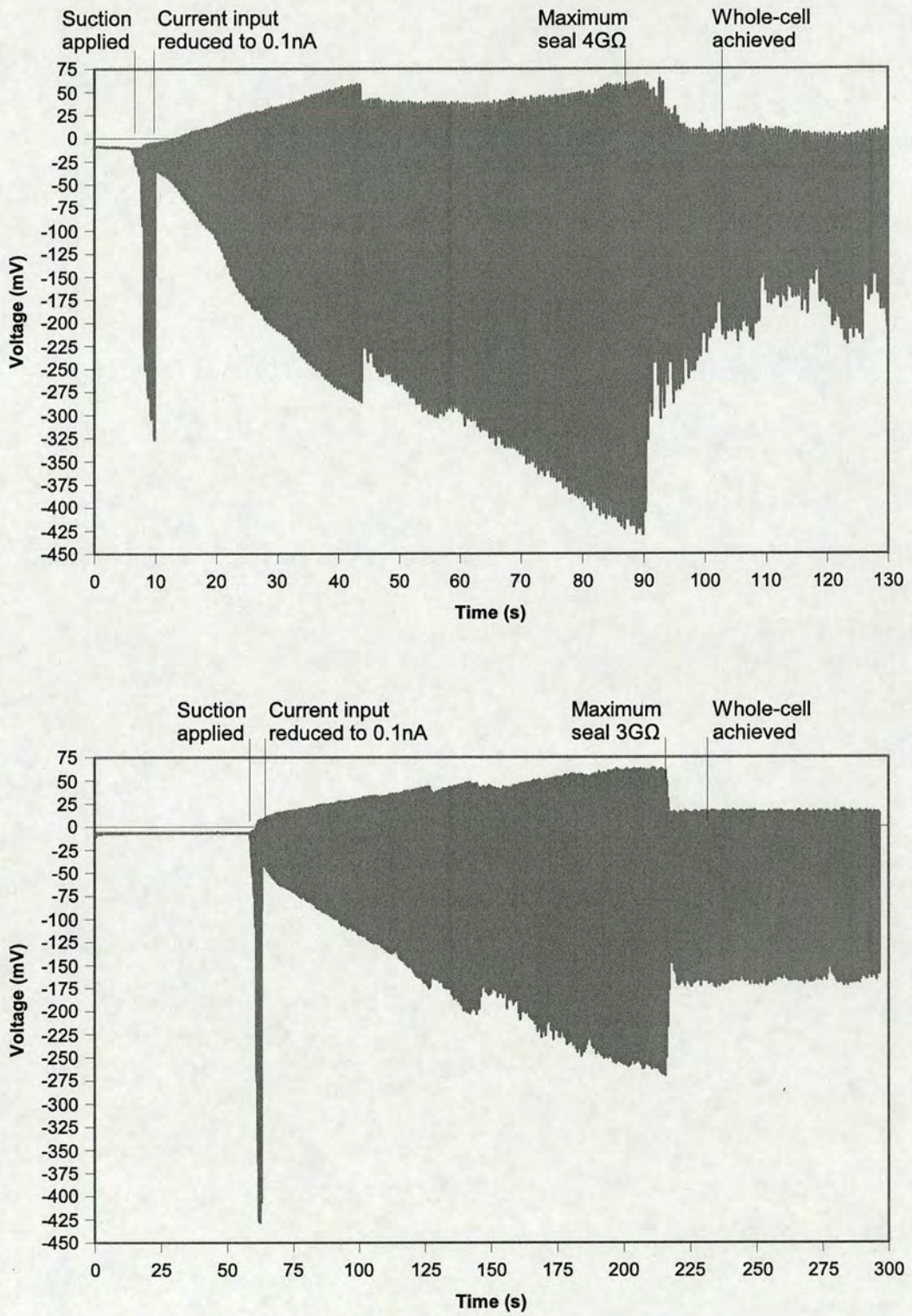

Figure 5.4: *Typical sealing traces obtained using a glass pipettes. As the seal resistance increased, the current amplitude is reduced from 1nA to 0.1nA to limit the voltage across the cell membrane.*

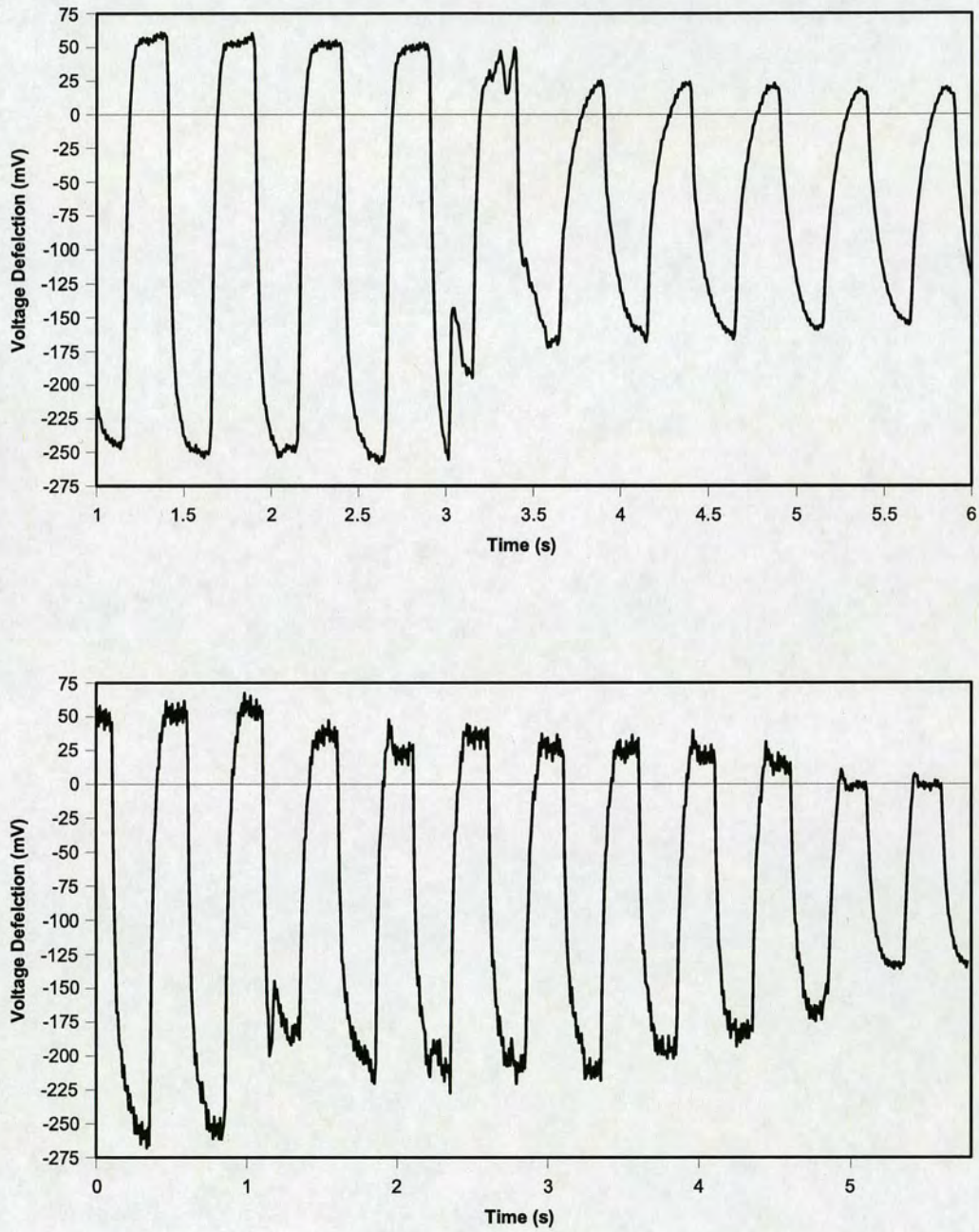

Figure 5.5: *Typical sealing traces highlighting the point of membrane rupture. Note the difference in resistance (proportional to the amplitude) and time constant between the cell-attached and whole cell configurations (top trace) and the reduction in noise and appearance of overshoot on the rising edge of the pulses (bottom trace).*

5.5 Patch Clamp Results

In most cases it was easy to achieve seals, with little suction required, and little damage to the cells. The average seal resistance was $1.55G\Omega$ and the maximum was $5G\Omega$. A breakdown of the results recorded with glass pipettes is shown in table 5.1.

	$(M\Omega)$
Maximum	5000
3^{rd} Quartile	2500
Median	1500
1^{st} Quartile	187.5
Minimum	0
Mean	1555
Std. Dev.	1351
Sample Size	172

Table 5.1: *Seal resistance results for glass pipettes.*

The mean and median are almost coincident, suggesting a normal distribution of seals. In fact this is not quite the case. There is a roughly normal distribution centred around $2G\Omega$ with a cluster of failed seals between 0 and $100M\Omega$. An important benchmark for seal formation is $1G\Omega$. Out of the 172 seals made, 103 (60%) reached this value or higher.

In many cases whole-cell characteristics were recorded. To ensure that these were in fact whole-cell characteristics, several experiments were performed with fluorescent dye in the patch solution. When the whole cell configuration was achieved, the dye flowed into the cell body, causing it to glow brightly. These experiments are discussed in greater detail below.

The whole cell characteristics recorded seemed to fall into three main types. The first type, denoted type 1, is illustrated in figure 5.6. This type is characterised by a higher resistance to positive going current than negative going current, and an overshoot on the relaxation from large negative current pulses. Type 2 (illustrated in figure 5.7) has a larger resistance to negative going current, and exhibits an overshoot on the response to large positive going pulses (analogous to spiking). Type 3 (figure 5.8) has an equal response to positive and negative going current but shows an overshoot after negative going pulses. Evidence for different cell types was also apparent from direct observation of the N2A cells in culture. Pyramidal cells, as well as spherical cells could be seen in the culture flask. However, after dissociation (i.e. during experimentation) all cells appeared roughly spherical. For comparison, a typical cell-attached

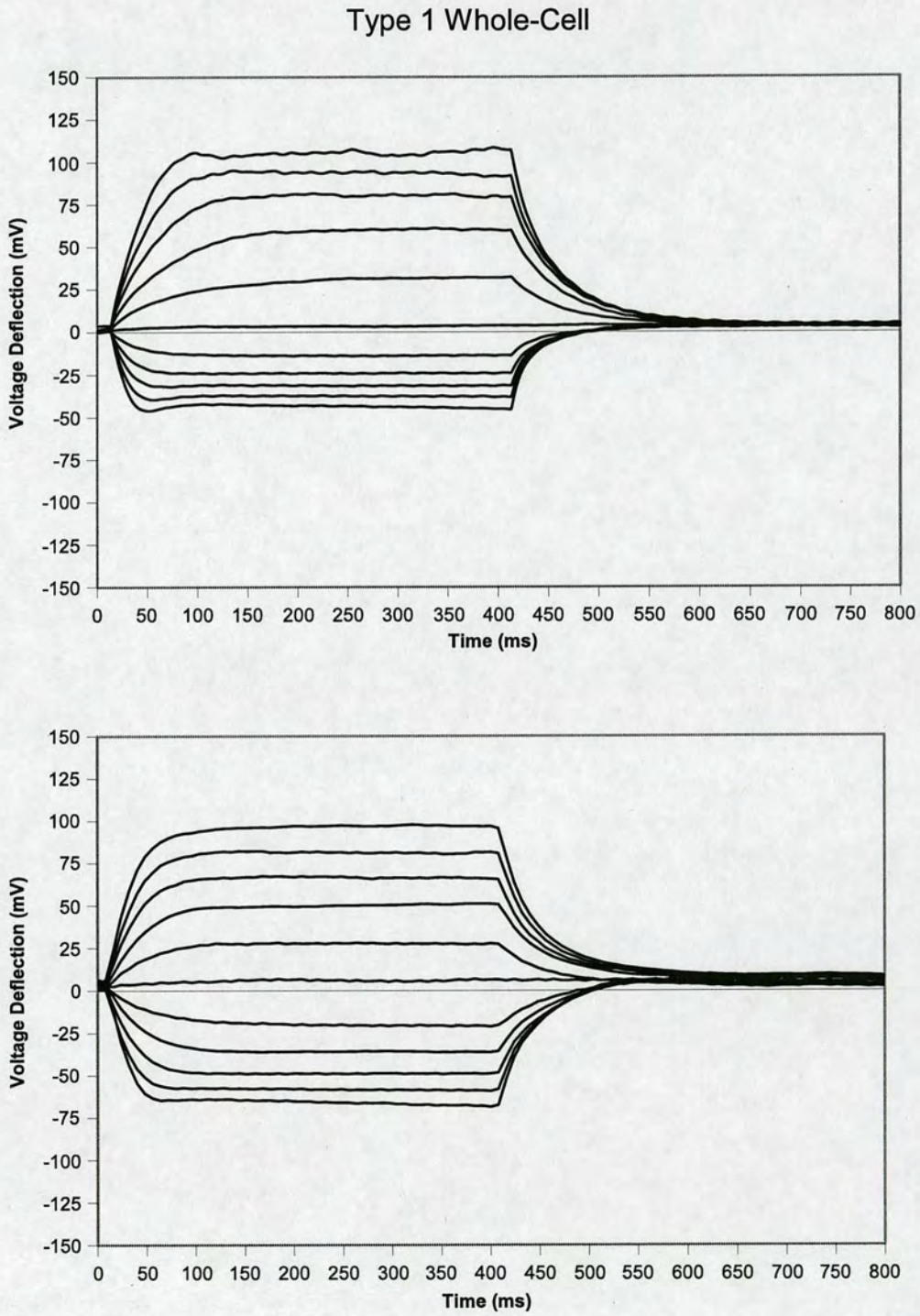

Figure 5.6: *Type 1 current-voltage characteristics recorded with glass pipettes. The top trace shows an example where the whole-cell traits are well defined, while the features of the bottom trace are less pronounced. Both traces were recorded with input currents pulses varying from -0.1nA to +0.1nA in steps of 0.02nA.*

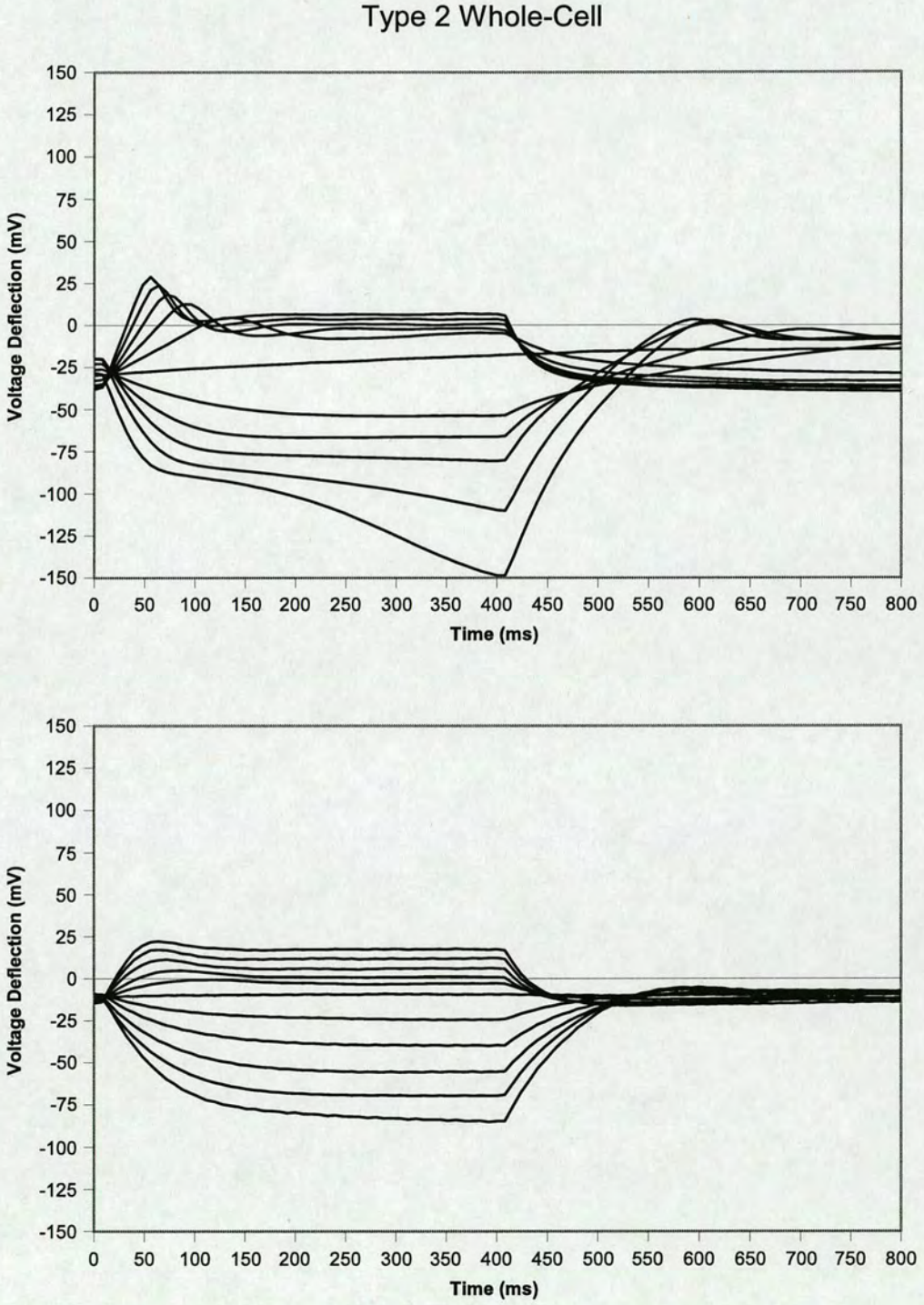

Figure 5.7: *Type 2 current-voltage characteristics recorded with glass pipettes. The top trace shows an example where the whole-cell traits are well defined, while the features of the bottom trace are less pronounced. Both traces were recorded with input currents pulses varying from -0.1nA to +0.1nA in steps of 0.02nA.*

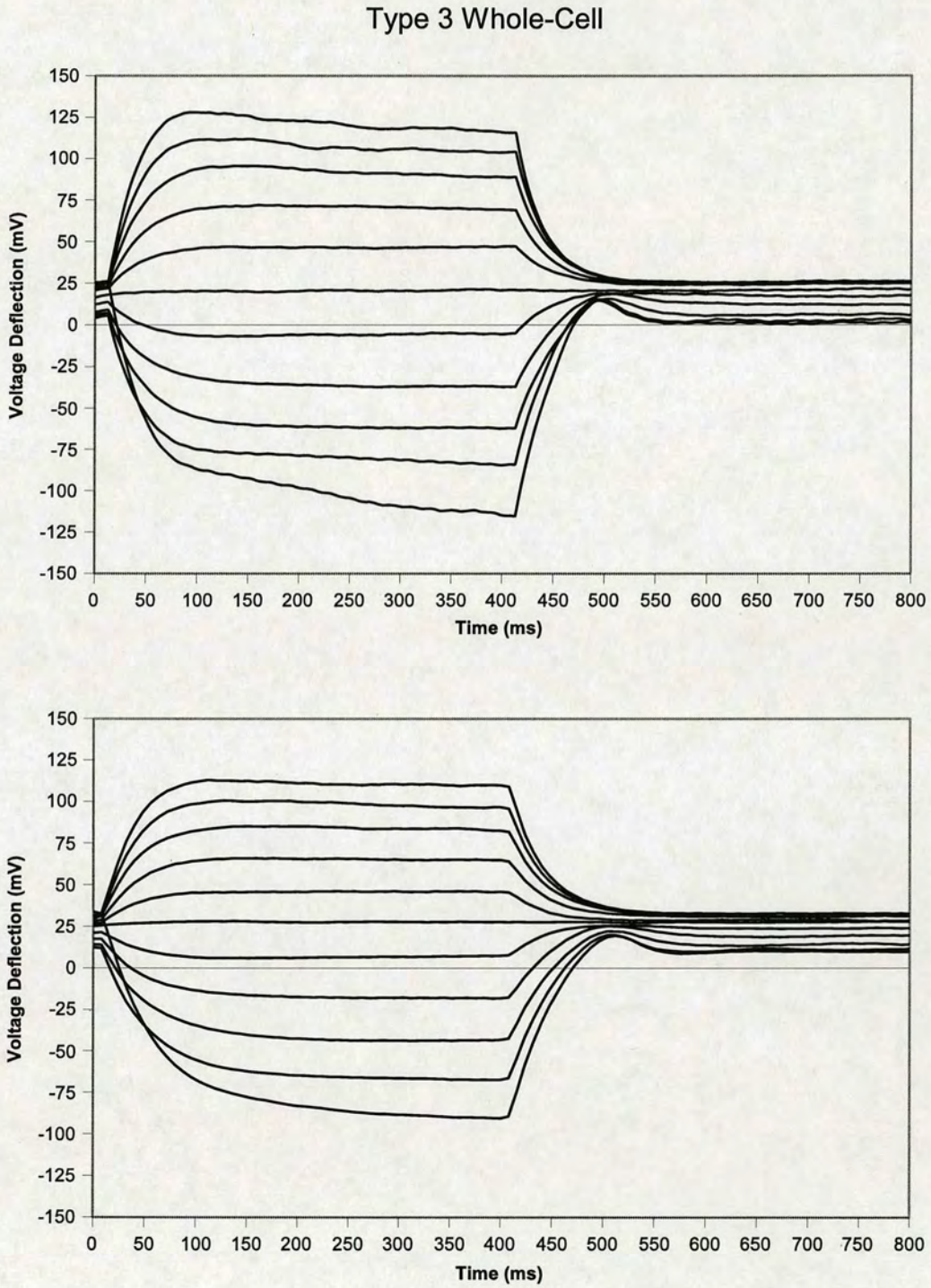

Figure 5.8: *Type 3 current-voltage characteristics recorded with glass pipettes. The top trace shows an example where the whole-cell traits are well defined, while the features of the bottom trace are less pronounced. Both traces were recorded with input currents pulses varying from -0.1nA to +0.1nA in steps of 0.02nA.*

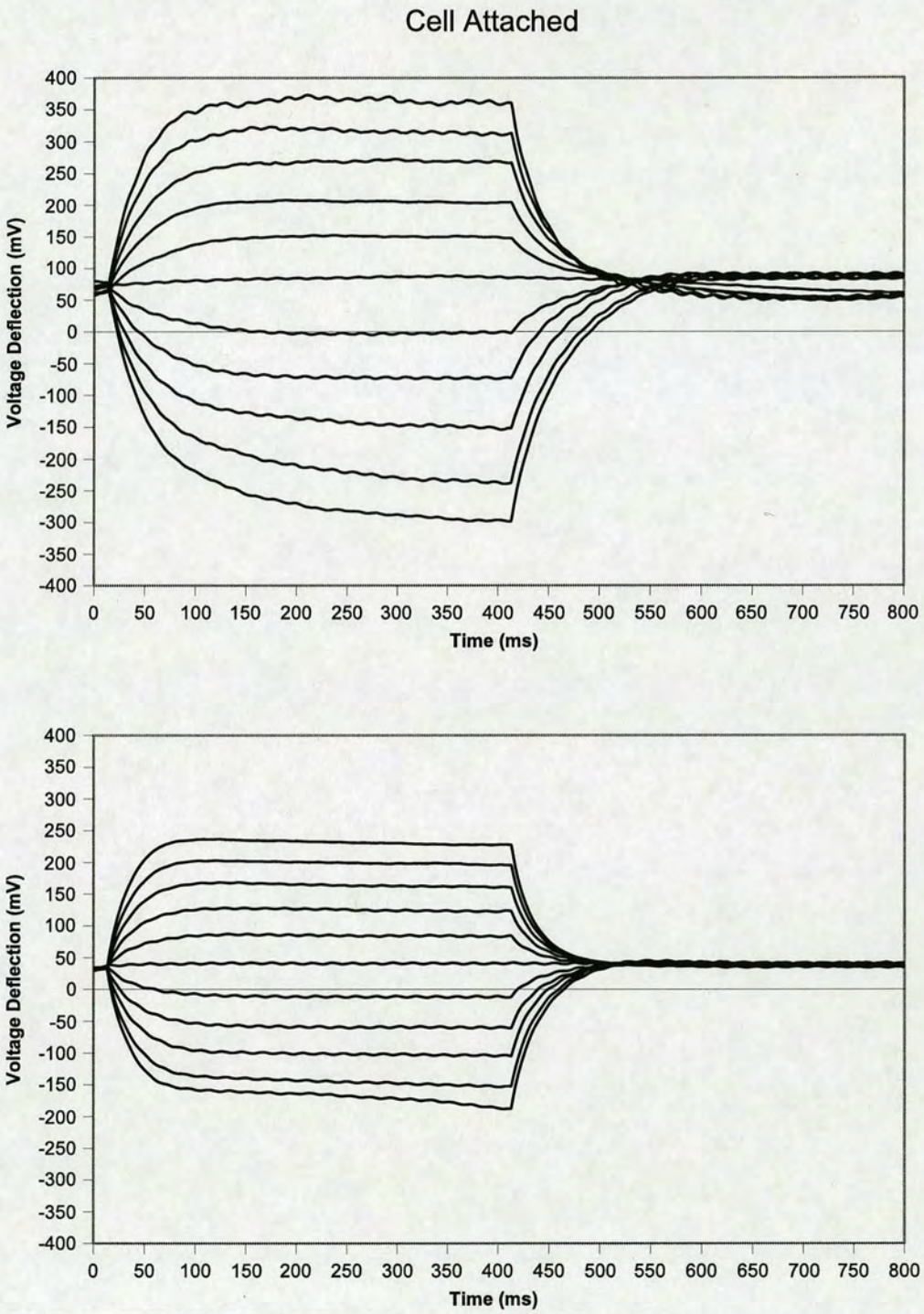

Figure 5.9: *Cell attached current-voltage characteristics recorded with glass pipettes. These traces generally showed a symmetrical response to positive and negative current. Note the difference in scale on the y-axis between these and the whole cell recordings. Both traces were recorded with input currents pulses varying from -0.1nA to +0.1nA in steps of 0.02nA.*

characteristic is shown in figure 5.9.

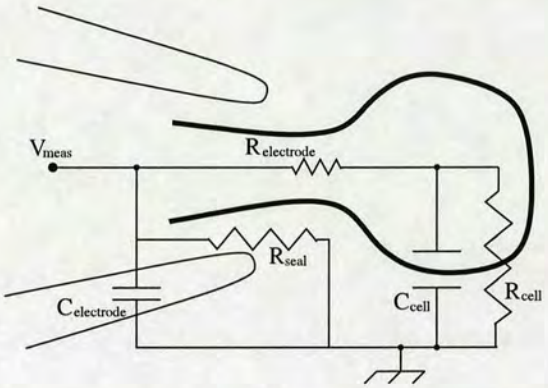

Figure 5.10: *A simple electrical model of the whole cell configuration. R_{seal} is the seal resistance. $R_{electrode}$ and $C_{electrode}$ are the electrical parameters of the device itself. R_{cell} and C_{cell} are the cell parameters it is desired to measure.*

The whole cell characteristics measured allowed extraction of resistance and capacitance parameters for the cell membranes. The resistance was measured by taking the average of the smallest positive and negative voltage deflections (divided by their respective current pulse sizes). The time-constant of the membrane was calculated by fitting exponential curves to the smallest positive and negative voltage deflections. The average of these time-constants was divided by the resistance to obtain an estimate for the membrane capacitance. Values for the resistance and capacitance of the cell-attached seals (before going whole cell) were calculated in the same way. The mean resistance and capacitance for each group (whole cell and cell attached) are given in table 5.2.

N2A cell type	Mean R ($M\Omega$)	Mean C (pF)	Adjusted R ($M\Omega$)	Adjusted C (pF)	Number of Recordings
type 1	1244	42	2321	15	14
type 2	1053	52	2531	11	11
type 3	1585	32	2864	15	7
All cells	1253	43	2494	14	32
Cell attached	2450	17	15	-	-

Table 5.2: *Breakdown of whole cell parameters recorded with glass pipettes. The different cell groups correspond to the different shapes of whole-cell characteristic witnessed during recording. The cell-attached figures are for those cells which had I-V characteristics recorded before rupturing the membrane (i.e. these represent the characteristics of selected seals.) The adjusted figures estimate the real cell parameters by taking account of the errors introduced by the pipette capacitance and seal resistance.*

The whole cell resistance is of the order of $1G\Omega$ large for all cell groups, as expected for N2A cells [86–88]. The capacitance is also of the same magnitude as reported elsewhere [88]. However, this means that the seal resistance, although slightly higher, is of the same order of magnitude as the membrane resistance measured. The seal resistance effectively adds in parallel with the membrane resistance (see figure 5.10). The pipette capacitance also has an effect on the whole cell trace, as it is effectively in parallel with the cell capacitance. The cell parameters were adjusted mathematically to remove the effects of these distortions. The adjusted values are calculated as follows:

$$\begin{aligned} R_{meas} = R_{seal}||R_{adj} \Rightarrow R_{adj} &= \frac{R_{seal}R_{meas}}{R_{seal} - R_{meas}} \\ C_{meas} = C_{electrode} + C_{adj} \Rightarrow C_{adj} &= \frac{\tau_{meas}}{R_{adj}} - C_{electrode} \end{aligned} \tag{5.1}$$

The adjusted membrane resistances and capacitances are also given in table 5.2.

5.6 Bleb Length Measurements

During the patch clamp experiments, it was noted that a substantial membrane 'bleb' was drawn into the tip of the pipette during seal formation. A separate set of experiments was devised to examine the size of the bleb in greater detail. Patch experiments were carried out as before, but this time with a fluorescent dye in the patch solution. The experimental process was illuminated with a monochromatic light source set at a wavelength of 500nm. The process was viewed with a CCD camera. When a bleb was drawn into the pipette, the fluorescent solution was pushed back up the tip, and it was thus possible to see clearly (and hence measure) how far the bleb had extended into the tip. See figure 5.12 for an illustration of a typical experiment. This was repeated a number of times using N2A cells with Lucifer yellow dye. (See appendix B for details of the dye solution.) On each attempt, a measurement of the bleb was made at the maximum stable seal value obtained. Attempts were also made to go whole cell. When this occurred, the membrane was ruptured and the dye diffused into the cell. This served as verification that the characteristics measured above were in fact those of the whole cell (see figure 5.12).

The average bleb length was $19\mu m$ and the maximum was $41\mu m$. The minimum length for a super-gigaohm seal was $8\mu m$. Pearson correlation and Spearman rank order correlation tests

	All blebs (μm)	$R_{seal} > 1G\Omega$ (μm)	$R_{seal} < 1G\Omega$ (μm)
Maximum	41	36	41
Median	17	18	17
Minimum	5.4	8.0	5.4
Mean	19	19	19
Std. Dev.	9	9	11
Sample Size	32	21	11

Table 5.3: *Bleb lengths measured with glass pipettes. The results show no significant correlation between bleb length and seal resistance.*

were performed on the bleb length vs. other parameters. This revealed no statistically significant link between bleb length and either seal resistance or cell diameter. However, tests performed on bleb length vs. pipette resistance return a correlation coefficient of -0.367 (P = 0.0389) for the Pearson test, and -0.404 (P = 0.0222) for the Spearman test. For seals greater than $1G\Omega$ only, the coefficients are -0.585 (P = 0.005) and -0.615 (P = 0.003) This suggests that as the pipette resistance decreases (as the bore increases), the bleb length increases. This trend is illustrated in figure 5.11 for seals greater than $1G\Omega$.

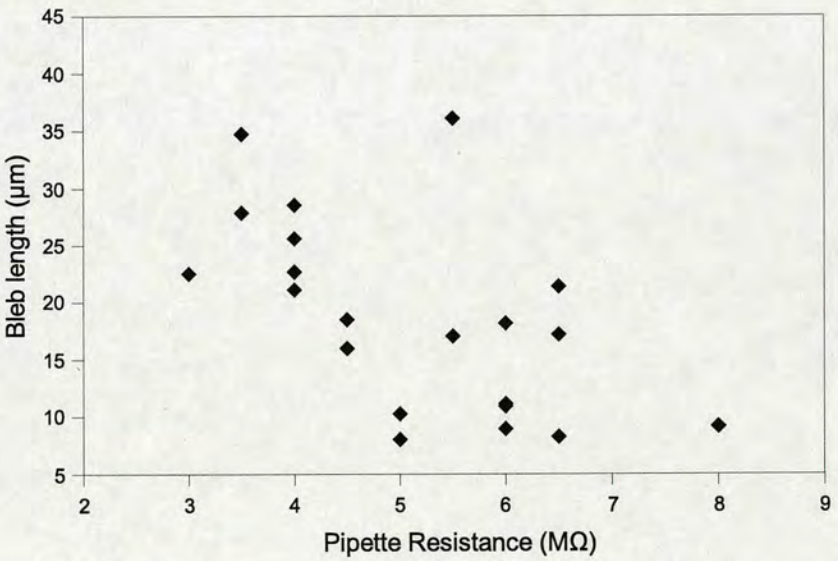

Figure 5.11: *The variation of bleb length with pipette resistance. The Pearson correlation test indicates a negative trend with a P value of 0.005. This suggests a positive dependence of bleb length on aperture diameter.*

The mechanism of seal formation observed was also interesting. In some cases a bleb formed at its maximum length, followed by an increase in seal resistance without further bleb growth.

In other cases, a small bleb formed first which then grew as the resistance increased. There were some instances where no seal formed despite the presence of a large bleb. In such cases, a bleb was just visible, but obscured by fluorescent dye leaking around its edges. The absence of any bleb at all generally meant a leak or blockage in the suction line, preventing pressure from being applied to the cell membrane.

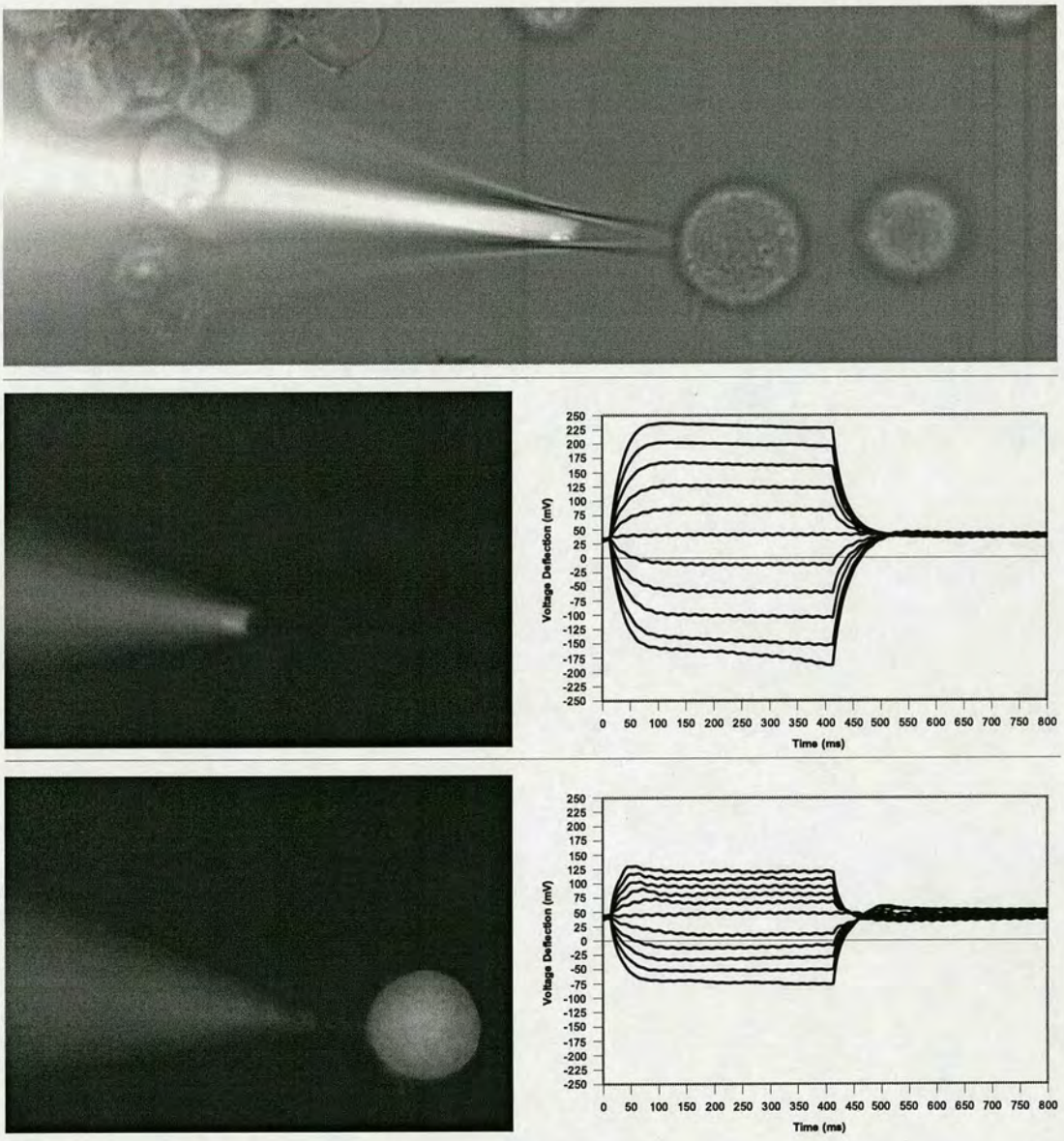

Figure 5.12: *Measurement of bleb length and verification of whole cell recordings using fluorescent dye. Top: front and back illumination showing both cell and the extent of bleb formation, allowing measurement of its length. Middle: front illumination only, showing only the dye, and hence that the cell membrane is still intact. The I-V trace for this configuration is also shown. Bottom: after applying suction to go whole-cell, the dye is observed entering the cell body. The corresponding I-V trace is also shown.*

Chapter 6
Evaluation of Planar Patch-Clamp Devices

6.1 Introduction

This chapter details the procedures involved in testing the planar-patch clamp devices and the results obtained from the testing. The chapter also presents the details of the test rig in which the devices were mounted to allow testing to take place. The details of the biological methods are largely the same as for the control experiments discussed in chapter 5 so only the differences are mentioned here.

6.2 Test Platform

In order to test the devices, a test platform was constructed to provide electrical contact and suction to the rear of the device. This platform is shown in figure 6.1. The design is based closely on that of a conventional glass pipette holder, in that as small a volume of intracellular (patch) solution as possible is used. This volume of solution is contained within a 3mm hole in a perspex frame, onto which the device is glued (with PDMS). This frame is then lowered onto a base unit, such that an upright intracellular electrode protrudes into the solution, and the perspex frame makes a seal with an o-ring. Once the frame is in position, it is secured in place using nuts and bolts. The chamber sealed by the o-ring has a suction port, allowing suction to be applied to the back side of the device. See appendix B for a detailed schematic of the base unit.

6.3 Device Testing Procedure

Subsequent to successful verification of the health of the cells with glass electrodes (as described in chapter 5), the N2A cells were used to test the silicon devices. Before the devices

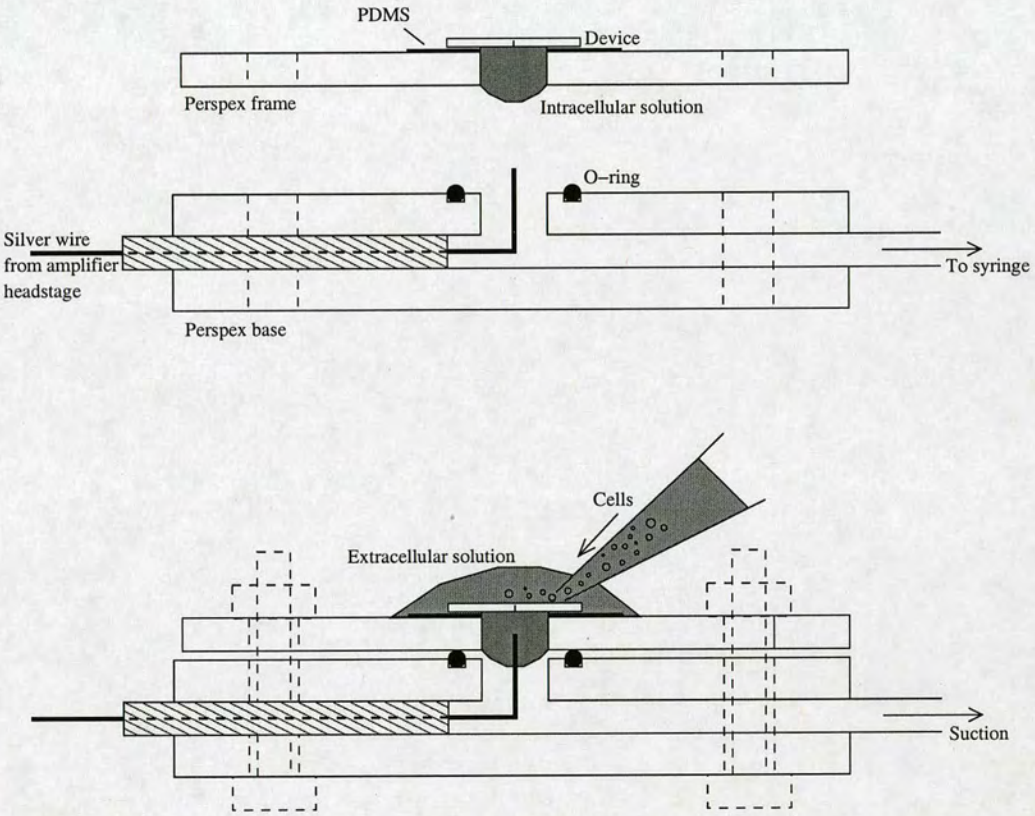

Figure 6.1: *The structure of the test platform used to test the planar-patch-clamp devices*

could be used, they first needed to be filled. This involved placing drops of patch solution on the front and back sides of the device. (The device having previously been glued into a 49mm perspex frame.) The device was then placed upside down in a vacuum jar and the vacuum jar was pumped down to less than 35mT. The jar was then sealed and left for 5 minutes to allow all bubbles to escape from the chamber of the device. The device was then taken from the bell jar and placed on the base unit described above. The frame was screwed in place, and the patch solution was removed from the top surface of the device, and replaced with extracellular solution.

An Axon Instruments headstage was connected to the intracellular electrode, and an earth wire attached to the same headstage was placed in the extracellular solution. The current-voltage characteristic of the device was recorded on to the computer (see chapter 4). The device was viewed using a microscope with a CCD camera and illuminated with white light from the underneath. The fact that the ($80\mu m$ square) device membrane was only $10\mu m$ thick allowed the transmission of orange light. This made it easy to locate the aperture (of the order of microns) in the centre of the 7mm silicon chip. Figures 6.2 and 6.3 illustrate the setup, and show images of a device taken with the CCD camera.

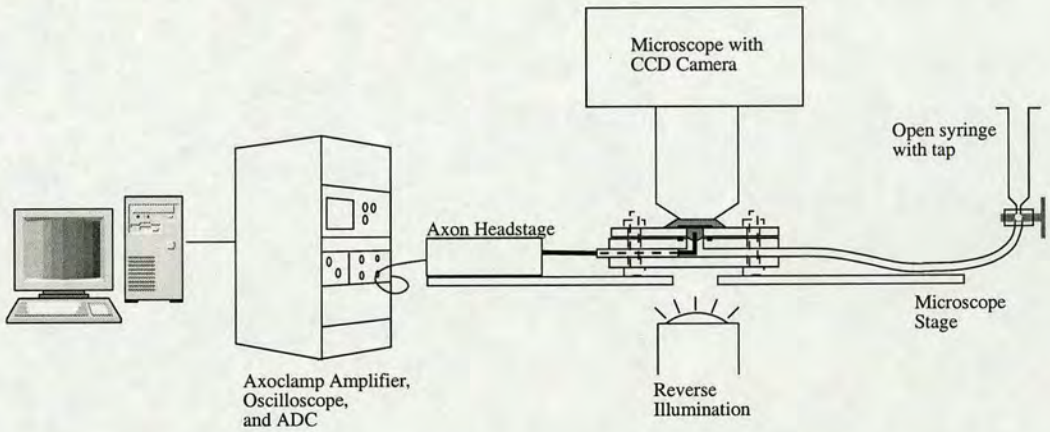

Figure 6.2: *The experimental setup for testing planar patch clamp devices.*

While viewing the device using the camera, $20 - 50\mu l$ of cell suspension (depending on cell density) was pipetted into the extracellular solution on top of the device. The device aperture was monitored and when a cell or clump of cells came close enough to the hole, suction was applied, and the cell sucked onto the hole. Care was taken not to suck cells that were too far away, or moving too rapidly, as these would most likely not be acquired, and the suction applied would instead attract unwanted cellular debris. As the cells approached the hole, suction was

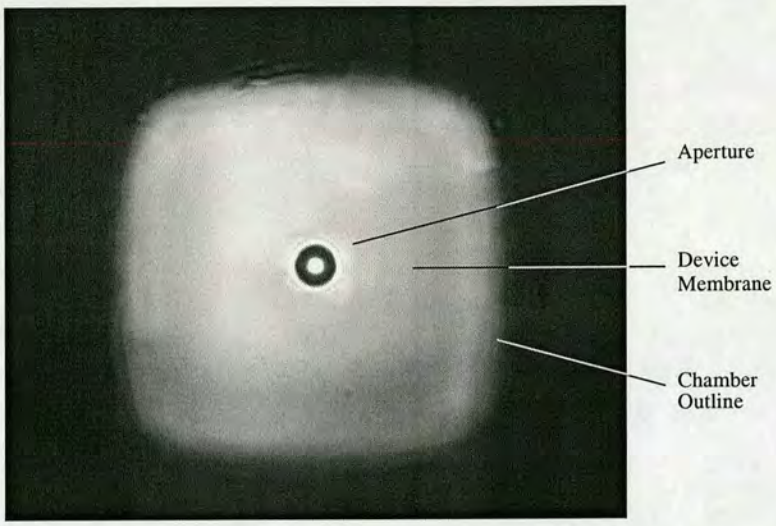

Figure 6.3: *A typical planar-patch-clamp device viewed with the CCD camera.*

released. Figure 6.4 shows a cell which has been successfully captured onto a device in this manner. Suction was then re-applied to encourage seal formation in the same manner as with glass pipettes. However, as sealing was generally less successful with devices, suction often had to be locked on (by means of a tap in the suction line) to achieve resistance increase. A typical trace for seal formation with a device is shown in figure 6.5 and figure 6.6. Note the increase in resistance on cell impact, and subsequent decay, detailed in figure 6.6. Of the 59 cells attempted with thermal oxide devices, 11 showed this behaviour, compared with zero of the 24 attempts made with PECVD devices.

In some cases, whole cell recordings were obtained. No specific attempt was made to go whole cell with the devices, rather the suction applied to increase the seal resistance caused a rupturing of the membrane. The presence of a rupture was indicated by the appearance of overshoot or sag on the sealing trace. With the device recordings, there was no measurable capacitance change to indicate that the whole cell configuration had been achieved, as the cell capacitance was masked by that of the device. There was also no resistance change, because the seal resistance was much smaller than the cell input resistance.

Devices were reused up to 3 times within one session. However, quite often devices became blocked with cell membrane debris, and either the resistance changed significantly, or the device no longer permitted fluid movement (and hence could no longer attract cells). When this occurred, a new device was used, following the same procedure. In many cases (in particular the devices with $1.5\mu m$ apertures) the devices were cleaned in acid piranha (see chapter 3) and

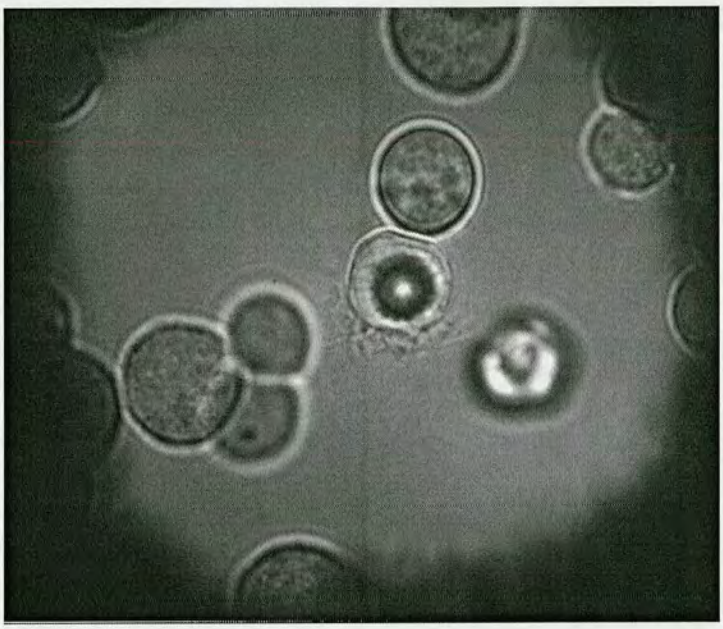

Figure 6.4: *An image of a typical planar-patch clamp experiment.*

re-tested on a different date.

Only the thermal oxide devices of $1.5\mu m$ and $2.5\mu m$ diameter and the PECVD devices could be tested with N2A cells. During the testing of the $2.5\mu m$ devices, cells were observed being completely sucked through the hole, (see figure 6.7) hence devices larger than $2.5\mu m$ were not tested with these cells.

6.4 Device Testing Results

The seal formation testing produced variable results. Unlike the glass pipettes, the cells did not seal readily onto the devices. Suction normally had to be locked on to encourage seal formation, and then only slow increases in seal resistance were observed. In total, 83 cells were positioned over a device aperture (a 'successful' attempt). Of these successful attempts, 24 were PECVD devices and 59 were the thermal oxide devices. The different device properties varied in the manufacturing process produced 8 subgroups of thermal oxide device. A summary of seal resistances obtained for each of these subgroups is given in table 6.1. However, one of these sub-groups ($1.5\mu m$ boron doped nozzles) produced no successful tests, and another ($1.5\mu m$ thermal oxide nozzles) produced only one. However, the single successful attempt with a $1.5\mu m$ nozzle device was the only device seal to reach a value of $1G\Omega$. Figure 6.8 shows a

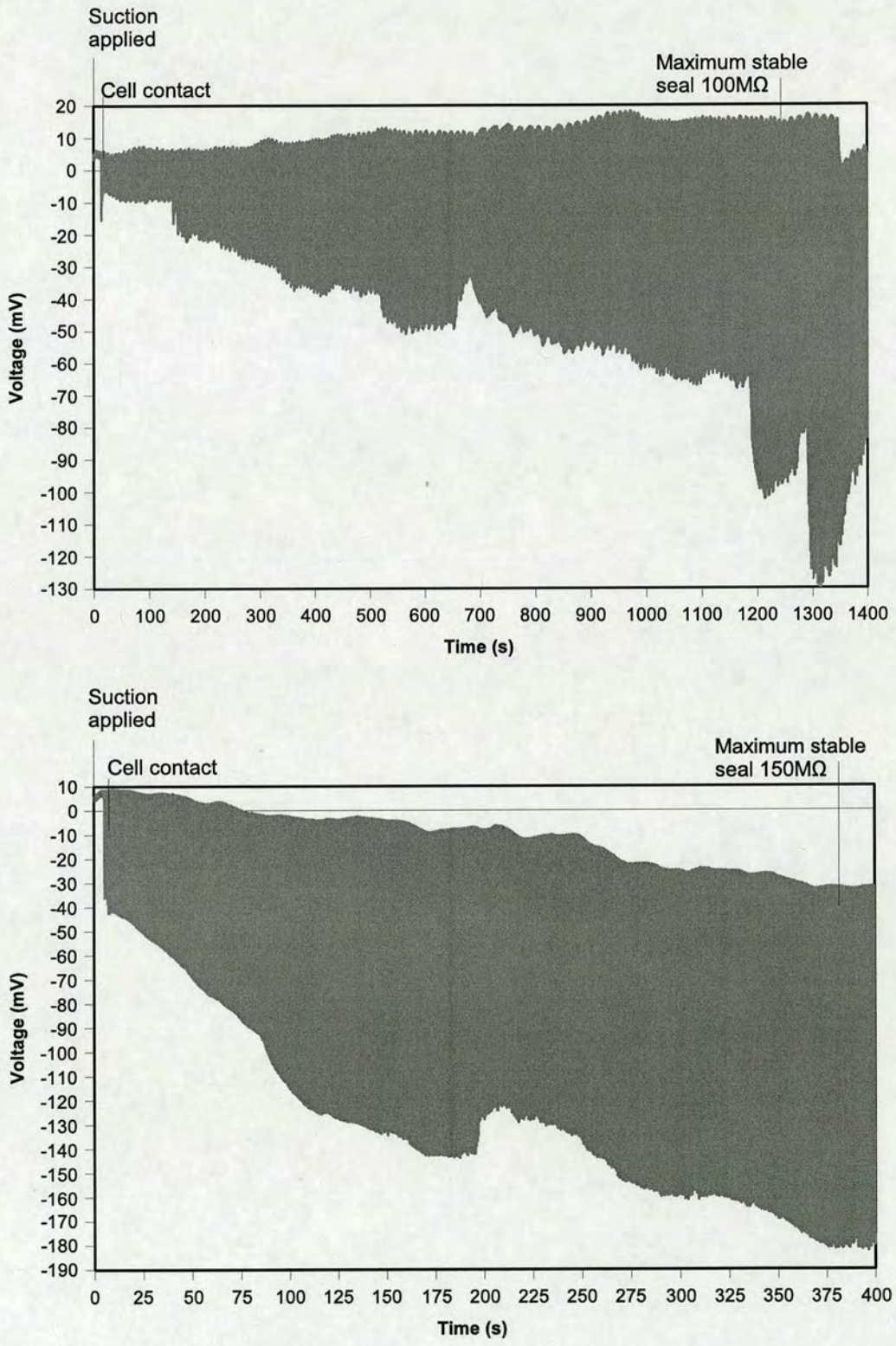

Figure 6.5: *A typical sealing trace for experiments performed using the planar patch-clamp devices. Both traces were recorded with 2.5μm diameter, boron-doped thermal oxide flat devices.*

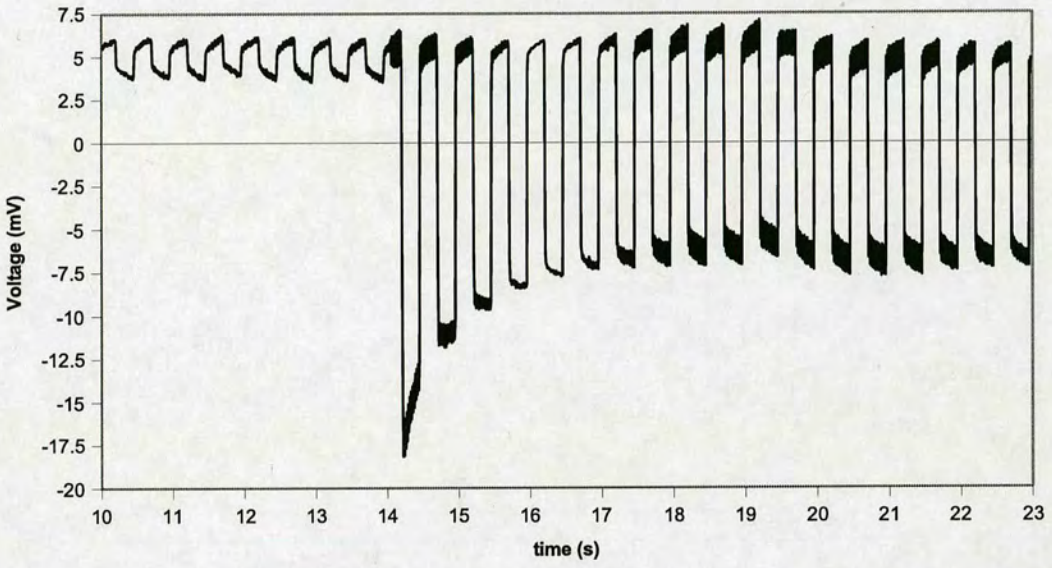

Figure 6.6: *A close-up of the cell contact point in figure 6.5*

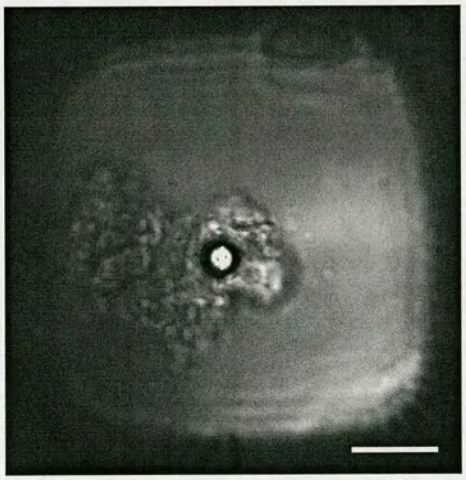

Figure 6.7: *Image taken of a* $2.5\mu m$ *device through which cells had been completely sucked. This negated the testing of larger devices. The scale bar is* $10\mu m$.

box and whisker plot of successful attempts for each subgroup (omitting $1.5\mu m$ nozzles).

Device Type	Successful Attempts	Mean Seal ($M\Omega$)	Std Dev	Max ($M\Omega$)	Min ($M\Omega$)
All Devices	83	78.6	121.4	1000	1.5
PECVD Devices (2μm)	24	34.0	40.3	160	1.5
Thermal Oxide Devices	59	99.6	140.2	1000	7
1.5μm	30	107.0	174.3	1000	30
Nozzle	1	1000	-	1000	1000
TO	1	1000	-	1000	1000
B	0	-	-	-	-
Flat	29	76.2	44.8	250	30
TO	16	71.3	29.4	130	30
B	13	82.3	59.5	250	30
2.5μm	29	83.5	63.7	250	7
Nozzle	14	66.6	57.5	200	7
TO	6	79.5	55.9	175	10
B	8	57.1	60.5	200	7
Flat	15	99.3	63.2	250	30
TO	9	93.3	66.0	250	30
B	6	108.3	63.7	200	50

Table 6.1: *Breakdown of seal results by subgroup. The subgroups are divided by device type, hole size, hole shape and surface material. For each group, the average seal resistance, standard deviation, maximum and minimum are given.*

6.4.1 Aperture properties

Statistical tests were performed on the resistances achieved with each subgroup (excluding $1.5\mu m$ nozzles). Each group was compared with every other using a Student's T-test, and (because many groups failed normality tests) a Mann-Whitney rank-sum test. A one-way analysis of variance (and ANOVA on ranks) was also performed on all subgroups together. However, none of these test revealed any statistically significant differences, other than the comparison between the thermal oxide devices and the PECVD devices. This returned a p-value of 0.027 for the T-test, and <0.001 for the rank-sum test. The PECVD devices were also tested against $1.5\mu m$ and $2.5\mu m$ devices separately. Both cases returned significant results: 0.05 and 0.03 for 1.5μ and 0.001 and 0.001 for $2.5\mu m$.

However, the results for the glass experiments indicate that aperture diameter at least should

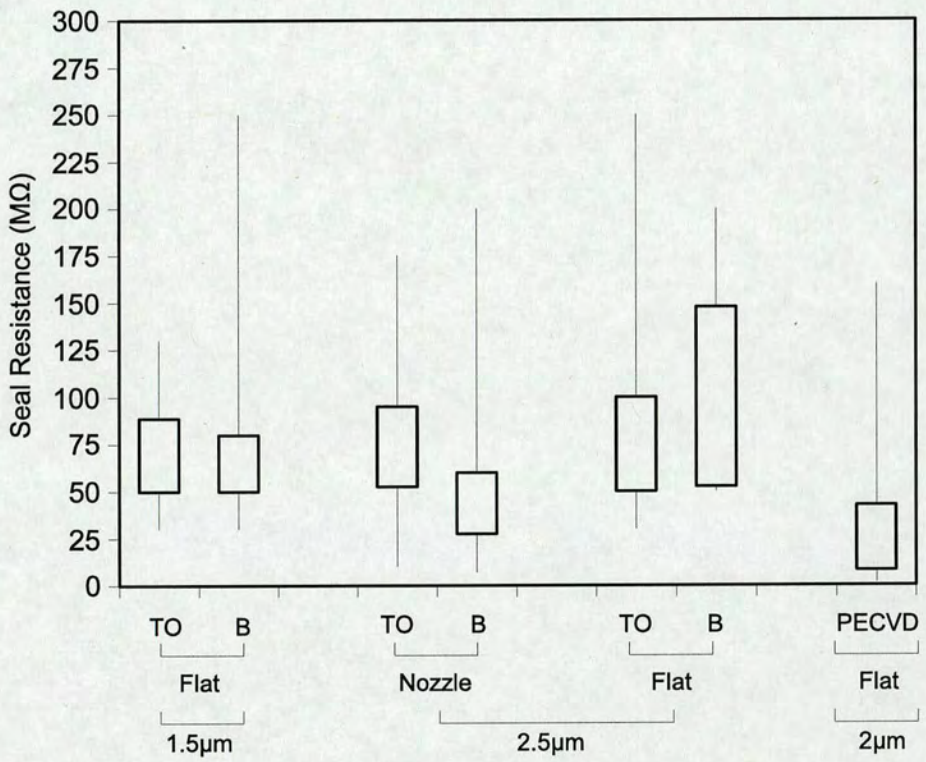

Figure 6.8: *Box and whisker plot of the seal resistances obtained for each device subgroup. The extent of the box in the y direction indicates the 1st and 3rd quartiles.*

play some role. Figure 5.1, in chapter 5 showed a scatter plot of seal resistance versus bubble number for the glass electrodes. This indicated a peak in seal resistance around bubble number 6. Figure 5.2 showed a plot of pipette diameter versus bubble number. Referring to this graph confirms that this bubble number corresponds to a hole diameter of about $1.5\mu m$. For a $2.5\mu m$ diameter the bubble number is around 7.5, which, referring back to figure 5.1 shows that $2.5\mu m$ pipettes perform significantly worse than $1.5\mu m$ pipettes. However, this seems not to be the case for the silicon devices.

6.4.2 Bleb Length/Aperture Depth

Although bleb length could not be measured directly for the silicon devices, there was evidence of bleb formation on cells that had been blown off the devices after seal formation. Examining figure 6.9 illustrates that bleb-shaped deformations were present in the cell after the seal had been broken. The mean length of these deformations was about $10\mu m$.

There is however, some variation in aperture depth, which permits an assessment of the effect of the depth of the sealable area. Figure 6.10 shows the variation of seal resistance vs. device membrane thickness, for different device groups (excluding PECVD devices as the membrane thicknesses of these devices were not measured individually). Qualitatively, it seems that the seal resistance increases with aperture depth for the flat devices, but not for the $2.5\mu m$ nozzles. Statistical tests (Spearman rank correlation) confirm this. The results of the statistical tests are given in table 6.2. A better measure of the sealing depth available is the estimated aperture depth (EAD) as calculated in chapter 3. Only $1.5\mu m$ devices show a significant trend for EAD vs. seal resistance.

6.4.3 Taper

The seal resistances obtained were also compared to the taper measured in chapter 3. However, there were no significant trends.

6.4.4 Whole Cell Recordings

Unlike the recordings made using glass electrodes, there was no specific attempt made to go whole cell with the devices as gigaohm seals were generally not achieved. Rather, during

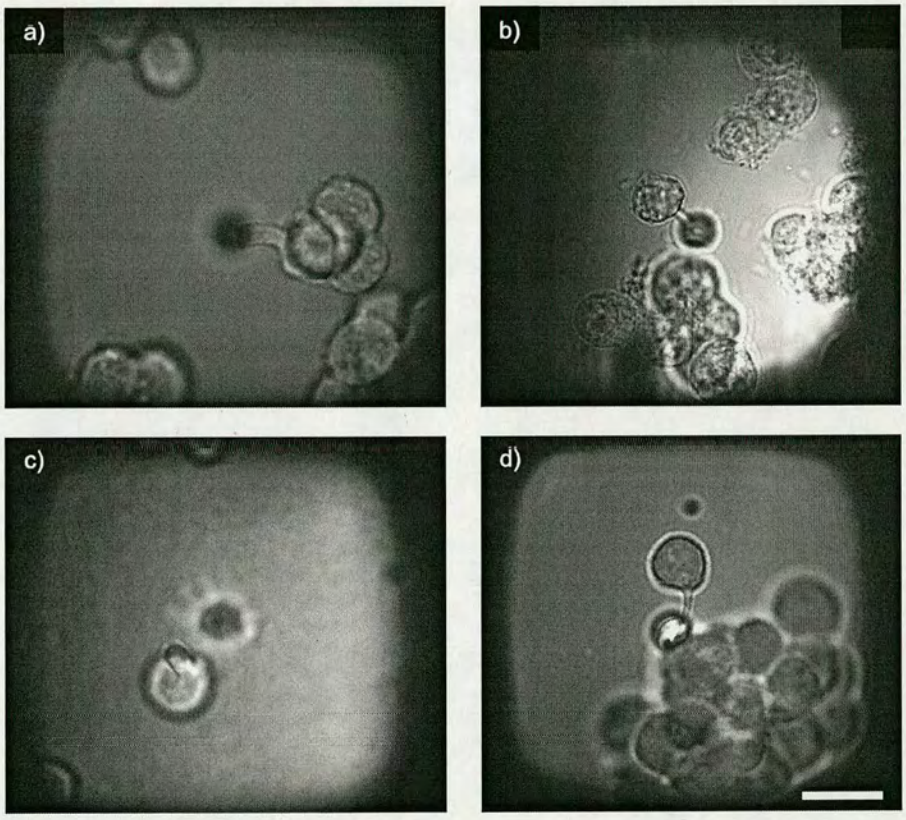

Figure 6.9: *Deformations of cell membrane caused by sealing on planar devices. All images are taken after sealing, i.e. after the cell has been blown away from the aperture. In image c) the cell is rotated and the deformation points upwards out of the plane of the page. The scale bar on image d) is* $20\mu m$.

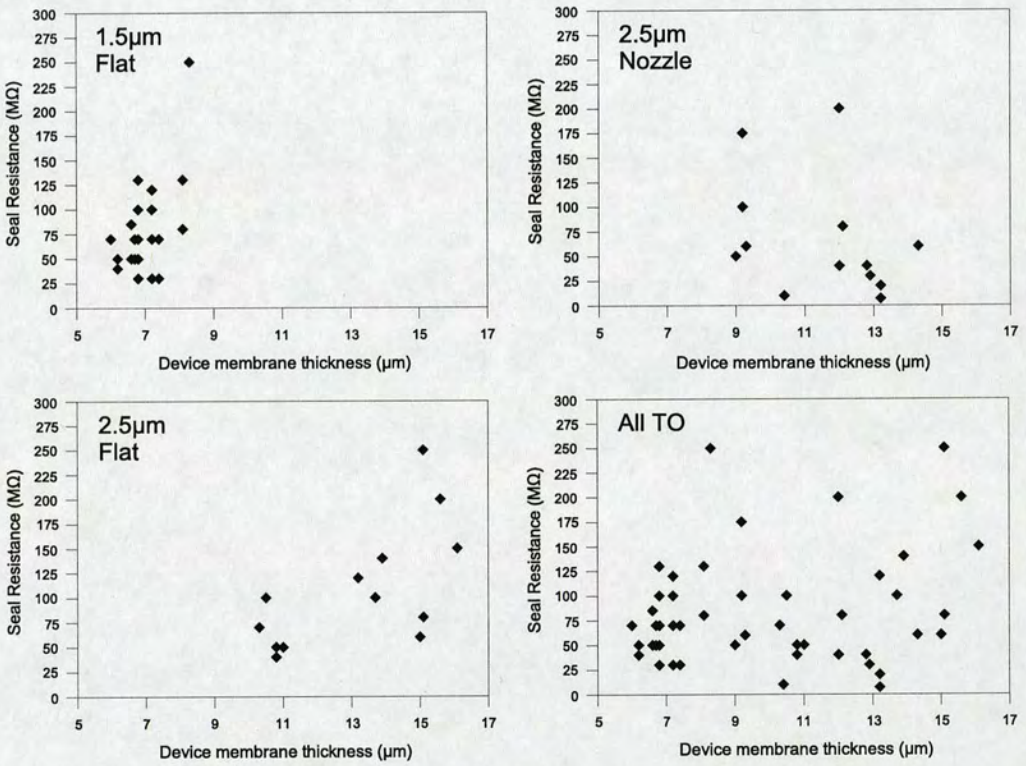

Figure 6.10: *Scatter plots showing variation of seal resistance with device membrane thickness used. Both the traces for flat devices (top left and bottom left) represent a statistically significant correlation.*

Device Group	Estimated Aperture Depth		Membrane Thickness	
	Spearman Coefficient	P Value	Spearman Coefficient	P Value
All Thermal Oxide	-	0.325	-	0.293
$1.5\mu m$	0.67	0.043	0.4	0.047
Nozzle	-	-	-	-
Flat	-	0.139	0.409	0.047
$2.5\mu m$	-	0.38	-	0.166
Nozzle	-	0.91	-	0.212
Flat	-	0.11	0.656	0.010

Table 6.2: *Results of Spearman correlation testing for estimated aperture depth vs. seal resistance. Only the* $1.5\mu m$ *devices returned a P-value less than 0.05 for the estimated aperture depth. However, the membrane thickness, for which there is a larger sample size, additionally shows a correlation with seal formation for* $1.5\mu m$ *flat and* $2.5\mu m$ *flat devices.*

the attempts to form gigaohm seals, characteristics were observed, similar to the whole cell characteristics achieved with glass. The rupturing of the membrane was believed to have been caused by the suction applied to encourage seal formation. Out of all successful attempts, eight seals were obtained which exhibited possible whole cell characteristics. Current-voltage traces were recorded for four of these seals, shown in figures 6.11 and 6.12. Since the seal resistance was an order of magnitude smaller than for glass, the current input was an order of magnitude higher, to attempt to replicate the current input to the cell itself.

Despite the lower seal resistances with which these traces were recorded, the distinguishing features are still visible. All the cell characteristics seem to belong to the second type of N2A characteristic identified in chapter 5, with the exception of trace D (taken with the $1.5\mu m$ thermal oxide nozzle) which seems to be of type 1. It is unlikely that any of the traces obtained from the device is not whole cell to some degree. The traces all show some asymmetry, and some overshoot or sag. In all of the cell-attached seal characteristics recorded with glass electrodes, not one showed any of these traits.

Values for resistance and capacitance for each seal (measured as described in chapter 5) are given in table 6.3. As the seal resistances are considerably lower than what is expected for the membrane resistance, it is desirable to adjust these values to compensate for the seal, as performed for the whole cell recordings taken with glass. However, because the membranes were ruptured accidentally, the seal resistance was not properly measured for those devices that went whole-cell. However, it is possible to measure the effect of the device capacitance on

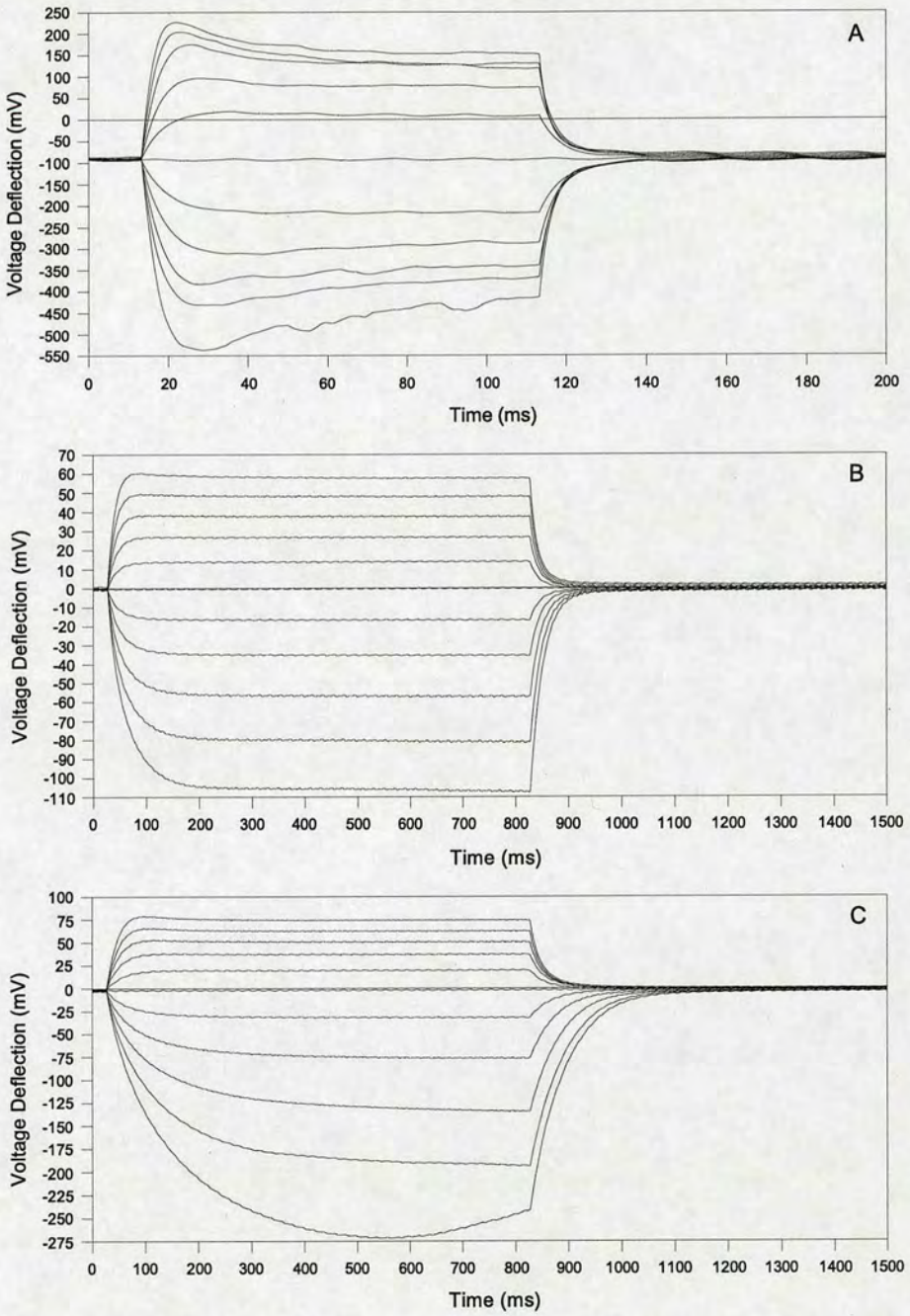

Figure 6.11: *Device whole cell A: I-V trace recorded with a* $2.5\mu m$ *boron doped flat device. The maximum seal resistance was* $200M\Omega$*. The current input ranged from -10nA to +10nA in steps of 2nA. Device whole cell B: I-V trace recorded with a* $1.5\mu m$ *boron doped flat device. The maximum seal resistance was* $130M\Omega$*. The current input ranged from -1nA to +1nA in steps of 0.2nA. Device whole cell C: I-V trace recorded with a* $2.5\mu m$ *boron doped flat device. The maximum seal resistance was* $250M\Omega$*. The current input ranged from -1nA to +1nA in steps of 0.2nA.*

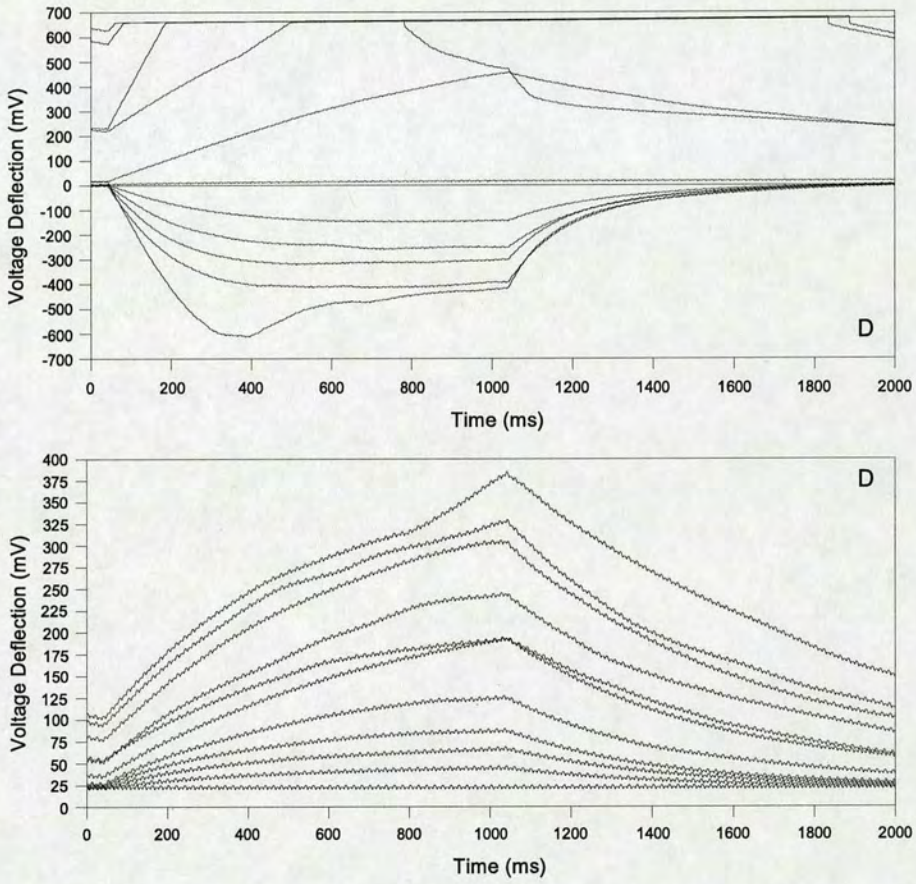

Figure 6.12: *Device whole cell D: I-V trace recorded with a* $1.5\mu m$ *thermal oxide nozzle device. The maximum seal resistance was* $1000M\Omega$*. The current input in the top trace ranged from -0.5nA to +0.5nA. This revealed a substantial asymmetry in the cell characteristics. To examine the positive going section of the characteristic, a second trace was recorded, from 0 to +0.1nA.*

the traces. The capacitances of these devices are significantly greater than those expected for the whole-cell capacitance. In some cases, the measured device capacitance is greater than the measured whole-cell capacitance. This can be attributed to errors in the measurement of these values, as the measured whole cell capacitance should be equal to the device capacitance plus the cell capacitance. This suggests however, that the device capacitance is the major contributor to the measured whole cell capacitance.

Recording	Resistance ($M\Omega$)	Capacitance (pF)	Device Capacitance (pF)	Expected Cell Capacitance (pF)
A	54	101	185	11
B	76	250	320	11
C	124	288	260	11
D	1240	168	300	15

Table 6.3: *Breakdown of whole cell parameters recorded with devices. The device capacitance is the major contribution to the capacitance measured on the trace as it is significantly larger than the cell capacitance. (see figure 5.10)*

6.5 Device Re-use

It should be noted that not all sealing attempts were made with clean (i.e. unused) devices. Although it was desirable to use a clean device with every cell (as with glass pipettes) this was not always possible, in particular because of the small number of $1.5\mu m$ devices produced. Multiple attempts had to be made with many devices. Thus not all successful seals were made on the first attempt with that device, and the total number of successful sealing attempts does not represent the number of physical devices tested. Table 6.4 illustrates this point.

Figure 6.13 shows the distribution of successful and unsuccessful attempts versus reuse. It is apparent that the distribution of attempts with $1.5\mu m$ devices is skewed towards the second and third attempts. This is caused by the small number of these devices that was available, which increased the need for reuse. This skew was exacerbated by a significant proportion of the $1.5\mu m$ devices being tested erroneously on their first attempt. Thus, although these first attempts brought the devices into contact with biological material, meaningful seal resistances were not obtained. The cause of the error in these recordings was a leak in the recording setup, which connected the front and back of the devices with conductive solution. Hence the resistance measured was that of the leak ($5M\Omega$) rather than that of the seal. However, it is worth noting that during these failed attempts, although the seal resistance could not be measured,

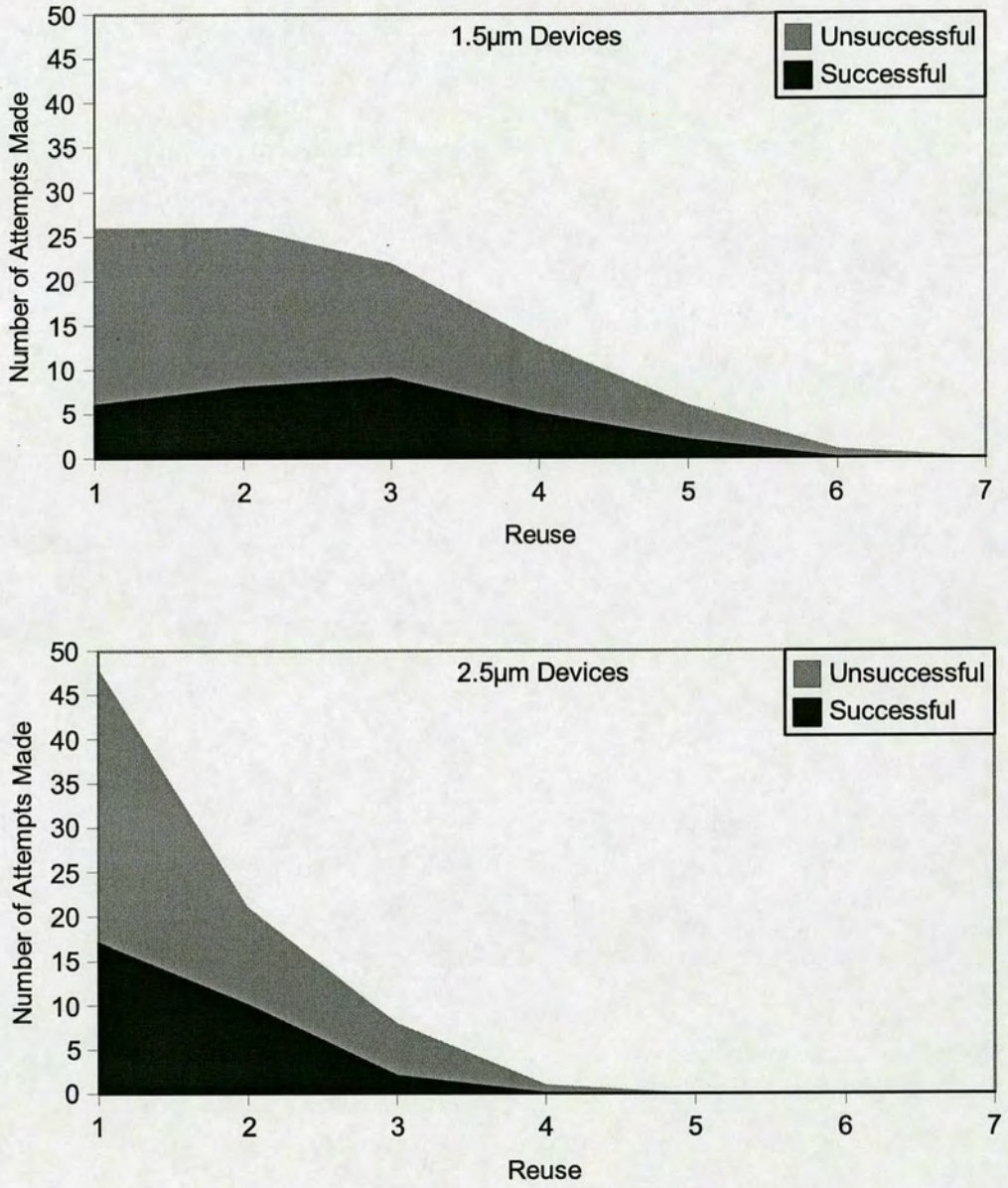

Figure 6.13: *The number of attempts made after each reuse. Top:* $1.5\mu m$ *devices. Bottom:* $2.5\mu m$ *devices. The black area represents the successful attempts made, the grey area total attempts. The top of the grey area thus represents the total attempts made. Note that the* $1.5\mu m$ *distribution is skewed by the smaller number of devices available.*

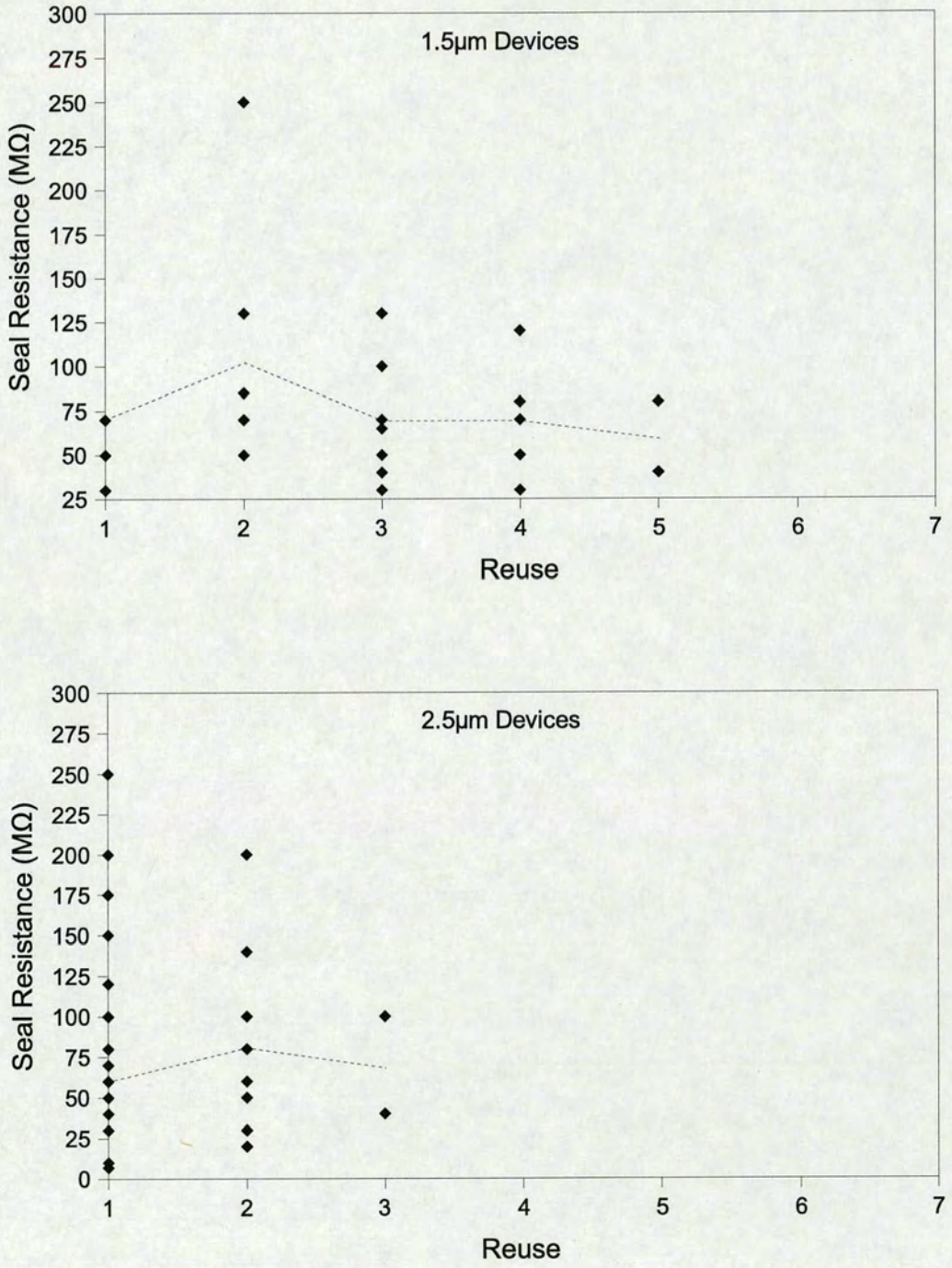

Figure 6.14: *The variation of seal resistance with device reuse. Top:* $1.5\mu m$ *devices. Bottom:* $2.5\mu m$ *devices. The dotted line indicates the average seal. Note that the* $1.5\mu m$ *plot does not include the single giga-ohm seal achieved, although this is included in the average.*

significant bleb formation was witnessed on the cells after blowing off (as in figure 6.9).

The implications of reuse are that biological debris might obscure the hole, blocking the hole completely, or changing its effective shape. Also, it is possible that cell membranes could deposit protein on the surfaces of the devices, altering the sealing properties. To ameliorate these problems, the devices were cleaned in acid piranha solution between uses, as discussed in chapter 3. A scatter plot of seal resistance vs. attempt is shown in figure 6.14. Figure 6.14 shows $1.5\mu m$ and $2.5\mu m$ devices separately along with the average values for each reuse. It can be seen that the number of successful attempts drops with re-use, as holes become blocked to the point where they no longer conduct or attract cells. However, the mean seal resistance remains roughly constant as the devices are re-used, suggesting that the sealing properties are not altered. In addition, there is no statistical difference detectable between the seal values obtained on any reuse (Student's T-test).

Device Type	Devices Tested	Total Attempts	Successful Attempts	Yield
All Thermal Oxide Devices	38	172	59	34%
1.5μm	16	94	30	32%
Nozzle	1	30	1	3.3%
Flat	15	64	29	45%
2.5μm	22	78	29	37%
Nozzle	10	50	14	28%
Flat	12	28	15	54%

Table 6.4: *Breakdown of device yield by subgroup. The subgroups are divided by device type, hole size, hole shape and surface material. For each group, the number of physical devices tested is given, in addition to the yield of successful attempts.*

Chapter 7
Discussion of Seal Formation Results

This chapter explains the device seal formation results presented in chapter 6 in the context of the literature discussed in chapter 2 and the conventional patch-clamp experiments detailed in chapter 5. Firstly, the nature of the experimental procedures is examined, and attempts are made to explain how these could be improved. The sealing results are then used to explain how the different device properties affect sealing. There follows a discussion of seal formation and what the results obtained tell us about its nature. Finally, the potential for using the devices in a multi-channel array for neuronal recording is examined.

7.1 Device Testing

7.1.1 N2A Cell Line

The N2A cell line was extremely successful as a tool for the study of seal formation. The attempts made previously by Dworak [1] to patch onto dissociated snail cells using devices had always been dogged by being unable to obtain good seals on these cells with glass pipettes. This suggested that there were problems with the health of the cells, which reduced confidence in the device evaluation results themselves. However, the N2A cell line provided extremely good reliability and repeatability in terms of seal formation on glass pipettes, which permitted a much greater confidence in the device testing.

The N2A cells allowed evaluation of the PECVD devices and the thermal oxide devices of $1.5\mu m$ and $2.5\mu m$ diameter. In some cases, the $2.5\mu m$ devices consumed entire cells, so larger devices were not tested. If the larger devices were to be tested, it would have to be with large cells such as Xenopus Oocytes (the snail neurons for which they were originally intended have somas as large as $80\mu m$).

Only one other study [47] (Cytocentrics) uses N2A cells, in which an average seal resistance of $1.2G\Omega$ is obtained. Although these results are superior to those presented here, an even higher seal resistance ($2.6G\Omega$) is achieved by the same group with Chinese Hamster Ovary (CHO)

cells. CHO cells are by far the most widely used cell type in the planar patch-clamp literature. Human Embryo Kidney and Xenopus Oocyte are also commonly used, with one study [64] suggesting that the oocytes form seals even more successfully than CHO. As the ultimate goal of the work presented here is to study neuronal networks, the N2A cell line is more applicable as it has some neuronal characteristics.

7.1.2 Planar Patch-Clamp Test Platform

The test platform was also largely successful. It was certainly an improvement over the test platform described by Dworak, with which the snail experiments were performed [1]. The platform described here followed the design of a micro-pipette headstage more closely, and hence contained a smaller volume of intracellular solution. The main benefit of this is that the solution does not cross the o-ring seal between the frame and the base unit, eliminating one path by which bubbles can be drawn in from outside. This also means that there is a smaller volume of solution in which bubbles can form when suction is applied.

The filling technique was also modified so that only two drops were required to fill the device, rather than submerging the entire frame as had been done previously. This dramatically reduced wastage of intracellular solution.

Nevertheless, there are some problems which are intrinsic to the planar patch-clamp setup. The main problem is that the setup is inverted so that the aperture points upwards. This means that any bubbles that form in the chamber tend to float to the top, obscuring the aperture. This is particularly problematic when suction is applied as this causes bubbles to expand, in many cases breaking the circuit. This problem was worsened by the backside etch undercut (caused by the deep etch hitting the oxide stop layer, as shown in figure 4.11). This undercut creates a pocket in which bubbles can be trapped, only to be drawn out when suction was applied. With glass pipettes bubbles are not a problem, as the electrode is always pointed downwards, so bubbles float away from the tip.

Hung et al. [67] have alleviated this problem (intentionally or not) by creating a lateral patch-clamp array where the apertures are horizontal. Other groups have, with few exceptions, removed the problem of bubbles by having a wide conical chamber underneath the aperture, which can be filled easily without trapping bubbles. However, the need to position many of these devices in close proximity necessitates that the devices discussed here have a narrow in-

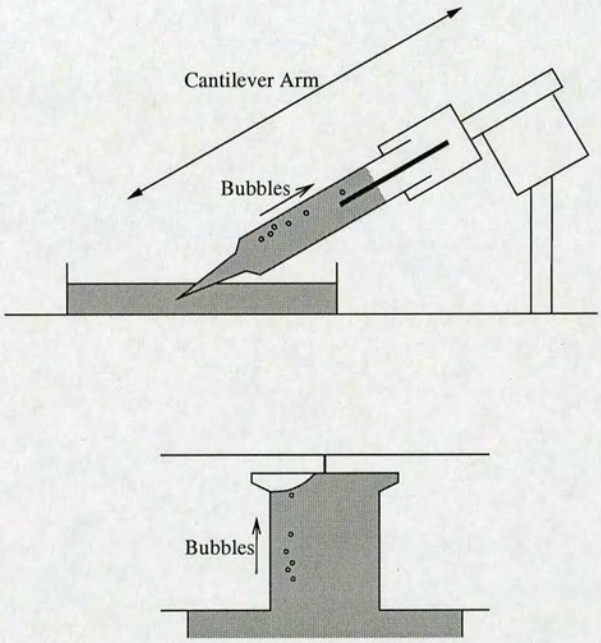

Figure 7.1: *Advantages and disadvantages of the planar-patch clamp test rig. In the conventional setup (top) bubbles float away from the electrode aperture, but the relatively long pipette arm with a single point of attachment is susceptible to vibration. The planar setup (bottom) is more resistant to vibration, but any bubbles will float towards the aperture, preventing recording.*

tracellular chamber. One possibility to improve the situation is to incorporate a 'reed' in the chamber as found in the capillaries from which pipettes are pulled [89]. This is simply a matter of changing the mask with which the chamber is defined.

Another problem is that the devices cannot be manoeuvred to the cells like a glass pipette. The implications of this are that the cells have to be attracted towards the hole, in this case, using suction. However, suction also attracts cellular debris to the patch site, which can prevent seal formation. This is a particular problem, since cellular debris is often lighter than the cells themselves, and hence more readily attracted by suction. To alleviate this problem, suction was only applied to the aperture when a cell was in close proximity to the aperture.

Cell positioning methods other than the direct suction method used here have been tested elsewhere. Cytocentrics [47] have integrated an additional suction port, concentric with the aperture, to firmly locate cells over the aperture before suction needs to be applied through it. Further, this allows positive pressure to be applied to the aperture during cell positioning, to reduce the likelihood of contaminating the aperture with debris before cell contact. Cytocentrics report a 100 percent cell capture success rate using their 'cytocentering' technique. Sophion Biosciences [43] have developed an electro-osmotic flow pump for drawing cells towards the aperture of their Q-patch devices. Aviva [90] have employed electric fields to guide cells towards the apertures. Pantoja et al [51] and Matthews and Judy [55] make use of fluidic micro-channels to guide cells towards their apertures. These channels are $100\mu m$ or $30\mu m$ in diameter and thus still require suction to perform the final positioning of the cell.

As well as attracting cells, applying suction also causes the device membrane to flex, which is not ideal when attempting to form a stable seal. However, this problem has its analogy in conventional patching - the pipette can retract under suction. This problem is actually of greater significance when using glass pipettes as the cell is generally anchored to a culture dish, as well as the pipette. These competing forces can cause the seal to be lost when the pipette retracts. In planar patch-clamp the cell moves with the aperture when suction causes the membrane to flex.

Having a single anchor point for the cell is probably the greatest advantage of the planar-patch clamp setup. This makes the setup much less sensitive to vibration than a conventional patch-clamp experiment. In conventional patch-clamp the pipette arm is essentially a cantilever (shown in figure 7.1). Vibrations in this cantilever have a great effect on the seal stability, because the cell is anchored to the culture dish as well as the pipette tip.

7.2 Seal Formation Results

Establishing a seal with a super giga-ohm resistance is the aim in any patch-clamp experiment. The larger the seal resistance, the smaller the leakage pathway is between the cell and the electrode, and the less error there is in the application of current and the measurement of the membrane potential [25]. Moreover, the process of sealing which creates a gigaohm seal also increases the stability of the seal. Sub-gigaohm seals tend to vary in resistance with the suction applied, whereas gigaohm seals maintain their resistance when suction is removed [73]. The glass electrodes achieved gigaohm seals with good repeatability (60 percent of all attempts made). The devices, on the same cell type achieved one seal of this magnitude out of 83 successful attempts. Nonetheless, the variations in the values of sub-gigaohm seals are a good indicator of the quality of the seal, and hence the merit of a particular device for sealing. These variations can thus be used to investigate the effects of particular device parameters on seal formation.

7.2.1 PECVD Devices vs. Thermal Oxide Devices

The results show that the seal values obtained for the thermal oxide devices are significantly different from those for the PECVD devices (in favour of the thermal oxide devices). This result is most likely to be caused by the surface roughness. The PECVD devices are rougher on a small scale ($\sim nm$) than the thermal oxide devices. The PECVD devices do appear smoother than the thermal oxide devices on a large scale ($\sim \mu m$) due to the increased scalloping visible in the thermal oxide devices. However, the glass pipettes have a large scale deformation in the form of a reed about 250nm in diameter at the tip, suggesting that the cell membrane can conform to features of this scale. Glass pipettes are, furthermore, very smooth on a small scale. We speculate that small scale variations in the PECVD oxide present a surface to which the membrane cannot conform, preventing continuous membrane contact over the sealing surface of the device.

The literature clarifies little about the role of surface roughness. Some of the best results from industry have been achieved with glass substrates (Nanion [61] and Aviva [62]) which, like pipettes, are expected to be very smooth. However, Sordel et al. [53] suggest that the roughness of the PECVD oxide may in fact improve seal formation by providing a greater surface area for contact between the cell and the device.

The aperture diameter is another variable which differs between the PECVD and thermal oxide devices. This seems unlikely to be the cause of the difference in seal formation, as the PECVD devices ($2\mu m$) are significantly different from both the $1.5\mu m$ and $2.5\mu m$ aperture devices. The membrane thickness of the devices is another difference. Again the PECVD devices have a membrane thickness between that of the $1.5\mu m$ and the $2.5\mu m$ devices. It is, however, possible to speculate that the thinner membrane makes the PECVD devices less effective than the $2.5\mu m$ devices, and the wider aperture makes them less effective than the $1.5\mu m$ devices.

The radius of curvature of the aperture is another possible cause for this result, but there is little reason to believe that a large radius (as the PECVD devices have) should have a detrimental effect on seal formation. It seems intuitively more likely that a larger radius would be better, as it would let the cell membrane curve continuously into the hole, rather than causing abrupt changes of direction. This is the motivation for fire-polishing pipettes [28][91]. Contrarily, the glass pipettes used in this study were not fire-polished and show a very small radius of curvature.

Therefore, it is possible to say that the thermal oxide devices are more successful than PECVD devices, and are more like glass pipettes in terms of radius of curvature, and surface roughness. But it seems most likely that the surface roughness of PECVD oxide is the determining factor. Other studies have made use of PECVD [51][53] and thermal silicon dioxide [55], and formed gigaohm seals on both, but it is not possible to compare these studies directly to this or to each other because of the different cell types used. However, the study by Sordel et al. [53] describes a situation similar to the one described here. Sordel et al. have tested thermal oxide devices ($2.5\mu m$) against PECVD devices ($1.7\mu m$), finding the smaller PECVD devices to be significantly better in forming seals. Sordel's experiment is almost identical to the comparison of the $2.5\mu m$ thermal oxide devices with the $2\mu m$ PECVD devices. In our case however, it is the larger thermal oxide devices which perform significantly better. The difference between these two cases is the aperture depth. In this study the aperture depth is greater for the large thermal oxide apertures, in the Sordel study, it is the depth of the small PECVD apertures which is greater. This represents a strong indication that the aperture depth affects the performance of the device, regardless of other aperture properties.

Figure 6.6 alludes to one final difference between thermal oxide and PECVD devices. The figure shows the voltage response at the point of cell impact. It seems to increase sharply, as in giga-seal formation, but the sealing is interrupted and the resistance decays exponentially. Ex-

amination of the sealing traces reveals this behaviour occurs in 11 out of the 59 cells positioned on thermal oxide devices, but in not one of the 24 PECVD device attempts. This indicates that the thermal oxide could have a greater predisposition to form giga-ohm seals, given a deeper aperture.

7.2.2 Thermal Oxide Subgroups

The absence of any significant differences between the seals obtained with any of the sub groups of thermal oxide devices suggests a number of things.

Surface Chemistry

The first is that boron-doping a thermal silicon dioxide surface has no effect on its potential to form seals. The idea behind boron-doping the devices was to create a surface similar to glass, which is known to seal well. In addition, boron doping is known to lower the contact angle of thermal oxide [1], and hydrophilic surfaces are thought to be desirable for seal formation. The boron content achieved in the devices is smaller than that for patch glass, which may explain why no difference is observed. Alternatively, the process of boron doping may not have produced glass on the surface, but a layer of boric oxide instead. Corey and Stevens suggest that sodium in the glass plays an important role in defining its surface properties [28]. Unfortunately, sodium is not cleanroom compatible, so could not be incorporated into the devices to test this. However, given the limited understanding of the surface interactions which govern seal formation on a molecular scale, there is no reason to believe that a plain thermal oxide surface should not seal as well as glass. In fact, pipettes made of quartz, chemically similar to thermal oxide, have been used to successfully form seals with resistances as high as $40G\Omega$ [33].

In other planar patch-clamp studies, gigaohm seals have been achieved on a range of surfaces, namely: Glass [61][62], silicon dioxide(thermal [55] and PECVD [51][53]), Silicon Nitride [73], PDMS (plasma treated) [65] and Polyimide [74]. While most of the surfaces are hydrophilic, polyimide is hydrophobic, and gigaohm seals have also been reported from glass pipettes treated with HMDS to render the surface hydrophobic. We are led to conclude that, while contact angle itself is not critical, there are other chemical properties - common to all the surfaces mentioned - which are.

Presence of Nozzle

The presence or absence of a protruding nozzle seems to have little effect on seal formation. This, along with the indifference to radius of curvature suggested by the PECVD results, indicates that the shape of the tip of the patch device plays at most a minor role in seal formation. The images of glass pipette tips seen in figure 4.1 seem to support this argument. The end of the pipette appears rough, and the edge of the aperture very sharp, making the tip itself un-conducive to seal formation. The literature also suggests an indifference to tip profile. Cytocentrics have produced excellent results with sharp nozzles, while Sophion Biosciences have similar results using flat apertures with a large radius of curvature. The PECVD coated devices produced by Sordel et al. and Pantoja et al. are assumed to have rounded apertures as are the amorphous silicon devices produced by Matthews and Judy[55]. In contrast, the PDMS devices produced by Klemic et al. and the nitride coated polyimide membranes by Stett et al. appear sharper. These last five groups have all achieved similar results. This strongly suggests that aperture profile is not critical in the formation of gigaohm seals.

Corey and Stevens present anecdotal evidence that this is not the case for glass, citing the difference between pipettes which have and have not been fire-polished: "Although gigaseals can be formed with unpolished electrodes, seals seem not to be as stable". However, they seem to suggest that it is just the stability of seals that is affected by fire-polishing, and not the seal formation itself. Corey and Stevens also speculate that the key role of fire-polishing may be to remove impurities from the tip, rather than alter the tip profile [28].

Aperture Diameter

The final variable altered in in the thermal oxide devices was aperture diameter. Again, there was no significant difference between the $1.5\mu m$ and $2.5\mu m$ devices. This indicates that the aperture diameter has no direct effect on seal formation. However, the data gathered on seal formation with glass pipettes shows some variation of seal resistance with tip diameter. Figure 5.2 suggests that a $2.5\mu m$ pipette has a bubble number around 7.5. The seals obtained with pipettes of this bubble number are significantly poorer than those obtained with pipettes at bubble number 6 ($1.5\mu m$) (in fact, the seals are of the same order of magnitude as those obtained with the devices). Published data also indicate that the diameter of the aperture *is* important. Stett et al. found that $2\mu m$ apertures sealed significantly better than $4\mu m$ ones. When Lehnert et al. [49] shrunk $2.5\mu m$ with PDMS, and Sordel et al. [53] shrunk 2.5μ apertures with PECVD, both

groups recorded higher average seal resistances. Pantoja[51] reports that for apertures above $1\mu m$, smaller apertures perform better, though apertures below $1\mu m$ perform worse. Results obtained by Klemic et al. [64] also indicate a maximum in seal resistance for devices which have an aperture resistance of $\sim 6M\Omega$ (apertures with higher *and* lower resistances performed worse) though it is not clear to what diameter this corresponds. All groups that have tested the effect of aperture diameter variation conclude that smaller apertures produce higher seal resistances, down to a diameter of $1\mu m$. No gigaohm seals have been reported with diameters greater than $2\mu m$.

The absence of any significant difference between the $1.5\mu m$ and $2.5\mu m$ thermal oxide devices in this study suggests that other factors are involved. One possible factor is aperture depth. It transpired that the SOI wafer on which the $2.5\mu m$ devices were fabricated had a device layer thickness of $12\mu m$. These devices had aperture depths of around $10\mu m$. On the other hand, the $1.5\mu m$ devices were fabricated on a wafer with an average device layer thickness of $7\mu m$, producing apertures with an average depth of $5.7\mu m$. We postulate that the difference in the aperture depth has a significant impact on the seal formation, and thus accounts for the absence of any difference attributable to the change in diameter.

7.2.3 Aperture Depth

The statistical tests (chapter 6) of aperture depth against seal resistance back up this hypothesis. The tests confirm that there is a statistically significant correlation for the estimated aperture depth versus seal resistance for $1.5\mu m$ devices (seal resistance increases with aperture depth). The tests also show a correlation between membrane thickness and seal resistance for $1.5\mu m$ flat devices and $2.5\mu m$ flat devices individually. (Testing all thermal oxide devices together yielded no significant results, presumably because of the discontinuity in aperture diameter.) Although the estimated aperture depth is the best estimate of how deep the sealing surface is, many of the devices could not be measured, so the number of data points for this measure is reduced. The membrane thickness yields more data points, but is not as good an estimate of the actual depth of the aperture. However, it is assumed that the aperture depth will be strongly dependent on membrane thickness, as the undercut is relatively constant across the individual wafers on which the devices were made. As these tests were only performed on subgroups, each of which was fabricated on a single wafer, they give a good indication of how aperture depth affects seal resistance.

The measurements of bleb length taken with glass pipettes on N2A cells clarify this matter further. The average bleb length observed for stable seals was $19\mu m$, almost double the average depth for the $2.5\mu m$ devices. If this length is required for a stable bleb to form, it seems logical that the seal resistance achievable with a given aperture should increase as its depth approaches this length.

There is little emphasis on bleb length in the literature. Pantoja et al have produced different aperture depths but fail to analyse this. In fact, their apertures smaller than $1\mu m$ (which produce worse results) have a shallower aperture than those above $1\mu m$, but no mention of this is made. Nevertheless, gigaohm seals have been obtained with a range of aperture depths. All the companies which produce reliable gigaohm seals, seem to have apertures of $10\mu m$ or deeper. Some academic groups, on the contrary, have produced gigaohm seals with membranes as thin as $6.5\mu m$ [73] and $3.6\mu m$ [53], albeit not reliably. This could be explained by the dependence of bleb length on cell type [36]. It is possible that the cells used in these studies (CHO and HEK respectively) require shorter blebs to form gigaohm seals. Thus these devices may not produce gigaohm seals with the N2A cells used here. This is the only published study to have measured the effect of aperture depth directly.

7.3 Theories of Seal Formation

7.3.1 Gigaohm seal vs. Megaohm seal

The sealing results obtained here with the thermal oxide devices are typical among academic groups. Many groups [49, 51, 53, 55, 63, 73] have reported low success rates of gigaohm seals, with the majority of seal resistances recorded being of the order of $100M\Omega$. Very few seal resistances are reported in the range 500-$1000M\Omega$. This suggests a discontinuity in the spectrum of seal resistances, with seals either having resistances $< 500M\Omega$ or $> 1G\Omega$, but few between. The difference in stability between mega-ohm and giga-ohm seals reported by Stett [73] also suggests a fundamental division between the two classes of seal. The important task in improving seal formation, is to uncover the fundamental difference between the mechanisms of mega-ohm and giga-ohm seal formation.

Initial attempts to explain giga-ohm seal formation involved glass-membrane separation calculations, based on the resistance of the seal [28]. Although these proved to be inappropriate for giga-ohm seals on the basis of the small (<1Å) separation they predicted, they are more

appropriate for the mega-ohm resistances encountered here. The conductive pathway around the seal is assumed to be toroidal in cross section, extending for the length of the bleb. The toroid is assumed to be thin enough so that its cross section can be approximated as:

$$A = \pi t d$$

Where t is the separation between glass and membrane, and d is the diameter of the aperture. The resistance is given by:

$$R = \frac{\rho h}{\pi t d}$$

Where h is the length of the bleb. The separation can thus be calculated as:

$$t = \frac{\rho h}{\pi R d}$$

Using the average experimental values for d, h and R. The membrane-sidewall separation is calculated to be 86Å for the $1.5\mu m$ devices, 82Å for the $2.5\mu m$ devices and 200Å for the PECVD devices. These values are significantly greater than the ionic radii [92] of Na^+ (0.97Å), K^+ (1.33Å) or Cl^- (1.81Å), so this model is a more valid representation of seal conduction in this case than in the case of giga-ohm seals. These distances predicted by this model are beyond the range of inter-molecular interactions (the ranges of Van der Waals interactions and hydrogen bonds are typically <5Å [93]) indicating that no direct interaction occurs between the lipid membrane and the sidewall.

Corey and Stevens [28] highlight acetylcholine receptors as a barrier to seal formation as they protrude from the membrane surface by 50Å to 100Å. It is possible that such proteins act as spacers between the aperture sidewall, preventing direct contact with the entire membrane. If this were the case, it would only be possible for giga-ohm seals to form if these proteins became denatured and flattened onto the surface of the sidewall. Denaturation of proteins as a mechanism for seal formation has been previously proposed by Sokabe et al. [31]. Sokabe suggests that it is the high surface energy (low contact angle) of glass that causes the proteins to denature. However, proteins have also been shown to denature on hydrophobic surfaces [94, 95], which would account for the fact that giga-ohm seals have been shown to form on surfaces

with a large range of contact angles. Sokabe goes on to hypothesise that it is the proteins themselves which anchor the membrane to the glass and the lipid membrane is free to flow around these anchor points. However, Opsahl and Webb [30] have shown that lipid membranes do interact strongly with glass in the absence of proteins, and believe this to be the mechanism under lying seal formation. Regardless of the interaction mechanism, it is the denaturing of proteins which is critical for seal formation in this model.

Further, it seems reasonable - given the above argument - that seal formation should be more sensitive to roughness on a nanometer scale, than to micron-sized deformities. The proteins which must denature to allow seal formation will be most affected by surface variations of the same scale as the proteins themselves.

This leaves the question of why cells form giga-ohm seals on some devices, while others produce only mega-ohm seals. Following the argument laid out above, we are led to speculate that the cells which form giga-ohm seals have a lower density of proteins in the section of their membranes which are aligned with the sidewalls, allowing the sidewall to come into closer contact with the lipid itself.

The model suggests that membrane proteins denature onto glass, but not on to thermal oxide (with or without boron). However, the contact angle and roughness of these materials is very similar. Possible reasons for the difference are the presence of sodium in the glass, or the surface energy of the inside of a freshly pulled patch-clamp pipette being different from that for glass cover-slips.

7.3.2 Elastic deformation of membrane

However, this adhesion model alone does not explain the physical properties of the bleb. To address this, let us assume that proteins *have* denatured and either adhered to the surface (as proposed by Sokabe et al. [31]) or flattened, allowing lipid-glass interaction (which Opsahl and Webb [30] believe to be the cause of gigaohm seal formation.) Regardless of how the membrane interacts with the surface, there will be some adhesion force, binding the membrane to the sidewalls.

In opposition to this force, there will be some elastic tension caused by the deformation of the cell to create the bleb. Evidence for elastic deformation of the cell is given by the fact that sub-gigaohm seals recoil when suction is released (reported by Stett et al. [73] but also

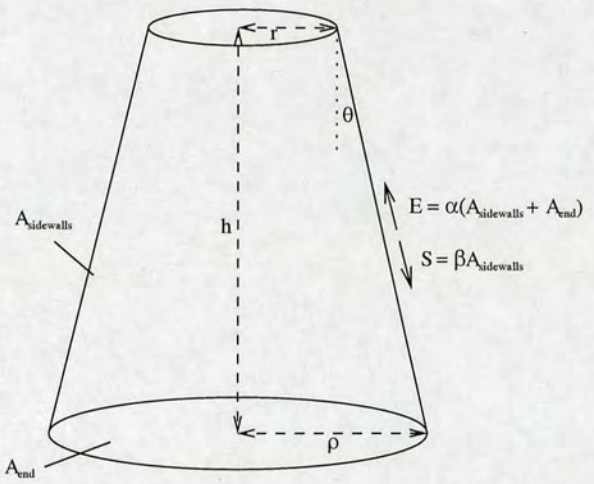

Figure 7.2: *A simplified representation of the membrane patch.*

observed here). Opsahl and Webb believe these elastic properties are a feature of the lipid membrane itself, while Sokabe et al. attribute the elastic force to the underlying cytoskeleton. Regardless of the underlying mechanism behind the force, we will assume that this force, E, is proportional to the area of membrane inside the tip, and works to contract the membrane bleb (i.e. acting parallel with the sidewalls of the aperture and towards the tip). We will assume that, the adhesion of the membrane to the sidewall produces a capacity to resist this force, S, proportional to the area of membrane in contact with the sidewalls. The bleb will be just stable when these two forces are balanced:

$$E = S$$

And thus,

$$\alpha A_{bleb} = \beta A_{sidewalls}$$

Thus the ratio of the area of the sidewall contact to area of membrane has a critical value γ.

$$\frac{A_{sidewalls}}{A_{bleb}} = \frac{\alpha}{\beta} = \gamma \tag{7.1}$$

If the bleb is approximated as a section of a cone with a flat end (as shown in figure 7.2), then

the area in contact with the sidewalls will be given by,

$$A_{sidewalls} = \frac{\pi}{sin\theta}(\rho^2 - r^2) \tag{7.2}$$

The area of the end of the bleb is,

$$A_{end} = \pi\rho^2 \tag{7.3}$$

The total bleb area is the sum of these two. Substituting this into equation 7.1,

$$\gamma = \frac{A_{sidewalls}}{A_{sidewalls} + A_{end}} = \frac{1}{1 + \frac{A_{end}}{A_{sidewalls}}}$$

$$\Gamma = \frac{1}{\gamma} - 1 = \frac{A_{end}}{A_{sidewalls}} = \frac{\pi\rho^2 sin\theta}{\pi(\rho^2 - r^2)}$$

Where $\rho = r + htan\theta$. Substituting this value, we get,

$$\Gamma = \frac{sin\theta(r^2 + h^2tan^2\theta + 2hrtan\theta)}{h^2tan^2\theta + 2hrtan\theta}$$

For small angles (less than 5°) we can make the approximation $sin\theta = tan\theta = theta$,

$$\Gamma = \frac{\theta(r^2 + h^2\theta^2 + 2hr\theta)}{h^2\theta^2 + 2hr\theta}$$

$$\Gamma = \frac{\theta r^2}{h^2\theta^2 + 2hr\theta} + \frac{\theta(h^2\theta^2 + 2hr\theta)}{h^2\theta^2 + 2hr\theta}$$

$$\Gamma = \frac{r^2}{h^2\theta + 2hr} + \theta \tag{7.4}$$

Rearranging yields a quadratic in h,

$$h^2\theta(\Gamma - \theta) + h(\Gamma - \theta)2r - r^2 = 0$$

One of the roots of this equation is always negative and does not represent a physical solution. The other is plotted in figure 7.3 in terms of d (=2r) and θ. The value of Γ (=0.0808) used to plot this equation was estimated from the results obtained with glass pipettes (i.e. by substituting the values $r = 1.5\mu m$, $h = 7.5\mu m$, and $\theta = 2.24°$ into equation 7.4). This value of Γ corresponds to $\gamma = 0.925$.

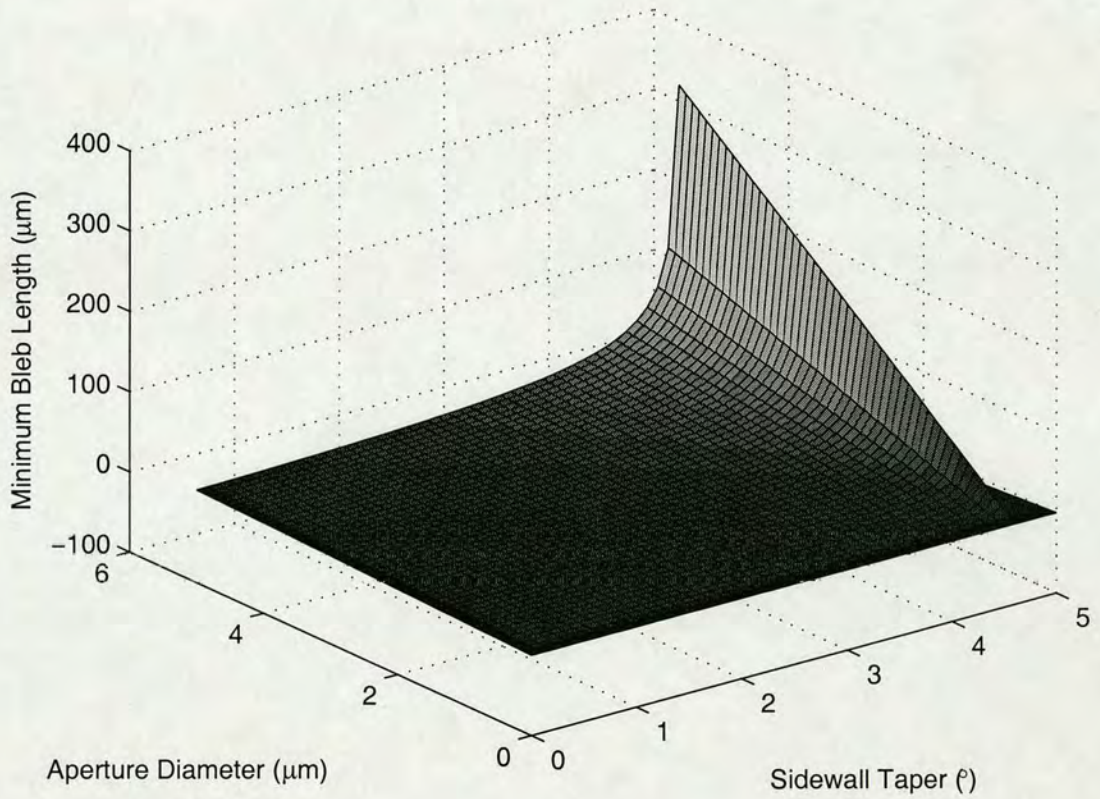

Figure 7.3: *Theoretical dependence of the minimum stable bleb length, h on θ and d. The graph shows a linear dependence of h with d, the aperture diameter, and an exponential variation in θ. Note that above a particular value of θ, the minimum bleb length becomes negative, suggesting blebs are not stable for sidewall tapers greater than a certain value. For this plot Γ = 0.0808*

As can be seen, the minimum bleb length h shows a linear variation with d, and an exponential variation with θ. Note that the bleb length shows a discontinuity at a particular value of theta

after which the bleb length becomes negative, suggesting that a bleb cannot be formed. These results seem correct intuitively, as a larger aperture diameter, or a larger taper, will require a larger bleb length to produce a large enough ratio of sidewall area to total membrane area.

Note that h represents the *minimum* length at which a stable bleb can form. The actual bleb length will be determined by the amount of lipid drawn into the aperture before seal formation occurs (assuming it is greater than the minimum, h). This agrees with observations reported by Ruknudin [36] that slower controlled suction produces smaller blebs than short, sharp sucks - sharp applications of suction will pull the membrane further up the pipette before seal formation can take hold. Assuming that suction is applied until the point of seal stability, the actual bleb length should show some correlation with the minimum.

This agrees with results recorded with glass pipettes, where the bleb length recorded showed an inverse dependence on aperture resistance (and hence a direct dependence on aperture diameter). These results are re-plotted in figure 7.4, along with the theoretical dependence of minimum bleb length on aperture diameter, as predicted by the model. As can be seen, the model does not precisely predict the minimum, but the trend is correct.

The model also supports anecdotal evidence given by Sakmann and Neher [3] regarding thick-walled glass pipettes (the type used here) in which they state: "...we have found that gigaohm seals of greater stability are obtained, and the success rate of obtaining gigaohm seals is significantly larger than with conventional, thin-walled pipettes." They go on to give a taper angle of 4-6° for thick walled pipettes, compared with 12° for thin-walled pipettes. The variation of seal stability with taper implied by the model could explain this observation.

If, as the model suggests, there is some taper angle past which no stable bleb can form, this may also explain why sealing does not continue when the bleb reaches the bottom of the aperture. At the bottom of the aperture, the sidewall angle is around 45° (caused by the deep etch undercut, see figure 4.12). Presumably, blebs cannot be supported at this angle. This explains why seals do not form on the underside of thin membranes, such as the nitride devices produced by Fertig et al [38].

Regardless of whether or not giga-ohm seal-style adhesion occurs between the membrane and the sidewall, a stable giga-ohm seal will not form unless there is suitable sidewall depth inside the aperture to support the elastic tension in the cell. If there is not, the membrane will be pulled from the sidewalls when suction is released.

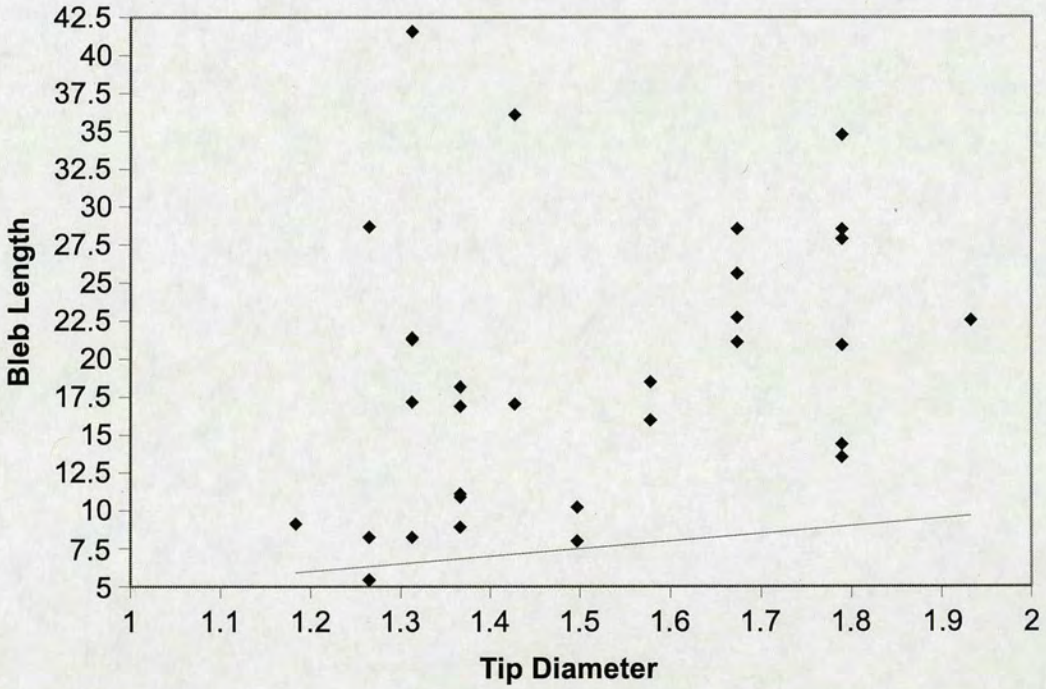

Figure 7.4: *Experimental dependence of bleb length on aperture diameter. The points are estimated diameter values (based on the pipette resistance) and the line represents the theoretical minimum bleb length calculated using* $\Gamma = 0.0808$.

The experiments performed here may provide some evidence of this occurring. The sealing trace of figure 6.6 shows the point of cell impact with a device. The resistance of the seal initially increases sharply, but then recoils unexpectedly. This behaviour was observed in 11 out of 59 thermal oxide device tests. The presence of this recoil leads us to hypothesise that the cell membrane seals progressively onto the surface of the device as the bleb is drawn into the aperture. When the bleb reaches the bottom of the aperture, the membrane runs out of space. As it has not reached the bleb length required for a stable seal, there is not enough membrane-wall adhesion to balance the elastic tension caused by the deformation of the membrane into the aperture, and the bleb retracts. This prompts us to speculate that adhesion between the membrane may occur in some of the thermal oxide devices, and gigaohm seals could be formed, given a deeper aperture. To determine whether this is the case, further investigation would be required.

7.4 Devices for Recording from Cells

7.4.1 Perforated patch

Seals of the magnitude observed here have been used in other studies to record meaningful data from cells. Of particular note is IonWorks HT produced by Molecular Devices [68]. This makes use of seals between $50M\Omega$ and $300M\Omega$ in conjunction with the perforated patch technique, and leak subtraction[1] to record whole cell currents, although only large currents ($>$100pA) can be recorded accurately. Given that post-synaptic currents in rat hippocampal neurons (one intended area of study) have an amplitude of the order of 1nA [96] it is possible that this technique could be used to record meaningful network data from neuronal networks. The thermal oxide devices produced here yielded seal resistances above $50M\Omega$ 75% of the time. Molecular devices report a success rate of 80% for the perforated patch technique (once seals have been obtained). Thus a 60% success rate for intracellular recording is theoretically possible with the physical device properties produced here.

[1] Leak subtraction is a method of compensating for low seal resistance by subtracting the current lost through the seal from the measured current signal

7.4.2 Direct whole-cell recordings

The whole-cell recordings obtained here suggest the possibility of intracellular recordings without the use of the perforated patch technique. Although the whole-cell recordings on N2A cells shown in chapter 6 are significantly compromised because the seal resistance ($\sim 100M\Omega$) is lower than that of the cell membrane ($\sim 1G\Omega$) this would be less of an issue for mammalian neurons, whose input resistance is typically less than $100M\Omega$ [85, 97].

Pantoja et al. [51] present whole cell potassium ion channel activity recordings with seal resistances of $80M\Omega$ and $150M\Omega$. With these seal resistances, they record currents smaller than 500pA. Sordel et al. [53] also recorded K^+ and Ca^{2+} channel activity. They state that $150M\Omega$ is sufficient for pharmacological characterisation of ion channels, having recorded (without leak subtraction) de-activation of Ca^{2+} channels with conductances as low as 20-30pS. They present equivalent recordings from glass pipettes, recorded with a gigaohm seal, which prove that the lower seal resistance causes little degradation of the recording quality with the lower seal resistance. Typical post-synaptic events in rat hippocampal neurons cause a conductance change of the order of 30pS [96]. It is therefore possible that devices with $100M\Omega$ seals could be used to record such changes, and hence gather meaningful network data from patch-clamped neurons. The yield of seals above $100M\Omega$ obtained with the thermal oxide devices is 25%, and the percentage of cells which showed whole-cell characteristics is 14%. The whole cell yield could be increased by improving seal resistance, as this will enhance membrane-sidewall adhesion, allowing suction to have a greater effect on the tip of the bleb, rather than simply increasing the bleb length. Ultimately, the best yield of intracellular recordings reported, and the greatest quality of recordings, has been obtained with tight (gigaohm) seal patch-clamp rather than perforated patch [46].

In any case, the sealing figures presented in chapter 6 are for N2A cells; for neurons in culture, these figures may be different. To uncover the truth regarding seal formation on neurons, it would first be necessary to ameliorate the problems associated with performing planar patch clamp on neuronal tissue. Cultures taken from living organisms have a greater quantity of biological debris than cells lines, and achieving clean seals is less likely. Also, the health of the cells is more variable, and consistency of seals is not guaranteed. This is why all studies on planar patch clamp to date have focussed on cell lines or xenopus oocytes.

7.4.3 Capacitive Degradation

Regardless of the intracellular configuration used, the device capacitance limits measurements of active cell properties as at present it is greater than that of the cells used here. However, based on their time constants, mammalian neurons have significantly greater capacitances than N2A cells ($\sim 100pF$) [85] which would reduce the detrimental effect of the device capacitance. Also, if the devices were integrated in a multichannel array, as discussed in chapter 4, the device capacitance would cause an insignificant distortion of the signal.

7.5 Caveats

There are complications in the above arguments. It is possible that there is some hierarchical order in which different device parameters affect seal formation. This is alluded to in the discussion of seal formation theories, where it is hypothesised that insufficient aperture depth prevents the surface properties from having an effect. It is possible that the inadequate aperture depth, diameter or roughness also prevent meaningful determination of the effect of radius of curvature or the presence of a nozzle. It is quite possible that radius of curvature, boron-doping and nozzles have some effect which is un-measurable because of other factors affecting seal formation.

However, more confidence should be placed in the results which do indicate a significant difference (that is surface roughness and aperture depth). It is intrinsic to the nature of null-hypothesis significance testing that it can only be used to determine if there *is* a significant difference between groups, rather than to detect if there is not [98, 99]. The credibility of the positive results is further enhanced by the fact that they were performed on groups with higher sample sizes (59 and 24) than the inter-subgroup tests.

The re-use of some devices may also introduce an error into the results. With glass pipettes every test was made with a new electrode. Given the small manufacturing yield and the increased manufacturing costs, this was not possible with devices, so many tests were made with devices which had been previously used. This may have been detrimental to seal formation, particularly to the $1.5\mu m$ devices with which a larger number of attempts were made with re-used devices. However, devices were thoroughly cleaned between uses and the analysis of the device re-use (figure 6.14) suggests that there is no significant change in seal resistance with successive attempts. It thus seems fair to conclude that the results with re-used devices are

valid.

Another possible source of error in the device sealing results is that all of the cells which went whole cell on devices seemed to do so spontaneously. The interesting point here is that the highest recorded resistance for such cells corresponds to the cells being whole cell. This implies that the seal resistance increased after cell membrane rupture, and hence that the maximum seal resistance was not properly measured. However, as this only applies to the 8 attempts which produced whole cell recordings, this is assumed not to affect the data substantially. Klemic et al. report similar findings [64].

Chapter 8
Conclusions and Further Work

8.1 Summary

Planar patch-clamp devices were constructed with a range of physical properties. Three different aperture diameters were created: $1.5\mu m$, $2\mu m$, $2.5\mu m$. The $2\mu m$ apertures were covered with PECVD silicon dioxide, the other two aperture were covered with thermal silicon dioxide. The PECVD covered apertures had a larger surface roughness and radius of curvature than the thermal oxide apertures. In addition, several subgroups were created within the thermal oxide devices. Devices of both aperture diameter were produced with and without the addition of a protruding nozzle creating four subgroups. These subgroups were in turn either left with a pure thermal oxide surface, or boron doped, creating a total of eight thermal oxide subgroups.

When seal formation was attempted with N2A cells, the thermal oxide devices produced an average seal resistance of $99.6M\Omega$ and one super-gigaohm seal. The thermal oxide devices performed significantly better than the PECVD devices. This is attributed to the surface roughness of the PECVD. There was no significant difference in performance between any of the thermal oxide subgroups. However, statistically significant correlations were detected between the seal resistance obtained and the aperture depth. This is proposed as the reason for there being no significant difference between the thermal oxide groups with different aperture diameters (the devices with different aperture diameters also had different aperture depths).

Experiments performed with glass pipettes on N2A cells show that the bleb which is drawn into the pipette tip during seal formation is substantially larger than the depths of the apertures produced in any of the device groups. This explains why the seal resistance should increase with aperture depth.

8.2 Further Work

8.2.1 Technological Issues with Multi-channel Planar Patch Clamp on Neurons

Many challenges lie on the path to a multi-channel planar patch-clamp assay. The first of these is achieving seals on neurons using planar patch clamp devices. The problem is that the neurons cannot be dissociated because the goal is to record network behaviour - this favours the use of in-vitro cultures of neurons. However, in-vitro cultures have a large amount of extracellular debris associated with them, which could seriously inhibit seal formation if it comes into contact with the aperture before the cells themselves. Another problem is the location of multiple neurons over multiple apertures simultaneously. Cell culture patterning is one possible solution [100][101]. If neuronal cell bodies can be aligned to a great enough precision, cells could be positioned on a cover-slip and then inverted onto an array of patch-clamp apertures. However, variation in the height of neurons above the cover-slip surface may produce a poor yield of seals. Alternatively, cells cultures could be patterned directly on to the device. This presents problems, as healthy neuronal cultures have a tendency to grow on top of a layer of glial cells, which would prevent recording from the neurons themselves. Another option, attempted previously by Fromherz [102] is to first dissociate neurons and position them manually, before allowing them to grow into a culture. In this case, cell positioning could be aided by suction through the aperture, which may also help retention of the cells over the recording sites during culture development.

Miniturisation of the headstage electronics also presents problems. A discussion of these problems and a possible solution are given in appendix D.

The final problem to be overcome in the implementation of a planar patch clamp array is the construction of a multi-channel base unit to supply all the recording sites with suction, and an electrical connection. Such a task is non-trivial, and some proposed solutions are described below.

Simultaneous suction

From a manufacturing point of view it would be convenient if the same suction could be applied simultaneously to all the recording sites of a multichannel device. This would remove the need for each recording site to have a separate suction channel. In one hypothesised implementation,

metal is sputtered on to the underside of the device, and patterned to provide isolated electrical contact to each hole individually. Tests have been performed on dummy silicon holes, to determine whether any metal was deposited on the sidewalls during sputtering. 1μm of Aluminium was sputtered at 4kW using a Balzers BAS450PM sputterer. The result of these tests (shown in figure 8.1) demonstrates that this is the case.

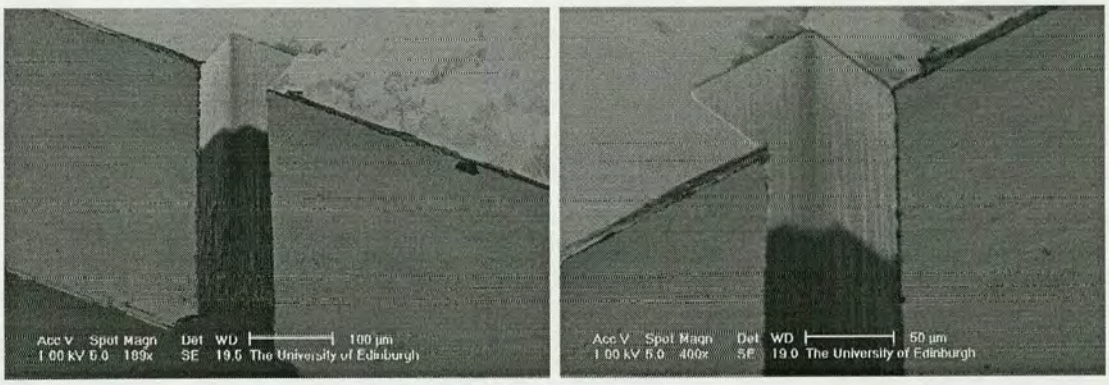

Figure 8.1: $1\mu m$ *aluminium sputtered onto deep etched cavities.*

The main problem associated with this implementation would be keeping the intracellular fluid in place. It was proposed that if the fluid was confined to a recording site, surface tension would hold it in place when suction was applied during seal formation. In addition, it was thought that making the underside of the device hydrophobic would minimise 'short circuits' caused by fluid leaking between recording sites. As this is essentially a scaled down version of the test platform described and successfully employed in chapter 6, it seems plausible that this would work.

Multiple discrete suction lines

However, it was thought that, given the difficulty in seal formation in conventional patch-clamp experiments, applying suction to all the recording sites at once might not give an acceptable yield of sealed cells per hole. For this reasons, a solution with a separate suction lines for each aperture is desirable.

The obvious disadvantage is that it is impossible for one human being to control the formation of many suction lines simultaneously, so some sort of control system is required, to apply pressure to each cell when needed. One such system is described by Heyward and Shipley [103]. More advanced control systems are used currently in commercial planar-patch clamp setups,

but their details are rarely disclosed.

The other inherent disadvantage is the complexity involved in the manufacture of discrete microfluidic channels for isolating the suction and intracellular solution for each hole. One possible design is to permenantly attach (by bonding or gluing) a secondary silicon wafer onto the back of the wafer containing the patch-clamp devices. The Ag/AgCl electrodes, in this case, would be located on the second chip, in such a position that they could be easily cleaned and re-chloridised. However, such a design would have serious implications for filling the devices (because the channels are permenantly bonded to the devices). Also, the resistance of these channels when filled with intracellular solution, might affect the quality of the signals recorded. A better option, is to have the microchannels removable, and place the electrodes underneath the recording sites. This allows the electrodes to be chloridised, and the devices filled, and should provide better signal quality. The drawback here is the integrity of the seal formed between the two chips.

If such a system were to be manufactured, it may be necessary to fabricate electrodes on a flat surface, and build up trench walls around them, rather than trying to print electrodes at the bottom of a trench. One material which could be used to do this is parylene.

8.2.2 Manufacturing processes for a multichannel base unit

Parylene microchannels

Some tests have been performed, using parylene to form the microchannels. A process was developed for manufacturing microchannels in $10\mu m$ thick parylene using 1000Åaluminium as a hard mask. The result of this process can be seen in figure 8.2.

Silver chloride electrodes

Another consideration is the manufacture of the electrodes themselves. The factor determining the size of the electrode (thickness of silver required) would be the amount of time required for a typical experiment, and the rate at which silver is converted to silver chloride. For an electrode of thickness t, and area A, passing constant current I, the number of moles of electrons passed per second (and hence the number of moles of silver converted per second) is given by:

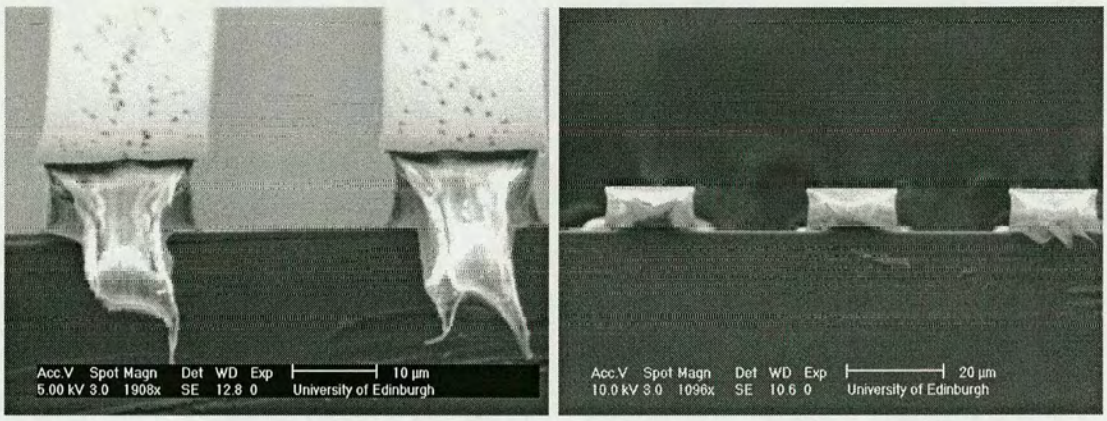

Figure 8.2: *Microfabricated parylene-C micro-channels*

$$N = \frac{I}{F} \tag{8.1}$$

where F is Faraday's constant, equal to 96500 moles/C

Given that the relative atomic mass of silver μ_{Ag}, is 108, the mass of silver lost per second is:

$$\begin{aligned} M &= N\mu_{Ag} \\ \Rightarrow \quad M &= \frac{I\mu_{Ag}}{F} \end{aligned} \tag{8.2}$$

Thus the volume of silver lost per second is (density of silver, $\rho_{Ag} = 10,500\ kg/m^3$ [92]):

$$\begin{aligned} V &= \frac{M}{\rho_{Ag}} \\ \Rightarrow \quad V &= \frac{I\mu_{Ag}}{F\rho_{Ag}} \end{aligned} \tag{8.3}$$

Hence the thickness lost per second is,

$$\begin{aligned} \tau &= \frac{V}{A} \\ \Rightarrow \quad \tau &= \frac{I\mu_{Ag}}{F\rho_{Ag}A} \end{aligned} \tag{8.4}$$

Therefore the electrode should last for duration d,

$$d = \frac{t}{\tau}$$

$$\Rightarrow \quad d = \frac{tF\rho_{Ag}A}{I\mu_{Ag}} \tag{8.5}$$

To verify this value, an experiment was conducted on evaporated silver (5000Å thick). Current was passed (at a constant voltage) through a silver electrode (the anode) in a saline solution of a concentration typically used in patch-clamp recordings. The time at which conduction ceased was measured (effectively the time at which the entire layer had been converted to silver chloride). A plot of current density versus time is shown in figure 8.3 for three different traces.

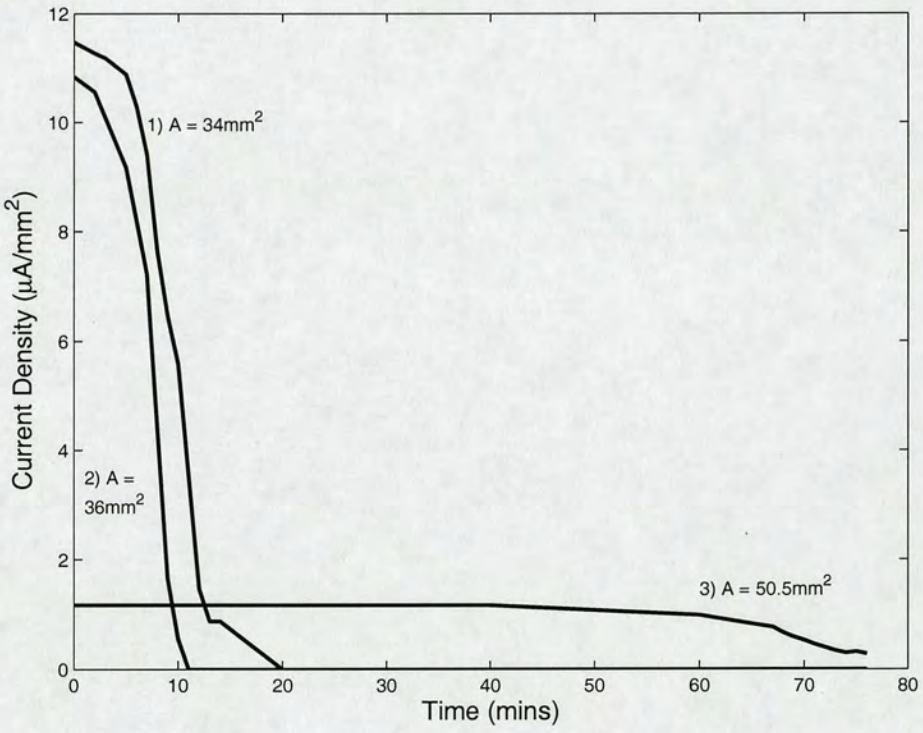

Figure 8.3: *Current degradation versus time for AgCl electrodes*

From equation 8.5, the time to completion for each plot should be:

$$1) \quad d = 6.8\ minutes \qquad 2) \quad d = 7.2\ minutes \qquad 3) \quad d = 66\ minutes \tag{8.6}$$

However, equation 8.5 assumes that a constant current is passed for the entire duration, until the electrode ceases to conduct. As can be seen from the graphs of figure reffig:silver, this is not the case, and the current declines slowly. Integrating these graphs yields the total charge passed per unit area during the whole experiment:

$$1) \quad Q = 7082\ \mu C/mm^2 \qquad 2) \quad Q = 5019\ \mu C/mm^2 \qquad 3) \quad Q = 4865\ \mu C/mm^2 \tag{8.7}$$

Dividing by the starting current density yields an estimation of the finishing point:

$$1) \quad d = 7.7\ minutes \qquad 2) \quad d = 10.3\ minutes \qquad 3) \quad d = 69.4\ minutes \tag{8.8}$$

To a first approximation, the values of equation 8.8 agree with the model of equation 8.6.

For the intended application, the electrodes will be 80μm square (the size of the cavity in the patch devices). Typical patch experiments to examine network activity could last up to 12 hours, with a possible maximum average current of 0.5nA. Rearranging equation 8.5:

$$t = \frac{dI\mu_{Ag}}{F\rho_{Ag}A} \tag{8.9}$$

Inserting the maximum values given above:

$$t = 360\ nm \tag{8.10}$$

Thus, a 360nm thick electrode will last for 12 hours if used to pass current constantly. However, some allowance should be made for the fact that the electrical properties of the electrode begin to degrade before the theoretical endpoint. As the plots of figure 8.3 seem to indicate, this degradation of the resistance becomes less significant as the duration of the electrode increases. As the intended current density would be one order of magnitude less than that of plot 3), this should be safely accounted for by a 50% margin for error. Thus an electrode of 500nm thickness is required. Furthermore, at the start of the experiment, it would be desirable to have

the electrode half chloridised, so that it can be used in either the forward or the reverse direction for 12 hours. Thus an electrode double this thickness is required. Thus the required thickness is about 1μm.

Although this thickness of silver could be patterned by lift-off or by directly etching the silver, the best approach for depositing silver is electroplating. This allows the process for manufacturing the base to remain CMOS compatible, until the final electroplating step. Also, this allows a thin seed layer to be deposited, ontop of which the microchannels can be built up with minimal disruption of the parylene surface. Electroplating of silver onto Titanium Nitride has been investigated by Cesiulis and Moroz [104]. TiN is used as an adhesion layer in ULSI processes, and will withstand the etching processes involved in the manufacture of the base unit, making it a suitable candidate for a seed layer.

8.2.3 Proposed multi-channel base construction

A summary of the proposed process for the manufacture of a multi-channel base unit follows. TiN is deposited on a silicon dioxide surface, and patterned so that isolated electrodes are formed, with tracks to allow external connections to be made. The oxide is then patterned, to allow the (later) back side silicon etch to break through. The parylene is deposited, 10μm thick and patterned to form the channels such that the channels coincide with the holes in the oxide. Subsequently, the silicon is etched from the back in TMAH to form a tapered suction port which contacts the channel. Finally, the TiN electrodes are electroplated with silver. The multichannel device would be sealed onto this base unit by pressure from the top side, and the base would in turn be sealed onto a PDMS or perspex platform with macroscopic suction lines.

8.2.4 Multichannel Recording

The problems described above regarding cell positioning, electronics, base manufacture and application of suction present a substantial obstacle to recording network behaviour with planar patch clamp. If this obstacle can be overcome, it may be possible to record from devices with seals of the resistances observed here. To do so, it would be necessary to adopt the perforated patch approach used by the IonWorks HT (Molecular Devices). The main benefit of this would be an increase in the yield of whole cell recordings, as the process of gaining intracellular access is dependent on chemical, rather than mechanical factors. This would also help maintain

the health of the cells for longer, as the membrane would remain intact, preventing diffusion of intracellular solutions [71] - this is particularly critical in situations where the seal resistance is low.

8.2.5 Optimisation of Seal Resistance

Nonetheless, with or without the use of the perforated patch techniques, increased seal resistances are always advantageous. Based on the results of this work, certain changes would be made to device fabrication procedure to obtain higher seal resistances.

The most important change would be to produce devices with a thicker membrane, up to $30\mu m$ thick. Using the electrical model presented in chapter 7, such apertures would have a resistance of $9M\Omega$ (for a $1.5\mu m$ diameter), which is within the acceptable range for patch clamp recording. However, there may be problems associated with locating apertures in $30\mu m$ thick membranes, as the light transmitted by the membranes will be faint. If required, location marks could be printed on the front of the devices.

One approach to creating such devices is to use SOI wafers with a thicker device layer. However, given the required thickness of the membrane, there may be enough tolerance to remove the need for an oxide stop layer in the process. This would eliminate the etch undercut on both the front and back etches, which would reduce the trapping of bubbles in the chamber. However, the trade-off would be the formation of grass by the backside etch [105]. This may also cause device filling problems, or may provide a mechanism for bubbles to escape from the chamber, in the same way in which a reed does in a pipette. A reed-like structure could also be included in the back-side chamber. This is a simple matter of altering the mask used to define the chamber.

Steps could also be taken to remove the sidewall roughness of the aperture produced by Bosch etching. Hydrogen annealing [82] is an approach to this problem which has been demonstrated successfully. It involves heating exposed silicon to 1000°C in a hydrogen ambient. The hydrogen lowers the melting point of the silicon, such that it deforms, smoothing the surface. This would create a smooth rounded surface, similar in effect to fire-polishing a glass pipette. It is also anticipated that this process would disrupt the crystal structure of the silicon, allowing thermal oxide to be grown isotropically. If this is the case, thermal oxide could be used to shrink the size of the apertures, without squaring. This would allow larger, more repeatable aperture

sizes to be printed at the photo-lithography stage, removing the yield and variation problems associated with the thermal oxide devices. The final diameter could be controlled with thermal oxidation, allowing the apertures as small as $1\mu m$ to be produced consistently.

8.3 Conclusions

The hypothesis set out at the start of this thesis is:

Matching the physical properties of planar patch-clamp devices to those of glass pipettes will optimise seal formation.

In testing this hypothesis, it is useful to examine all of the information in existence. However, there is much knowledge on this topic which lies in the realm of industry, and so is not publicly available. On the basis of the experiments, and those performed elsewhere in academia, some conclusions can be drawn.

Aperture Depth The depth of the aperture is one respect in which planar patch clamp devices should mimic glass pipettes. Although glass micro-pipettes have a shank which is up to 10mm in length, it is only necessary to reproduce as much of this shank as the cell requires to form a seal. This bleb length is dependent on the type of cell used; for the neuroblastoma cells used here, about $30\mu m$ is sufficient. Indeed this aperture depth should be made as small as possible within the requirements of seal formation, in order to limit the resistance of the aperture. This is the only study to have measured the effect of aperture depth on seal formation.

Aperture Diameter Seal formation is also dependent on the diameter of the aperture, with smaller apertures generally producing higher resistance seals, down to some optimum aperture diameter. It is expected that this optimum aperture diameter will vary with cell type, though values between 1 and 1.5 micrometers are common. Gigaohm seals have not been formed on apertures greater than $2\mu m$ in diameter.

Surface Roughness It is *likely* that the roughness of the surface material affects seal formation. Rough materials (like PECVD silicon dioxide) are expected to seal less well than smooth surfaces (like thermal oxide and glass).

Aperture Profile The aperture profile has little effect on seal formation. Three different pro-

files were tested here, and none showed any significant advantage over the others. The literature confirms this, as devices with many profiles have produced gigaohm seals, though this is the only study to have tested different profiles in parallel.

Surface Chemistry It seems unlikely that the seal formation can be independent of surface chemistry, though the surfaces tested here show no significant differences in their capacity to form seals. The literature describes the formation of gigaohm seals on a greater range of surfaces encompassing a wide range of surface energies, both on planar devices and on micro-pipettes. It has to be concluded that this aspect of seal formation requires further investigation.

The conclusion of this thesis is that mimicking the physical properties of glass pipettes will improve seal formation on planar-patch clamp devices. Although there are some properties which do not seem to have an effect on seal formation, there are no properties which have a detrimental effect on the seal resistance, when matched to glass pipettes.

Appendix A
Device Fabrication Details

A.1 Equipment details

Photolithography

Optimetrix 8605 5x reduction stepper. G-line (436nm), 0.32 NA, 1.0 micron resolution over 1.4 cm square field. (Printing of apertures.)

Karl Suss MA8/B6 double sided contact/projection mask aligner. (Printing of chamber and cut lines.)

Brewer Science CEE 6000 75-200mm Coat/Develop system. (Photoresist coat.)

Layer Deposition

Hitech 8" furnace tube. (Thermal oxidation.)

Tempress 3" furnace tube, with Saint-Gobain boron nitride (BN-1100) planar sources. (Solid source boron dope.)

Surface Technology Systems Multiplex Plasma-Enhanced Chemical Vapour Deposition System. (PECVD silicon dioxide.)

Dry Etch

Plasmatherm PK244O RIE. (Oxide etch.)

Surface Technology Systems Multiplex Inductively Coupled Plasma. (Deep silicon etch.)

Electrotech Barrel Asher. (Photoresist removal.)

Wafer dicing

Disco DAD Dicing Saw

A.2 PECVD process details

Parameter	Value
N_2 flow	392sccm
N_2O flow	1420sccm
SiH_4 flow	10sccm
Pressure	900mT
Coil Power	30W (13.56MHz)
Platen Temperature	300°C

A.3 Bosch process details

	Etch Cycle	Passivation Cycle
SF_6 flow	130sccm	0sccm
O_2 flow	13sccm	0sccm
C_4F_8 flow	0sccm	85sccm
Pressure	25mT	25mT
Platen Power	12W	0W
Coil Power	600W	600W
Duration	12s	8s

A.4 Non-bosch Process details

	Etch Cycle
SF_6 flow	50sccm
O_2 flow	0sccm
C_4F_8 flow	90sccm
Pressure	15mT
Platen Power	14W
Coil Power	800W

A.5 Acid piranha

The procedure used for cleaning the devices was as follows:

1. Pour 15ml of 98% Sulphuric Acid into reaction vessel.

2. Pour 25ml of 30% Hydrogen Peroxide into acid.
3. Leave to stand for 2 minutes to reach temperature.
4. Immerse sample in solution for 10 minutes.

A.6 Mask Set

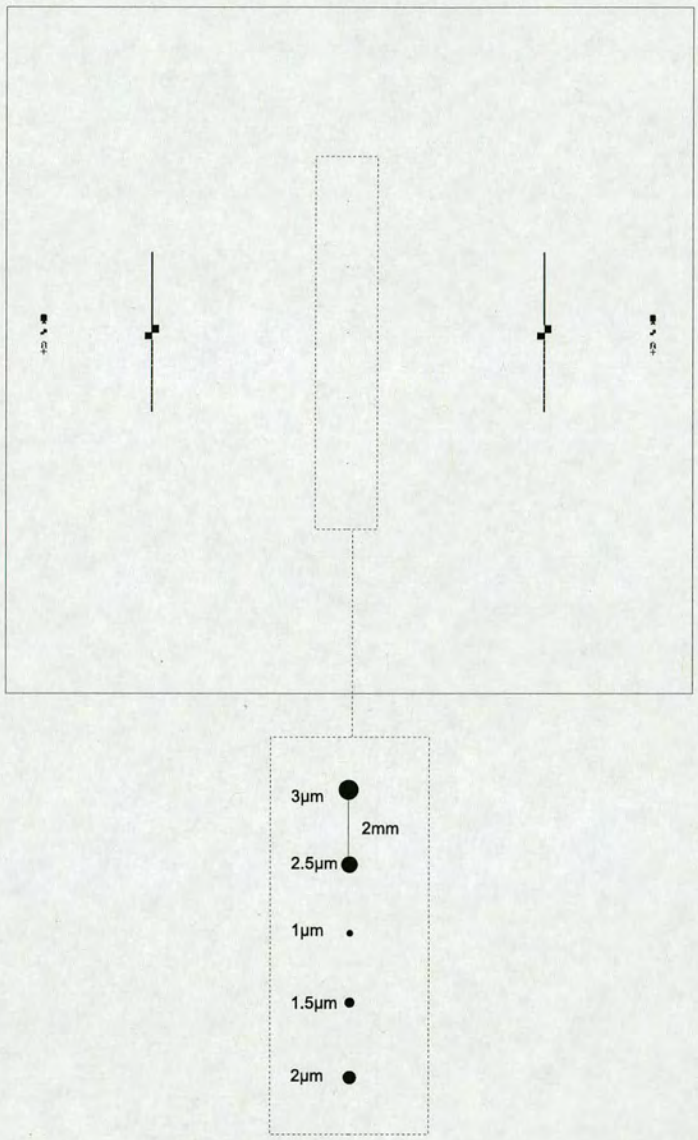

Figure A.1: *The mask used for projection printing of the apertures on the frontside. This image is a negative of the actual mask. The mask was printed in chrome on a 5-inch plate*

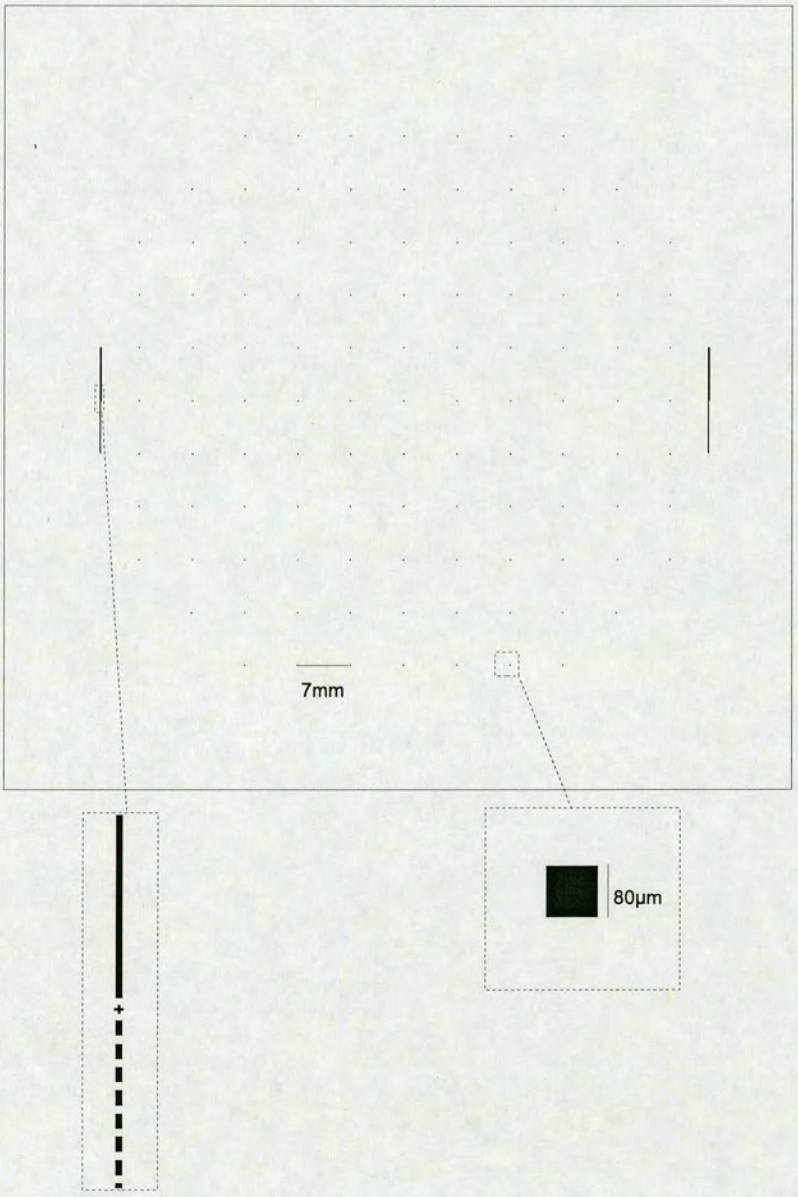

Figure A.2: *The mask used for contact printing of the chambers on the back side. The alignment marks are used to align the pattern to those shown in figure A.2. This image is a negative of the actual mask. The mask was printed in emulsion a 5-inch plate*

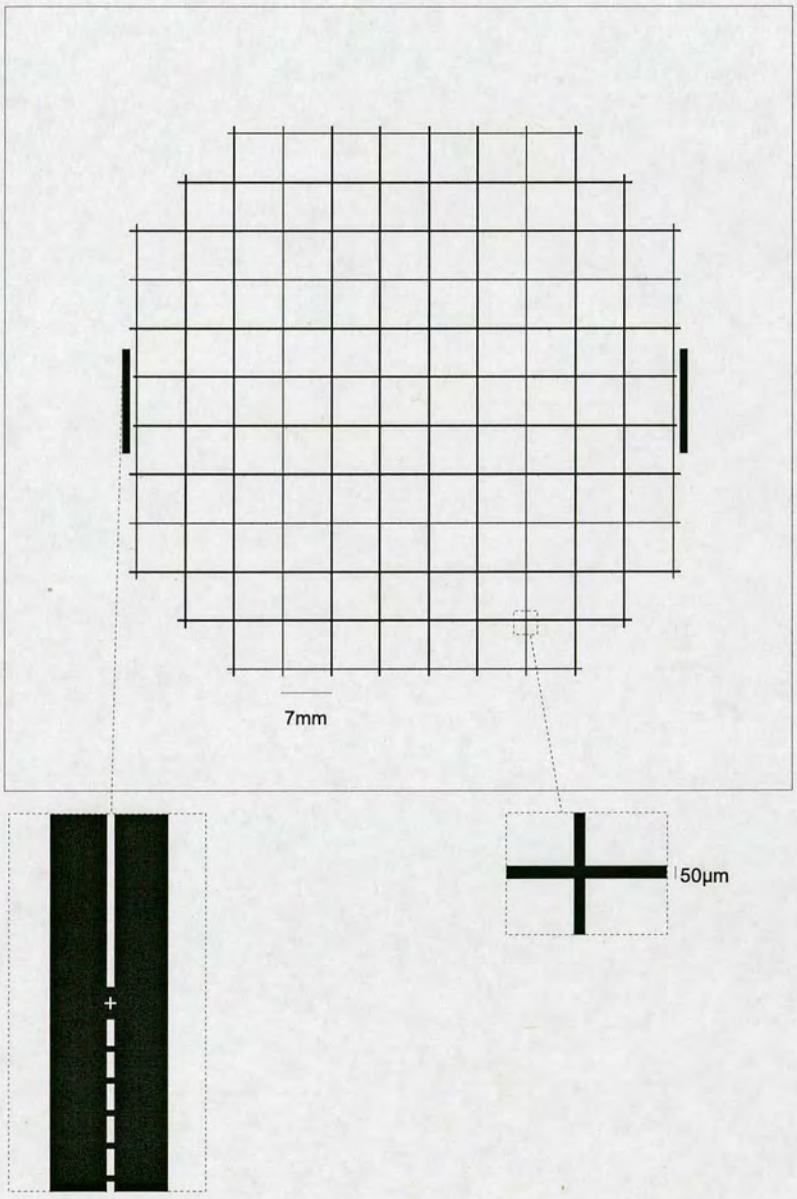

Figure A.3: *The mask used for contact printing of the streets on the front side. The alignment marks are used to align the pattern to those shown in figure A.3. This image is a negative of the actual mask - note the dark-field alignment marks, required to view the corresponding marks on the front of the wafer. The mask was printed in emulsion on a 5-inch plate*

Batch ID: runsheet v5		Quantity:	Mask set ID:			Wafer diameter: 4"	Customer contact: 650-7450 650-3032
Step	Process		Equipment	Parameter		Date	Comments
				Target	Actual		Use double side polished 4" SOI wafers (1um sandwiched oxide between 300um handle and 15um top section)
1	Thermal oxidation	WOX14 2^h30^m	Furnace #1	1μm			
2	Resist Coat Frontside SPR350, 3300rpm, 1min 110C	SPR3300	Brewer Science Track				Need to match resist thickness on BS Track with 1,4,3 on SVG.
3	5x Expose Apertures		5x Stepper	2um			print global alignment marks at 80mm separation + small holes
4	PEB, Develop Frontside, non-HB	PEBDEV	Brewer Science Track				
5	RIE Oxide Etch Frontside	CF4+H2 (gasses 1+4)	Plasmatherm				4" in Plasmatherm on 3" wafer
6	Ash Resist	60mins	Barrel Asher				
7	Resist Coat Frontside SPR350, 3300rpm, 1min 110C	SPR3300	Brewer Science Track				
8	KS Align and Expose Streets	Program 6	Karl Suss				Need to put in 4" chuck + 5" mask holder
9	PEB, Develop Frontside, HB	PEBDEV	Brewer Science Track				Paint out alignment marks after this step, otherwise we won't be able to align backside!!!
10	RIE Oxide Etch Frontside	CF4+H2 (gasses 1+4)	Plasmatherm				
11	Ash Resist	60mins	Barrel Asher				Resist coat front side here?

Batch ID: runsheet v5		Quantity:	Mask set ID:			Wafer diameter: 4"	Customer contact: 650-7450 650-3032
Step	Process		Equipment	Parameter		Date	Comments
				Target	Actual		**Use double side polished 4" SOI wafers (1um sandwiched oxide between 300um handle and 15um top section)**
12	**ICP Etch Silicon Frontside**	scuba_6	STS ICP	15um			Either an increased platen power etch, or a two step anisotropic/isotropic to get a bit of undercut.
13	**Resist Coat Frontside SPR350, 3300rpm, 1min 110C**	SPR3300	Brewer Science Track				We've come this far without putting the frontside down on any surface, so resist coat to protect
14	**Thick Resist Coat, Backside, HPR206, 2000rpm**	HPR206	Manual Spinner				Syringe resist.
15	**KS Expose Windows**	prog 6 20s exposure	KS aligner				align mask to front side need long exposure for thick resist increase exposure time.
16	**Develop, HB**	PEBDEV	Brewer Science Track				
17	**RIE Oxide Etch, Backside**	CF4+H2 (gasses 1+4)	Plasmatherm				do not ash after etch, leave pr for icp.
18	**ICP Etch Backside**	scuba_6	STS ICP	300um			Etch until Oxide stop layer, this leaves 15um for membrane
19	**Ash Resist**	60mins	Barrel Asher				may need to do this twice
20	**HF strip**	48% HF	Wet Bench	1um			Remove frontside oxide mask, so that when we thermally oxidise, the oxide grows in a more rounded manner. Also, break through sandwich layer to back side. Will need some agitation to ensure that the oxide sandwich layer breaks through.
21	**Thermal oxidation**	WOX14 2.5h	Furnace #1	1um			1um on bare si sidewalls but only 0.4um on the already oxidised back side.
22	**HF strip**	Buffered HF 4:7:1	Wet Bench	6mins			Until Hydrophobic

Batch ID: runsheet v5		Quantity:	Mask set ID:			Wafer diameter: 4"	Customer contact: 650-7450 650-3032
Step	Process		Equipment	Parameter		Date	Comments
				Target	Actual		Use double side polished 4" SOI wafers (1um sandwiched oxide between 300um handle and 15um top section)
23	Thermal oxidation	WOX14 2.5h	Furnace #1	1um			
24	PECVD Frontside	HFSIO	STS PECVD	1um			
25	PECVD Backside	HFSIO	STS PECVD	1um			
26	Boron Dope/Annealing	BNDP12 - 1000°C	Furnace #10	15mins			How do we boron dope with 4" solid source?
27	Break Wafers at 7mm sq.						Nick edges and score streets right to the edge of wafer before breaking

Batch ID: PCS041108		Quantity: 5	Mask set ID:			Wafer diameter: 4"	Contact: Keith 505610, 503032
Step	Process		Equipment	Parameter		Date	Comments
				Target	Actual		Use double side polished 4" SOI wafers (1um sandwiched oxide between 300um handle and 15um device layer)
1	Thermal oxidation	WOX14 $2^{h}17^{m}$	Furnace #1	1μm			Measure wafer thickness
2	Resist Coat Frontside SPR350, 3300rpm, 1min 110C	SPR3300	Brewer Science Track				Need to match resist thickness on BS Track with 1,4,3 on SVG. Need to do HMDS in a box, 15 mins
3	5x Expose Apertures		5x Stepper	2um			print global alignment marks at 80mm separation + small holes
4	PEB, Develop Frontside, HB	PEBDEV	Brewer Science Track				
5	RIE Oxide Etch Frontside	CF4+H2 (gases 1+4)	Plasmatherm				4" in Plasmatherm on 3" wafer
6	Ash Resist	60mins	Barrel Asher				
7	Resist Coat Frontside SPR350, 3300rpm, 1min 110C	SPR3300	Brewer Science Track				Need to do HMDS in a box, 15 mins
8	KS Align and Expose Streets	Program 6	Karl Suss				Need to put in 4" chuck + 5" mask holder
9	PEB, Develop Frontside, HB	PEBDEV	Brewer Science Track				Paint out alignment marks after this step, otherwise we won't be able to align backside!!!
10	RIE Oxide Etch Frontside	CF4+H2 (gases 1+4)	Plasmatherm				
11	Ash Resist	60mins	Barrel Asher				

Batch ID: PCS041108		Quantity: 5	Mask set ID:			Wafer diameter: 4"	Contact: Keith 505610, 503032
Step	Process		Equipment	Parameter		Date	Comments
				Target	Actual		**Use double side polished 4" SOI wafers (1um sandwiched oxide between 300um handle and 15um device layer)**
12	**ICP Etch Silicon Frontside**	Negramp	STS ICP	15um			Negramp ramps process parameters to taper
13	**Resist Coat Frontside SPR350, 3300rpm, 1min 110C**	SPR3300	Brewer Science Track				We've come this far without putting the frontside down on any surface, so resist coat to protect. Need to do HMDS in a box, 15 mins
14	**Thick Resist Coat Backside, HPR206, 2000rpm**	HPR206	Manual Spinner				Syringe resist. Need to do HMDS in a box, 15 mins
15	**KS Expose Windows**	prog 6 20s exposure	KS aligner				align mask to front side need long exposure for thick resist increase exposure time.
16	**Develop, HB**	PEBDEV	Brewer Science Track				
17	**RIE Oxide Etch, Backside**	CF4+H2 (gases 1+4)	Plasmatherm				do not ash after etch, leave pr for icp.
18	**ICP Etch Backside**	scuba_6	STS ICP	300um			Etch until Oxide stop layer, this leaves 15um for membrane. Measure thickness with micrometer before this.
19	**Ash Resist**	60mins	Barrel Asher				may need to do this twice
20	**Piranha**	5mins, 100C	Wet Bench				To remove any remaining passivation.
21	**HF strip**	48% HF + TritonX	Wet Bench	1um			Remove frontside oxide mask, so that when we thermally oxidise, the oxide grows in a more rounded manner. Also, break through sandwich layer to back side. Will need some agitation to ensure that the oxide sandwich layer breaks through.
22	**Thermal oxidation**	WOX11	Furnace #1	0.6um			Do this at 950°C to accentuate the cut into the silicon

Batch ID: PCS041108		Quantity: 5	Mask set ID:			Wafer diameter: 4"	Contact: Keith 505610, 503032
Step	Process		Equipment	Parameter		Date	Comments
				Target	Actual		Use double side polished 4" SOI wafers (1um sandwiched oxide between 300um handle and 15um device layer)
23	HF strip	Buffered HF 4:7:1	Wet Bench	6mins			Until Hydrophobic
24	Thermal oxidation	WOX14	Furnace #1	0.5um			Do this at 1100°C, all wafers
25	Quarter wafers		Disco Dicing Saw				So that we can process quarters differently
26	RIE Oxide Etch Frontside	CF4+H2 (gases 1+4)	Plasmatherm				Nozzle process on half of each wafer, to remove oxide on top surface
27	ICP Etch Backside	SF6	STS ICP	2um			Nozzle process on half of each wafer, to create nozzle
28	Thermal oxidation	WOX14	Furnace #6	500nm			Nozzle process on half of each wafer, to reoxidize
29	Boron Dope	BNDP12 - 1000°C	Furnace #10	30mins			Must do this on quarter wafers. One nozzle quarter and one flat quarter of each wafer.
30	Dice Wafers at 7mm sq.		Disco Dicing Saw				Saw wafers on Disco Dicing Saw

Appendix B
Device Testing Details

B.1 N2A Culture Medium Composition

DMEM (with L-glutamine, pyruvate, glucose (1000mg/l)(invitrogen cat no. 31885-023)

+10% Foetal bovine serum(FBS)(invitrogen cat no. 10108-165)

+1% non - essential aminoacids (100x stock)

+125 units pen/ml Penicillin-Streptomycin (optional)

B.2 N2A Passage and harvest protocol

Before passage or harvest make sure all solutions are pre warmed.

Passage

1. Remove medium from flask.
2. Add 1ml trypsin/EDTA rinse cells then remove.
3. Add another 1ml trypsin. Put flask into incubator for approximately 2 mins.
4. Rock gently until cells detach.
5. Re-suspend cells in 5ml of media.
6. Pipette 0.5-1.5ml cells into new flask.
7. Add more media to new flask 3.5-4.5ml (in order to make up to 5ml total).

Harvest

1. Remove medium from flask.

2. Add 1ml trypsin/EDTA rinse cells then remove.
3. Add another 1ml trypsin. Put flask into incubator for approximately 2 mins.
4. Rock gently until cells detach.
5. Re-suspend cells in 5ml of DMEM.
6. Transfer to 15ml centrifuge tube, and centrifuge for 4 minutes at 400rpm.
7. Pour out DMEM and re-suspend cells in ~2ml extracellular solution.
8. Mix $20\mu l$ of Cell suspension with $20\mu l$ of trypan blue solution, leave for 5 minutes and observe under a microscope to check the integrity of cell membranes.
9. Leave cells in centrifuge tube on shaker table until required, to prevent clumping.

(Values given are for 25ml flasks) for 75ml flasks multiply quantities by 3.

B.3 Recording solutions

Intracellular (patch) solution (pH to 7.2 with KOH):

Constituent	Concentration (mM)
NaCl	10
KGluconate	102
$CaCl_2$	1
$MgCl_2$	1
HEPES	10
EGTA	10

Extracellular solution (pH to 7.2 with NaOH):

Constituent	Concentration (mM)
NaCl	140
$CaCl_2$	2
$MgCl_2$	1
HEPES	5
KCl	4
Glucose	10

Fluorescent intracellular solution:

As standard intracellular solution, with lucifer yellow, lithium salt (Invitrogen, L453) <1mg/ml.

B.4 Micropipette pulling program

step	HEAT	PULL	VEL	TIME
1	360	30	30	100
2	325	10	20	35
3	300	10	25	20
4	300	10	7	20
5	300	10	7	20
6	300	20	43	40

The capillary is heated by applying current specified by HEAT to the filament. Its ends are held under gravitational tension until the ends reach the velocity VEL. Then the filament is switched off and the capillary is air cooled for TIME miliseconds before the hard pull (of intensity determined by PULL) is engaged. After the hard pull, the next line is executed. The air pressure setting was 500.

B.5 Electrode chloridisation

Chloridised silver wires were used as reference (ground) and working electrodes. They were prepared as follows:

1. Solder 3cm of silver wire on to a lead of suitable length.
2. Immerse the silver wire in 10mM KCl solution, taking care only to immerse the silver (i.e. not the solder joint).
3. Connect the other end of the lead to the positive terminal of a 5V supply through a $2k\Omega$ resistor.
4. Connect the negative terminal to a similarly prepared piece of silver wire and immerse this in the solution also.
5. Pass current in this direction for about 5 minutes, reversing the polarity for 20 seconds every two minutes. (A cross-over switch was used to do this.)
6. When coated, the wire should appear white. Rinse the wire in distilled water.

B.6 Patching protocol

Glass

Pipettes were pulled as detailed above. Their bubble number was measured in alcohol, and then they were kept in an electrode storage jar, with a little distilled water in the bottom. $100\mu l$ of cell suspension as prepared above, was pipetted into a 35ml Petrie dish. This was then topped up (slowly as not to disturb the cells) with extracellular solution to the top of the dish. The dish was placed on a microscope stage and an earth electrode was placed in the solution.

A pipette was filled with patch solution, using a syringe with a $0.2\mu m$ filter and a flexible needle. A pipette was secured in an Axoclamp headstage (attached to and Axon Instruments Axoclamp 2B microelectrode amplifier) mounted on a micromanipulator, and positive pressure was applied to the pipette. The tip was then lowered into the cell-containing dish and moved into the microscope's field of view.

Current pulses were passed through the electrode (using an AMPI Master-8 pulse generator) and the resistance was measured. A suitable cell was located under the microscope, and the pipette was manoeuvred so that it was as close to the cell as possible without the positive pressure repelling the cell. Recording of the voltage response onto the PC was started, using Axon Instruments' Axoclamp software. The signal from the Axoclamp-2B was conditioned using a Warner Instruments LPF202A signal conditioner (to equalise the gain of both channels) and input to the PC using an Axon Instruments Digidata 1320.

The positive pressure was then removed from the pipette. In some cases, the pipette tip was close enough to the cell for the release of positive pressure to initiate seal formation. Otherwise, gentle suction was applied to initiate seal formation. When the seal had stabilised above 1 giga-ohm, the Axoclamp recording was stopped, and a current-voltage trace of the seal was recorded using Axon Instruments' Clampex. Extra suction was then applied, in order to rupture the membrane (this was optionally recorded using Axoscope). Once the whole cell configuration had been achieved, a current-voltage trace of the cell itself was recorded using Clampex.

This process was repeated for at least three pipettes (to ensure consistent formation of gigaohm seals) before attempting device recordings.

Devices

Devices were fabricated as discussed in chapter 6. The chips were placed on a 49mm perspex frame, and PDMS was painted around the edge, to attach the chip to the frame and ensure encapsulation of the edge. In order to fill the device, drops of $0.2\mu m$ filtered patch solution were placed over the back and front of the aperture, it was inverted and placed in the bottom of a vacuum jar. The vacuum jar was pumped down to below 35mT, so that the solution bubbled. This was left under vacuum for 5 minutes.

The device was removed from the solution and patch solution was removed from the top of the device. The well formed in the perspex frame was filled with patch solution and the solution was mounted in the base unit, so that the wire electrode in the base protruded into the well. The perpsex frame was screwed into place, and a few drops of extracellular solution were placed ontop of the device. The device assembly was placed onto the microscope stage, and the device was illuminated from the underside (to facilitate location of the aperture, and reduce noise). A reference electrode was placed in the extracellular solution and the impedance of the aperture was recorded as a current-voltage characteristic using Clampex.

A pipette was used to apply $20\mu l$ of cell suspension to the top of the device. Recording of the sealing trace was started with Axoclamp. When a slow moving cell was within $50\mu m$ of the aperture (i.e. close enough so that it could be viewed by the light transmitted through the device membrane) suction was applied in an attempt to capture the cell onto the aperture. Suction was applied gently, in order not to damage the cell. The aim was to locate the cell over the aperture slowly, then apply gentler suction still to encourage seal formation. However in many cases the cell moved more quickly than anticipated, and the suction applied to position the cell also initiated seal formation.

In most cases, suction had to be applied for prolonged periods to gain any increase in seal resistance. On the few occasions where whole cell-like behaviour was observed, the axoclamp recording was stopped, and a current-voltage relationship was recorded with Clampex. Otherwise, the cell was blown off when the seal had reached its maximum value. Note that the value recorded for the seal resistance is the maximum stable value (without suction). Marginally greater values were often obtained under suction.

This process was repeated for a maximum of three cells, where possible, with each device.

Base

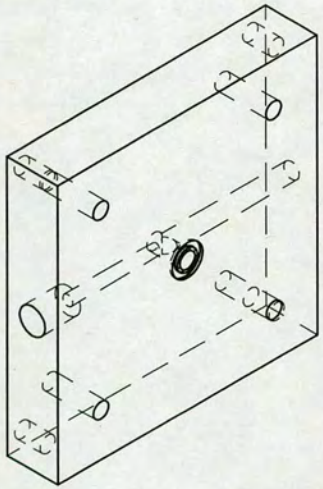

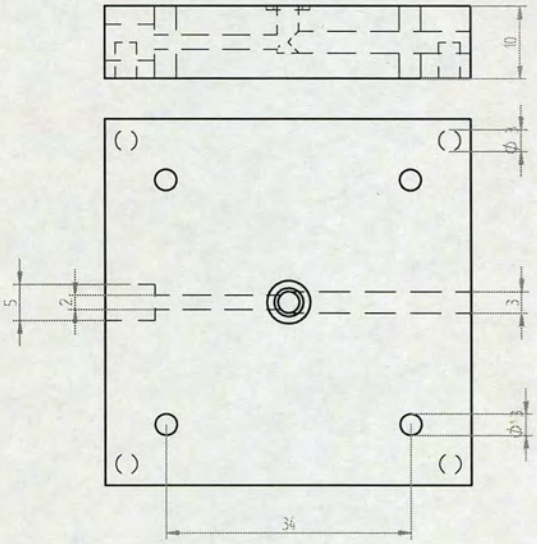

Base Chamber Detail

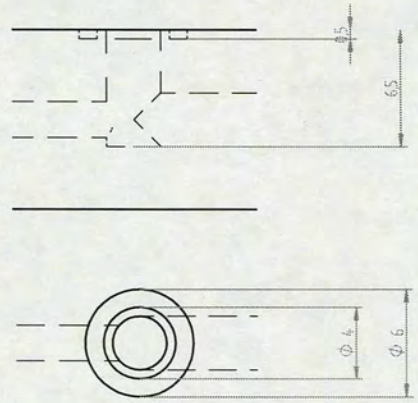

Frame

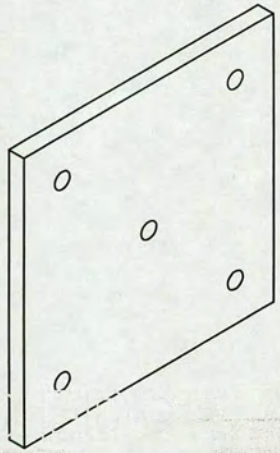

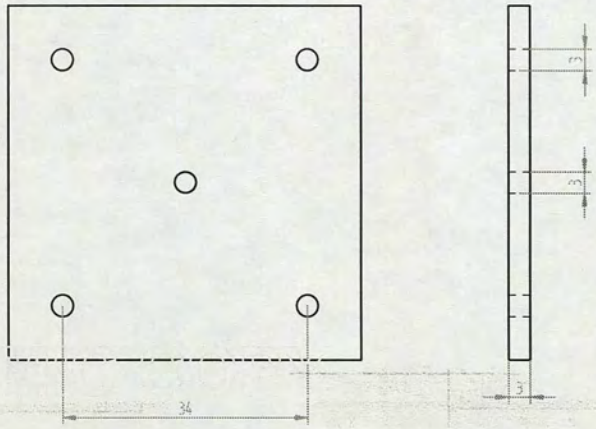

B7. Device Test Platform Schematic

	NAME	DATE
DRAWN	9383103772	03/13/06
CHECKED		
ENG APPR.		
MGR APPR.		

UNLESS OTHERWISE SPECIFIED
DIMENSIONS ARE IN MILLIMETERS
ANGLES ±X.X°
2 PL ±.XXX 3 PL ±.XXXX

SOLID EDGE
UGS - The PLM Company

TITLE

SIZE A2 | DWG NO | REV

FILE NAME: base.sldprt

SCALE: | WEIGHT: | SHEET 1 OF 1

Appendix C
Oxidation of Circular Features

C.1 Introduction

The first attempt at a model for the thermal oxidation of circular silicon features was based purely on the differences in oxidation rates of the crystal planes. It was assumed that the rates at which the planes undercut the silicon were directly proportional to the rate of oxide growth. Thus by stripping and re-oxidising, it should be possible to recover the circular shape of the feature (see figure 3.4).

However, the amount of undercut is determined by the ratio of the volumes of the oxide grown and the silicon consumed. For a planar surface this ratio is 0.44. But for a circular feature, these volumes can differ for a given surface area, depending on the radius of the feature. This idea is illustrated in figure C.1.

Figure C.1: *The variation of oxide/silicon thickness with topography. (i) The ratio (b/(a+b)) of the thickness of the silicon consumed to the thickness of the oxide grown is given by the ratio of the volumes (B/(A+B)), and hence the ratio of the molar volumes of Si and SiO_2 (0.44). (ii) The ratio of the thicknesses (b/(a+b)) is not directly proportional to the ratio of the volumes (B/(A+B)) and hence $b/(a+b) < 0.44$.*

C.2 A New Model

Considering the entire circular feature to consist solely of one crystal plane, it is possible to calculate the relative thickness of the oxide and silicon layers for a given crystal plane (see figure C.2).

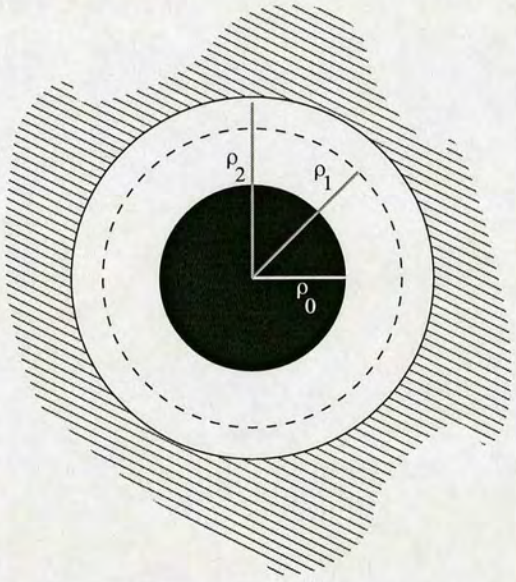

Figure C.2: *The different radii involved in oxidation. The starting radius of the silicon hole is designated ρ_1. The final inner and outer oxide radii are ρ_0 and ρ_2 respectively.*

It is apparent that the volume of silicon consumed must be equal to the volume of oxide grown multiplied by the ratio of the molecular densities of the two substances:

$$\pi\rho_2^2 - \pi\rho_1^2 = 0.44(\pi\rho_2^2 - \pi\rho_0^2) \tag{C.1}$$

Cancelling π from both sides and re-arranging gives:

$$\rho_1^2 = 0.44\rho_0^2 + 0.56\rho_2^2 \tag{C.2}$$

Equation C.2 describes, for a given crystal plane, the relationship between the starting silicon radius, the final silicon radius, and the final oxide inner radius. When oxidising a perpendicular feature in <100> silicon, The greatest disparity in oxidation rates is between the <100> and the <110> planes. Let equation C.2 represent the <110> plane, and a new set of radii, ρ_a

(inner) , ρ_b (starting) and ρ_c (outer) represent the <100> plane.

$$\pi\rho_c^2 - \pi\rho_b^2 = 0.44(\pi\rho_c^2 - \pi\rho_a^2) \tag{C.3}$$

$$\rho_b^2 = 0.44\rho_a^2 + 0.56\rho_c^2 \tag{C.4}$$

On a planar surface, the ratio of growth on the <100> plane to growth on the <110> plane is,

$$\frac{x_{100}}{x_{110}} = \sqrt{\frac{B_{100}}{B_{110}}}$$

As the thickness is radius dependent for the circular case, we will assume that this relationship applies to the ratio of volumes of oxide produced also.

$$\frac{V_{100}}{V_{110}} = \frac{\rho_c^2 - \rho_a^2}{\rho_2^2 - \rho_0^2} = \sqrt{\frac{B_{100}}{B_{110}}} \tag{C.5}$$

This allows us to determine a value for the <100> consumption (ρ_c), given the <110> undercut (ρ_2). Equating ρ_1 and ρ_b, and combining equations C.3 and C.5 we get,

$$\rho_1^2 = \rho_c^2 + 0.44\sqrt{\frac{B_{100}}{B_{110}}}(\rho_0^2 - \rho_2^2)$$

Comparing this with equation C.2 and eliminating terms in ρ_0 by substituting for equation C.2 yields,

$$\rho_c^2 = \rho_2^2\sqrt{\frac{B_{100}}{B_{110}}} + \rho_1^2(1 - \sqrt{\frac{B_{100}}{B_{110}}}) \tag{C.6}$$

This expression can be used to find a value for the silicon consumption radius. If we perform a double oxidation process (i.e. strip and then re-oxidise) the consumption radii, ρ_2 and ρ_c represent the starting radii for the second oxidation. The finishing inner radii are denoted ρ_3 and ρ_d. In analogy with equation C.5, we derive a relationship for the ratio of the volumes of oxide produced,

$$\frac{V_{100}}{V_{110}} = \frac{\rho_c^2 - \rho_d^2}{\rho_2^2 - \rho_3^2} = \sqrt{\frac{B_{100}}{B_{110}}} \tag{C.7}$$

Rearranging this equation we get,

$$\rho_3^2 - \rho_d^2 = \rho_2^2\sqrt{\frac{B_{100}}{B_{110}}} - \rho_c^2 - \rho_3^2(\sqrt{\frac{B_{100}}{B_{110}}} - 1)$$

Substituting for ρ_c^2 (equation C.6),

$$\rho_d^2 - \rho_3^2 = (\rho_3^2 - \rho_1^2)(\sqrt{\frac{B_{100}}{B_{110}}} - 1) \tag{C.8}$$

This can be used to determine the difference between the final inner radii (that of the oxide layer) of the different planes, given the starting radii of the first oxidation ρ_1 and the final inner radius of the second oxidation ρ_3. The aim should be to minimise this value. We can see that the right hand side of equation C.8 is equal to zero when $\rho_3 = \rho_1$ (the starting and finishing radii are coincident). The difficulty is in predicting the oxidation times to achieve the required thicknesses. Though attempts were made to verify this model experimentally, these failed due to poor repeatability of the measurements obtained from the tests. This may have been due to process variations, or more likely, to variability in the measurement process itself. Note that the model here assumes both oxidations are performed at one temperature. In reality better results may be achieved by performing the first oxidation at a lower temperature.

Appendix D
Planar Patch-Clamp Electronics

D.1 Introduction

This chapter discusses the challenges faced and the approaches taken to develop a recording system for planar patch clamp that is scalable across many recording sites. The approach taken is based around the circuits used in conventional, single cell patch clamp amplifiers, such as those supplied by Axon Instruments or Dagan, which are described in the Axon Guide [84] or 'Voltage Clamping with Microelectrodes' [106].

D.2 Scalability for multi-channel patch-clamp

Patch-clamp amplifiers generally have a small section of electronics (known as the 'headstage') remote from the main system, so that it can be positioned close to the source of the signal (the pipette) to achieve acceptable noise performance. In most cases this consists of an op-amp buffer and some passive components (such as a capacitor for capacitance neutralisation, and a resistor for delivering current).

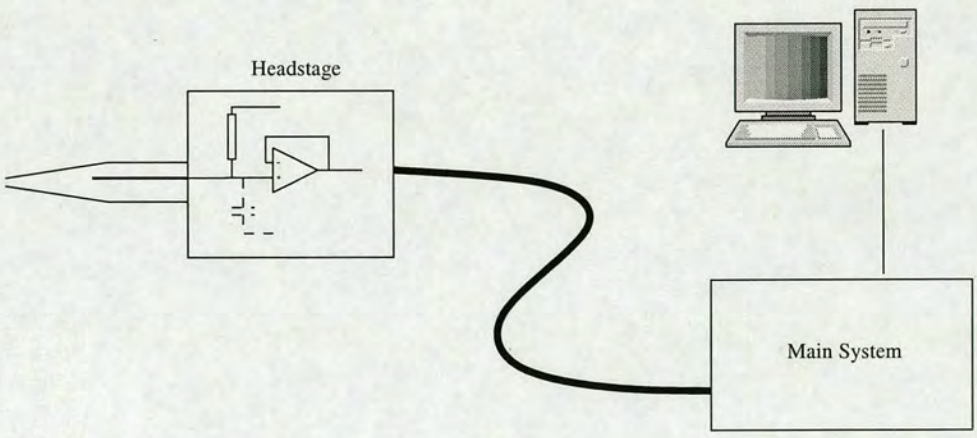

Figure D.1: *A typical patch-clamp system. The headstage is separate from the main unit to allow the headstage to be positioned in close proximity to the signal source.*

If one considers the practicality of constructing a multi-channel patch clamp system in which many (>20) headstages must be located close to the experimental set-up, it becomes apparent that VLSI integration is desirable for the headstages. For optimum noise performance it would be beneficial to integrate the headstages into the same substrate as the patch-clamp electrodes.[1].

In traditional patch-clamp systems, many components are trimmed (by hand) to achieve the required accuracy, making integration difficult. Therefore, the goal is to integrate as little of the electronics as possible, and to devise a method of trimming the circuit digitally.

The absolute minimum circuit which must be integrated is an operational amplifier (as a buffer or amplifier) to reduce the impedance of the signal source. Associated with this amplifier are an output offset voltage and input leakage current. In comercially available patch-clamp systems, the offset voltage is used to cancel out the input leakage current, by virtue of the fact that the current is derived from the buffer voltage (see figure D.2 for an explanation of the current source operation).

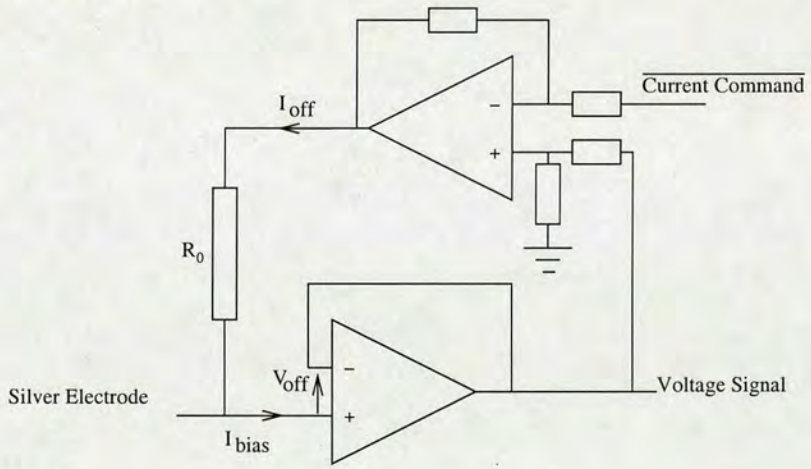

Figure D.2: *Headstage trimming in patch-clamp systems. The current into the electrode is controlled by setting the voltage across the resistor R_0. By trimming the voltage offset V_{off}, a current offset I_{off} is produced which cancels the input bias current of the amplifier I_{bias}.*

However, the fact that an integrated headstage current cannot be trimmed means that there will always be an offset current present on the output of the current source. This can be adjusted 'digitally' - compensated for by adding an offset to the current command - so that the offset always equals the bias current.

[1]The technical details of doing this are somewhat complicated and are not discussed here

D.3 Digital trimming with a micro-controller

The simplest way of digitally trimming the headstage is to connect the headstage output directly to an analogue-to-digital converter, and to connect a digital-to-analogue converter directly to the input of the current source. This is acceptable for bridge-mode (assuming some voltage gain is included to boost the signal before conversion). Post processing, such as bridge balance could be performed digitally. Trimming could also be performed by computer, after presenting the electrode input with a known value.

The problem with this approach is obviously voltage-clamp. Having digital control of the current source excludes the possibility of applying analogue feedback. However, if one is prepared to omit the continuous voltage clamp mode, and instead use only the discontinuous version, it becomes theoretically possible to implement the feedback digitally.

Figure D.3 shows a patch clamp headstage with a microcontroller providing digital feedback.

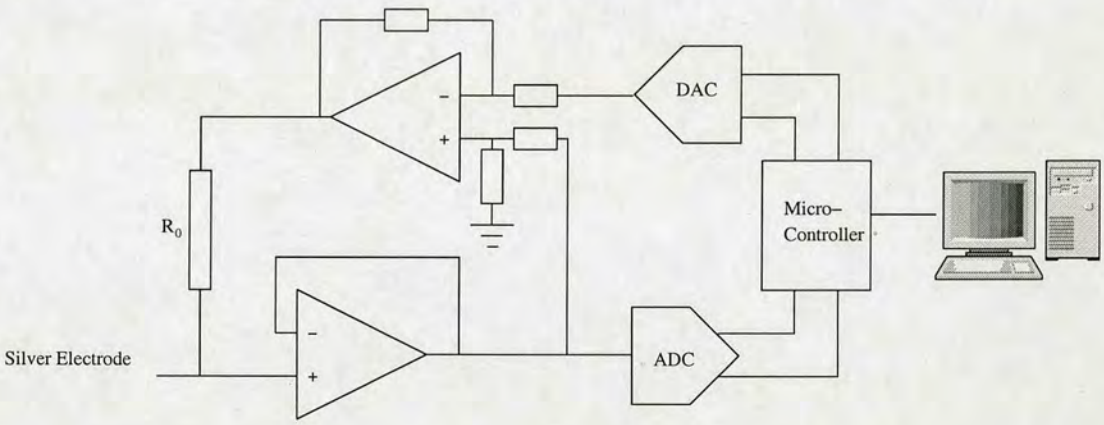

Figure D.3: *Voltage-clamp with digital feedback.*

D.4 Conversion time issues for discontinuous voltage clamp

However, using digital feedback presents other problems. The time required for both A-D and D-A conversions could cause stability problems if it is significant compared to the sampling period. The problem arises because a large conversion time does not allow the electrode to discharge fully before conversion begins, introducing a voltage error (see figure D.4). This error, in addition to changing the voltage at which the cell is clamped, could cause stability

problems.

The stability analysis of the discontinuous voltage-clamp given by Finkel and Redman [107] takes no account of the voltage error introduced by the electrode (in order to simplify the calculation) and the calculation becomes intractable if this error is included. In order to solve this problem, a z-transform method can be used.

The discontinuous voltage clamp circuit is redrawn as a discrete time system in figure D.5.

Following Finkel and Redman, the membrane voltage in one cycle is related to that in a previous cycle by:

$$V_m(n) = V_m(n-1)e^{-\alpha} + i(n)R_N(1 - e^{-D\alpha})e^{-(1-D)\alpha}$$

where T is the sampling period, D is the duty cycle ($0 < D < 1$) and R_N, C_N are the cell membrane resistance and capacitance. $\alpha = \frac{T}{R_N C_N}$ is the cell membrane time-constant.

Taking a z-transform of both sides:

$$V_m(z) = z^{-1}V_m(z)e^{-\alpha} + i(z)R_N(1 - e^{-D\alpha})e^{-(1-D)\alpha}$$

Rearranging gives,

$$V_m(z) = \frac{i(z)R_N(1 - e^{-D\alpha})e^{-(1-D)\alpha}}{1 - z^{-1}e^{-\alpha}} \tag{D.1}$$

Similarly, for the electrode voltage,

$$V_e(z) = \frac{i(z)R_E(1 - e^{-DT_1})e^{-(1-D)T_1}}{1 - z^{-1}e^{-T_1}} \tag{D.2}$$

$T_1 = \frac{T}{R_e C_e}$ is the electrode time constant. Equations D.2 and D.1 are simplified by substituting $\rho_N = R_N(1 - e^{-D\alpha})e^{-(1-D)\alpha}$ and $\rho_E = R_E(1 - e^{-DT_1})e^{-(1-D)T_1}$.

$$V_e(z) = \frac{i(z)\rho_E}{1 - z^{-1}e^{-T_1}}, V_m(z) = \frac{i(z)\rho_N}{1 - z^{-1}e^{-\alpha}} \tag{D.3}$$

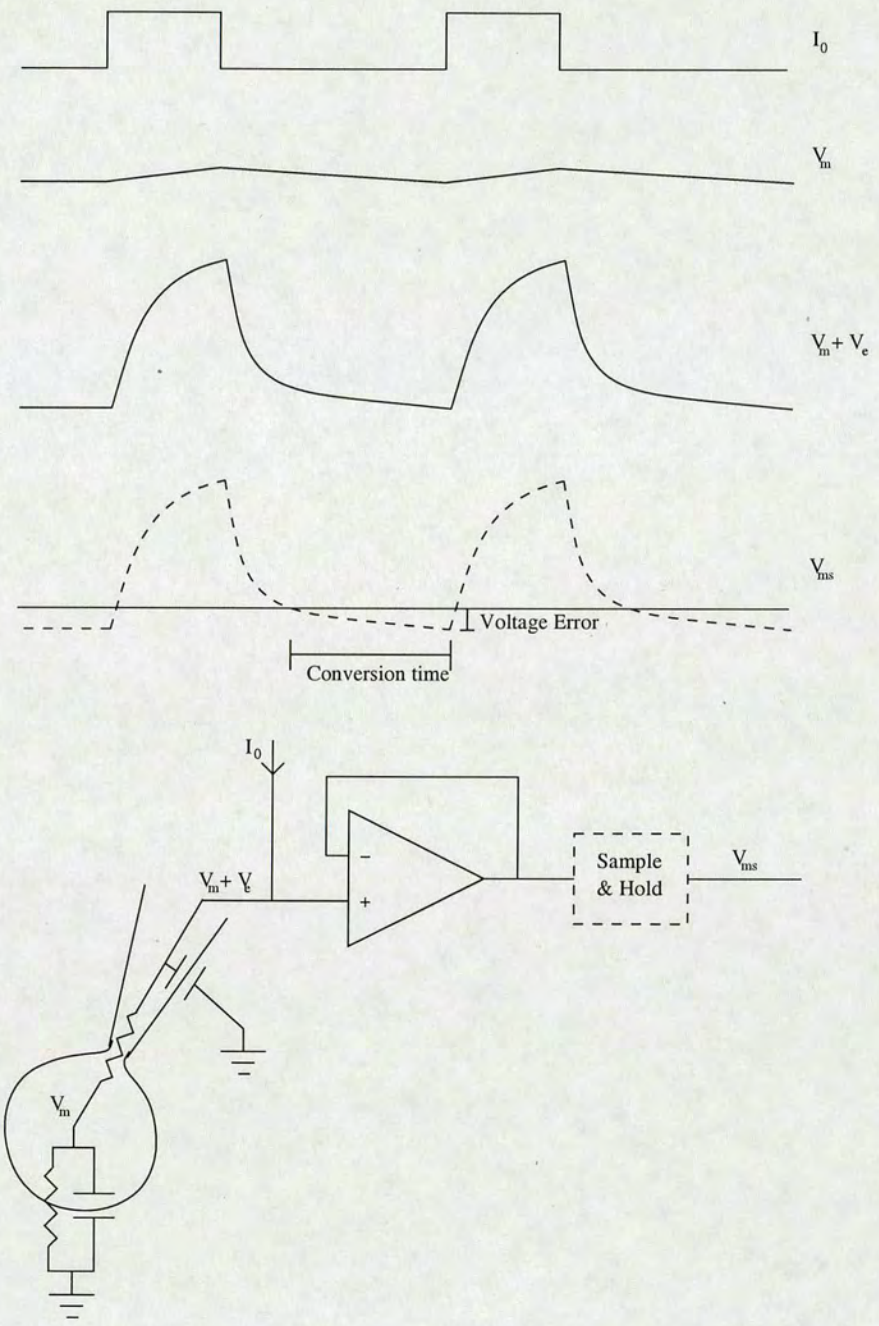

Figure D.4: *Signal traces for discontinuous voltage clamp. The impedance of the electrode adds a voltage error to the membrane voltage measured by the amplifier. The sampling period is made sufficiently long to allow the electrode time to discharge before sampling occurs. However, a significantly large A-D conversion time reduces the time available for the electrode discharge. Hence, the voltage error in the signal increases exponentially with conversion time.*

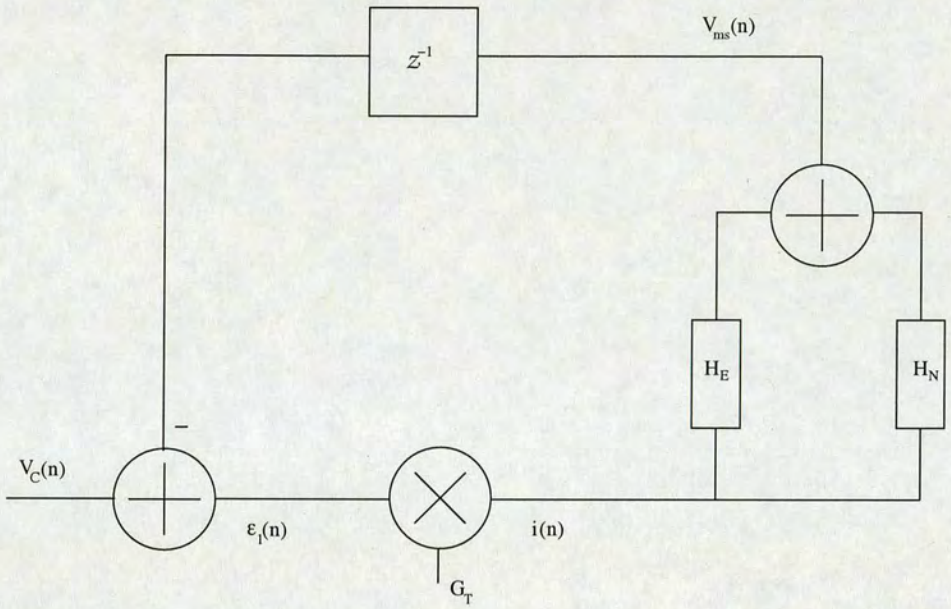

Figure D.5: *Discontinuous voltage clamp as a discrete time system. H_N and H_E represent the impedances of the cell and electrode respectively. $\epsilon_1(n)$ is the voltage error between the sampled signal and the voltage command.*

Equations D.1 and D.2 give expressions for H_N and H_E. Examining the circuit as a whole, the error voltage ϵ_1 is given by:

$$\epsilon_1(n) = V_c(n) - V_{ms}(n-1)$$

Taking a z-transform of both sides:

$$\epsilon_1(z) = V_c(z) - z^{-1}V_{ms}(z)$$

$$\epsilon_1(z) = V_c(z) - z^{-1}(V_m(z) + V_e(z)) \tag{D.4}$$

Now,

$$i(z) = G_T\epsilon_1$$

Substituting equation D.4,

$$i(z) = G_T(V_c(z) - z^{-1}(V_m(z) + V_e(z))) \tag{D.5}$$

Rearranging gives,

$$z(V_c(z) - \frac{i(z)}{G_T}) = V_m(z) + V_e(z)$$

Substituting in the results from equation D.3 we get,

$$\frac{V_c(z)}{i(z)} = \frac{1}{G_T} + \frac{\rho_N}{z - e^{-\alpha}} + \frac{\rho_E}{z - e^{-T_1}} \tag{D.6}$$

To analyse the stability of the whole system, we need an expression for $H(z) = \frac{V_m(z)}{V_c(z)}$:

$$\frac{V_m(z)}{V_c(z)} = \frac{i(z)}{V_c(z)} \frac{V_m(z)}{i(z)}$$

Inserting equations D.6 and D.1,

$$H(z) = \frac{\frac{z\rho_N}{z-e^{-\alpha}}}{\frac{1}{G_T} + \frac{\rho_N}{z-e^{-\alpha}} + \frac{\rho_E}{z-e^{-T_1}}}$$

Multiplying top and bottom by $(z - e^{-T_1})(z - e^{-\alpha})$,

$$H(z) = \frac{(z - e^{-T_1})z\rho_N}{\frac{1}{G_T}(z - e^{-\alpha})(z - e^{-T_1}) + (z - e^{-T_1})\rho_N + (z - e^{-\alpha})\rho_E}$$

Grouping z terms on the bottom,

$$H(z) = \frac{(z - e^{-T_1})z\rho_N}{\frac{1}{G_T}z^2 + z(\rho_N + \rho_E - \frac{(e^{-T_1}+e^{-\alpha})}{G_T}) + \frac{e^{-\alpha}e^{-T_1}}{G_T} - \rho_E e^{-\alpha} - \rho_N e^{-T_1}} \tag{D.7}$$

Now, a system will be stable if all of its poles lie within the unit circle on the z-plane,

$$|p_n| < 1 \qquad \forall \quad n$$

The poles of equation D.7 can be derived by finding the roots of the quadratic equation (in z) on the bottom line.

$$z = \frac{-b \pm \sqrt{b^2 - 4ac}}{2a}$$

$$a = 1$$

$$b = G_T\rho_E + G_T\rho_N - e^{-\alpha} - e^{-T_1}$$

$$c = e^{-T_1}e^{-\alpha} - G_T\rho_E e^{-\alpha} - G_T\rho_N e^{-T_1}$$

$$p_{+,-} = \frac{-b \pm \sqrt{b^2 - 4ac}}{2a}$$

$$b^2 = G_T^2(\rho_E + \rho_N)^2 + (e^{-\alpha} + e^{-T_1})^2 - 2G_T(\rho_E + \rho_N)(e^{-\alpha} + e^{-T_1})$$

$$= G_T^2(\rho_E^2+\rho_N^2+2\rho_N\rho_E)+e^{-2\alpha}+e^{-2T_1}+2e^{-\alpha}e^{-T_1}-2G_T(\rho_E e^{-\alpha}+\rho_N e^{-\alpha}+\rho_N e^{-T_1}+\rho_E e^{-T_1})$$

$$4ac = 4e^{-T_1}e^{-\alpha} - 4G_T\rho_E e^{-\alpha} - 4G_T\rho_N e^{-T_1}$$

Cancelling like terms,

$$b^2 - 4ac =$$

$$G_T^2(\rho_E^2+\rho_N^2+2\rho_N\rho_E)+e^{-2\alpha}+e^{-2T_1}-2e^{-\alpha}e^{-T_1}+2G_T(\rho_E e^{-\alpha}-\rho_N e^{-\alpha}+\rho_N e^{-T_1}-\rho_E e^{-T_1})$$

$$b^2 - 4ac = G_T^2(\rho_E + \rho_N)^2 + (e^{-\alpha} - e^{-T_1})^2 + 2G_T(\rho_E - \rho_N)(e^{-\alpha} - e^{-T_1})$$

Thus, the zeros are given by,

$$p_{+,-} =$$

$$\frac{-G_T(\rho_E + \rho_N) + e^{-\alpha} + e^{-T_1} \pm \sqrt{G_T^2(\rho_E + \rho_N)^2 + (e^{-\alpha} - e^{-T_1})^2 + 2G_T(\rho_E - \rho_N)(e^{-\alpha} - e^{-T_1})}}{2}$$

Adopting the approximation made by Finkel and Redman, that is, that there is no electrode artifact, $e^{-T_1} = 0 \Rightarrow \rho_E = 0$:

$$p_{+,-} = \frac{-G_T\rho_N + e^{-\alpha} \pm \sqrt{G_T^2\rho_N^2 + e^{-2\alpha} - 2G_T\rho_N e^{-\alpha}}}{2}$$

$$p_{+,-} = \frac{-G_T\rho_N + e^{-\alpha} \pm \sqrt{(-G_T\rho_N + e^{-\alpha})^2}}{2}$$

$$p_- = 0$$

$$p_+ = -G_T\rho_N + e^{-\alpha}$$

$$p_+ = -G_T R_N(1 - e^{-D\alpha})e^{-(1-D)\alpha} + e^{-\alpha}$$

$$p_+ = e^{-\alpha}(1 - G_T R_N(e^{D\alpha} - 1))$$

Assuming that $\alpha << 1$ and thus $e^{\alpha} \simeq 1 + \alpha$

$$p_+ = (1 - \alpha)(1 - G_T R_N D\alpha)$$

$$p_+ = 1 - G_T R_N D\alpha$$

Thus the stability criterion becomes:

$$-1 < 1 - G_T R_N D\alpha < 1$$

$$2 > G_T R_N D\alpha > 0$$

$$2 > \frac{G_T DT}{C_N} > 0$$

Which is the result obtained by Finkel and Redman.

Appendix E

Paper under review: Fabrication and Characterisation of a Silicon Planar Patch-Clamp Microstructure

Fabrication and Characterisation of a Silicon Planar Patch-Clamp Microstructure

Brad Dworak, Keith Baldwin, John Curtis, Alan Gundlach, Tom Stevenson, Leslie I. Haworth, Anthony J. Snell, Anthony J. Walton, Nikki K. MacLeod and Alan F. Murray

Abstract— **This paper presents a microfabricated planar patch-clamp electrode designed for integration into a 'patch array'. The device consists of a 2-μm patch aperture approximately 8 μm deep with a reverse-side deep-etched 80-μm well. The small footprint of this electrode will allow for integration into an array. The patch aperture profile has been smoothed by PECVD oxide deposition (radius of curvature = 0.47-0.71 μm) and the oxide surface roughness (R_a=3.12 nm) reduced by boron doping (R_a=2.14 nm). The electrical characteristics of the device are favourable in comparison with glass pipettes (R_{mean} = 1.37 MΩ, τ_{mean} = 0.073 ms). Transient seals on isolated snail neurons of up to 600MΩ have been achieved, but the lack of recorded electrical activity makes verification as a genuine cell attached patch difficult.**

Index Terms— **patch-clamp, microstructure, MEMS, neuron**

I. Introduction

Studies of ionic conduction of nerve cells, particularly the pioneering work of Hodgkin, Huxley and Katz, have greatly advanced the understanding of the ionic nature of neuronal function [1]–[4]. Many studies of neuronal activity and network behaviour use conductive electrodes to detect individual electrical signals. Typically this is carried out *in vivo* or in acute *in vitro* preparations such as brain slices. Advances in cell culturing and MEA fabrication have however provided an additional pathway to the detailed study of living neuronal networks [5]–[7]. To date, many attempts to investigate *in-vitro* network activity involve multiple planar surface electrodes to link electrical connections to nerve cells, coupled resistively or capacitively to the neuron for extracellular measurements [8].

MEA devices made with up to 60 electrodes or more offer a significant bandwidth of data extraction to distinguish network behaviour (e.g. circadian rhythms and differentiating firing patterns in dissociated cell cultures of hippocampal neurons) [9], [10]. Also, under certain conditions long-term neurological studies can be conducted for periods of up to several months [11]. However, the extracellular nature of these recordings make it difficult to map and isolate single synaptic events to individual cells and synapses. Typically, only spiking events are detected and counted. Other evidence suggests that this approach has limitations regarding cell/substrate adhesion and the proximity between the cell and electrode [12]. Furthermore, it has been suggested that neurons do not form ion channels well along the contact surface, decreasing the quality of electrode recordings [13].

An intracellular recording approach has two main advantages over extracellular recordings; the certainty with which one can associate recorded activity with a single particular neuron, and the ability to study not only spiking activity but the behaviour of sub-threshold events that integrate and determine the spiking activity of the network under study. Indeed the importance of sub-threshold activity to the output of a network is becoming increasingly clear. The measured biophysical properties of a neuron in isolation or in a low activity deafferented *in-vitro* preparation (brain slice) may not represent that found *in vivo*. Here there is a constant barrage of EPSP's and IPSP's resulting in a network activity dependent fluctuation of membrane resistance and membrane potential [14]. With this in mind attempts have been made to assess the biophysical properties of neurones more accurately by injecting them with computer simulated network activity modelled noise [15]. A multi-electrode patch study of a neuronal network would therefore provide an insight into the interaction between spike output and sub-threshold activity and also how components of the network interact to produce any given level of sub-threshold activity.

The technique of intracellular recording was introduced to neuroscience in the 1950s with the development of the sharp microelectrode by Sir John Eccles [16]. The Patch-clamp technique was introduced in the cell attached form in 1976 by Neher and Sakmann [17] and then extended to the intracellular whole cell form in the 1980's [18]. The giga-ohm seal between cell and glass electrode that the patch technique introduced and the typically low resistance electrodes used, improved the signal to noise ratio and therefore the resolution of intracellular recordings. The giga-ohm seal also reduces artefacts associated with membrane damage around the penetration site of sharp electrode recordings [19]. The patch method of intracellular recording is thus favourable especially when small sub-threshold events are of particular interest.

Extending the use of intracellular techniques to networks of neurons has inherent limitations. Generally, examining the neuronal activity of multiple patch clamped neurons is not an easy task. Manoeuvring patch-pipettes is difficult because the positioning devices are bulky and are sensitive to vibration from the surrounding environment. To date, up to three neurons have been recorded simultaneously using conventional

sharp or patch micropipette recordings to study synaptic transmission [20]. The development of a multi-electrode planar patch device would therefore have significant impact on the study of neuronal interaction, signal integration and the formation of coherent behaviour in neuronal networks.

In recent years, attempts have been made to develop patch-clamp devices using microfabrication technology. Micro-fabricated patch electrodes (generally called planar-patch electrodes) have been produced since the year 2000. In 2000 Fertig et al [21] used a 0.12μm thick silicon nitride membrane to stabilize an excised patch of rat striatal neuron for study with scanning probe microscopy techniques. This was achieved but no attempts at electrophysiological recordings were reported. Also, in 2000 Schmidt et al [22] used a silicon nitride membrane, the surface of which had been modified with poly-L-lysine and were able to obtain giga-ohm seals with giant lipid vesicles. Fertig et al have gone on to use glass and quartz based planar devices to achieve giga ohm seals in lipid bilayers [23], cell attached single channel recordings with giga-ohm seals [24] and whole cell recordings in Chinese hamster ovary and neuroblastoma cells (although seal resistances were not reported for this data) [25]. The Sigworth lab have also reported giga-ohm seal formation and cell attached current recordings from Xenopus oocytes using a PDMS based planar device [26]. The development of a silicon oxide based planar device has been reported by Matthews and Judy [27], although no seal or cell recording attempts have been made. The last few years however has seen the emergence of several commercial automated patching robots based on a planar patch design developed for the high throughput drug screening market [28]. Many of these groups have reported success in the production of working planar patch devices. Molecular Devices have developed the Ion Works system which uses a perforated patch approach and the Seal Chip system from Aviva Biosciences that uses a chemically modified glass substrate device. A silicon based 'Q-patch' device in combination with a microfluidics system for rapid fluid exchange has been developed by Sophion Biosciences.

The long term aim of this group is the production of a multi electrode planar patch array that will facilitate intracellular recording from multiple connected neurons to further the analysis of neuronal interaction and network behaviour. The first step in this process is to design a protocol to produce a functional patch aperture. The final patch aperture and reverse side aperture should have the characteristics described below. The patch aperture should be of the appropriate shape and dimensions and should have sufficient depth to allow a large enough area of membrane/silicon apposition to facilitate seal formation. The cell side of the aperture should have a profile conducive to seal formation i.e smooth and clean with no sharp edges. The fabrication must be reliably repeatable and the dimensions of any features should be compatible with the eventual aim of the design of an array of such features. Finally the electrical characteristics of the aperture and associated reverse side features should have electrical characteristics compatible with recording neuronal electrical activity without signal distortion or loss of information.

II. Materials and Methods

A. *Patch Device Fabrication*

BESOI (bonded and etched back silicon on insulator) 100-mm wafers (Virginia Semiconductor Inc.) were used for device fabrication. They consisted of prime grade n-type (phosphorous doped) silicon of <100> orientation; polished silicon on both sides; a buried oxide (insulation) layer 1.3 μm thick; a handle wafer thickness of 500±25 μm; and a measured device layer 8±3 μm thick. Before and after each process step, the wafers were routinely inspected, air blown and rinsed in distilled water. The fabrication process is listed below and shown in fig 1.

1. Wet thermal oxidation at 1100 °C for 150 min to grow a 1-μm oxide layer.
2. Photoresist coat front-side and expose 1.5 μm diameter patch-clamp aperture using a 5x reduction Optimetrix© stepper. Post exposure bake and develop. RIE etch to remove the top side oxide, ash photoresist. Recoat with photoresist and print scribe marks around the holes using a MicroTec© Karl SUSS MA8 mask aligner. RIE etch to remove the top side oxide, ash photoresist; Deep-silicon etch using an STS© Multiplex inductively coupled plasma (ICP) etcher.
3. Thick photoresist (Shipley© HPR206) coat on bottom side, resulting in a uniform thickness of 3.2 μm. Alignment of the top side apertures and bottom side 80 μm square features by back side alignment using Karl SUSS mask aligner. Develop and hard-bake. RIE to remove bottom oxide. Deep-silicon bottom side etch using the sandwiched oxide as a stop layer; ash to remove photoresist.
4. Dip in 48% HF, 0.01% Triton™ X-100 solution for 1 min to remove the exposed buried oxide layer and the thermal oxide from the complete wafer.
5. Thermal oxidation (1 μm) and immediate stripping using the above HF/Triton solution for 2 min. Thermal oxide re-grown to 1 μm.
6. Front-side oxide deposition using an STS Plasma-Enhanced-Chemical-Vapour-Deposition (PECVD) system.

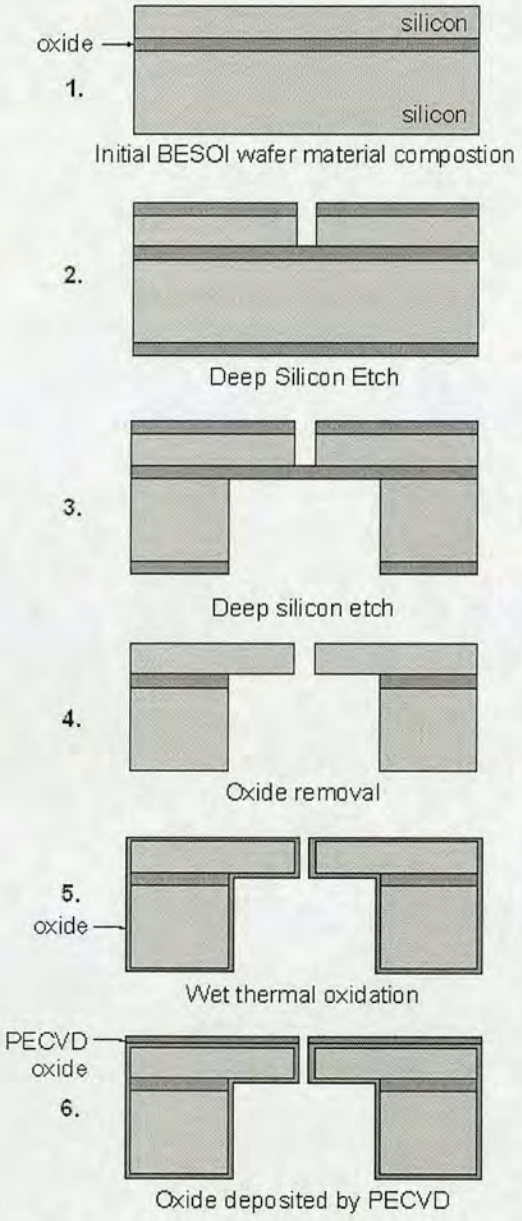

Fig. 1: Cross-section pictorial representation of the process fabrication steps.

As part of the post-process development, the wafer was quartered to test the effects of different surface modifications on PECVD oxide. These modifications were carried out in order to look for effects on surface roughness or cell/surface interaction that may improve seal formation (i.e. creating a surface more akin to borosilicate glass). The four different surfaces tested were: untreated (no modification), annealed (1000 °C, 30 mins), solid source boron doped (800 °C, 30mins) and solid source boron doped (1000 °C 30 mins). The surface modification steps were carried out in Tempress© furnace tubes with a constant N_2 flow of a 1000 sccm.

The wafers were diamond-scribed and snapped by hand into 7 mm square chips, each containing a single device. To reduce the capacitance of the device, the bottom side of each device was hand painted with PDMS. An area of approximately 1 mm diameter was left uncoated around the cavity to prevent the PDMS from creeping into the aperture. The devices were cured in an oven for 2.5 hours at 85 °C.

For the final post-processing step, device chips were fixed into a perspex base frame with PDMS (see section on platform design).

After curing, in order to remove any remaining silicon dust and fragments, frames were cleaned with deionised water and IPA in a Marangoni drier. The individual frames were stored in dust-free containers until use.

B. AFM Analysis

Surface roughness may have a considerable impact on seal formation during patch-clamping. Thus, the surface roughness of ten devices was studied. An atomic force microscope (AFM) Digital Instruments™ D5000 in Tapping Mode was used with a high-aspect-ratio tip (Nanosensors© part no. AR5-NCHR). A 4-μm square area was profiled, with the aperture positioned in the centre. The scans were recorded at 0.3 Hz and 256 lines/scan. The mean roughness (R_a) was measured by averaging the values of four 100,000±15,000-nm^2 areas in each corner of the scan in close proximity to the aperture.

The curvature of the aperture profile was also examined using the AFM data mentioned above. A typical trace can be seen in fig 5. The radius of curvature for each point was calculated as derivative of tangential angle with respect to arc length [29].

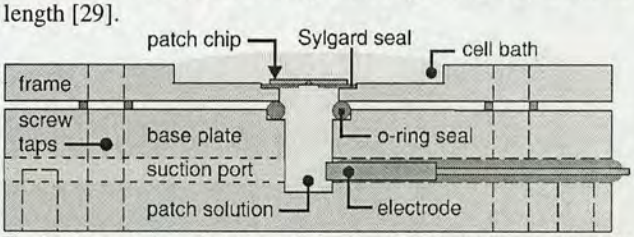

Fig. 2: Cross section of platform designed and fabricated to accommodate patch-clamp devices during recording.

C. Platform Design and Construction

A platform (illustrated in Fig. 2) was designed to hold each device during recording. The platform consisted of a 51mm square base, 10 mm thick. A port was bored into the device allowing an external suction line to be attached on the side. A similar port was added to allow the location of an AgCl electrode. An O-ring was inserted around the patch solution well to create a seal between the well and the device.

To allow the devices to be attached to the platform, they were mounted on Perspex frames, which could be easily located on screws protruding from the platform. To fill the devices, the entire device (plus Perspex frame) was submerged in filtered patch solution in a vacuum jar. The chamber pressure was then lowered to ≤35 mTorr, past the point at which the solution boils. During this process, the chamber was subjected to mechanical vibration to drive out air bubbles. After a few minutes, the device was removed and placed on the Perspex base plate. A bath plate was positioned on top of

the device frame and the whole ensemble was screwed together, creating a seal between the device frame and the O-ring.

D. Device Electrical Characterisation

The device under test was connected to an Axoclamp-2B current and voltage clamp amplifier (Axon Instruments). Input and output signals were monitored and controlled using Axoscope and Pclamp (Axon Instruments) software on a computer via a Digidata 1320B (Axon Instruments) A/D converter. The device characteristics were compared to glass pipettes (filled with the same intracellular solution) that had inner tip diameters matching those of the device apertures. The DC current-voltage characteristics of the devices were measured by passing current pulses of increasing magnitude (-10 nA to +10 nA). The resistance was calculated by performing a linear fit on this data and measuring the gradient. By measuring the relaxation response to the current pulses, it was also possible to estimate the time-constant, and hence the capacitance.

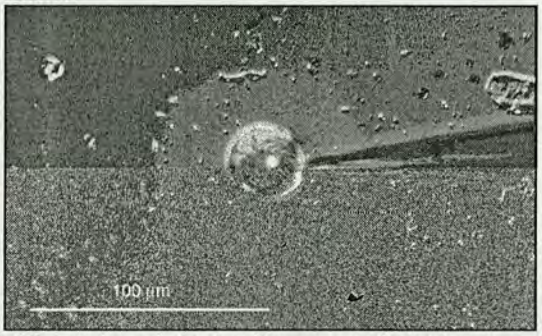

Fig. 3: Manoeuvring an isolated snail neuron onto the patch aperture. Scale bar = 100 µm. The soma diameter is approximately 35 µm. Transmission microscopy allows the backside cavity walls (85-µm square) to be dimly lit; the aperture is indicated by the bright light shining from underneath the device.

E. Snail Neuron Preparation

Attempts at obtaining gigaohm seals and patch clamp recordings with the devices were made using acutely isolated neurons from pond snails (*Lymnaea stagnalis*). Snails were purchased from Blades Biological (Kent) and were maintained in an aquarium containing mineral salt supplemented water [30]. Snails were feed *ad libitum* with lettuce. Neurons were isolated using a dissociation method based on the method described for Aplysia neurons [31], [32].

Following dissociation, neuron viability was checked by adding 20 µl of a 10 mM stock solution of Cell Tracker™ (Molecular Probes©) to 300 µl of dissociated neurons. The solution was left for 1 hr to allow for tracker diffusion. The suspension was centrifuged at 1000 g for 10 s. For purposes of recording, approximately 25 µl of cell suspension was added to either a 35-mm Petri dish or the frontside of a device. The neurons were allowed to settle for 5-10 min. After settling, 1-5 ml of additional extracellular solution was added to the cell-bath of the device platform.

Using an epi-fluorescence microscope (Olympus BX50W1), cell tracker green labeled neurons could be easily visualised. A neuron was positioned on the device aperture using a 5-10 µm diameter fire-polished glass pipette (see fig 3). Suction was then applied to the patch-clamp device in order to facilitate seal formation.

III. Results

A. Physical Device Properties

Initial evaluation of the physical structure of the device was performed by sectioning the membrane with a focussed ion beam microscope (FIB). Fig 4 shows an image of this cross section taken with the FIB at 45°. The V-groove visible on the bottom of the aperture is due to over etching of the aperture from top side deep silicon etching. The aperture opening, as well as the thermal oxide layer (dark inside band) and PECVD oxide layer (outside band) are all clearly visible. The black empty space below the aperture is the bottom side cavity.

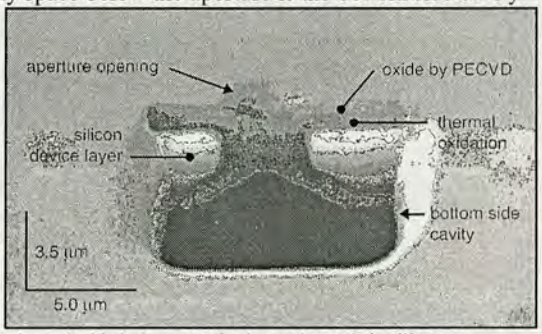

Fig. 4: An embedded planar patch-clamp electrode in silicon.

The mechanical structure of the devices is very stable (i.e., they withstand the mechanical stresses associated with solution filling and attempts to patch cells). The microfabrication yield of the devices was generally acceptable (4-5% failure rate for PECVD untreated, 1000 °C anneal, 800 °C boron deposition). However, 25% of the devices subjected to boron deposition at 1000 °C had defective apertures. Defects included notches and shards around the aperture walls.

The mean aperture diameter of 25 completed devices measured from scanning electron micrographs was 1.99 µm ± 0.131 S.D.

Table 1 shows the measurements obtained from the AFM analysis.

TABLE 1: MEAN ROUGHNESS RA (AND STANDARD DEVIATION) AND MINIMUM RADIUS OF CURVATURE RMIN FOR 10 DEVICES.

Device	Group	R_a (nm)	Std. Dev.	r_{min} (µm)
1	Control	2.649	0.577	0.58
2	Control	3.595	1.405	0.49
3	800°C Boron	1.848	0.378	0.47
4	800°C Boron	2.428	0.154	0.70
5	1000°C Boron	5.781	5.771	0.54
6	1000°C Boron	4.583	1.560	0.65
7	1000°C Boron	3.125	1.051	0.85
8	1000°C anneal	5.911	3.971	0.73
9	1000°C anneal	3.231	0.761	0.63
10	1000°C anneal	7.439	2.692	0.71

The mean surface roughness values (R_a) of ten devices consisting of four measurements per device are given in the third column. The roughness of the PECVD oxide surface ranged from 7.5 nm to 1.8 nm. Even the low value of 1.8 nm following boron treatment is considerably greater than that of borosilicate glass (Ra ~0.15 nm), which may make seal formation less likely. Analysis of the raw data underlying the device surface roughness means, indicates that the boron doping at 800 °C significantly smoothes the PECVD surface (control surface 3.12±0.39 nm, 800 °C boron doped surface 2.14±0.145 nm, n=8, t-test P=0.034). However, the treatments at 1000 °C do not show this effect and although not significant, show a trend towards producing slightly roughened surfaces. In addition, the 1000 °C boron treated quarter wafer showed a greater number of defects than any other quarter suggesting some deleterious effect of this treatment. Further studies on unprocessed silicon surfaces however show that 1000 °C boron treatment smoothes the surface relative to untreated PECVD (data not shown, manuscript in preparation). The high roughness values of the boron doped devices may therefore be related to device fabrication steps.

Table 1 also shows minimum radius of curvature values for the different devices (r_{min}), these range from 0.47-0.71 μm. Fig 5 shows typical AFM scans and the cross sectional profile of apertures at two stages of the fabrication process. The lower trace and micrograph show an aperture profile following the thermal oxidation (step 5 in fig 1). The characteristic dishing of the aperture caused by non-uniform growth of oxide can clearly be seen. The upper trace shows the aperture profile following the final PECVD deposition step. Clearly the oxide vapour deposition has a dramatic effect and produces a smooth profile that is theoretically advantageous for seal formation.

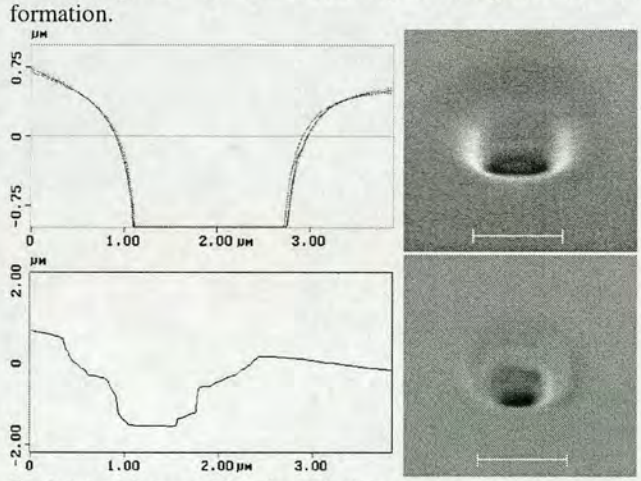

Fig. 5: A typical cross-section of a patch-clamp aperture. Top, a hole covered with PECVD oxide; Bottom, a hole that has been thermally oxidised.

B. Patch Device Electrical Characteristics

The resistance characteristics of 2 out of the 6 devices tested are plotted in fig 6. It can be seen that the current voltage relationship is linear over the current passing range shown, which was true for all devices tested. This range was chosen so as to be well within the required limits for typical experimental neuronal current injection.

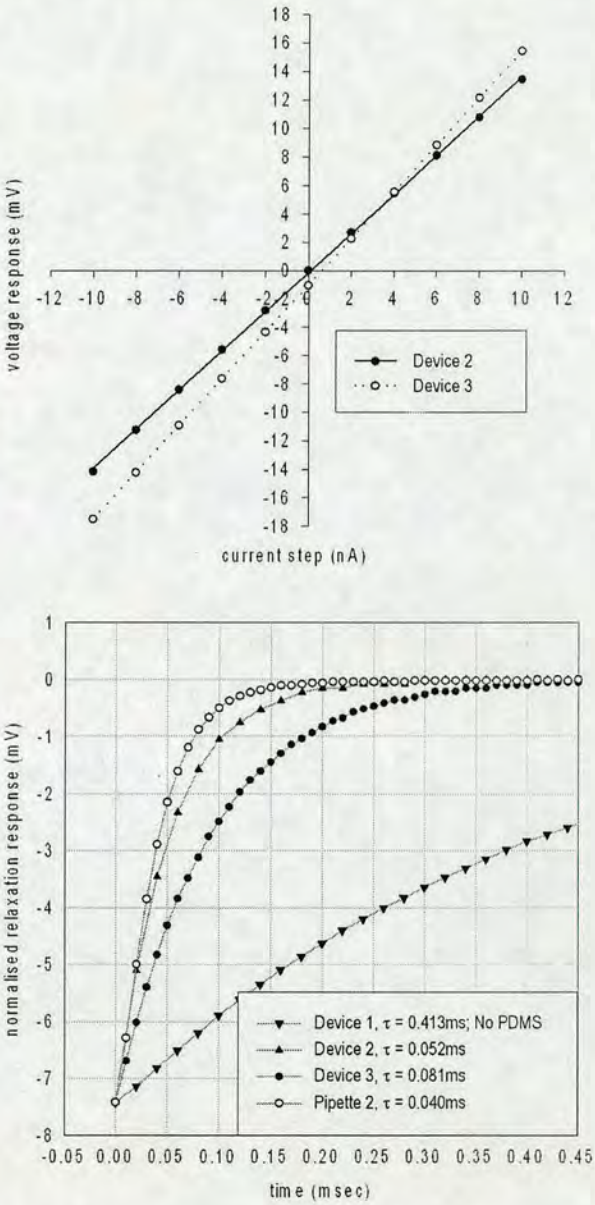

Fig. 6: Top: I-V plots for devices 2 and 3 showing a linear relationship for the tested current range of ±10 nA. Bottom: Relaxation responses for several device examples compared to conventional glass pipettes. The stimulus was a 5-nA inward current step.

Fig 6 (bottom) shows the relaxation responses of various devices and pipettes. Device 1 had no PDMS backside coating. The high τ value obtained for this device illustrates the obvious need to insulate the underside of the silicon from the ionic solution forming the conductive pathway from the device aperture to the silver chloride electrode in the base unit. The other devices show relaxation responses much closer to

those obtained with non-coated borosilicate glass patch pipettes. The values associated with the devices are still higher and more variable than those obtained with glass pipettes.

Table 2 summarises the electrical characteristics data. Although the resistance of each device compares favourably with those of glass pipettes of a similar bore, the capacitance, and hence the time constant, is significantly greater.

TABLE 2: ELECTRICAL PARAMETERS FOR THE DEVICES AND PIPETTES. THE TIME CONSTANT (TAU), RESISTANCE, CAPACITANCE AND CUT-OFF FREQUENCIES (FC=1/2πτ) ARE INCLUDED. C IS MEASURED FROM THE RELAXATION RESPONSES, AND FC IS CALCULATED USING THIS VALUE. THE VALUES FOR DEVICE 1 (NO PDMS) WERE OMITTED WHEN CALCULATING THE MEAN VALUES.

Electrode	τ (ms)	R (MΩ)	C (pF)	f_C (Hz)
Device 1	0.41	2.53	163.	385
Device 2	0.05	1.38	37.7	306
Device 3	0.08	1.65	55.4	196
Device 4	0.08	0.95	84.2	198
Device 5	0.05	1.40	40.8	279
Device 6	0.09	1.48	62.7	171
Mean	0.07	1.37	56.2	230
Std. dev.	0.01	0.26	18.8	587
Pipette 1	0.04	4.14	10.5	370
Pipette 2	0.04	3.73	10.7	397
Pipette 3	0.03	3.63	10.9	430
Mean	0.04	3.83	10.7	399
Std. dev.	0.00	0.2	0.2	300

The equivalent electrical circuit is useful in explaining the electrical characteristics of the devices, and how to improve them. The equivalent circuit diagram is shown in fig 7.

The component values can be calculated from the material parameters. Taking the resistivity of patch solution to be 510 k□·μm,

$$R_S = \frac{\rho L}{A_{conduction}} = \frac{(510\times10^3\Omega\cdot\mu m)(500\mu m)}{(80\mu m)^2} = 40k\Omega \quad \ldots 1$$

$$R_S = \frac{\rho L}{A_{conduction}} = \frac{(510\times10^3\Omega\cdot\mu m)(8\pm3\mu m)}{\pi(1\mu m)^2} = 1.3\pm0.49M\Omega$$

... 2

Hence, the shank resistance R_S can be neglected from the model, and the resistance of the device can be represented by R_A alone. This agrees with the experimental values given in table 2.

Similarly, the capacitance values can be calculated, assuming ε_r for SiO_2 = 3.9,

$$C_T = \frac{\varepsilon_0\varepsilon_r A}{d} = 850pF$$
$$C_A = 0.0017pF$$
$$C_B = 0.22pF \qquad \ldots 3$$
$$C_I = 1700pF$$
$$C_S = 5.5pF$$
$$C_U = 27pF$$

Firstly, we neglect C_A and C_B because they are so small. Then we note that the parallel combination of C_S and C_U is in series with C_T and C_I. Since C_S and C_U are much smaller, they will dominate the series combination and hence the overall capacitance of the device.

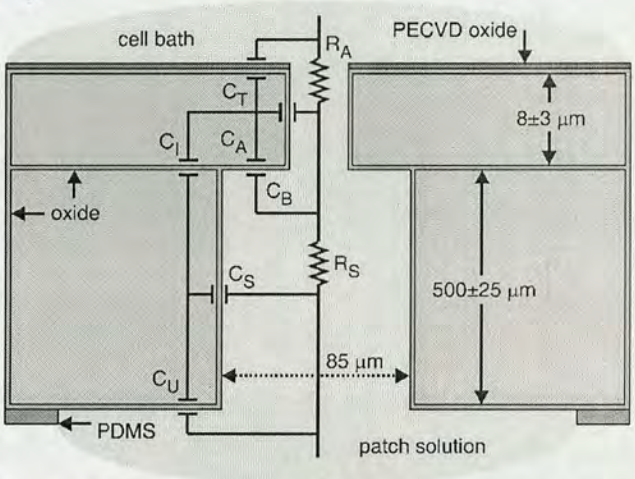

Fig. 7: Electrical circuit diagram illustrating the capacitive and resistive components in the patch device. The Figure is not drawn to scale.

Hence, the capacitance of the device is approximately equal to C_S + C_U = 32.5 pF. The variation in device capacitance values probably arises from variation in C_U. C_U is largely determined by the underside area covered by PDMS. Since this was applied by hand there was limited control over this process (see table 2). Although the capacitance values are considerably larger than those of pipettes of a similar bore, the resistance is somewhat smaller, so the time constant of the device is within an acceptable range.

C. Seal formation results

Fig 8 shows voltage deflection versus time associated with seal formation on an isolated snail neuron. Negative current pulses of constant amplitude were passed through the device and the resultant voltage deflection was used to assess seal resistance.

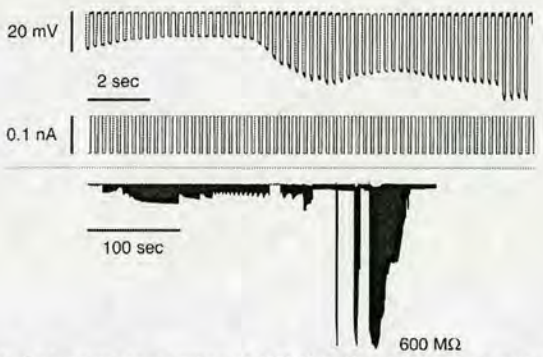

Fig. 8: Seal-resistance recording at 600 M□. Resistance was monitored by injection of 0.1-nA current steps at a period of 250 ms.

Seal resistances of up to 600 M□ were obtained, however these were usually transient in nature. Electrical activity was not observed during seal formation and whole cell access was not achieved. It was therefore impossible to verify that the increase in resistance observed following the application of negative pressure was anything other than aperture blockage and seal formation onto debris. Attempts at improved seal formation and verification of real cellular attachment are ongoing using a variety of cell types.

IV. Discussion

The data presented in this paper shows that we have achieved our main goals in terms of the physical attributes of the patch devices. We have produced circular apertures of an appropriate diameter. We have used a buried oxide layer to produce an aperture with a depth of approximately 8μm to allow sufficient area of silicon/membrane interaction for seal formation. By using PECVD deposition we have improved the profile of the aperture from that formed by thermal oxidation alone. All of these features are potentially important in the facilitation of seal formation as reviewed for planar patch devices in Sigworth and Klemic [33]. In addition by using a vertical deep etch process for the reverse side hole we have allowed for the integration of these electrodes into a 100μm pitch array.

As outlined in the electrical circuit model the main problem associated with the electrical characteristics of the devices was the parasitic capacitance associated with solution /silicon contact on the underside. This was reduced substantially by the application of PDMS. However, our inability to automate this process meant that there was a limit to how close to the hole one could apply the PDMS by hand without the risk of blocking the hole. The underside area that was successfully coated inevitably varied from device to device and probably introduced the variability in capacitance measured between devices.

How much does this comparatively large capacitance limit the usefulness of the device? During discontinuous voltage clamp the electrode capacitance limits the frequency of the sample/current inject cycle. A familiar rule of thumb is that the membrane time constant of a cell should be ten times that of the pipette [34]. Typical membrane time constants of mammalian hippocampal pyramidal cells range from 20 to 40 ms [35]. These values are well within the limiting value of 0.8 ms (10×0.08 ms see table 2) obtained for our electrodes. However, if one considers the intended application of these patch devices (that is, in an array with ~100 μm spacing) it is apparent that some sort of micro-fluidic platform will be required to confine the solution for each hole. In this case, C_U (see circuit model in results section) will be eliminated, and C_S (=5.5 pF) will be the sole contributor to device capacitance, which will be superior to that of a pipette.

At present there is no definitive model that explains the physical processes that underlie the phenomena of seal formation. The initiation of seal formation involves the application of negative pressure to draw a membrane 'bleb' into the pipette [18], [36], [37]. Sokabe, Sachs and Jing [38] produced evidence to suggest that during giga-seal formation the lipid bilayer moves up the pipette while a separate sealable region remains stationary. It was suggested that membrane proteins denature, anchor and support the lipid attachment to the pipette wall. This requirement for lipid flow over the sealable surface without membrane damage would suggest the need for a smooth aperture profile without sharp edges. In addition Sokabe and Sachs [37] suggest that once the membrane is drawn into the pipette the high seal resistance is distributed throughout the length of the patch and that the seal resistance per unit length is very high. In our electrode design the smooth aperture profile and the 8μm aperture depth should allow for both of these requirements to be fulfilled [36].

Common to most examples of seal formation is the use of high energy surfaces. In a conventional patch clamp this takes the form of borosilicate glass. The disorder inherent in the amorphous structure of glass presents non-bonded oxygen groups at the surface. This is also true for non glass silicon oxide used in microfabrication processes. The surface is composed of a mixture of siloxane (Si-O-Si) and silanol (Si-OH) groups. The silanol groups dissociate in an aqueous environment in a pH dependent manner [39]. For silicon oxide the isoelectric point is at a pH of about 3, meaning that in a physiologically buffered media most of the hydroxyl groups will dissociate revealing a negatively charged oxygen moiety [40]. This allows for electrostatic interaction with other chemical groups and is responsible for the surface high energy nature (considered below). The overall similarity in chemical structure between the surface of glass and other forms of silicon oxide would suggest that seal formation is a possibility with the latter. In the design outlined in this paper we have attempted to make the similarities even greater by introducing a boron doping step as a final surface treatment. The possible benefits of using a high energy surface was shown by Klemic et al, [26] where they showed an increased probability of seal formation on a planar device, associated with an increase in the hydrophilic nature of PDMS following 'activation' with oxygen plasma.

In 1983 Corey and Stevens [41] developed a mathematical

model to estimate separating distances required between glass and membrane to produce seal resistances ranging from 1-10 giga-ohm. The values obtained of 1-10 angstrom suggest chemical bonding may be responsible for high seal resistance. Many types of electrostatic bond are possible between a glass and lipid/protein surface. These include electrovalent bonding, hydrogen bonding, formation of salt bridges [42], dispersion forces and dipole-dipole interaction. Regardless of the exact types of bond involved it is thought that in general a close apposition, in the order of angstroms, is required for seal formation. Thus a limiting factor of huge significance in the process of seal formation is surface roughness. Unfortunately, although the use of PECVD as a surface has allowed us to modify the profile of the etched aperture, the surface roughness may well be preventing adequate seal formation. Even the reduced roughness of the boron doped surfaces are higher than that measured for a borosilicate coverslip (see results section A) and it is probable that a freshly fire polished pipette tip is even smoother. So, although our aperture design has fulfilled many of the requirements for a successful patch aperture (size, depth of patchable surface, smooth profile and appropriate surface in terms of electrostatic bonding potential) the surface roughness may well be precluding the successful formation of high resistance seals. Work to test these devices with other cell types and preparations is on going.

REFERENCES

[1] P. F. Baker, T. I. Shaw and A. L. Hodgkin, , "Replacement of axoplasm of giant nerve fibres with artificial solutions", *Journal of Physiology-London*, vol. 164, no. 2, p. 330-&, 1962.

[2] A. L. Hodgkin, A. F. Huxley and B. Katz, "Ionic currents underlying activity in the giant axon of the squid", *Archives des Sciences Physiologiques*, vol. 3, no. 2, pp. 129-150, 1949.

[3] A. L. Hodgkin, A. F. Huxley and B. Katz, "Measurement of current-voltage relations in the membrane of the giant axon of Loligo", *Journal of Physiology-London*, vol. 116, no. 4, pp. 424-448, 1952.

[4] B. Katz, *Nerve, Muscle, and Synapse,* McGraw-Hill, London, 1966.

[5] P. Connolly, P. Clark, A. S. G. Curtis, J. A. T. Dow and C. D. W. Wilkinson, "An extracellular microelectrode array for monitoring electrogenic cells in culture", *Biosensors & Bioelectronics*, vol. 5, no. 3, pp. 223-234, 1990.

[6] A. S. G. Curtis, L. Breckenridge, P. Connolly, J. A. T. Dow, C. D. W. Wildinson and R. Wilson, "Making real neural nets - design criteria", *Medical & Biological Engineering & Computing*, vol. 30, no. 4, pp. CE33-CE36, 1992.

[7] M. Maher, J. Pine, J. Wright and Y. C. Tai, "The neurochip: a new multielectrode device for stimulating and recording from cultured neurons", *Journal of Neuroscience Methods*, vol. 87, pp. 45-56, 1999.

[8] M. Jenkner and P. Fromherz, "Bistability of membrane conductance in cell adhesion observed in a neuron transistor", *Physical Review Letters*, vol. 79, no. 23, pp. 4705-4708, 1997.

[9] T. B. DeMarse, D. A. Wagenaar, A. W. Blau and S. M. Potter, "The neurally controlled animat: biological brains acting with simulated bodies", *Autonomous Robots*, vol. 11, pp. 305-310, 2001.

[10] W. Nakamura, S. Honma, T. Shirakawa and K. I. Honma, "Clock mutation lengthens the circadian period without damping rhythms in individual SCN neurons", *Nature Neuroscience*, vol. 5, no. 5, pp. 399-400, 2002.

[11] S. M. Potter and T. B. DeMarse, "A new approach to neural cell culture for long-term studies", *Journal of Neuroscience Methods*, vol. 110, pp. 17-24, 2001.

[12] E. Neher, "Molecular biology meets microelectronics", *Nature Biotechnology*, vol. 19, p. 114, 2001.

[13] P. Fromherz, "Extracellular recording with transistors and the distribution of ionic conductances in a cell membrane", *European Biophysical Journal*, vol. 28, pp. 254-258, 1999.

[14] M. Steriade, "Impact of network activities on neuronal properties in cortico-thalamic systems", *Journal of Neurophysiology*, vol. 86, no. 1, pp. 1-39, 2001.

[15] A. Rauch, G, La Camera, H. R. Luscer, W. Senn and S. Fusi, "Neocortical pyramidal cells respond as integrate and fire neurons to invivo-like input currents", *Journal of Neurophysiology*, vol. 90, pp. 1598-1612, 2003.

[16] L. G. Brock, J. S. Coombs and J. C. Eccles, "The recording of potentials from motor neurones with an intracellular electrode", *Journal of Physiology-London*, vol. **117**, no. 4, pp. 431-460, 1952.

[17] E. Neher and B. Sakmann, "Single channel currents recorded from membrane of denervated frog muscle fibres", *Nature*, vol. 260, pp. 799-802, 1976.

[18] O. Hamill, A. Marty, E. Neher, B. Sakmann and F. Sigworth, "Improved patch-clamp techniques for high-resolution current recording from cells and cell-free membrane patches", *Pflügers Archiv European Journal of Physiology*, vol. 391, pp. 85-100, 1981.

[19] K. J. Staley, T. S. Otis and I. Mody, "Membrane properties of dentate gyrus granule cells: comparison of sharp microelectrodes and whole cell recordings", *Journal of Neurophysiology*, vol. 67, pp. 1346-1358, 1992.

[20] R. M. Fitzsimonds, H. J. Song and M. M. Poo, "Propagation of activity-dependent synaptic depression in simple neural networks", *Nature*, vol. 388, no. 6641, pp. 439-448, 1997.

[21] N. Fertig, A. Tilke, R. H. Blick and J. P. Kotthaus, "Stable integration of isolated cell membrane patches in a nanomachined aperture", *Applied Physics Letters*, vol. 77, no. 8, pp. 1218-1220, 2002..

[22] C. Schmidt, M. Mayer and H Vogel, , "A chip-based biosensor for the functional analysis of single ion channels", *Angewandte Chemie*, vol. 39, no. 17, pp. 3137-3140, 2000.

[23] N. Fertig, Ch. Meyer, R. H. Blick, Ch. Trautmann and J. Behrends, , "Microstructured glass chip for ion-channel electrophysiology", *Physical Review E*, vol. 64, pp. 040901-1-040901-4, 2002.

[24] N. Fertig, M. Klau, M. George, R. H. Blick and J. Behrends, , "Activity of single ion channel proteins detected with a planar microstructure", *Applied Physics Letters*, vol. 81, no. 25, pp. 4865-4867, 2002..

[25] N. Fertig, R. H. Blick and J. Behrends, "Whole cell patch clamp recording performed on a planar glass chip", *Biophysical Journal*, vol. 82, pp. 3056-3062, 2002.

[26] K. Klemic, J. Klemic, M. Reed and F. Sigworth, "Micromolded PDMS planar electrode allows patch clamp electrical recordings from cells", *Biosensors and Bioelectronics*, vol. 17, pp. 597-604, 2002.

[27] B. Matthews and J. Judy, "Characterization of a micromachined planar patch clamp for cellular electrophysiology", *Proceedings of the 1st International IEEE EMBS Conference on Neural Engineering* pp. 648-651, 2003.

[28] P. Moore, "Cell biology: ion channels and stem cells", *Nature*, vol. 438, pp. 699-702, 2005.

[29] H. M. S. Coxeter, "Differential geometry of curves," in *Introduction to Geometry*, 2nd edn, John Wiley & Sons, Inc., 1969, pp. 307-327.

[30] J. D. Thomas, A. S. Lough and R. W. Lodge, "Chemical ecology of biomphalaria-glabrata (say), snail host of schistosoma-mansoni sambon - search for factors in media conditioned by snails which inhibit their growth and reproduction", *Journal of Applied Ecology*, vol. 12, no. 2, pp. 421-436, 1975.

[31] D. J. Goldberg and S. Schacher, "Culturing the large neurons of aplysia," in *Culturing Nerve Cells*, 2nd edn, G. Banker & K. Goslin, eds., MIT Press, London, 1998, pp. 213-236.

[32] P. F. Soest and K. S. Kits, "Conopressin affects excitability, firing, and action potential shape through stimulation of transient and persistent inward currents in mulluscan neurons", *Journal of Neurophysiology*, vol. 79, no. 4, pp. 1619-1632, 1998.

[33] F. Sigworth and K Klemic, *Patch Clamp on a Chip*, Biophysical Society, 2002.

[34] R. Sherman-Gold, , *The Axon Guide for Electrophysiology & Biophysics Laboratory Techniques* Axon Instruments, Inc., Foster City, CA., 1993.

[35] N. P. Staff, H. Jung, T. Thiagarajan, M. Yao and N. Spruston, , "Resting and active properties of pyramidal neurons in subiculum and CA1 of rat

hippocampus", *Journal of Neurophysiology*, vol. 84, no. 5, pp. 2398-2408, 2000.

[36] B. Sakmann and E. Neher, "Geometric parameters of pipettes and membrane patches," in *Single-Channel Recording*, 1st edn, Plenum Press, New York, 1983, pp. 37-51.

[37] M. Sokabe and F. Sachs, "The structure and dynamics of patch-clamped membranes: a study using differential interference contrast light microscopy", *The Journal of Cell Biology*, vol. 111, pp. 599-606, 1990.

[38] M. Sokabe, F. Sachs and Z. Jing, "Quantitative video microscopy of patch clamped membranes stress, strain, capacitance, and stretch channel activation", *Biophysical Journal*, vol. 59, pp. 722-728, 1991.

[39] W. Stumm, *Chemistry of the Solid Water Interface* Wiley, New York. 1992.

[40] G. A. Parks, "The isoelectric points of solid oxides, solid hydroxides and aqueous hydroxo complex systems", *Chemical Review*, vol. 65, pp. 177-198, 1965.

[41] D. P. Corey and C. F. Stevens, , "Science and Technology of Patch-Recording Electrodes," in *Single-Channel Recording*, 1st edn, Plenium Press, New York, 1983, pp. 53-68.

[42] Z. Gil, A. Priel, V. T. Moy, K. L. Magleby and S. D. Silberberg, "Conditions affecting seal formation in patch-clamp recording", *Biophysical Journal*, vol. 80, no. 1, p. 1858, 2001.

References

[1] B. Dworak, *The Integration and Miniaturisation of the Patch-Clamp Technique into Planar Silicon-based Microstructures for the Electrophysiological Study of Network Behaviour.* PhD thesis, School of Engineering and Electronics, University of Edinburgh, February 2005.

[2] S. Potter, "http://www.neuro.gatech.edu/," 2005.

[3] B. Sakmann and E. Neher, "Geometric parameters of pipettes and membrane patches," *In 'Single Channel Recording' Ed. Sakmann and Neher*, pp. 37–51, 1995.

[4] B. Deal and A. Grove, "General relationship for thermal oxidation of silicon," *Journal of Applied Physics*, vol. 36, p. 3770, 1965.

[5] Inspec, *Properties of Silicon.* EMIS datareviews series No.4, Inspec, 1988.

[6] S. Mittman, D. Flaming, D. Copenhagen, and J. Belgurn, "Bubble pressure measurement of micropipet tip outer diameter," *Journal of Neuroscience Methods*, vol. 22, p. 161, 1987.

[7] P. Baker, T. Shaw, and A. Hodgkin, "Replacement of axoplasm of giant nerve fibres with artificial solutions," *Journal of Physiology-London*, vol. 164 (2), p. 330, 1962.

[8] A. Hodgkin, A. Huxley, and B. Katz, "Ionic currents underlying activity in the giant axon of the squid," *Archives des Sciences Physiologiques*, vol. 3 (2), pp. 129–150, 1949.

[9] A. Hodgkin, A. Huxley, and B. Katz, "Measurement of current-voltage relations in the membrane of the giant axon of loligo," *Journal of Physiology-London*, vol. 116 (4), pp. 424–448, 1952.

[10] B. K. and, "Nerve, muscle, and synapse," *McGraw-Hill, London.*, 1966.

[11] P. Connolly, P. Clark, A. Curtis, J. Dow, and C. Wilkinson, "An extracellular microelectrode array for monitoring electrogenic cells in culture," *Biosensors & Bioelectronics*, vol. 5 (3), pp. 223–234, 1990.

[12] A. Curtis, L. Breckenridge, P. Connolly, J. Dow, C. Wilkinson, and R. Wilson, "Making real neural nets - design criteria," *Medical & Biological Engineering & Computing*, vol. 30 (4), pp. ce33–ce36, 1992.

[13] M. Maher, J. Pine, J. Wright, and Y. Tai, "The neurochip: a new multielectrode device for stimulating and recording from cultured neurons," *Journal of Neuroscience Methods*, vol. 87, pp. 45–56, 1999.

[14] M. Jenkner and P. Fromherz, "Bistability of membrane conductance in cell adhesion observed in a neuron transistor," *Physical Review Letters*, vol. 79 (23), pp. 4705–4708, 1997.

[15] T. DeMarse, D. Wagenaar, A. Blau, and S. Potter, "The neurally controlled animat: Biological brains acting with simulated bodies," *Autonomous Robots*, vol. 11, pp. 305–310, 2001.

[16] W. Nakamura, S. Honma, T. Shirakawa, and K. Honma, "Clock mutation lengthens the circadian period without damping rhythms in individual scn neurons," *Nature Neuroscience*, vol. 5 (5), pp. 399–400, 2002.

[17] S. Potter and T. DeMarse, "A new approach to neural cell culture for long-term studies," *Journal of Neuroscience Methods*, vol. 110, pp. 17–24., 2001.

[18] E. Neher, "Molecular biology meets microelectronics," *Nature Biotechnology*, vol. 19, p. 114, 2001.

[19] P. Fromherz, "Extracellular recording with transistors and the distribution of ionic conductances in a cell membrane," *European Biophysical Journal*, vol. 28, pp. 254–258, 1999.

[20] M. Steriade, "Impact of network activities on neuronal properties in cortico-thalamic systems," *Journal of Neurophysiology*, vol. 86 (1), pp. 1–39, 2001.

[21] A. Rauch, C. La, H. Luscer, W. Senn, and S. Fusi, "Neo-cortical pyramidal cells respond as integrate and fire neurons to invivo-like input currents," *Journal of Neurophysiology*, vol. 90, pp. 1598–1612, 2003.

[22] L. Brock, J. Coombs, and J. Eccles, "The recording of potentials from motor neurones with an intracellular electrode," *Journal of Physiology-London*, vol. 117 (4), pp. 431–460, 1952.

[23] K. Brown and D. Flaming, "New microelectrode techniques for intracellular work in small cells," *Neuroscience*, vol. 2, pp. 813–827, 1977.

[24] E. Neher and B. Sakmann, "Single channel currents recorded from the membrane of denervated frog muscle fibres," *Nature*, vol. 260, pp. 799–802, 1976.

[25] O. Hamill, "Improved patch-clamp techniques for high resolution current recording from cells and cell-free membrane patches," *Pflugers Archiv*, vol. 391, pp. 85–100, 1981.

[26] K. Staley, T. Otis, and I. Mody, "Membrane properties of dentate gyrus granule cells: comparison of sharp microelectrodes and whole cell recordings," *Journal of Neurophysiology*, vol. 67, pp. 1346–1358, 1992.

[27] R. Fitzsimonds, H. Song, Poo, and MM, "Propagation of activity-dependent synaptic depression in simple neural networks," *Nature*, vol. 388 (6641), pp. 439–448, 1997.

[28] D. Corey and C. Stevens, "Science and technology of patch-recording electrodes," *In 'Single Channel Recording' Ed. Sakmann and Neher*, pp. 53–68, 1995.

[29] Z. Gil, A. Priel, V. Moy, K. Magleby, and S. Silberberg, "Conditions affecting seal formation in patch-clamp recording," *Biophysical Journal*, vol. 80 (1), p. 1858, 2001.

[30] L. Opsahl and W. Webb, "Lipid-glass adhesion in giga-sealed patch-clamped membranes," *Biophysical Journal*, vol. 66, pp. 75–79, 1994.

[31] M. Sokabe, F. Sachs, and Z. Jing, "Quantitative video microscopy of patch clamped membranes stress, strain, capacitance, and stretch channel activation," *Biophysical Journal*, vol. 59(3), p. 722728, 1991.

[32] F. Sachs and F. Qin, "Gated, ion-selective channels observed with patch pipettes in the absence of membranes: Novel properties of a gigaseal," *Biophysical Journal*, vol. 65, pp. 1101–1107, 1993.

[33] R. Levis and J. Rae, "The use of quartz patch pipettes for low noise single channel recording," *Biophysical Journal*, vol. 65, pp. 1666–77, 1993.

[34] P. Coleman and R. Miller, "Measurement of passive membrane parameters with whole-cell recording from neurons in the intact amphibian retina," *J Neurophysiology*, vol. 61, pp. 218–230, 1989.

[35] M. Sokabe and F. Sachs, "The structure and dynamics of patch-clamped membranes: A study using differential interference contrast light microscopy," *Journal of cell biology*, vol. 111, pp. 599–606, 1990.

[36] A. Ruknudin, M. Song, and F. Sachs, "The ultrastructure of patch-clamped membranes: a study using high voltage electron microscopy," *Journal of Cell Biology*, vol. 112 (1), pp. 125–134, 1991.

[37] R. Penner, "A practical guide to patch clamping," *In 'Single Channel Recording' 2nd Edition ed. Sakmann and Neher*, pp. 3–30, 1995.

[38] N. Fertig, A. Tilke, R. Blick, J. Kotthaus, J. Behrends, and B. ten, "Stable integration of isolated cell membrane patches in a nanomachined aperture," *Applied Physics Letters*, vol. 77, p. 1218, 2000.

[39] C. Schmidt, M. Mayer, and H. Vogel, "A chip-based biosensor for the functional analysis of single ion channels," *Angew. Chem. Int. Ed. Engl.*, vol. 39, p. 3137, 2000.

[40] S. Pandey, R. Mehrotra, S. Wykosky, and M. White, "Characterization of a mems biochip for planar patch-clamp recording," *Semiconductor Device Research International Symposium*, pp. 278–279, 2003.

[41] F. Sigworth and K. Klemic, "Patch clamp on a chip," *Biophys. J.*, vol. 82(6), pp. 2831–2, 2002.

[42] S. Pandey, R. Mehrotra, M. Chabalko, A. Bortei-Doku, and M. White, "A biomems platform for planar patch-clamping," *Semiconductor Device Research International Symposium*, pp. 316–317, 2005.

[43] S. Pedersen, J. Kutchinsky, S. Friis, K. Krzywkowski, C. Tracy, R. Vestergaard, C. Sorensen, H. Vennerberg, and R. Taboryski, "An electrophysiological lab on a chip," *Transducers*, vol. 2, pp. 1059–1062, 2003.

[44] M. Asmild, "Upscaling and automation of electrophysiology: Toward high throughput screening in ion channel drug discovery," *Receptor and Channels*, vol. 9, pp. 49–58, 2003.

[45] N. Willumsen, "Increased throughput in ion channel drug development and exploration by automation of electrophysiology," *American Biotechnology Laboratory*, vol. March, 2006.

[46] P. van Stiphout, T. Knott, T. Danker, and A. Stett, "3d microfluidic chip for automated patch-clamping," *Mikrosystemtechnik Kongress*, pp. 435–438, 2005.

[47] A. Stett, C. Burkhardt, U. Weber, S. van, and T. Knott, "Cytocentering: A novel technique enabling automated cell-by-cell patch clamping with the cytopatch chip.," *Receptors and Channels*, vol. 9 (1), pp. 59–66, 2003a.

[48] T. Lehnert, M. Gijs, R. Netzer, and U. Bischoff, "Realization of hollow sio2 micronozzles for electrical measurements on living cells," *App. Phys. Let.*, vol. 81(26), pp. 5063–5065, 2002.

[49] T. Lehnert, A. Laine, and M. Gijs, "Surface modification of sio2 micro-nozzles," *7th lnternational Conference on Miniaturized Chemical and Blochemical Analysis Systems*, p. 1085, 2003.

[50] S. Gilmour, "Low-contact-angle polydimethyl siloxane (pdms) membranes for fabricating micro-bioarrays," *Proc.of the 2nd Ann. International IEEE-EMBS Special Topic Conference on Microtechnologies in Medicine & Biology*, vol. 52, 2002.

[51] R. Pantoja and al. et, "Silicon chip-based patch-clamp electrodes integrated with pdms microfluidics," *Biosensors and Bioelectronics*, vol. 20 (3), pp. 509–517, 2004.

[52] N. Picollet-D'Hahan, "A silicon based multipatch device for ion channel current sensing," *Sensor Letters*, vol. 2, pp. 91–94, 2004.

[53] T. Sordel, "Hourglass sio2 coating increases the performance of planar patch-clamp," *Journal of Biotechnology*, vol. 125(1), pp. 142–154, 2006.

[54] B. Matthews and J. Judy, "Characterization of a micromachined planar patch clamp for cellular electrophysiology," *Proceedings of the First International IEEE EMBS Conference on Neural Engineering*, pp. 648–51, 2003.

[55] B. Matthews and J. Judy, "Design and fabrication of a micromachined planar patch-clamp substrate with integrated microfluidics for single-cell measurements," *JMEMS*, vol. 15 (1), pp. 214–222, 2006.

[56] R. Erdrei, E. Shauly, and A. Hoffman, "Atomic force microscope study of amorphous silicon and polysilicon low-pressure chemical-vapor-deposited implanted layers," *Journal of Vacuum Science & Technology B: Microelectronics and Nanometer Structures*, vol. 18, pp. 41–47, 2000.

[57] K. Cheung, T. Kubow, and L. Lee, "Individually addressable planar patch clamp array," *2nd Annual International IEEE-EMB Special Topic Conference on Microtechnologies in Medicine and Biology*, pp. 71–5, 2002.

[58] N. Fertig, "Microstructured glass chip for ion-channel electrophysiology," *Phys. Rev. E*, vol. 64, pp. 040901 1–4, 2001.

[59] N. Fertig, M. Klau, M. George, R. Blick, and J. Behrends, "Activity of single ion channel protiens detected with a planar microstructure," *Applied Physics Letters*, vol. 81 (25), pp. 4865–4867, 2002a.

[60] N. Fertig, R. Blick, and J. Behrends, "Whole cell patch clamp recording performed on a planar glass chip," *Biophys. J.*, vol. 82(6), pp. 3056–62, 2002b.

[61] A. Brueggemann, M. George, M. Klau, M. Beckler, J. Steindl, J. Behrends, and N. Fertig, "Ion channel drug discovery and research: The automated nano-patch-clamp technology," *Current Drug Discovery Technologies*, vol. 1 (1), pp. 91–96, 2004.

[62] J. Xu, "A benchmark study with sealchip planar patch clamp technology," *Assay Drug Dev. Tech.*, vol. 1, pp. 675–684, 2003.

[63] K. Klemic and J. Klemic, "Micromolded pdms planar electrode allows patch clamp electrical recordings from cells," *Biosens. Bioelectron.*, vol. 17, p. 597, 2002.

[64] K. Klemic, J. Klemic, and F. Sigworth, "An air-molding technique for fabricating pdms planar patch-clamp electrodes," *Pflugers Archives*, vol. 449(6), pp. 564–572, 2005.

[65] X. Li, K. Klemic, M. Reed, and F. Sigworth, "Microfluidic system for planar patch clamp electrode arrays," *Nano Letters*, vol. 4(6), pp. 815–819, 2006.

[66] J. Seo, C. Ionescu-Zanetti, J. Diamond, R. Lal, and L. Lee, "Integrated multiple patch-clamp array chip via lateral cell trapping junctions," *Applied Physics Letters*, vol. 84, pp. 1973–1975, 2004.

[67] P. Hung, A. Lau, and L. Lee, "Raised lateral patch clamp array," *Microtechnology in Medicine and Biology, 3rd IEEE/EMBS Special Topic Conference on*, pp. 368–370, 2005.

[68] L. Kiss, "High throughput ion-channel pharmacology: Planar-array-based voltage clamp," *ASSAY and Drug Development Technologies*, vol. 1 (1), pp. 127–135, 2003.

[69] K. Schroeder, B. Neagle, D. Trezise, and J. Worley, "Ionworks ht: A new high-throughput electrophysiology measurement platform.," *Journal of Biomolecular Screening*, vol. 8 (1), pp. 54–60, 2003.

[70] R. Horn and A. Marty, "Muscarinic activation of ionic currents measured by a new whole-cell recording method," *Journal of General Physiology*, vol. 92, pp. 145–159, 1988.

[71] R. Mathias, I. Cohen, and C. Oliva, "Limitations of the whole cell patch clamp technique in the control of intracellular concentrations," *Biophys. J.*, vol. 58, pp. 759–770, 1990.

[72] A. Finkel and al. et, "Population patch clamp improves data consistency and success rates in the measurement of ionic currents," *Journal of Biomolecular Screening*, vol. 11 (5), pp. 488–496, 2006.

[73] A. Stett, V. Bucher, C. Burkhardt, U. Weber, and W. Nisch, "Patch-clamping of primary cardiac cells with microopenings in polyimide films," *Medical & Biological Engineering & Computing*, vol. 41 (2), pp. 223–240, 2003b.

[74] A. Han, E. Moss, R. Rabbitt, K. Engisch, and A. Frazier, "A single cell multi-analysis system for electrophysiological studies," *Transducers*, vol. 1, pp. 674–677, 2003.

[75] R. Compton, "Pecvd: A versatile technology," *Semiconductor International*, vol. July, pp. 60–65, 1992.

[76] S. M. Sze, *Semiconductor Devices, Physics and Technology*. Wiley, 2001.

[77] S. McAuley, H. Ashraf, L. Atabo, A. Chambers, S. Hall, J. Hopkins, and G. Nicholls, "Silicon micromachining using a high-density plasma source," *Journal of Physics D: Applied Physics*, vol. 34, pp. 2769–2774, 2001.

[78] M. Blauw, T. Zijlstra, and E. van-der Drift, "Balancing the etching and passivation ratio in time-multiplexed deep dry etching of silicon," *Journal of Vacuum Science and Technology B*, vol. 19 (6), pp. 2930–4, 2001.

[79] "www.warneronline.com."

[80] W. Hau, D. Trau, N. Sucher, M. Wong, and Y. Zohar, "Surface-chemistry technology for microfluidics," *Journal of Micromechanics and Microengineering*, vol. 13, pp. 272–278, 2003.

[81] M. Blauw, "Deep anisotropic dry etching of silicon microstructures by high density plasmas," *PhD Thesis, DIMES, Delft*, 2004.

[82] M. Lee and M. Wu, "Thermal annealing in hydrogen for 3-d profile transformation on silicon-on-insulator and sidewall roughness reduction," *JMEMS*, vol. 15 (2), pp. 338–43, 2006.

[83] M. Tyagi, "Introduction to semiconductor materials and devices," *John Wiley & Sons*, 1991.

[84] R. Sherman-Gold, "Axon guide," *Axon Instruments Inc.*, 1993.

[85] N. Staff, H. Jung, T. Thiagarajan, M. Yao, and N. Spruston, "Resting and active properties of pyramidal neurons in subiculum and ca1 of rat hippocampus," *Journal of Neurophysiology*, vol. 84 (5), pp. 2398–2408, 2000.

[86] R. Veenstra, "Voltage clamp limitations of dual whole-cell gap junction current and voltage recordings. i. conductance measurements," *Biophysical Journal*, vol. 80, pp. 2231–2247, 2001.

[87] X. Lin and R. Veenstra, "Action potential modulation of connexin40 gap junctional conductance," *American Journal of Physiology*, vol. 286, pp. 1726–1735, 2003.

[88] C. Smith-Maxwell, R. Eatock, and T. Begenisich, "Induction of k-channel expression in a neuroblastoma cell line," *Journal of Neurobiology*, vol. 22 (4), pp. 327–341, 1991.

[89] R. Purves, "Microelectrode methods for intracellular recording and ionophoresis," *Academic Press*, 1981.

[90] A. Guia, X. Wang, J. Xu, K. Sithiphong, Z. Yang, C. Cui, L. Wu, E. Han, and J. Xu, "Micro-positioning enabled patch-clamp recordings on a chip," *Biophys. J. (Annual Meeting Abstracts)*, vol. 82 (1), p. 161, 2002.

[91] E. Neher, B. Sakmann, and J. Steinbach, "The extracellular patch clamp: A method for resolving currents through individual open channels in biological membranes," *Pflugers Archiv*, vol. 375, pp. 219–228, 1978.

[92] D. Lide, "C.r.c. handbook of chemistry and physics, 72nd ed.," *CRC Press*, 1991.

[93] C. Housecroft and A. Sharpe, "Inorganic chemistry," *Prentice Hall*, 2001.

[94] B. Keselowsky, D. Collard, and A. Garcia, "Surface chemistry modulates fibronectin conformation and directs integrin binding and specificity to control cell adhesion," *Journal of Biomedical Materials Research*, vol. 66A (2), pp. 247–259, 2003.

[95] C. Wertz and M. Santore, "Effect of surface hydrophobicity on adsorption and relaxation kinetics of albumin and fibrinogen: Single-species and competitive behavior," *Langmuir*, vol. 17, pp. 3006–3016, 2001.

[96] M. Segal and J. Barker, "Rat hippocampal neurons in culture: voltage-clamp analysis of inhibitory synaptic connections," *Journal of Neurophysiology*, vol. 52, pp. 469–487, 1984.

[97] B. Connors, M. Gutnick, and D. Prince, "Electrophysiological properties of neocortical neurons in vitro," *Journal of Neurophysiology*, vol. 48 (6), pp. 1302–1320, 1982.

[98] R. Sokal and F. Rohlf, "Biometry, 2nd ed.," *W.H. Freeman and Co.*, 1981.

[99] S. Glantz, "Primer of biostatistics, 4th ed.," *McGraw Hill*, 1997.

[100] A. Curtis, "Breaking the neural code," *Nature*, vol. 416, pp. 274–275, 2002.

[101] J. Chang, G. Brewer, and B. Wheeler, "A modified microstamping technique enhances polylysine transfer and neuronal cell patterning," *Biomaterials*, vol. 24, pp. 2863–2870, 2003.

[102] G. Zeck and P. Fromherz, "Noninvasive neuroelectronic interfacing with synaptically connected snail neurons immobilized on a semiconductor chip," *Proceedings of the National Academy of Sciences*, vol. 98 (18), pp. 10457–10462, 2001.

[103] P. Heyward and M. Shipley, "A device for automated control of pipette internal pressure for patch-clamp recordings," *Journal of Neuroscience Methods*, vol. 123, pp. 109–115, 2003.

[104] H. Cesiulis and M. Moroz, "Electrocystallization and electrodeposition of silver on titanium nitride," *Journal of Applied Electrochemistry*, vol. 30, pp. 1261–1268, 2000.

[105] G. Oehrlein, J. Rembetski, and E. Payne, "Study of sidewall passivation and microscopic silicon roughness phenomena in chlorine-based reactive ion etching of silicon trenches," *Journal of Vacuum Science & Technology B*, vol. 8, pp. 1199–1211, 1990.

[106] T. Smith, "Voltage and patch clamping with microelectrodes," *American Physiological Society*, 1984.

[107] A. Finkel and S. Redman, "Theory and operation of a single microelectrode voltage clamp," *J. Neurosci. Meth.*, vol. 11, pp. 107–127, 1984.